e -ISSN No: 2320 – 0847 p -ISSN No: 2320 - 0936

American Journal Of Engineering Research

Volume 2 Issue 8 - August 2013

American Journal of Engineering Research

American Journal of Engineering Research

Editorial Board

American Journal of Engineering Research (AJER)

CONTENTS

Volume-2 Issue-8

S.No.	Title Name	Page No.
01.	**The Overview of The Electrical Properties of Barium Titanate** Burcu Ertuğ	01-07
02.	**An Approach to Finite Element Analysis of Boiler Tube-Sheet** R. D. Patil, Dr. Bimlesh Kumar	08-11
03.	**GAPOD and GA DC-voltage regulator based UPFC supplementary cont roller for damping low frequency oscillations in Multi-machine power systems** Dakka. Obulesu, Dr. S.F. Kodad, Dr. B.V. Sankar Ram	12-23
04.	**Comparative Analysis of Empirical Path Loss Model for Cellular Transmission in Rivers State** B.O.H Akinwole, Biebuma J.J	24-31
05.	**Contribution of Night Time Yield to The Overall Water Production Capacity of A Simple Basin Solar Still Under Makurdi Climate** Edeoja, Alex Okibe, Ibrahim, J. Sunday, Adaba, Sediyetu	32-43
06.	**Energy Analysis For Production Of Local Alcohol (Burukutu) In Benue State, Nigeria** Ibrahim J. Sunday, Alex O. Edeoja, Ierve I. Aondover	44-50
07.	**Experimental Validation of Hottel's Transmittance Model for Estimating Beam Radiation In Makurdi Location** Edeoja, Alex Okibe, and Eloka-Eboka, C. Andrew	51-57
08.	**Industrial electrochemical: a new teaching approach** Fernando B. Mainier, Luciane P. C. Monteiro, Antonio Carlos M. Rocha, Renata J. Mainier	58-64
09	**Sustainable Power Generation by Plasma Physics** Anyaegbunam F. N. C. (Ph.D.)	65-75
10.	**Optimum Position of Outrigger System for High-Rise Reinforced Concrete Buildings Under Wind And Earthquake Loadings** P.M.B. Raj Kiran Nanduri, B.Suresh, MD. Ihtesham Hussain	76-89
11.	**Investigation of Brazed Plate Heat Exchangers With Variable Chevron Angles** S. Muthuraman	90-107
12.	**Intelligent Power Economy System (Ipes)** Salman Afghani, Mehwish Iqbal, Tayyaba Sabir, Muhammad Ishfaq Javed	108-114

13.	**Studies on Relationship Between Water/Binder Ratio And Compressive Strength Of High Volume Fly Ash Concrete** Dr Sravana, Sarika.P, Dr.Srinivasa Rao, Dr.Seshadri Sekhar T, Apparao.G	115-122

American Journal of Engineering Research (AJER)
e-ISSN : 2320-0847 p-ISSN : 2320-0936
Volume-02, Issue-08, pp-01-07
www.ajer.org

Research Paper Open Access

The Overview of The Electrical Properties of Barium Titanate

Burcu Ertuğ[1]
[1]Istanbul Technical University, Department of Metallurgical and Materials Engineering, 34469 Maslak, Istanbul, Turkey.

Abstract: **-** The perovskite family includes many titanates used in various electroceramic applications, for example, electronic, electro-optical, and electromechanical applications of ceramics. Barium titanate, perovskite structure, is a common ferroelectric material with a high dielectric constant, widely utilized to manufacture electronic components such as mutilayer capacitors (MLCs), PTC thermistors, piezoelectric transducers, and a variety of electro-optic devices. Pure barium titanate is an insulator whereas upon doping it transforms into a semiconductor. Besides PTCR properties, semiconductor barium titanate is used in the sensor applications. The ferroelectricity observed in barium titanate is utilized in memory applications, i.e RAMs. The pyroelectricity and piezoelectricity are also used in the passive infrared detectors and Sonars (Sound Navigation and Ranging). In the present study, various electrical properties of barium titanate based ceramics were explained and examples of the relevant applications were given.

Keywords: - Barium titanate, semiconductor, ferroelectricity, piezoelectricity.

I. INTRODUCTION

One of the most interesting application of $BaTiO_3$ is as semiconductor with positive temperature coefficient of resistivity (PTCR). Dopant additions are needful to the host titanate composition to achieve PTCR property enhancement. It is possible to use some trivalent rare earth elements for substitution and to produce semiconducting behavior in the pervoskite lattice. Similarly, pentavalent dopants (Sb, Nb, Ta) can also produce semiconduction by substitution at Ti^{4+}lattice sites[1].

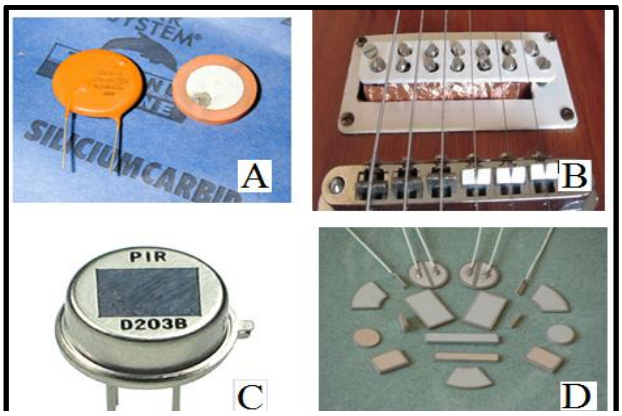

Figure 1 A. Ferroelectric capacitor[2], B. Piezoelectric electronic guitar pick up[3], C.Passive infrared sensor[4] and D. PTC elements[5].

$BaTiO_3$ is well known as fundamental ferroelectric perovskite oxide and is often used in multilayer ceramic capacitors due to high dielectric constant and low loss characteristics as shown in Fig.1. Despite its relative low Curie temperature and piezoelectric properties inferior to those of $Pb(Zr,Ti)O_3$, lead-free $BaTiO_3$ remains attractive for environmental reasons[6]. $BaTiO_3$ has become one of the most important electroceramic

materials among all the ferroelectric materials.$BaTiO_3$-based ferroelectrics transform from paraelectric phase to ferroelectric phase at Curie temperature (Tc 130°C). This transformation normally causes a complicated stress system in this ferroelectric material, and then results in a generation of internal stresses at room temperature which significantly affect properties of $BaTiO_3$[7]. Also, the $BaTiO_3$ based normal ferroelectrics are strong candidates for field induced piezoelectric transducers due to their large polarizations, large permittivity and the large induced strains achievable in these materials[8]. Infrared detection employing ferroelectric sensing elementsas pyroelectrics was demonstrated over 40 years ago. Sincethat time, there have been a host of studies describing ferroelectric-based pyroelectric detectors. The mostcommercially successful pyroelectric technology to date hasutilized barium strontium titanate (BST) materials[9].

II. BARIUM TITANATE AS A SEMICONDUCTOR

II. I Donor Doping Of $BaTiO_3$

In a stoichiometric solid solution the extra positive charge of a donor center can be compensated by a cation vacancy or an anion interstitial

$$D_2O_3(2MO) = 2D^{\cdot}_M + Oo + O''_I \quad (1)$$

$$D_2O_3(3MO) = 2D^{\cdot}_M + V''_M + 3Oo \quad (2)$$

(1) maintains a perfect cation sublattice, while the anion sublattice is perfect in (2). A shift from the stoichiometric solid solution with its compensation by a lattice defect, to a non-stoichiometric solid solution with compensation by an electronic defect, requires an interaction with the ambient atmosphere. The stoichiometric solution may gain or lose oxygen at oxygen activities greater than or less than, in equilibrium with the stoichiometric composition. In this way, The compensating lattice defect is eliminated and is replaced by electrons in the case of donor dopants [10].

When La^{3+} replaces Ba^{2+} on the A-site (La is too large to replace Ti on the B-site), charge imbalance is created which must be compensated by either cation vacancies on the A- or B- site (ionic compensation), or by electrons (electronic compensation) as in (3)-(5).

$$2La_2O_3 + 3TiO_2 = 4La^{\cdot}_{Ba} + 3Ti_{Ti}^{x} + 12Oo^{x} + V_{Ti}'''' \quad (3)$$

$$2La_2O_3 + 3TiO_2 = 2La^{\cdot}_{Ba} + 3Ti_{Ti}^{x} + 9Oo^{x} + V_{Ba}'' \quad (4)$$

$$2La_2O_3 + 2TiO_2 = 2La^{\cdot}_{Ba} + 2Ti_{Ti}^{x} + 6Oo^{x} + 1/2O_2 + 2e' \quad (5)$$

Ionic compensation ([3] and [4]) should have negligible effect on the room temperature conductivity due to the immobility of cation vacancies; La doped $BaTiO_3$ compensated in this way should, therefore, remain insulating. In contrast, electronic compensation ([5]) should cause a substantial increase in conductivity, in which the number of carriers equals the La concentration[11].

Fig.2. indicates the effect of donor concentration (La^{3+}) on the electrical conductivity and grain size of $BaTiO_3$. As the donor concentration increases initially the conductivity increases up to 0.15% of La^{3+} and then decreases up to 0.3% of La^{3+}. The high conductivity region is where the electronic compensation dominates, after a critical donor concentration, cation vacancy compensation dominates and electrical conductivity decreases. Up to 0.3% of La^{3+}, the grain size of $BaTiO_3$ is not affected by donor concentration being 25 µm, however, above 0.3% of La^{3+}, grain size decreases to 5µm.

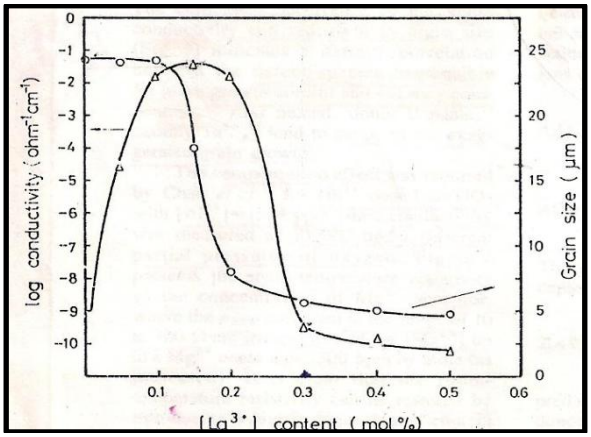

Figure 2 Schematic of donor concentration influence on room temperature electrical conductivity and grain size[10].

Donor dopant incorporation is achieved by either electronic compensation at low concentrations or vacancy compensation at high concentrations. High concentrations of segregating donors at grain boundaries inhibites grain growth. At small concentrations, donor incorporation by electronic compensation explains the high conductivity. As the average dopant concentration increases, the local donor concentration at the grain boundary increases rapidly due to segregation. The donor incorporation at the grain boundary shifts from electronic to vacancy compensation, resulting in the formation of highly resistive layers and also, grain size decreases due to significant dopant drag on the boundary mobility[12].

Poly-crystalline n-type semiconducting barium titanate ($BaTiO_3$) exhibits a behaviour known as the positive temperature coefficient of resistivity (PTCR) effect. The electrical resistivity of n-type semiconducting barium titanate increases by several orders of magnitude near the ferroelectric Curie temperature (120°C)[13].At the Curie temperature, barium titanate undergoes ferroelectric to paraelectric transition[14]. This behaviour is indicated in Fig. 3 [15].It has also been reported that single crystals of barium titanate exhibit negative temperature co-efficient of resistivity (NTCR) properties.

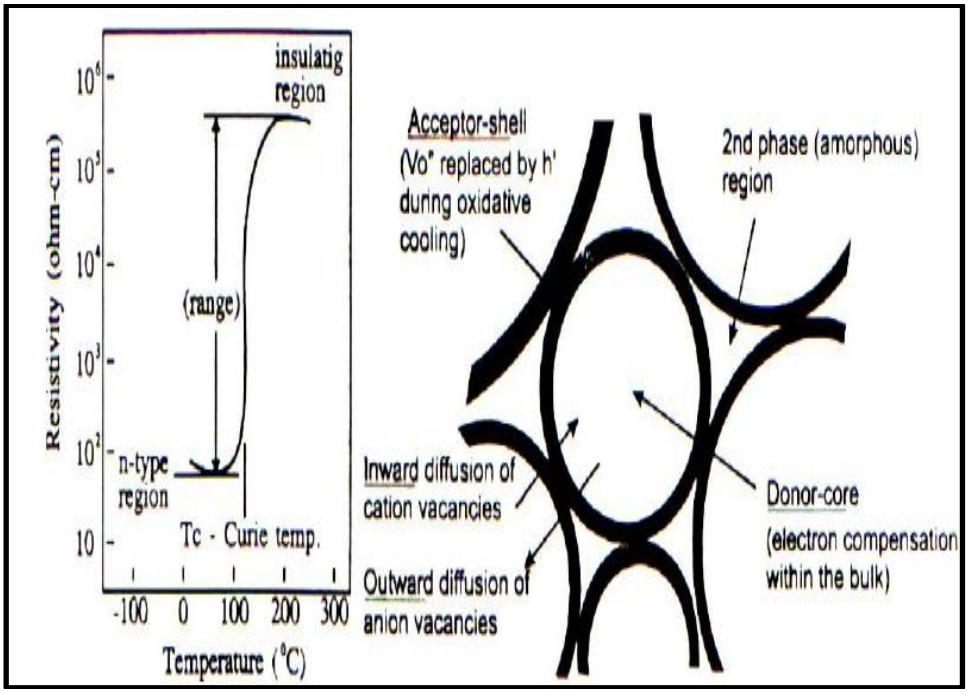

Figure 3 Electrical resistivity for typical PTCR device and schematic presentation of defect chemistry responsible for PTCR effect [16].

Sintering under O_2 atmosphere affects not only barrier height but the resistance and capacitance of grain boundaries. The effect is due to variation of the adsorbed gases at the grain boundaries. The diffusion coefficient of oxygen at grain boundary is much higher than that in bulk, which implies that there is a gradient of adsorbed oxygen density in the surface of the grain. Sintering under O_2 atmosphere results in increasing number of oxygen acceptors at the grain boundary and increase in resistance. The barrier height also increases with sintering[17]. These PTC materials prepared from doped semiconducting $BaTiO_3$ ceramics can be used in various kinds of electronic circuitry as a switching device or as a constant temperature heater. Other important application of a PTC thermistor is the measurement/detection/control of temperature or parameters related to temperature. These PTC materials are known to have the highest temperature coefficient of resistance among all sensor materials available [16].

III. FERROELECTRIC PROPERTIES OF BARIUM TITANATE

Amongst other ferroelectric materials, barium titanate ($BaTiO_3$) is a useful and technologically important material owing to its ferroelectric behavior at and above room temperature (T_c 393°K), and having polarization (Ps) values several orders higher than the potassium dihydrogen phosphate-type ferroelectrics[18]. In order to improve the electrical reliability of barium titanate, nano-sized second phases were incorporated into matrix. Dielectric constant, ε_r was 3279, which increased with additive and dielectric loss, tan δ remained constant. $BaTiO_3$ ceramic showed a slim ferroelectric loop with 4.55 kV/cm of E_c, 3.72 $\mu C/cm^2$ of P_r and 0.59 of

loop squareness (R_{sq})[7]. In an attempt to improve the dielectric properties, microwave sintering was used. As a result, ε_r and tan δ were measured as 2500 and 0.03, respectively. The sharpness of the P–E hysteresis loop indicates the better homogeneity and crystallinity of the prepared system. P_r and E_c are 6 $\mu C/cm^2$ and 1.45 kV/cm, respectively[8]. Al doped and undoped barium titanate indicated P_r of 11.4 and 5 $\mu C/cm^2$ and E_c of 4 and 3.1 kV/cm. The dielectric constant increased and dielectric loss factor decreased by doping. However, Curie transition shifted to lower temperature (from 121 to 113°C) [19].

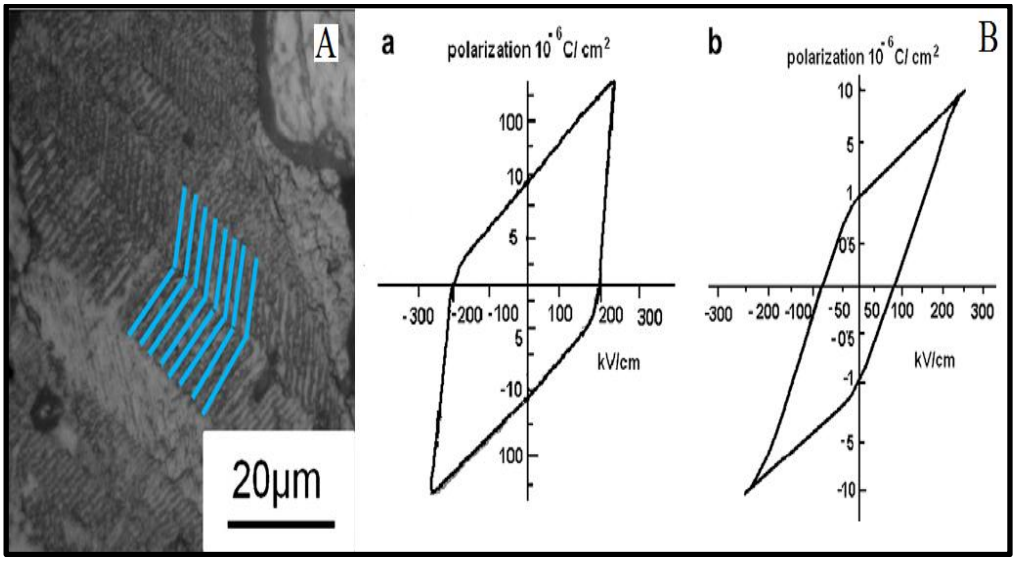

Figure 4 A. Ferroelectric domain pattern of $BaTiO_3$[20] and B. Hysteresis loop of a. pellet form and dispersed[18].

The effect of sintering temperature on the ferroelectric properties was also investigated. When the sintering temperature was raised, Curie transition shifted to higher temperature (125°C). The improved densification resulted in the reduction of cavities, thereby the dielectric constant increased. E_c and E_c are 10.2$\mu C/cm^2$ and 6.4 kV/cm, respectively. The remanent polarization, P_r first increased and then decreased with sintering temperature while coercive field, E_c increased continously. However, oxygen vacancies were easier created at high sintering temperature, which strengthen the pinning effect to the ferroelectric domain as in Fig.4.A under an electric field, thereby inducing a continuous increase of the E_c and a decline of the P_r [20].

Nano-sized barium titanate was synthesized by solid state reaction. A 100% c-oriented system gives a square loop, whereas the loop for randomly oriented grains is likely to be tilted. The hysteresis loops obtained for this study is shown in Fig.4.B.The hysteresis loop is found to be wide and stretched in the case of barium titanate nanopowders used in the form of a pellet. In contrast, the polymer-dispersed $BaTiO_3$ nanoparticle system showed a relatively narrow loop, with long tails at the ends. The remanent polarization (P_r) was found to be 10 times larger in the case of a compact nanoparticle system (10 $\mu C/cm^2$) compared to the dispersed nanoparticles (1 $\mu C/cm^2$). It is already known that a single-crystal $BaTiO_3$ system could show a P_r as large as 26 $\mu C/cm^2$. The coercive fields were found to be 200 and 70 kV/cm, respectively[18].

IV. PIEZOELECTRIC PROPERTIES OF BARIUM TITANATE

The $BaTiO_3$ based normal ferroelectrics are strong candidates for field induced piezoelectric transducers due to their large polarizations, large permittivity and the large induced strains achievable in these materials[8]. The synthesis of $BaTiO_3$ by conventional solid-state reaction and oxalate coprecipitation route was carried out. The properties of the ceramics from the coprecipation process are very good and superior to those usually published especially for the d_{33} piezoelectric coefficient. The quasi-linear relation found between d_{33} and ε_r corresponds to a g_{33} value of $14x10^{-3}$ Vm/N. In the relationship, $g_{33} = d_{33} / \varepsilon_{r33}$; $g_{33}$is the piezoelectric voltage constant (Vm / N) is the induced electric field in direction 3 (parallel to direction in which ceramic element is polarized) per unit stress applied in direction 3, d_{33} is the piezoelectric coefficient and ε_{r33} is the relative permittivity of ceramic material. This is the permittivity for dielectric displacement and electric field in direction 3 (parallel to direction in which ceramic element is polarized). $BaTiO_3$ ceramics prepared from chemical process shows dielectric and piezoelectric coefficients superior to those of other lead free materials.The piezoelectric d_{33} coefficient shows a very good stability up to $3x10^5$ V/m.The piezoelectric d_{33} constant is more than 260 pC/N at

around 25C. This value is largely higher than usually published ones for barium titanate ceramics: classically room temperature ε_r (1kHz) and d_{33} values are respectively around 1700 and 190 pC/N[6]. Fig.5 shows the development of strain vs. electric field (S–E) butterfly loop with a max. strain 0.13% at 25 kV/cm electric field, which confirms the piezoelectric nature of the microwave sintered $BaTiO_3$ samples. Piezoelectric coefficient, d_{33}, has also been calculated from converse piezoelectric effect, i.e. by using the slope of the S–E plot in the higher field region, using the relation d_{33} = ΔStrain % / Δelectric field at higher side. The d_{33} piezoelectric coefficient calculated from the slope of S–E plot is found to be 335 pm/V. The very high value of d_{33} piezoelectric coefficient in microwave sintered $BaTiO_3$ samples suggests the importance of this system for piezoelectric applications. From P–E hysteresis loop of microwave sintered $BaTiO_3$ samples, the coercive field (E_c) of microwave sintered $BaTiO_3$ samples is 1.45 kV/cm. The decrease of E_c in BaTiO3 ceramics hintstowards the easy poling process and improvement in thepiezoelectric properties[8].

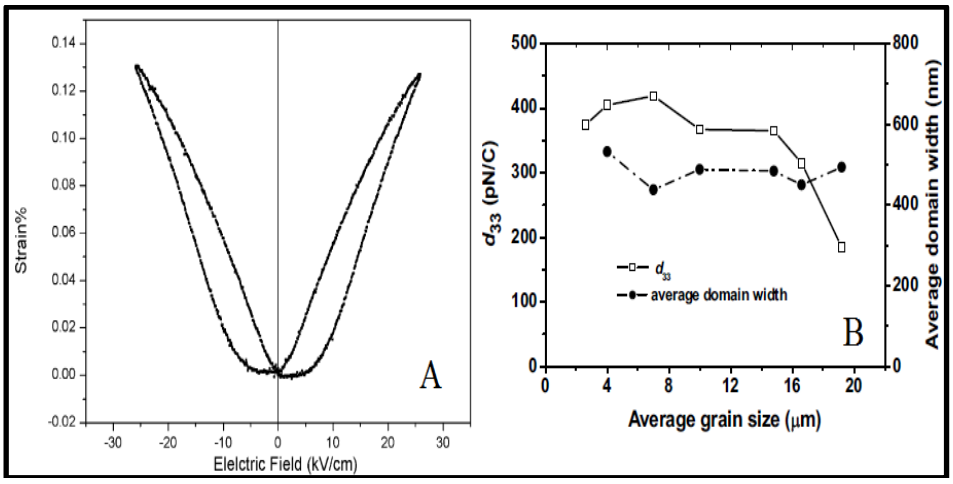

Figure 5 A. Strain vs. bipolar electric field loop of $BaTiO_3$ samples[8] and B. Changes in d_{33} and the domain width with the grain size[12].

After Al doping, d_{33} piezoelectric coefficient increased from 75 to 135pC/N. The planar electromechanical coupling factor (k_p) also increased by Al doping. Since d_{33} and k_p are proportional to P_r, large remanent polarization resulted in high piezoelectric properties. Strains of 0.085 and 0.042% were obtained for Al doped and pure samples. The planar electromechanical coupling factor (k_p) was 1.86 and 1.53 for pure and Al doped samples [19]. The effect of sintering temperature on the piezoelectric properties was also examined. Besides the high relative density and moderate grain size, the sample sintered at 1190°C is closer to the phase transition between tetragonal symmetry and orthorhombic one, which provides a favorable condition for easier motion of domain and thus gives rise to high piezoelectric properties. This may be the main reason for the excellent piezoelectric properties of the sample sintered at 1190°C[20].

The piezoelectric constant d_{33} increased significantly at room temperature with the reduction of the average grain size and reached the maxima (338 pC/N) at 0.94 μm. The average 90 domain width decreases monotonically with grain size. Both the 90 domain wall density and the area dimension of domain wall are considered as important factors that greatly influence the d_{33} value. The piezoelectric effect in perovskite-type ferroelectric ceramics is known to be greatly influenced by the movement of the 90 domain walls. The domain walls of small area dimension will respond more actively to the external electrical or stress signal. Consequently, those $BaTiO_3$ ceramics with smaller grain size showed higher d_{33} values[21]. $BaTiO_3$ ceramics with excellent piezoelectric properties of d_{33}419 pC/Nand k_p0.453 have been successfully obtained using ordinary $BaCO_3$ and TiO_2 powders. d_{33} increases with the decrease in grain size and the domain width in the poled $BaTiO_3$ ceramics is nearly independent of grain size. The d_{33} change with grain size has been explained by the area change in the domain walls[22].

V. PYROELECTRIC PROPERTIES OF BARIUM TITANATE

A common figure-of-merit for pyroelectrics is FOM= p/c (K.tanδ) $^{1/2}$. pis the pyroelectric charge coefficient, c the specific heat, and tanδ the dielectric loss tangent. Maximizing the performance of a material then involves selecting a ceramic with a high pyroelectric coefficient and low specific heat, dielectric constant, and dielectric loss factor[23].

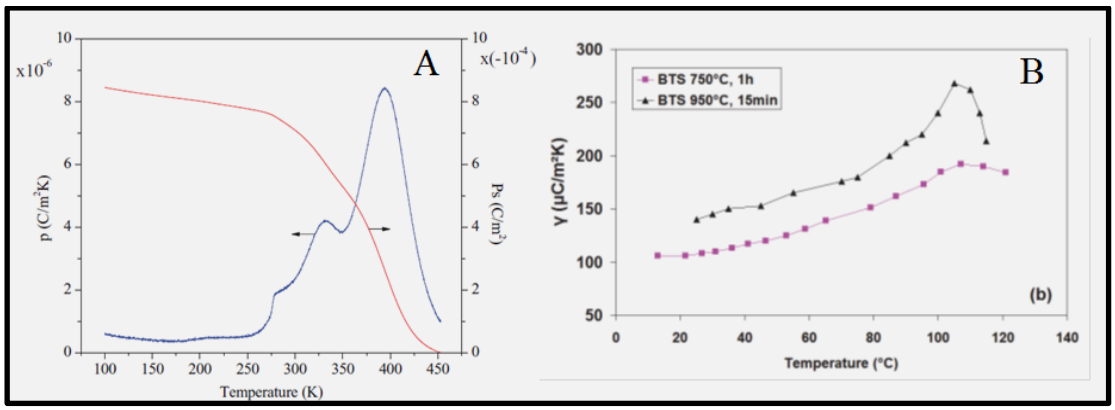

Figure 6 A. Polarization Ps and pyroelectric coefficient vs. temperature[24] and B. pyroelectric coefficient vs. temperature[25].

HA-40 wt% $BaTiO_3$ and HA-60 wt% $BaTiO_3$ composites were produced and pyroelectric properties were measured. The roomtemperature pyroelectric coefficients for both the compositions are 2.35 and 21 $\mu C/m^2K$,respectively.The pyroelectric coefficient was calculated from the pyroelectric current by p= i/A. (dT/dt) where p is the pyroelectric coefficient, i is the pyroelectric current, A is the electrode area, and (dT/dt) is the heating rate. For H6B4, the pyroelctric coefficient reaches its maximum value, 8.6 $\mu C/m^2$ K at temperature of 393°K. This temperature corresponds to the maximum polarization change and phase transition.With further increase in temperature, the polarization decreases rapidly and finally, attains a small value. For H4B6, the phase transitions at 380° K and 270 °K are clearly evident, where the peak value of the pyroelectric coefficients are 85 $\mu C/m^2K$ and 29 $\mu C/m^2K$, respectively[24]. In another study, the change in surface charge is given simply by $\Delta Q=A.\Delta Ps$ where A is the area and ΔPs is the change in spontaneous (or induced) polarization due to a temperature change, ΔTp. This formula is often normalized to produce an intrinsic quantity, called the pyroelectric coefficient, defined as $p=\Delta Q/A$. $\Delta Tp=.\Delta Ps/\Delta Tp$ [9]. In another study, the evolution of the pyroelectric coefficientas a function of temperature for two $BaTiO_3$ films doped with Tin (BTS), annealed at 750 °C during 1 h and at 950 °C 15 min. The pyroelectric coefficient varies linearly temperature. For the BTS film annealed at 950°C for 15 min, it increases from 140$\mu C/m^2K$ at 25°C to 240$\mu C/m^2K$ at 100°C. The pyroelectric properties confirms that the dielectric and the ferroelectric properties are much better with an annealed at 950°C than at 750°C. For the two BTS films the pyroelectric coefficient reaches a maximum for a temperature of 105°C which corresponds to the ferroelectric to paraelectric transition[25].

VI. CONCLUSION

Initally the discovery of the high dielectric constant and later that the discovery of the enhancement of the dielectric constant by the ferroelectricity of barium titanate ceramics led to utilization of ABO_3 crystals as ferroelectrics. The electrical poling of barium titanate provided the complete alignment of all the domains in the ceramic as in the single crystals. The relatively low Curie temperature (120°C) of barium titanate restricts its usage in high power transducers. Also the electromechanical coupling factor, kp of barium titanate is low (i.e, 0.35) with regards to other piezoelectric materials. However, barium titanate based ferroelectrics are strong candidates due to its large polarization, high permittivity and large strain. Being a lead free ferroelectric ceramic, $BaTiO_3$ is an environmentally friendly material, thus making it a good candidate for various applications. Despite a low piezoelectric constant d_{33} of 191 pC/N, the piezoelectric properties are considered to be closely related to both grain and domain sizes.

VII. ACKNOWLEDGEMENTS

This review on the electrical properties of barium titanate could not have been written without Prof.Dr.A.Okan Addemir who not only served as my PhD supervisor but also encouraged me to study on semiconducting sensors based on barium titanate. Another faculty member,Prof.Dr. Ercan Açma led me to a scheduled work on the particular subject. Assistant Prof.Dr.Tahsin Boyraz from Cumhuriyet University guided me through accomplishing experimental work on barium titanate sensors.

REFERENCES

[1]. S.Chatterjee, B.D. Stojanovic, H.S. Maiti, Effect of additives and powder preparation techniques on PTCR properties of barium titanate, Materials Chemistry and Physics, 78, 2003, 702–710.

[2]. http://www.flickr.com
[3]. http://www.gizmag.com
[4]. http://letsmakerobots.com
[5]. http://www.atct.co.il
[6]. L. Simon-Seveyrat, A. Hajjaji, Y. Emziane, B. Guiffard, D. Guyomar, Re-investigation of synthesis of $BaTiO_3$ by conventional solid-state reaction and oxalate coprecipitation route for piezoelectric applications, Ceramics International, 33, 2007, 35–40.
[7]. O. Namsar, A. Watcharapasorn, S. Jiansirisomboon, Structure–property relations of ferroelectric $BaTiO_3$ ceramics containing nano-sized Si3N4 particulates, Ceramics International, 38S, 2012, S95–S99.
[8]. Sonia, R.K. Patel, P. Kumar, C. Prakash, D.K. Agrawal, Low temperature synthesis and dielectric, ferroelectric and piezoelectric study of microwave sintered $BaTiO_3$ ceramics, Ceramics International, 38, 2012, 1585–1589.
[9]. G. Akcay, S. Zhong, S.P. Alpay, J.V. Mantese, Dynamic pyroelectric enhancement of homogeneous ferroelectric materials, Solid State Communications, 137, 2006, 589–594.
[10]. D.M. Smyth, The effects of dopants on the properties of metal oxides. Solid State Ionics, 129, 2000, 5-12.
[11]. F.D. Morrison, A.M. Coats, D.C. Sinclair, A.R. West, Charge Compensation Mechanisms in La-doped $BaTiO_3$, Journal of Electroceramics, 6, 2001, 219-232.
[12]. S.B. Desu, Interfacial Segregation in Perovskites: III, Microstructure and Electrical Properties, J. Am.Ceram.Soc., 73, 1990, 3407-15.
[13]. J.G. Kim, W.S. Cho and K. Park, PTCR characteristics in porous (Ba,Sr)TiO_3 ceramics produced by adding partially oxidized Ti powders, Materials Science and Engineering B, 77, 2000, 255-260.
[14]. J.G. Kim, W.P. Tai, K.J. Lee, W.S. Cho, Effect of polyethylene glycol on the microstructure and PTCR characteristics of n-$BaTiO_3$ ceramics, Ceramics International, 30, 2004, 2223-2227.
[15]. H.L. Wang, Structure and Dielectric Properties of Perovskite-Barium Titanate ($BaTiO_3$), Submitted in Partial Fulfillment of Course Requirement for MatE 115, San Jose State University, 2002.
[16]. M.M. Vijatovic, J.D. Bobic, B.D. Stojanovic, History and Challenges of Barium Titanate: Part II, Science of Sintering, 40, 2008, 235-244.
[17]. S. Jiang, D. Zhou, S. Gong and X. Guan, Effect of heat-treatment under oxygen atmosphere on the electrical properties of $BaTiO_3$ thermistor, Microelectronic Engineering, 66, 2003, 896-903.
[18]. A.C. Roy and D. Mohanta, Structural and ferroelectric properties of solid-state derived carbonate-free barium titanate ($BaTiO_3$) nanoscale particles, Scripta Materialia, 61, 2009, 891–894.
[19]. A.I. Ali, C.W. Ahn, Y.S. Kim, Enhancement of piezoelectric and ferroelectric properties of $BaTiO_3$ ceramics by aluminum doping, Ceramics International (In Press)
[20]. N.M., B.P. Zhang, W.G. Yang, D. Guo, Phase structure and nano-domain in high performance of $BaTiO_3$ piezoelectric ceramics, Journal of the European Ceramic Society, 32, 2012, 1059–1066.
[21]. P. Zheng, J.L. Zhang, Y.Q. Tan, C.L. Wang, Grain-size effects on dielectric and piezoelectric properties of poled $BaTiO_3$ ceramics, Acta Materialia, 60, 2012, 5022–5030.
[22]. S. Shao, J. Zhang, Z. Zhang, P. Zheng, M. Zhao, J. Liand C. Wang,High piezoelectric properties and domain configuration in $BaTiO_3$ ceramics obtained through the solid-state reaction route, J. Phys. D: Appl. Phys.,41, 2008, 125408 (5pp)
[23]. G. H. Haertling, Ferroelectric Ceramics: History and Technology, J. Am. Ceram. Soc.,82, 1999, 797–818.
[24]. A. K. Dubey, B. Basu, K. Balani, R. Guo & A. S. Bhalla, Dielectric and Pyroelectric Properties of HAp-$BaTiO_3$ Composites, Ferroelectrics, 423, 2011, 63-76.
[25]. J.C. Carru, M. Mascot and D. Fasquelle, Electrical Characterizations of Lead Free Sr and Sn Doped $BaTiO_3$ Ferroelectric Films Deposited by Sol-Gel, Ferroelectrics - Material Aspects, August, 2011.

American Journal of Engineering Research (AJER)
e-ISSN : 2320-0847 p-ISSN : 2320-0936
Volume-02, Issue-08, pp-08-11
www.ajer.org

Research Paper Open Access

An Approach to Finite Element Analysis of Boiler Tube-Sheet

R. D. Patil, Dr. Bimlesh Kumar
(Research Scholer, North Maharashtr University Jalgaon, MS, India)
(Principal, J. T. Mahajan College of Engineering, Faizpur, 425524, India.)

Abstract: - This paper work deals with the stress analysis of plates perforated by holes in square pitch pattern. For this consider the in plane loading condition. In this paper, for in plane loading a 4 x 4 pattern of hole i.e. 16 holes arranged in square pattern and subjected to uniaxial tension is considered. For this case first photo elastic models are fabricated by using photo elastic materials. Then the same models are analyzing by using the photo elastic method. The same configuration is used and tested for uniaxial tension by using the finite element method.

I. INTRODUCTION

For the structural design of various types of pressure vessels, various equations are used. These equations are based on the strength of material approach. This approach assumes that there is a continuous elastic action throughout the member and the stress distributed on any cross section of the member by a mathematical law. But these assumptions are not valid for geometric discontinuity, which is present in the section of the member. The geometric discontinuity is in the form of crack or hole or any cutout of some different shape. Due to these irregularities stresses of large magnitudes are developed in the small portion of the member. These stresses are called as the localized stresses or stress concentrations.

Flat plates with a hole, which may be subjected to different types of loads, are the best example of such localized stresses. For this analytical formulae have been developed to find out the stress concentration effects. But when there are large numbers of holes in the plate, the problem becomes complicated. Stress distribution around each hole is altered due to interaction effect of other holes. These holes may be arranged in the uniform pattern or they may be arbitrarily oriented. The holes arranged in the uniform pattern are of practical importance. Such a plate popularly known as tube plate or tube sheet.

Tube plates or tube sheets have rows of holes with diameter of 'D' and pitch 'P'. The material remaining between these holes are called ligament and the cross sectional area of the ligament compared to the area in a normal unpierced cross section of width 'P' is called ligament efficiency. In other words SCF is defined as the ratio of maximum principal stress σ_1 in the stressed model to the nominal stress applied at the boundary of the plate (σ_{nom}).

II. STATEMENT OF THE PROBLEM

The main objective is to obtain the stress distribution in a flat plate that is perforated by equal circular holes and subjected to uniaxial loads. Square pattern of holes is considered for study. The stress distribution changes with the change in ligament efficiency for any given type of loading. Therefore effect of ligament efficiency on stress concentration factor will be studied for uniaxial loading condition.

III. FINITE ELEMENT METHOD

Many times the governing differential equation for stress analysis in the field of plane stress problem for plate is invariably complex. It is extremely difficult and tedious. Sometimes it is impossible to obtain analytical solutions. Hence numerical methods are used to solve these partial differential equations. One of the most powerful techniques that have been developed in the engineering analysis is the Finite Element Method. In work, use popular software of finite element i. e. ANSYS.

Due to symmetry of geometry and load only one quarter part of the plate was modeled. Figure (1) shows plate geometry and loading for quarter part of the model.

Normal stress = 100 N/mm^2

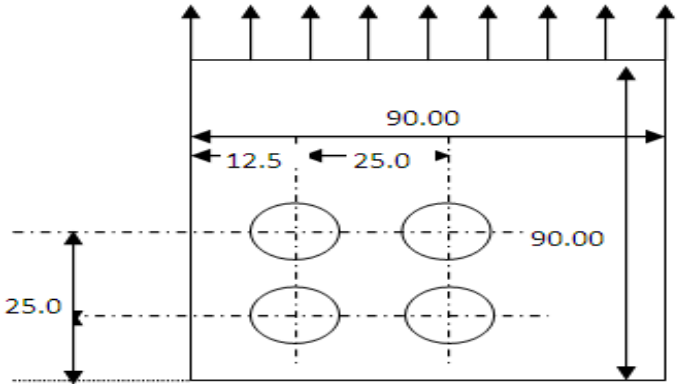

Fig.1 Plate geometry and boundary conditions.

Boundary conditions For X-Axis Ux ≠ 0 and Uy= 0 For Y-Axis Ux= 0 and Uy ≠ 0 All dimensions are in mm.

The typical area pattern used for making entire model is as shown in figure (2) Entire model was constructed by taking symmetry and translation of this typical area pattern about appropriate axis and in appropriate direction respectively. For each small area defined the element size of 3 was specified. This resulted in three divisions for each side of the area and hence 9 elements per area. Then meshing was done with the help of in built meshing facility available with ANSYS program. More fine mesh (i.e. small element size) was used around the boundaries of the holes and at the bottom left corner of the model. Figure (3) shows the mesh generated for the plate model with details regarding number of element and nodes used for analysis. Boundary conditions used for the model are as shown in figure (1).

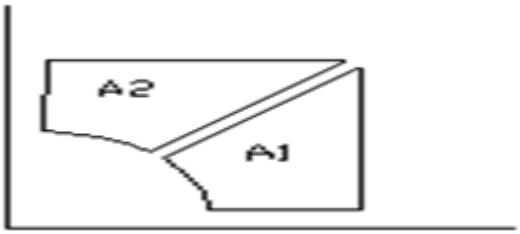

Fig.2 Typical area pattern used for model generation.

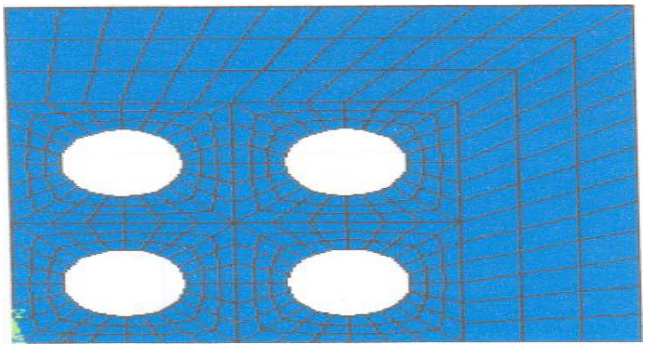

Fig. 3 Mesh generation for plate geometry.

IV. MACHINING OF MODEL

Machining of photoelastic model should not give rise to lock in stresses or residual stresses in the model. Otherwise these stresses will affect the actual stress distribution and hence fringe pattern in the model. Therefore models were machined on CNC machine or any other automatic machine, which gives constant speed and constant feed. Drilling operation was done at very low value of feed. Final hole size was obtained by using drills of gradually increasing sizes upto the desired hole size. The material fringe value is f_σ taken as 11 N/mm.

V. EXPERIMENTAL METHOD

The main motive of the experimentation is to support analytical and numerical solution. The most commonly used methods for determining stress values experimentally are strain gauges and photoelasticity principles. Overall picture of the stress distribution and regions of both high stress and low stress, are available for much detailed stress analysis in photoelasticity.

VI. EXPERIMENTAL SETUP

To give the uniformly distributed loading i. s. tensile force at the edge of the plate in the principle direction, a fixture was designed and manufactured with following guidelines. The assembly drawing of the fixture is shown in fig. 4. Figure 4 shows the modified load frame, mounted in the polariscope and the table1 shows the part list with material. The load frame consists of a power screw connected to a horizontal square bar of 25 mm size at the topside of the plate. A hole of 11mm diameter is drilled, at the center, to hold the frame under experimentation. The load cell is mounted with the help of connector 1 and connector 2 as shown in fig. 4 The load cell was employed to measure the applied tensile force. Application of the load at connector 1 configures in point load. To have the uniformly distributed load, the linkage 4 was incorporated as shown in fig. 4.This enabled the connector 1 to share the load into two parts of the boss plate.The applied load was transferred to the specimen in uniformly distributed way, through, specimen clamping plates. The clamping plates held the specimen with the help of 10 mm diameter holes, along the edge as shown in fig.4. To ensure, proper vertical alignment, welded boss, on each side of plate2 were provided. The same configuration of linkage as used in the upper edge of specimen was employed at lower edge of specimen to ensure proper fixing and loading.

The M. S. plates of thickness 5 mm were used in the fixture. The 10 mm diameter holes were drilled in the specimen plates for alignment, as shown in fig.4. The thickness of the plates was governed by the equation d = 6□t = 3mm for holes 10mm, was required but 5mm thickness is provided for safe configuration. Figure 5 and 6 shows the photograph for the experimental setup.

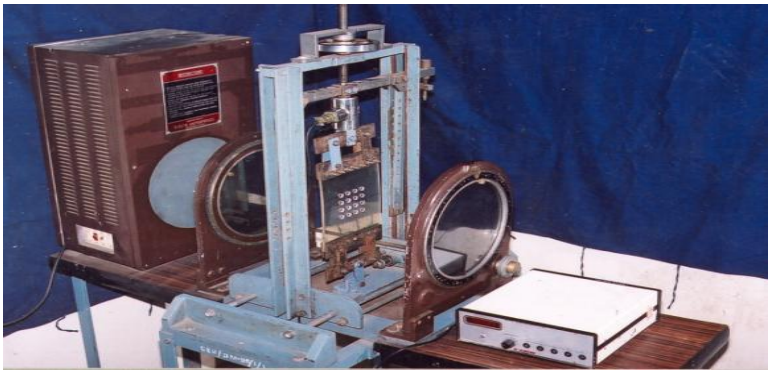

Fig.5 Experimental setup for uniform tension in photo-elasticity method.

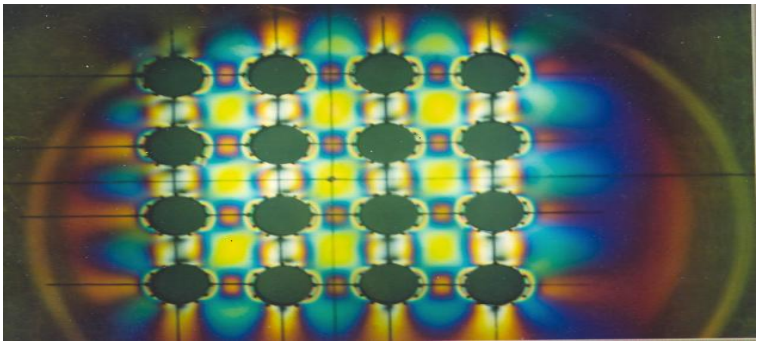

Fig.6 Fringes developed in photo-elasticity method for uniform tension.

VII. THE TEST AND RESULT

Analyzer and polariser were kept in crossed position i. s. dark field setup. Model was gradually loaded to observe the fringe growth. Fractional fringe order was measured by Tardy's compensation method. Fig 6 shows the photograph of the fringes produced on the model with holes in square pattern due to uniaxial tension. The load suspended at the pulley was 30 kg. Maximum stress is produced at the boundary of the hole shown in fig. 6.The procedure to find out the maximum stress is given below.

A circular disk specimen was employed as calibration model and obtained material fringe value, which is near about 11 N/mm for each plate. Then point of interest is marked on the specimen and plate is connected to the fixture for loading. The fixture designed for tensile tension was mounted on the polariscope along with the specimen and tensile force was given with the help of power screw. Direction of the principle stress and exact fringe order were determined by using Tardy's compensation method at point of interest. In this case the point of interest is at the hole boundary at which the value of $\sigma_2 = 0$ and σ_1 was determined by the formula.

$\sigma_1 = N \times f_\sigma / t$, Then value of SCF is given by the following equation

$SCF = \sigma_1/\sigma_{nom}$

The tests were carried out on the models with different ligament efficiencies for square pattern of holes the result for square hole pattern is tabulated in table 2. Values of SCF obtained by ANSYS program are also given in the table 6.2.The graph of SCF Vs Ligament efficiency for FEM and Photo-elasticity method are given in graph.1

LIGAMENT EFFICIENCY	SCF BY	
	FEM	PHOTOELASTICITY
18	6.33	6.47
28	4.49	4.46
38	3.70	4.12
44	3.41	3.43

Table-1 SCF for square plate having square pattern, Uniaxial Loading.

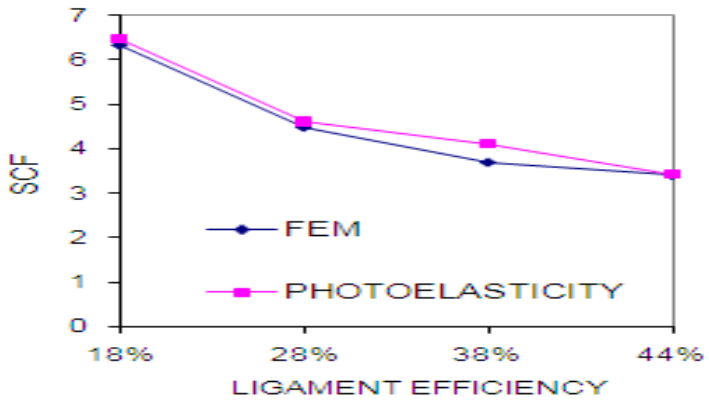

Graph.1 Graph of SCF for FEM and Photo-elasticity method.

VIII. CONCLUSION

While comparing the results with finite element analysis it is found that the percentage variation of experimental values with FEM were about 10- 15%.

This can be attributed to following points.

1) The load applied to the model may not be uniformly distributed over entire cross section of model. Some bending may result due to misalignment of upper and lower clamping plates of the loading frame.

2) In spite of extreme care being taken in manufacturing of models, some small amount of machining stress are developed in the model, which changes the fringe pattern in the model.

REFERENCES

[1]. Jones D. P., " Finite element analysis of perforated plates of 5 and 10 percent ligament efficiency ", *Transactions of the ASME Journal of pressure vessel technology*, Aug-1975, PP 199-205.

[2]. Ukadgaonkar V. G. Kale P. A., Agnihotri N. A., R. Shanmuga Babu, " Review of analysis of tube sheets", *International Journal of pressure vessel and piping*, 1996, PP 279-297.

[3]. Ukadgaonker V. G. Agnihotri N. A. , " Interaction effect of number of circular holes in a circular plates" , *Indian Journal of engineering and material sciences*, Aug-1997 VOL-4, PP123-128.

[4]. Ukadgaonker V. G., Kale P. A., " Finite element stress analysis of tube sheets perforated by circular holes in square pitch pattern", *Transactions of the ASME Journal of pressure vessel technology*, Feb-1998, PP 12-16.

[5]. Dr. Sadhu Singh, Experimental Stress Analysis (Khanna publishers, 1996).

American Journal of Engineering Research (AJER)
e-ISSN : 2320-0847 p-ISSN : 2320-0936
Volume-02, Issue-08, pp-12-23
www.ajer.org

Research Paper Open Access

GAPOD and GA DC-voltage regulator based UPFC supplementary cont roller for damping low frequency oscillations in Multi-machine power systems

Dakka. Obulesu, Dr. S.F. Kodad, Dr. B.V. Sankar Ram
[1](*Asso Professor, Department of Electrical & Electronics Engg., VEMU.I.T. P.Kothakota, Chittoor dist, Andhra Pradesh-517325,India)*
[2](*Principal, Krishna Murthy Institute of Technology and Engineering, Hyderabad, India.)*
[3](*Director, Admissions, J.N.T.U.C, Hyderabad, India.)*

Abstract: **-** The Unified Power Flow Controller (UPFC) is the most versatile device in the FACTS (Flexible AC Transmission Systems) which has emerged to enhance power system stability spectrum and dynamic performance. This paper briefs the effectiveness of the proposed GAPOD and GA DC-voltage regulator which has been tested on a 3-Machine, 9-Bus power system in comparison with Particle swarm optimization based Multi-Stage Fuzzy (PSOMSF) DC-voltage regulator. The non-linear time-domain simulation results show that the oscillations of synchronous machines could be quickly and effectively damped with proposed GAPOD and GA DC-voltage regulator. The construction and implementation of this controller is fairly easy, which can be useful in real world power system.

Keywords: **-** *FACTS, UPFC, GAPOD (Genetic Algorithms based Power oscillation damping) controller, PSOMSF, low frequency oscillations.*

I. INTRODUCTION

The present day interconnected power system comprises of a large number of generators being connected together through a high-voltage long transmission network, supplying power to loads through lower-voltage distribution. Day by day the electric power demand on the utilities is increasing due to the rapid urbanization and over growing population. Today's power system is thus much more loaded than before and operating near their stability limits and expansion in transmission and generation is restricted with the limited availability of resources and the environmental conditions. According to IEEE, FACTS - which is the abbreviation of Flexible AC Transmission Systems, is defined as "alternating current transmission systems incorporating power electronics based and other static controllers to enhance controllability and power transfer capability". Dynamic reactive power compensation and damping power system oscillations can also be achieved using FACTS controllers. Injecting the series voltage phasor, with desirable voltage magnitude and phase angle in a line can provide a powerful means of precisely controlling the active and reactive power flows, by which system stability can be improved, system reliability can be enhanced while operating and transmission investment cost can be reduced. It is possible to vary the impedance of specific transmission line to force power flow along a desired "contract path" in the emerging power systems, and to regulate the unwanted loop power flows and parallel power flows in the interconnected system. The FACTS controllers have been broadly developed on two different principles, one that alters the line series reactance or bus shunt reactance or voltage phase difference across a line and utilizes conventional thyristor switches for control. In general, FACTS controllers can be divided into four categories based on their connection in the network, viz., series, shunt, combined series-series, and combined series-shunt. In our work, we have used the series-shunt combination [2].

FACTS devices enhance the stability of the power system with its fast control characteristics and continuous compensating capability. The controlling of the power flow and increasing the transmission capacity of the existing transmission lines are the two main objectives of FACTS technology [4]. Thus, the utilization of the existing power system comes into optimal condition and the controllability of the power system is increased

with these objectives. Gyugyi proposed the Unified Power Flow Controller which is the new type generation of FACTS devices in the year 1991 [5]. Unified Power Flow Controller (UPFC), being one the member of the FACTS device thus emerged as one of the effective controllers for controlling and optimization of the power flow in the electrical power transmission systems [7]. This device was formed due to the combination of the two other FACTS devices, namely Static Synchronous Compensator (STATCOM) and the Static Synchronous Series Compensator (SSSC). These are connected to each other by a common DC link, which is a typical a storage capacitor. The all parameters of the power transmission line (impedance, voltage and phase angle) can be control simultaneously by UPFC [6,8]. In the modern day power system stability, operation & control (PSOC), FACTS (Flexible AC Transmission Systems) plays a very important role. Usage of FACTS in the power systems not only enhances the dynamic performance, but also increases the stability of the power systems, enhances the controllability and increases its power transfer capability. Some of the devices used in the control of FACTS are the SVC, TCSC, STATCOM, UPFC, and the IPFC [1]. The FACTS controllers utilize power electronics based technology and can provide dynamic control on line power flows, bus voltages, line impedance & phase angles. One of the controllers being used in the work presented in this paper is the GAPOD and GA DC- voltage regulator scheme for the damping of power system oscillations. The FACTS initiative was originally launched in 1980's to solve the emerging problems faced due to restrictions on transmission line construction, and to facilitate growing power export/import and wheeling transactions among utilities. The two basic objectives behind the development of FACTS technology; is to increase power transfer capability of transmission systems, and to keep power flow over designated routes, significantly increase the utilization of existing (and new) transmission assets, and play a major role in facilitating contractual power flow in electricity markets with minimal requirements for new transmission lines. FACTS devices have shown very promising results when used to improve the power system steady state performance. In addition, because of the extremely fast control action associated with FACTS-device operations, they have been very promising candidates for utilization in power system damping enhancement. The first generation FACTS devices include SVC, TCPS, and TCSC. It has been found that SVCs can be effective in damping power system oscillations if a supplementary feedback signal is applied [9-10]. Compared with other FACTS devices, little attention has been paid to TCPS modeling and control. Based on the equal area criterion, the TCPS control problem has also investigated using linear control techniques [11-13]. Many research efforts have been devoted to the control of TCSC. Chen *et. al.* designed a state feedback TCSC controller based on the pole placement technique [14]. Other TCSC optimal and nonlinear control schemes proposed in the literature [15-17]. A unified power flow controller (UPFC) is the most promising device in the FACTS concept. Several trials have been reported in the literature to model a UPFC for steady-state and transient studies. Based on Nabavi-Iravani model [18], Wang developed two UPFC models which have been linearized and incorporated into the Heffron-Phillips model [3].

II. MULTI-MACHINE SYSTEM WITH UPFC

In Fig(1), the generators and the line with UPFC are shown to be connected to the network with the bus admittance[Yt].

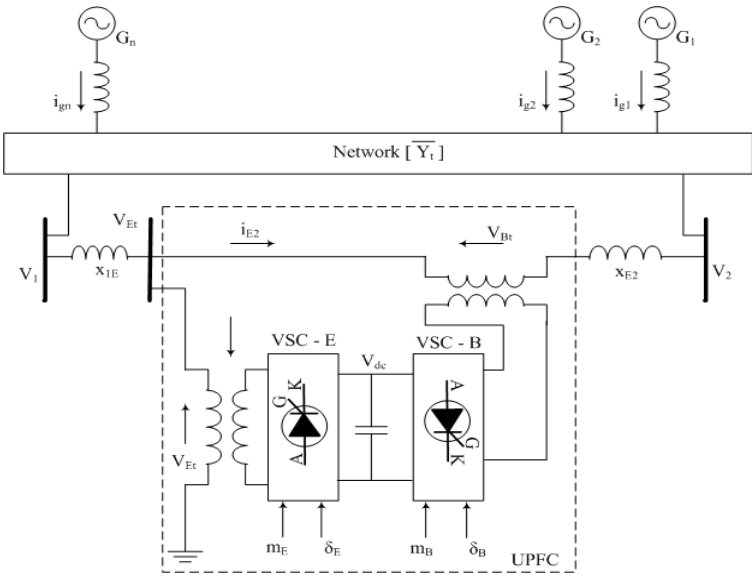

Fig.1 Multi-machine power system with UPFC.

The four input control signals to the UPFC are m_E, m_B, δ_E, and δ_B where m_E is the excitation amplitude modulation ration, m_B is the boosting amplitude modulation ratio, δ_E is the excitation phase angle and δ_B is the boosting phase angle. The UPFC is installed for the purpose of multiple control functions, one of which will be the suppression of low-frequency oscillations occurring in the system. Various feedback signals namely, deviation in generator rotor angle, deviations in real power flow through the transmission line, accelerating power, have been identified as capable of contributing direct electric damping torque to the electromechanical oscillation loop of the generator. A wise selection of the feedback signal can be done based on its capability in improving the damping of desired mode of oscillation.

II.A PSO based MSF (PSOMSF) controllers for UPFC

Structure of a PSO based Multi-Stage Fuzzy control strategy are shown in fig.2. In this structure, input values are converted to truth-value vectors and applied to their respective rule base.

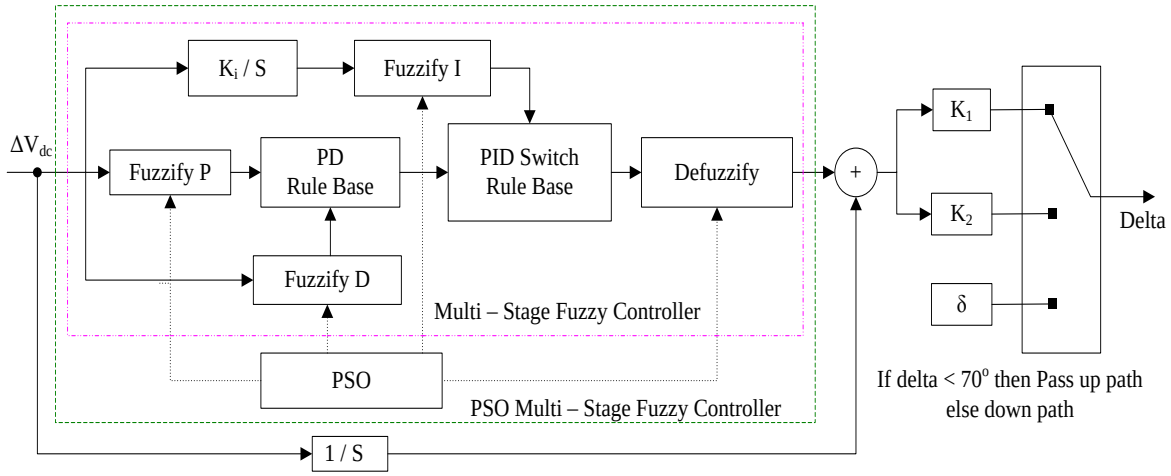

Fig.2. Structure of a PSO based Multi-Stage Fuzzy control strategy

Table.1 PD rule base

		Δe						
		NB	NM	NS	ZO	PS	PM	PB
$e = \Delta V_{dc}$	NB	NB	NB	NB	NB	NM	NS	ZO
	NM	NB	NB	NB	NM	NS	ZO	PS
	NS	NB	NB	NM	NS	ZO	PS	PM
	ZO	NB	NM	NS	ZO	PS	PM	PB
	PS	NM	NS	ZO	PS	PM	PB	PB
	PM	NS	ZO	PS	PM	PB	PB	PB
	PB	ZO	PS	PM	PB	PB	PB	PB

The output truth-value vectors are not defuzzified to crisp value as with a single stage fuzzy logic controller but are passed onto the next stage as a truth value vector input. To improve controller performance under very heavy loading of power systems ($\delta > 70^o$) a functional switch is provided, which provides sufficient amount of damping magnitude. In this effort, all membership functions are defined as triangular partitions with seven segments from -1 to 1. Two rule bases used in the new proposed controller are PD rule base and PID rule base these are shown in Table.1 and Table.2 respectively.

Table .2 PID switch rule base

		PD values						
		NB	NM	NS	ZO	PS	PM	PB
$\int e$	NB	NM	NS	NB	PS	PM	PB	NM
	NM	NM	NS	NM	PS	PM	PB	NM
	NS	NM	NS	NS	PS	PM	PB	NM
	ZO	NM	NS	ZO	PS	PM	PB	NM
	PS	NM	NS	PS	PS	PM	PB	NM
	PM	NM	NS	PM	PS	PM	PB	NM
	PB	NM	NS	PB	PS	PM	PB	NM

II.B POD controller design using genetic algorithm

The damping function of FACTS devices is preformed mainly through the changes of the power delivered along the transmission line. With appropriate lead-lag compensation, the damping torque provided by FACTS damping control is proportional to gain of the controller. Since FACTS devices are located in transmission systems away from generating stations, local availability of the feedback signal is of a major concern. Thus, the selection of feedback signal is done on the basis of availability of the signal locally. Another concern is choosing the proper candidate feedback signal is its effectiveness in damping the desired mode of oscillations. Residue method is an approach widely adopted for identifying the most appropriate local feedback signal. Fig.3 shows the transfer function model G(s) of a power system for FACTS device with POD (FACTSPOD). The location of FACTS devices in power system is decided based on its assigned functions and the design of POD is carried out assuming that the location is decided and the input signal u(s) is available. The output signal y(s) can be chosen based on maximum residue provided by the selected outputs.

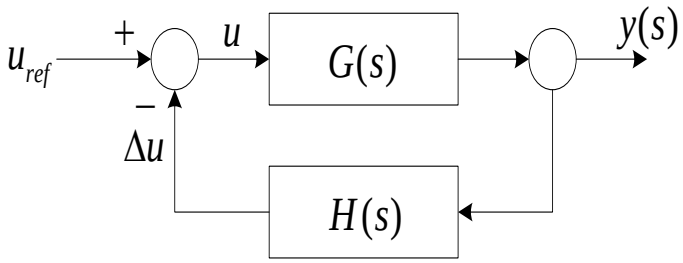

Fig.3. Closed-loop system with POD control

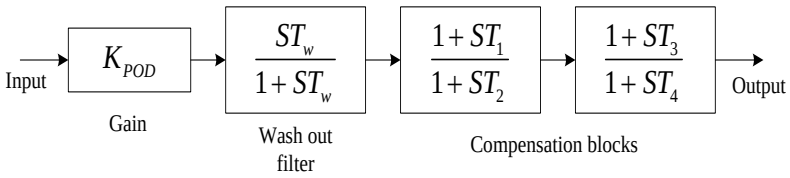

Fig.4. POD controller structure

The POD controller consists of an amplification block, a wash-out and low-pass filters and mc stages of lead-lag blocks as depicted in Figure.4.The transfer function, H(S) of the POD controller is given by

$$H(s) = K_{POD}\frac{sT_w}{1+sT_w}\left[\frac{1+sT_{lead}}{1+sT_{lag}}\right]^m$$

m: no of compensation stages
T_w: Washout time constant
K_{POD} : Gain constant,
T_{lead}, T_{lag} : Lead, lag time constants

The parameters of the POD controller are designed based on the genetic algorithm. Before proceeding with GA approach, the suitable coding and fitness function should be chosen. In this study, the parameters K_{POD}, T_1 and T_2 for POD controllers are expressed in term of string consisting of 0 and 1 by binary code. For our optimization, the following fitness function is proposed:

$$Fitness = \frac{1}{100 * ITAE}, \quad ITAE = \int_0^t t\,|\Delta\omega|\,dt$$

For acquiring better performance, number of generation, population size, crosser over rate and mutation rate is chosen 20, 10, 0.97 and 0.08 respectively. The proposed flowchart of the genetic algorithm is shown in Fig.5.

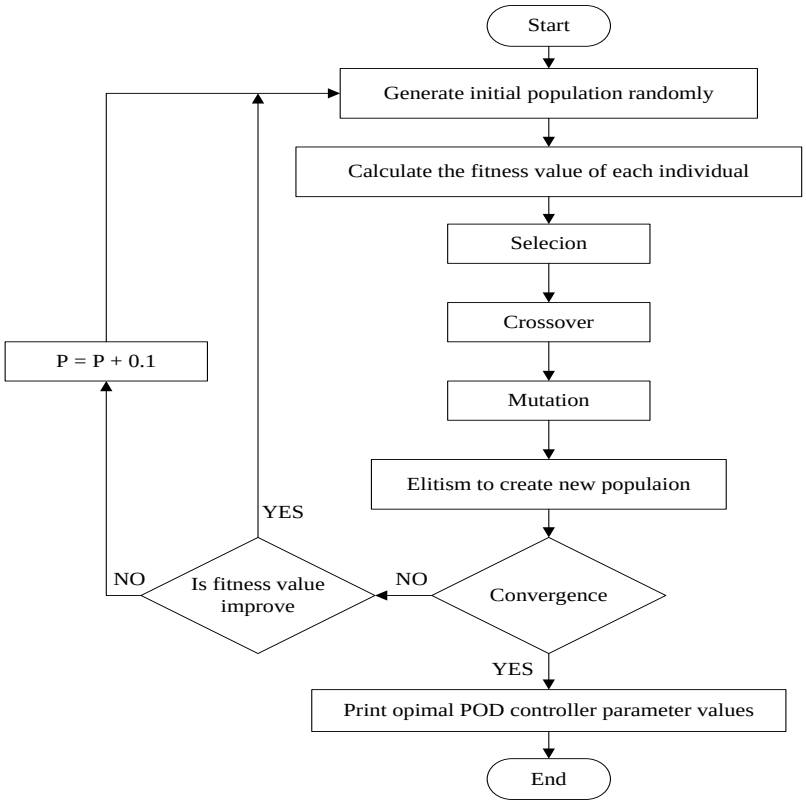

Fig.5. GA flowchart for optimization of POD parameters

III. SIMULATION RESULTS

The disturbance is given as step input and the output response is taken from ' $\Delta\delta$ ', ' $\Delta\omega$ ', ' ΔP_e ', and ' ΔV_{dc} ', which gives rotor angle deviation, angular frequency deviation, deviation in ' P_e ' deviation in capacitor voltage ' V_{dc} ' respectively. The proposed method is simulated with a step disturbance of 0.1pu at various operating conditions (Nominal load (operating point 1): P_e =0.8 Q_e =0.15 V_t =1.032; heavy load(operating point 4): P_e =1.1 Q_e =0.28 V_t =1.032; very heavy load(operating point 7): P_e =1.15 Q_e =0.3 V_t =1.032) and the results are shown in figures from 6 to 17. From these Figures we concluded that UPFC with GAPOD and GA DC- voltage regulator has more effect compared with PSOMSF DC-voltage regulator, proposed GAPOD and GA DC-voltage regulator successfully increases damping rate and decreases the amplitude of low frequency oscillations.

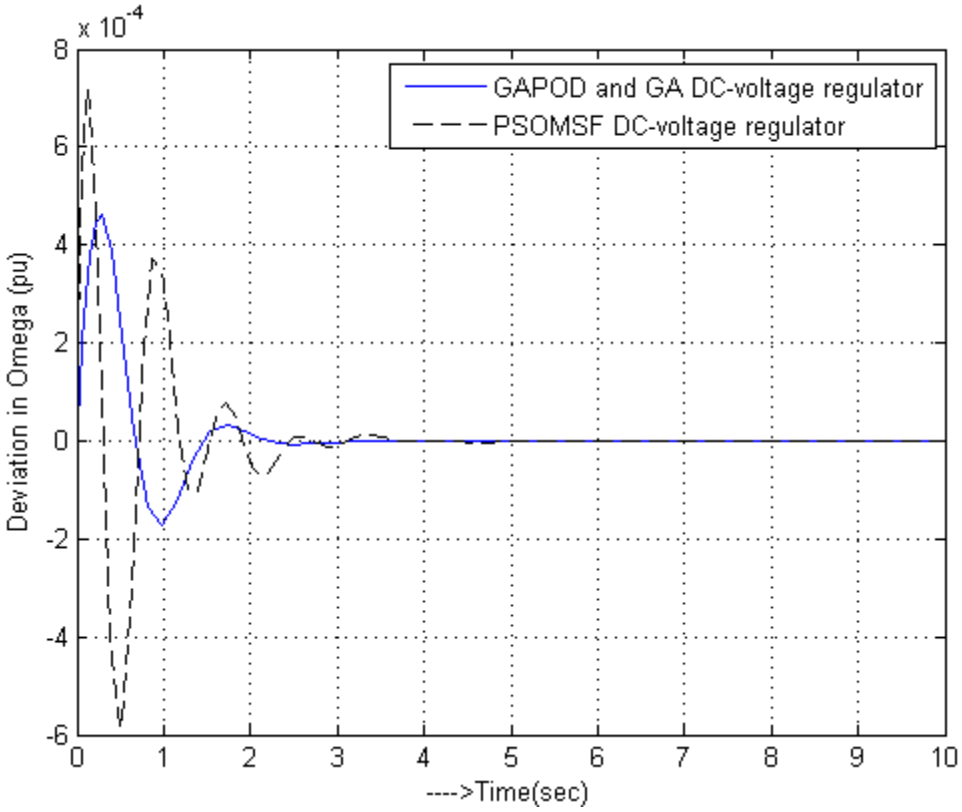

Fig:6. Time response of Δω with PSOMSF DC-voltage regulator, GA POD and GA DC- voltage regulator at operating point 1.

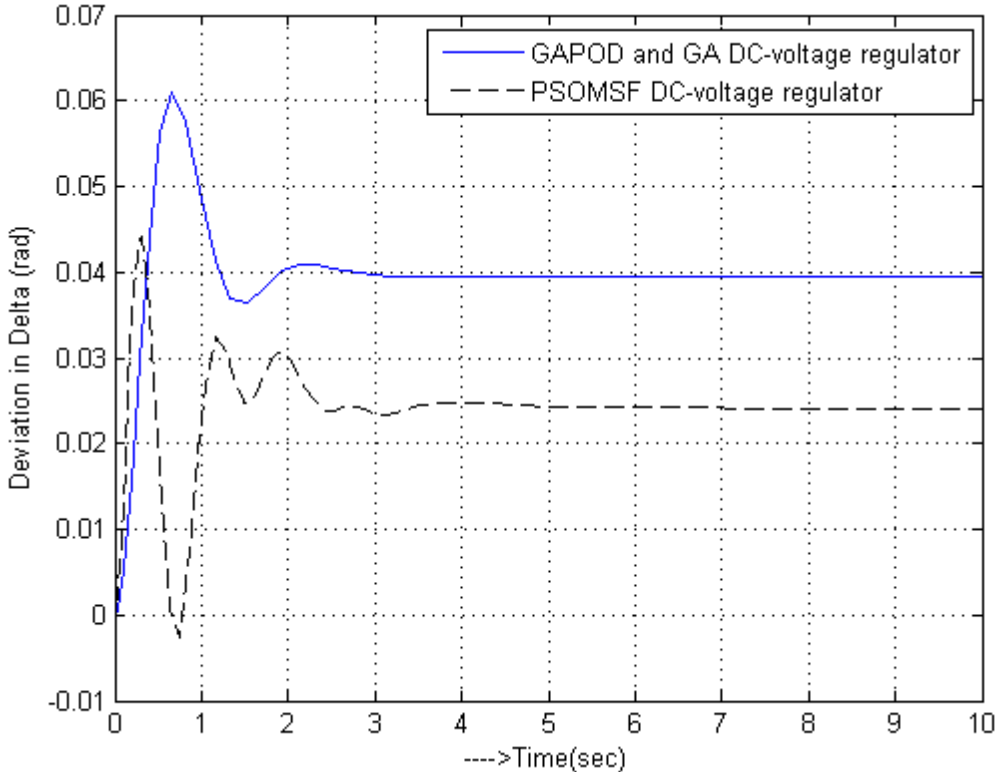

Fig:7. Time response of Δδ with PSOMSF DC-voltage regulator, GA POD and GA DC- voltage regulator at operating point 1

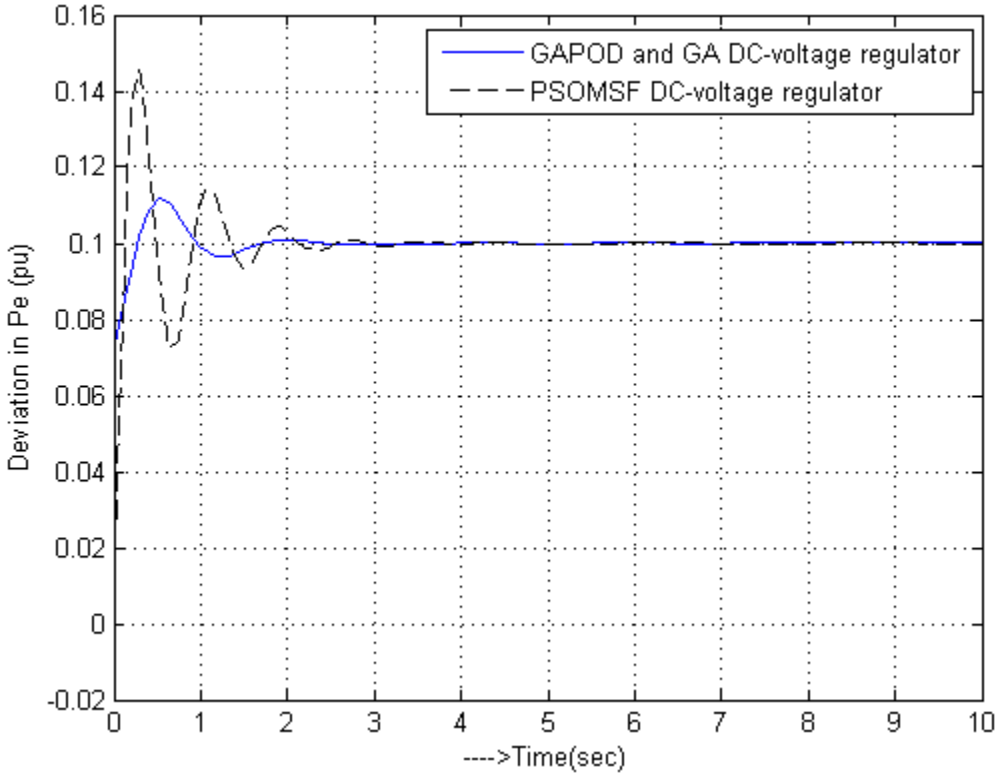

Fig:8. Time response of ΔP_e with PSOMSF DC-voltage regulator, GA POD and GA DC- voltage regulator at operating point 1

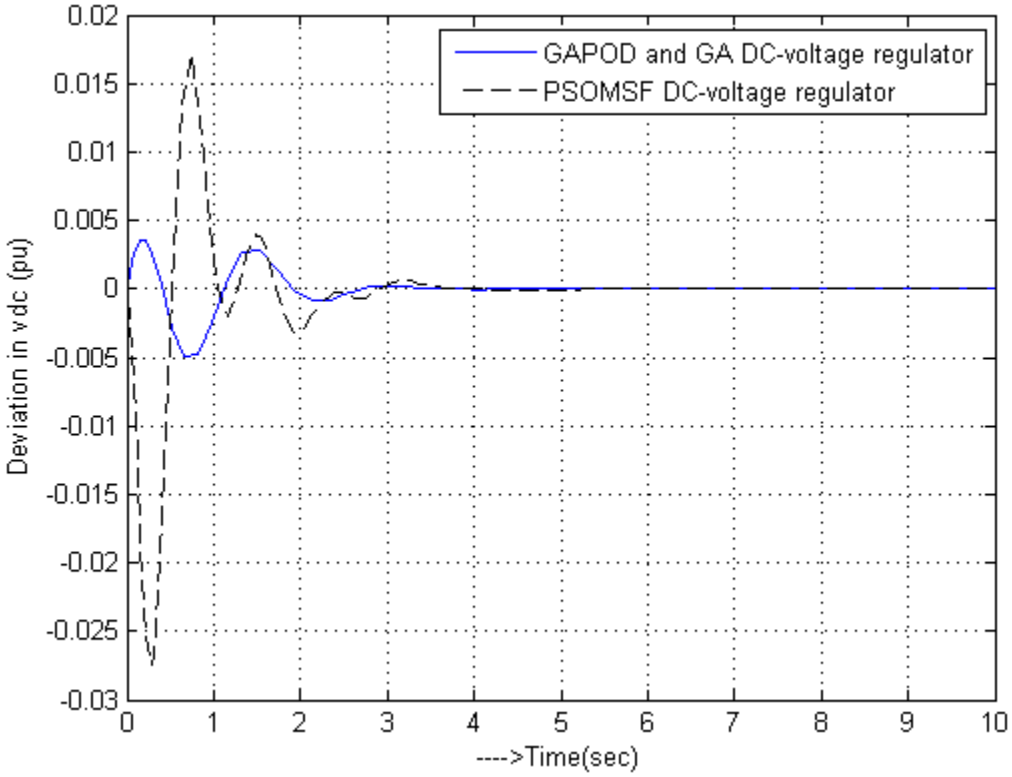

Fig:9. Time response of ΔV_{dc} with PSOMSF DC-voltage regulator, GA POD and GA DC- voltage regulator at operating point 1

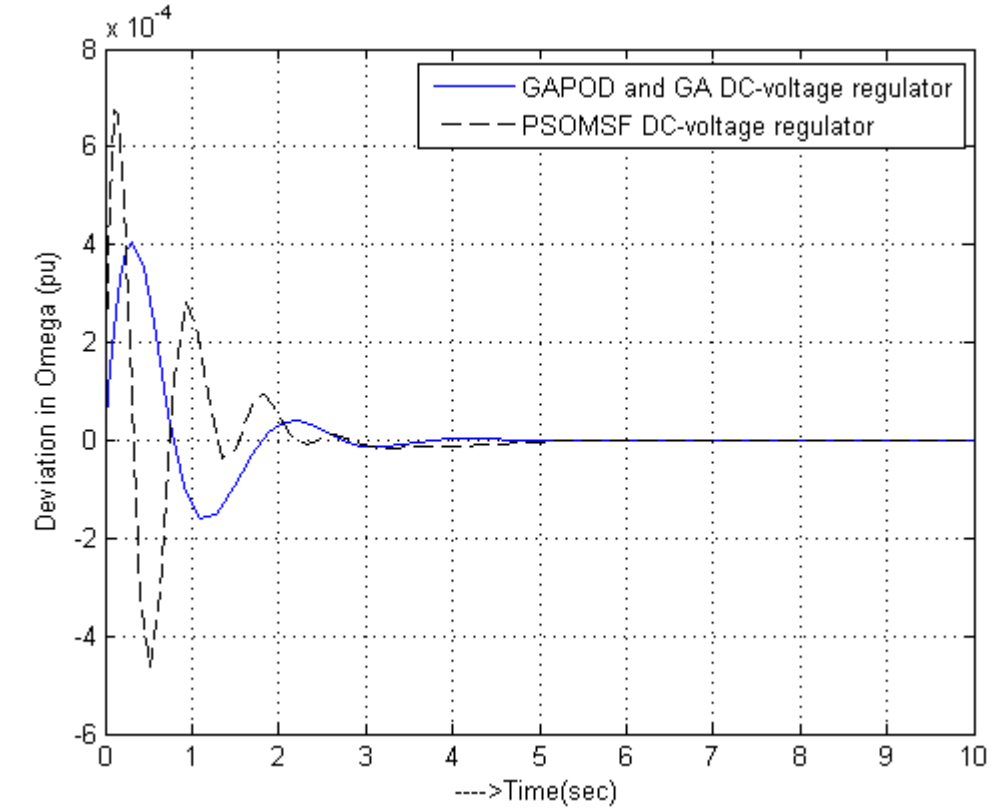

Fig:10. Time response of Δω with PSOMSF DC-voltage regulator, GA POD and GA DC- voltage regulator at operating point 4

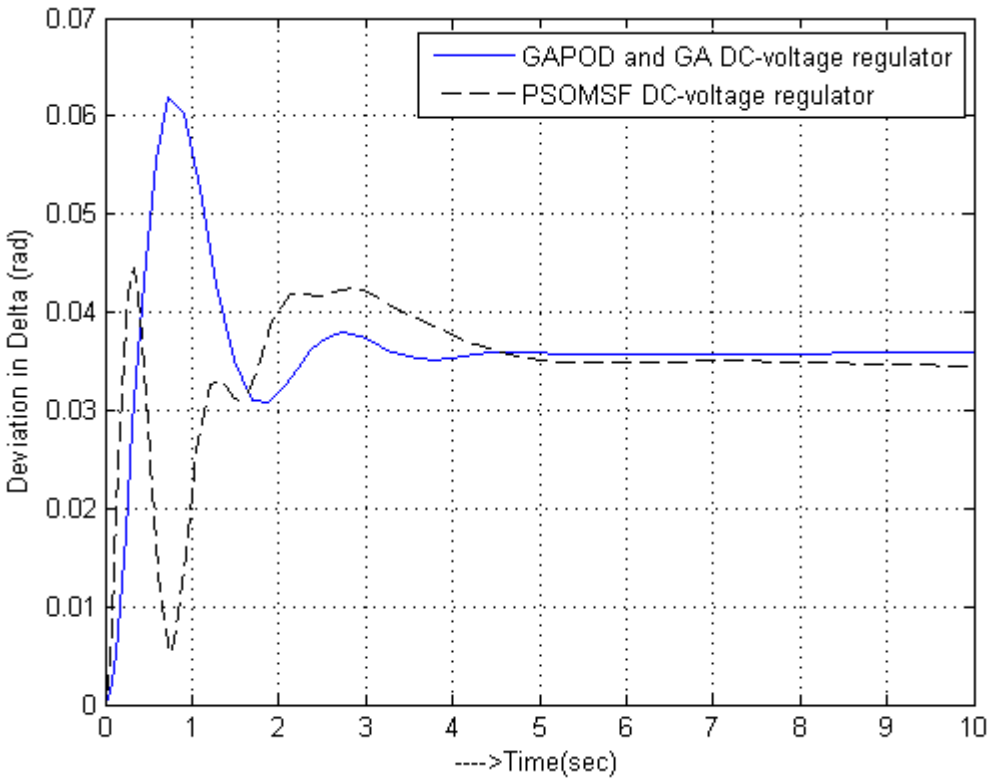

Fig:11. Time response of Δδ with PSOMSF DC-voltage regulator, GA POD and GA DC- voltage regulator at operating point 4

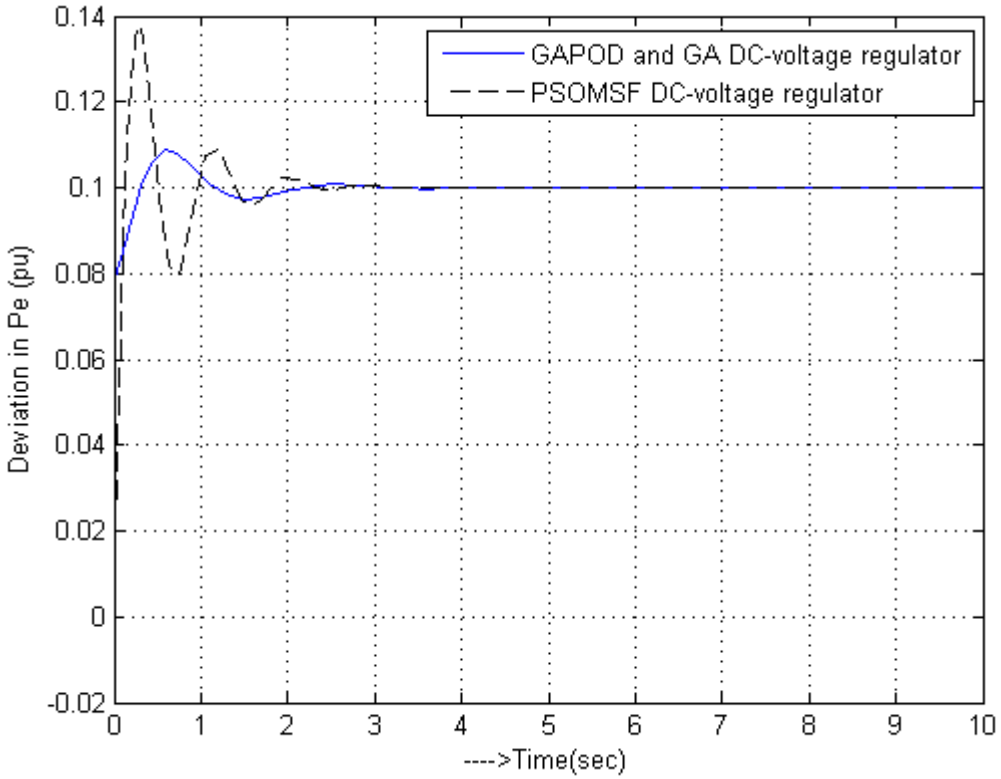

Fig:12. Time response of ΔP_e with PSOMSF DC-voltage regulator, GA POD and GA DC- voltage regulator at operating point 4

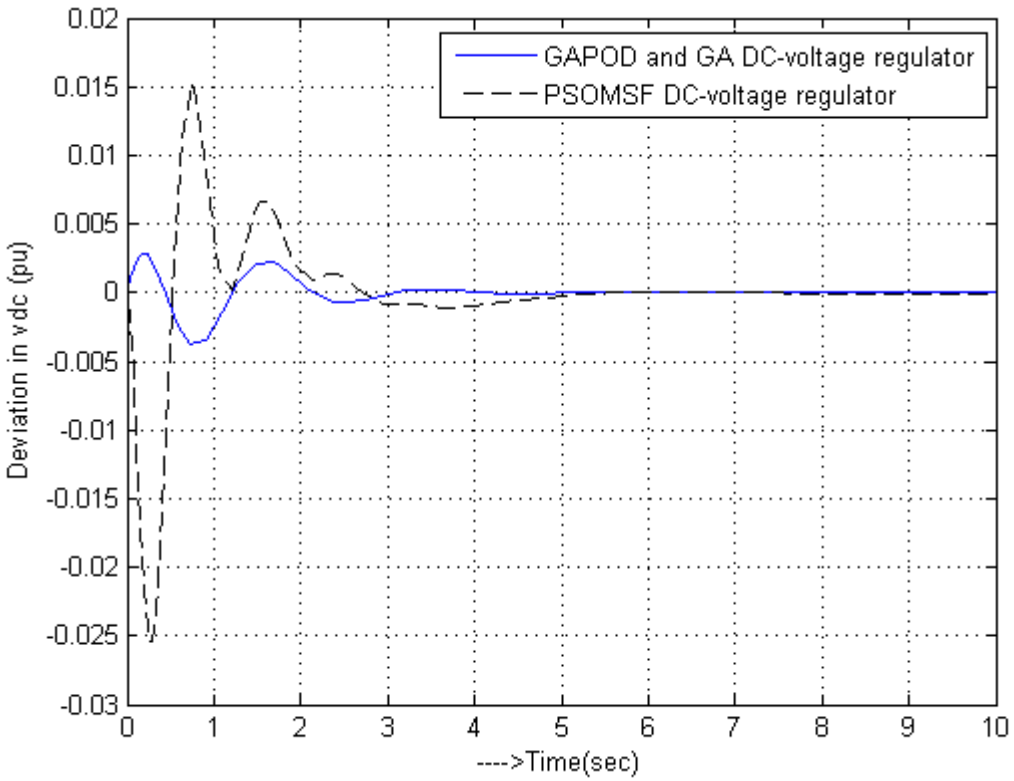

Fig:13. Time response of ΔV_{dc} with PSOMSF DC-voltage regulator, GA POD and GA DC- voltage regulator at operating point 4

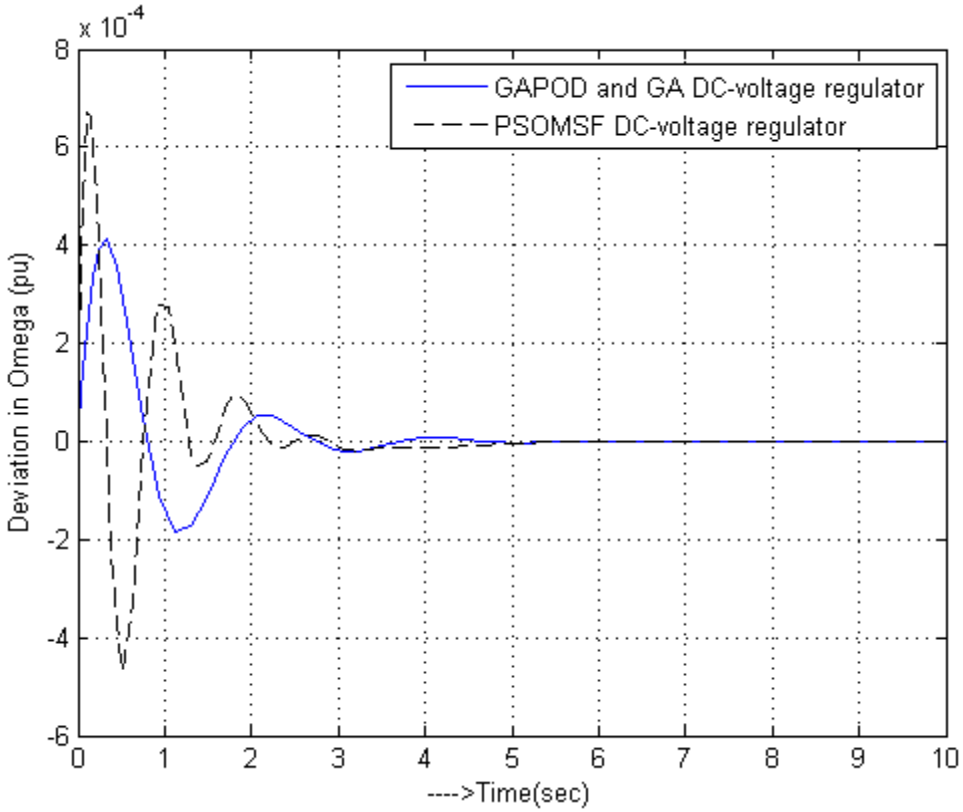

Fig:14. Time response of Δω with PSOMSF DC-voltage regulator, GA POD and GA DC- voltage regulator at operating point 7

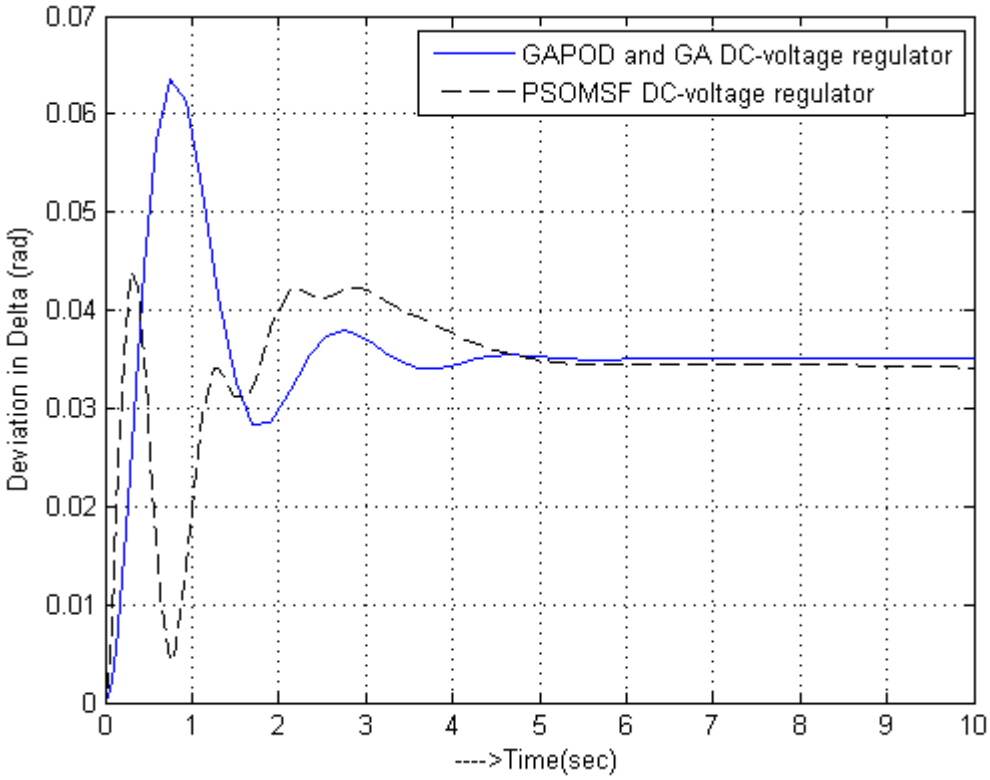

Fig:15. Time response of Δδ with PSOMSF DC-voltage regulator, GA POD and GA DC- voltage regulator at operating point 7

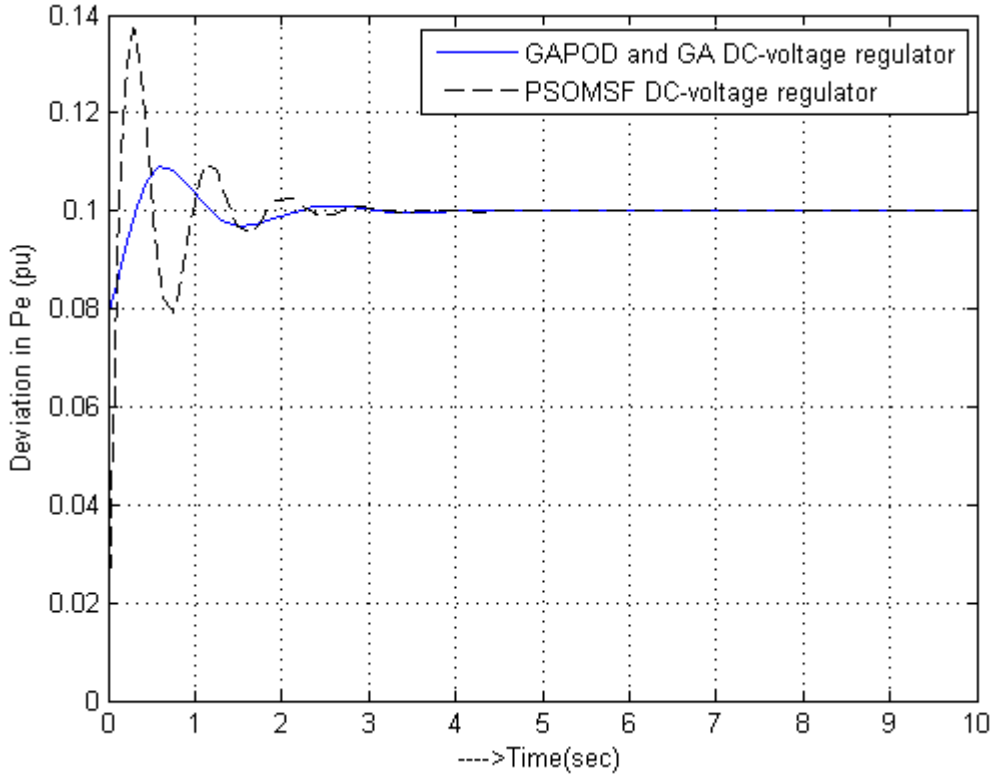

Fig:16. Time response of ΔP_e with PSOMSF DC-voltage regulator, GA POD and GA DC- voltage regulator at operating point 7

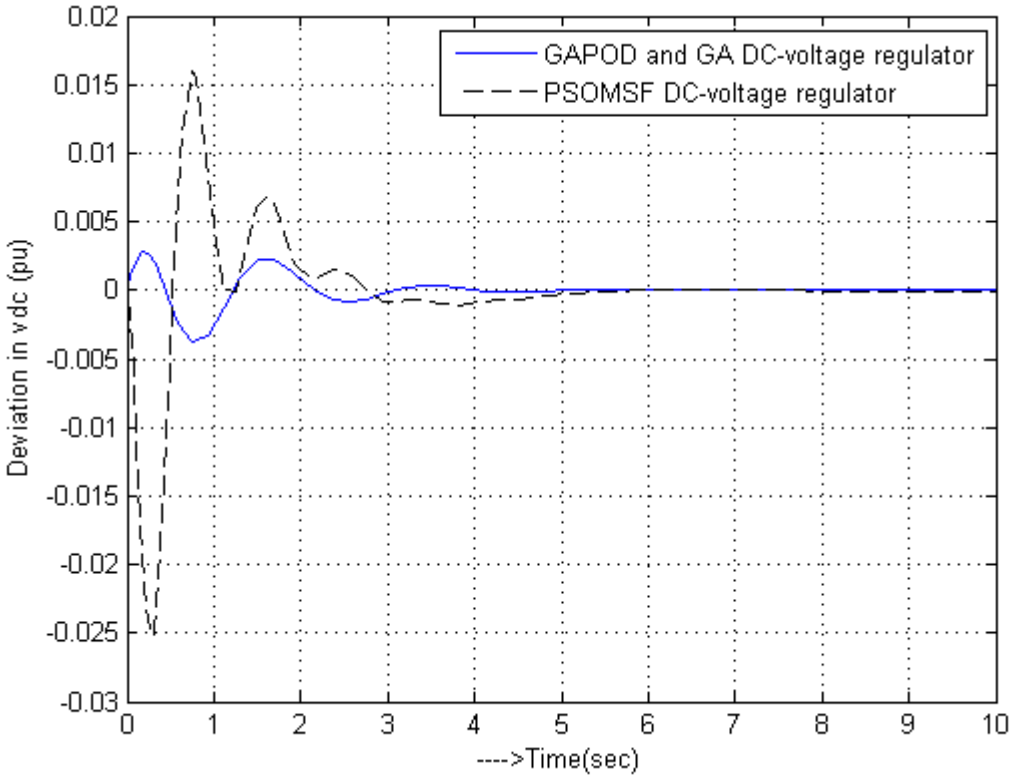

Fig:17. Time response of ΔV_{dc} with PSOMSF DC-voltage regulator, GA POD and GA DC- voltage regulator at operating point 7

IV. CONCLUSIONS

In this paper, the effectiveness of the proposed GAPOD and GA DC-voltage regulator has been tested on a 3-machine 9-bus power system in comparison with PSOMSF DC-voltage regulator under different operating conditions. GAPOD and GA DC-voltage regulator has more effect compared with PSOMSF DC-voltage regulator. The nonlinear time-domain simulation results show that the oscillations of synchronous machines can be quickly and effectively damped with the proposed GAPOD and GA DC- voltage regulator. The simulation results show the effectiveness of the method presented.

REFERENCES

[1]. L. Gyugi, "Unified Power flow concept for flexible AC transmission systems", IEE Proc., Vol. 139, No. 4, pp. 323–332, 1992

[2]. M. Noroozian, L. Angquist, M. Ghandari, and G. Anderson, "Use of UPFC for optimal power flow control", IEEE Trans. on Power Systems, Vol. 12, No. 4, pp. 1629–1634, 1997.

[3]. H.F. Wang, "Application of Modeling UPFC Into Multi-Machine Power Systems", IEE Proc. Gen. Trans. and Distrib., Vol. 146, No. 3, pp. 306–312, 1999.

[4]. S. Hongbo, D.C Yu. Luo Chunlei, "A novel method of power flow analysis with unified power flow controller (UPFC)", Power Engineering Society Winter Meeting, 2000, pp. 2800 – 2805, Vol. 4, 23-27 Jan. 2000.

[5]. Narain G. Hingorani, Laszlo Gyugyi "Understanding FACTS: Conceptsand Technology of Flexible AC Transmission Systems", Power electronics sponsored by the Institute of Electrical and Electronics Engineers, Inc. 3 Park Avenue, New York, NY 10016-5997, 2000.

[6]. R.P Kalyani, G.K. Venayagamoorthy, M. Crow, "Neuroidentification of system parameters for the shunt & series branch control of UPFC", Power Engineering Society General Meeting, 2003, IEEE Vol. 4, 13-17 Jul. 2003.

[7]. V.K.Chandrakar, A.G.Kothari, "RBFN Based UPFC for Improving transient stability Performance", WSEAS Transactions on Power Systems, Issue 1 , Vol. 2 , pp.1-6 , Jan 2007.

[8]. S. Kannan, S. Jayaram, M. M. A. Salama, "Real and Reactive Power Coordination for a Unified Power Flow Controller", IEEE Transactions on Power Systems, Vol. 19, Issue 3, pp. 1454 – 1461, 2004.

[9]. L. Gyugi, "Unified Power flow concept for flexible AC transmission systems", IEE Proc., Vol. 139, No. 4, pp. 323–332, 1992

[10]. M. Noroozian, L. Angquist, M. Ghandari, and G. Anderson, "Use of UPFC for optimal power flow control", IEEE Trans. on Power Systems, Vol. 12, No. 4, pp. 1629–1634, 1997.

[11]. H.F. Wang, "Application of Modeling UPFC Into Multi-Machine Power Systems", IEE Proc. Gen. Trans. and Distrib., Vol. 146, No. 3, pp. 306–312, 1999.

[12]. S. Hongbo, D.C Yu. Luo Chunlei, "A novel method of power flow analysis with unified power flow controller (UPFC)", Power Engineering Society Winter Meeting, 2000, pp. 2800 – 2805, Vol. 4, 23-27 Jan. 2000.

[13]. Narain G. Hingorani, Laszlo Gyugyi "Understanding FACTS: Conceptsand Technology of Flexible AC Transmission Systems", Power electronics sponsored by the Institute of Electrical and Electronics Engineers, Inc. 3 Park Avenue, New York, NY 10016-5997, 2000.

[14]. R.P Kalyani, G.K. Venayagamoorthy, M. Crow, "Neuroidentification of system parameters for the shunt & series branch control of UPFC", Power Engineering Society General Meeting, 2003, IEEE Vol. 4, 13-17 Jul. 2003.

[15]. V.K.Chandrakar, A.G.Kothari, "RBFN Based UPFC for Improving transient stability Performance", WSEAS Transactions on Power Systems, Issue 1 , Vol. 2 , pp.1-6 , Jan 2007.

[16]. S. Kannan, S. Jayaram, M. M. A. Salama, "Real and Reactive Power Coordination for a Unified Power Flow Controller", IEEE Transactions on Power Systems, Vol. 19, Issue 3, pp. 1454 – 1461, 2004.

[17]. A. E. Hammad, "Analysis of Power System Stability Enhancement by Static VAR Compensators", IEEE Trans. PWRS, Vol. 1, No. 4, pp. 222–227, 1986.

[18]. S. Lee and C. C. Liu, "An Output Feedback Static VAR Controller for the Damping of Generator Oscillations", Electric Power System Research, Vol. 29, pp. 9–16, 1994.

American Journal of Engineering Research (AJER)
e-ISSN : 2320-0847 p-ISSN : 2320-0936
Volume-02, Issue-08, pp-24-31
www.ajer.org

Research Paper Open Access

Comparative Analysis of Empirical Path Loss Model for Cellular Transmission in Rivers State

B.O.H Akinwole, Biebuma J.J
Department of Electrical/Electronic Engineering, University of Port Harcourt Port Harcourt, Nigeria,

Abstract: **-** This paper presents a comparative analysis of three empirical path loss models with measured data for urban, suburban, and rural areas in Rivers State. The three models investigated were COST 231 Hata, SUI, ECC-33models. A downlink data was collected at operating frequency of 2100MHz using drive test procedure consisting of test mobile phones to determine the received signal power (RSCP) at specified receiver distances on a Globacom Node Bs located in some locations in the State. This test was carried out for investigating the effectiveness of the commonly used existing models for Cellular transmission. The results analysed were based on Mean Square Error (MSE) and Standard Deviation (SD) and were simulated on MATLAB (7.5.0). The results show that COST 231 Hata model gives better predictions and therefore recommended for path loss predictions in River State.

Keywords*: - Cellular transmission, RSCP, path loss prediction empirical path loss model, Mean Square Error, Standard Deviation,*

I. INTRODUCTION

One of the basic requirements for reliable and efficient transmissions of a Cellular system is the knowledge of the received signal and its variability at all distance points surrounding the base station. Propagation of radio frequency (RF) signals between a transmitting and receiving antenna is achieved by means of electromagnetic waves [1]. The signals, as they propagate through the free space, are subject to different propagation mechanisms and are heavily influenced by the environment resulting in a received power being significantly less than the original transmitted power. This phenomenon in Cellular systems is referred to as propagation loss (path loss). Path loss prediction plays an important role in estimation of received signal strength, interference optimization and analysis, link budget design and analysis, and cell size estimation. Path loss models are classified as deterministic, empirical, and semi-empirical [2].Deterministic models make use of the physical laws governing radio wave propagation mechanisms to predict transmission loss at a particular location. The models involve detailed and accurate description of all the objects in the propagating channel.

Empirical model is based on statistical characterisation of the received signal extensive measurements conducted with respect to several different parameters. It requires less computation effort unlike deterministic model that is site specific. A semi-empirical or semi-deterministic model combines the analytical formulation of physical phenomena with statistical fitting of variables by adjustment using experimental measurements. This paper presents a comparison between three empirical path loss models and the measured path loss for cellular transmission at WCDMA frequency of 2100MHz.

The paper is organised as follows. Section 2, presents an overview of the four common existing path loss model considered. The procedure and tools used for obtaining the measured data are described in section 3. Section 4 gives the comparative analysis between measured path loss and the existing path loss models. Results are presented in section 5.

II. EXISTING PATH LOSS MODEL

2.1 LOG-NORMAL SHADOWING PATH LOSS MODEL

This model describes the random shadowing effects that occur over a large number of measurement locations with the equal separation distance between the transmitter and the receiver. The path loss model is given as [3], $L(dB)=L(d)+10r\log\left(\frac{d}{do}\right)+X\sigma(1)$

L(dB) is random and log-normally distributed about the distance.

where, $X\sigma$ is a zero mean Gaussian distributed random variable (in dB).

2.2 COST 231 Hata Model

COST 231 Hata model is an empirical model used for calculating path loss in cellular mobile system. This model is an extension of the Okumura-Hata model designed to cover frequency ranges from 1700Mz to 2300MHz with receiving antenna heights up to 10m and transmitting antenna heights of 30m-200m.COST 231 Hata model contains correction factors for urban, suburban, and rural areas. The equation for COST 231 Hata path loss model is expressed as [4]:

$L_{COST231Hata} = 46.3+ 33.9\log_{10}(f_c) -13.82\log_{10}(h_t) -a(h_m) + [44.9- 6.55\log_{10}(h_t)]\log_{10}(d)+C_m$ (2)

where, d is the link distance in Kilometres, f_c is the frequency in MHz, h_t is the effective height of the transmitting antenna in meters, h_r is the effective height of the receiving antenna in meters, C_m is the correction factor and is defined 0dB for rural or suburban and 3dB for urban area.

For rural or suburban area,

Correction factor for receiver antenna height,

$a(h_m) = (1.11\log_{10} f_c-0.7)h_t – (1.5\log_{10} f_c - 0.8)$ (3)

For Urban,

$a(h_m) = 3.2 (\log_{10}(11.75h_m))^2 -4.79$ (4)

2.3 STANFORD UNIVERSITY INTERIM (SUI) Model

The Stanford University Interim was developed by the working group of Institute of Electrical Electronic Engineers (IEEE 802.16) for path loss prediction in all three macro-cellular environments. The model is formulated to operate based on an operating frequency above 1900MHz and a cell radius of 0.1km to 8km, base station antenna height 10m to 80m, and receiver antenna height of 1m to 10m. This model is divided into three categories of terrains namely A, B, C. The terrain category A is associated with maximum path loss, and densely populated region. Moderate path loss is captured in terrain category B. The terrain category C is associated with minimum path loss and flat terrain with light tree densities (Afric et al, 2006).

The basic path loss formula for SUI model is expressed as [4],

$L_{SUI} =A+10r\log_{10}(d/d_o) +X_f+ X_h+S$ (5)

For $d>d_o$, and d_o=0.1Km

The parameter for free space attenuation, A is expressed as,

$A=20\log_{10}(4\pi d_o/\lambda)$ (6)

r is the path loss exponent, h_t is the effective base station height, the constants used for a, b, and c are given in

Table 1

Table1: Numerical values for the SUI Model Parameters

Model parameter	Terrain A	Terrain B	Terrain C
A	4.6	4.0	3.6
b (m^{-1})	0.0075	0.0065	0.005
c (m)	12.6	17.1	20

X_f is the frequency correction factor

$X_f = 6.0\log_{10}\left(\frac{f_c}{2000}\right)$ (7)

X_h is the correction factor for receiving antenna height is defined as,

$X_h=$ (8)

$$\begin{cases} -10.8\log 10\left(\frac{H_R}{2000}\right), \text{for A, B} \\ -20\log 10\left(\frac{H_R}{2000}\right) \text{for terrain category C} \end{cases}$$ (9)

S is the correction for shadow fading factor, and is defined between 8.2dB and10.6dB.
where f_c is the operating frequency in MHz, and h_r is the receiver antenna height in meters.

2.4 ECC-33 Model

The Electronic Communication Committee 33 model was developed by Electronic Communication Committee. This model is designed to predict path loss at higher frequency greater than 3GHz. In this model, path loss is given by [5],

$$L_{ECC-33} = A_{fs} + A_{bm} - G_t - G_r \quad (10)$$

where, A_{fs} is the free space attenuation (dB), A_{bm} is the basic median path loss (dB), G_t is the transmitter antenna height gain factor, G_r is the receiver antenna height gain factor.
where: the free space attenuation,

$$A_{fs} = 92.4 + 20\log_{10}(d) + 20\log_{10}(f_c) \quad (11)$$

Basic median path loss,

$$A_{bm} = 20.41 + 9.83\log_{10}(d) + 7.894\log_{10}(f_c) + 9.56[\log_{10}(f_c)]^2 \quad (12)$$

Transmitter antenna height gain factor,

$$G_t = \log_{10}(h_t/200)\{13.958 + 5.8[\log_{10}(h_r)]\}^2 \quad (13)$$

For medium cities, the receiver antenna height gain factor Gr is expressed as,

$$G_r = [42.57 + 13.7\log_{10} f_c)][\log_{10}(h_r) - 0.585] \quad (14)$$

III. DATA COLLECTION METHOD AND PROCEDURE

To predict path loss model for cellular transmission, practical data from the field measurement are required. Downlink data were collected at various distances on live radio Globacomm WCDMA Node Bs at transmits frequency of 2100MHz. A drive test tools used for collecting data include a laptop equipped with drive test Ericsson software, Map info software (professional version 8.0), a communication Network Analyser software (ACTIX analyser 4.05), Garmin GPS 12XL receiver, Two C702 Sony Ericsson TEMS phone for idle and dedicated mode, an inverter and extension board. The test was carried out at three different locations in Rivers State:

Rumukoro, with co-ordinate ($4^o48'52''$N $7^o12'6E''$) is selected as urban area, Finima, Bonny Island with co-ordinate ($4^o26'12.8''$N $7^o10'25.5''$E) selected as sub-urban area, and Borokiri (Creek road) coordinates ($4^045'50.5''$N $7^o1'26.4''$E) selected as rural area.

The two Sony Ericsson UEs, GPS receiver and the Dongle probe were coupled to a laptop placed in a car. The laptop was powered on in order to launch TEMS investigation software. All the equipment were connected and detected on TEMS interface. The routes and the Node Bs were identified before setting out for the drive test. The car was driven around through a predefined route in the direction of the Active Sector (AS) of the directional antenna away from the site until it got to the coverage border. The car was driven at an average speed of 30Km/h. Two modes of configurations for the handsets were used for the monitored software during this drive–test. These were the idle and dedicated modes. M_1 was set at idle mode and M_2 was set at dedicated mode. M_2 was preset automatically to make a continuous call to a fixed destination number. The received signal power is measured using Ericsson handset and transferred to the TEMS log file in the laptop. The GPS receiver gave the location and distance from the Node B synchronously with the received power level reading and was recorded on the laptop. The experimental data were taken at distances ranging from 100meters to 1kilometer. Measurements were carried out between and October and November, 2012.The set up for the drive test measurement procedure is shown in

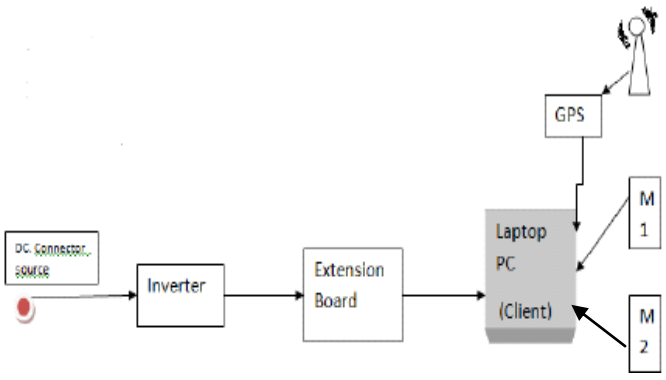

Fig 1: Drive test system set up

Table 2: Simulation Parameters.

Parameters	Values
Antenna type	S-wave 0809-65-15DV14
Operating frequency	2100MHz
Node B transmitter	43dBm in urban, 46dBm in sub-urban, 48dBm in rural.
Node B antenna height	30m in urban, 34m in suburban,38m in rural
UE antenna height	1.5m
Node B antenna gain	18dB
UE antenna gain	0dB
Connector loss	2dB
Cable loss	1.5dB
Duplexer loss	1.5dB
Body loss	3dB

The shadow fading factor of 8dB, 6dB, and 5dB for Urban , suburban and Rural areas respectively were assumed through out the research work.
Figs (2) to (4) show the log files obtained for the field measured data obtained during the drive test for urban, suburban and rural areas respectively.

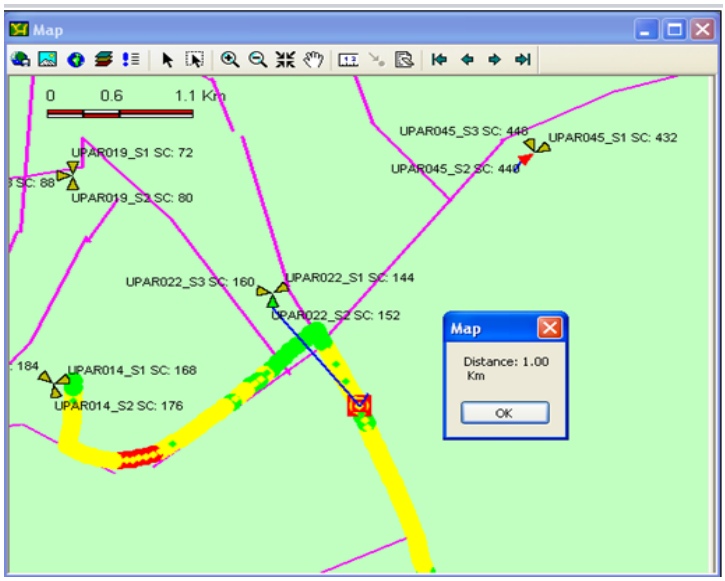

Fig 2 Log file showing the received signal level distribution for Urban area (Rumokoro)

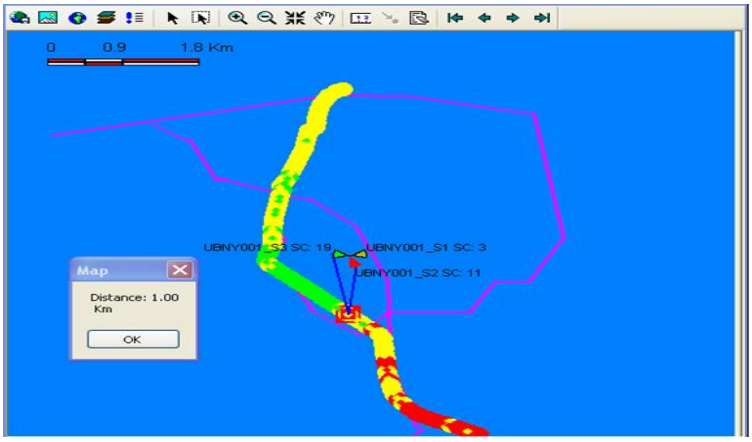

Fig 3: Log file showing the received signal level distribution for Sub-urban area (Finima, Bonny Island)

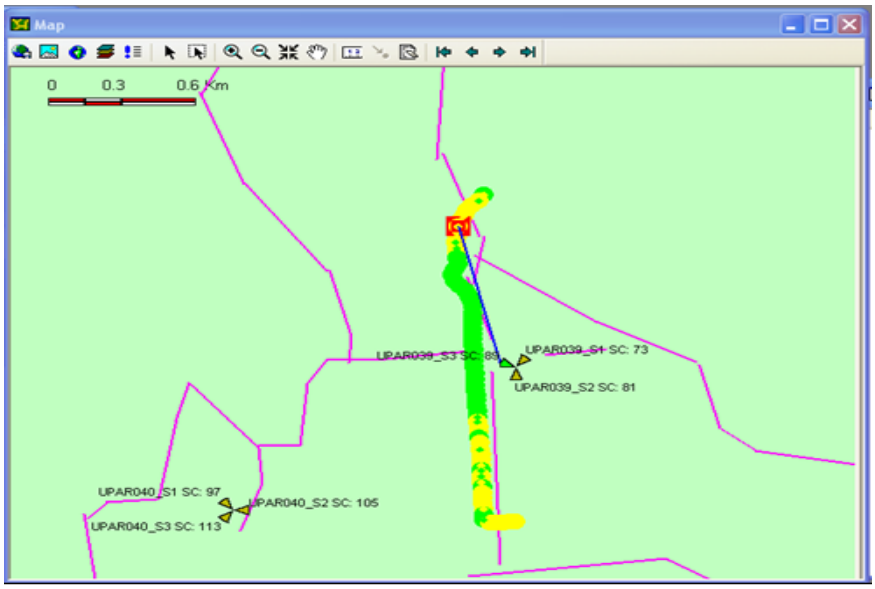

Fig4: Log file showing the received signal level distribution for rural area (Borokiri)

3.1 Field Measured Path loss. These tables below show the data obtained from the investigated areas.

Table 3: Measured Path Loss for Urban area.

Distance between the Node B and the UE, d (Km)	Mean received level (dBm)	Measured Path Loss, (dB)
0.10	-69	115
0.20	-74	120
0.30	-79	125
0.40	-80	126
0.50	-82	128
0.60	-85	131
0.70	-89	135
0.80	-93	139
0.90	-97	143
1.00	-99	145

Table 4: Measured Path Loss for Suburban area.

Distance between the Node B and the UE, d (Km)	Mean Received Level (dBm)	Measured Path Loss, (dB)
0.10	-62	110
0.20	-68	116
0.30	-71	119
0.40	-75	123
0.50	-77	125
0.60	-81	129
0.70	-83	131
0.80	-85	133
0.90	-87	135
1.00	-89	137

Table 5: Measured Path Loss for Rural area.

Distance between the Node B and the UE, d (Km)	Mean Received Level (dBm)	Measured Path Loss, (dB)
0.10	-60	110
0.20	-62	112
0.30	-67	117
0.40	-71	121
0.50	-74	124
0.60	-77	127
0.70	-79	129
0.80	-81	131
0.90	-83	133
1.00	-85	135

3.2 STATISTICAL MODELLING OF FIELD MEASURED PATH LOSS.

The values of the path loss exponent, r and the reference path loss L(d), for each of the environments are obtained from the measured data by linear regression algorithm . Considering other losses stated in Table 2, the resultant Path loss model for field measurement is expressed as,

$$L_{estimated}(dB)=L(d)+10*r*\log_{10}(\frac{d}{d_o})+X_\sigma +(G_T+G_R)-(L_R+L_T) \quad (15)$$

Referring to equation (15), the path loss exponent, r and the reference path loss L(d) are calculated for each environment using EXCEL worksheets.

IV. COMPARISON OF MEASURED PATH LOSS WITH EXISTING PATH LOSS MODEL

The path loss values for the three existing models investigated are estimated using equations (2), (5), and(10).The results were compared with the resultant path loss from the field measurements for the three locations using equation(15) and the results are shown in Figs (5) to (7) **.**

V. RESULTS AND DISCUSSION

The relationship between the predictions from the three path loss models considered and the measured path loss are simulated on MATLAB software and are showed on the path loss distributed graph in Figs (5) to (7).

The comparison between measured path loss and the predicted path loss models are also done based on MSE and SD as give in equations (16) [6] and (17) respectively. The results of the comparison are given in Table (6). From the results obtained, it shows that ECC-33 model overestimates the measured path loss and has the highest predictions for the three environments, followed by SUI model. COST 231 Hata model under estimates measured path loss with high prediction values when compared with the minimum acceptable limit for good signal propagation.

$$MSE = \sqrt{\frac{\sum_{i=1}^{n}(P_m-P_r)^2}{n-1}} \quad (16)$$

$$\sigma = \sqrt{\frac{(\sum_{i=1}^{n}(P_m-P_r)^2}{n}} \quad (17)$$

Where, P_m Where, $P_{m=}$ the measured path loss (dB), P_r is the predicted path loss (dB), and n is the number of measured data points. The results are tabulated in Table (6).

Table (6): Statistical evaluation of MSE and SD for COST 231 Hata , SUI, ECC-33 models

Verification items	COST 231 Hata model		SUI model		ECC-33 model	
	MSE	SD	MSE	SD	MSE	SD
Urban	20.440	19.391	37.185	35.277	162.646	154.299
Suburban	17.156	16.276	36.284	38.247	169.379	160.687
Rural	14.799	14.002	36.786	38.776	118.75	

The acceptable limit for good signal propagation is 6dB [7]. COST 231 Hata model has the least MSE and SD for the three environments. COST 231 Hata model is selected as the best path loss model for effective predictions for Cellular transmission in Rivers state.

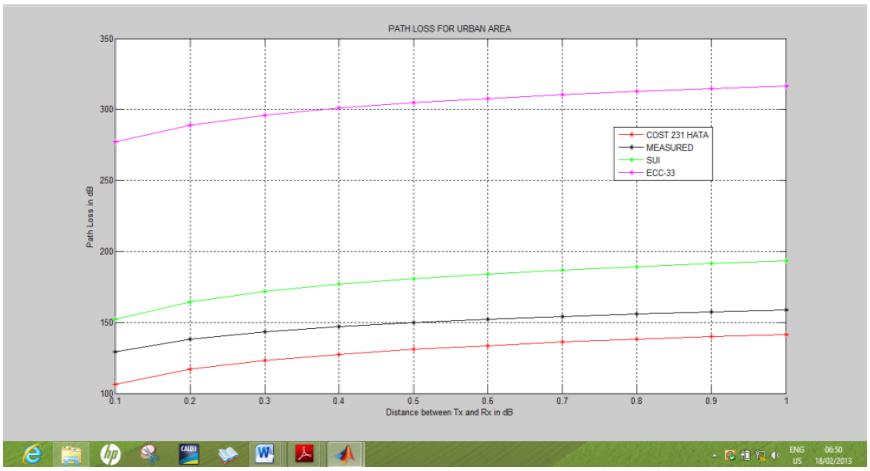

Figure 5: Comparison of path loss models with the measurement from urban area.

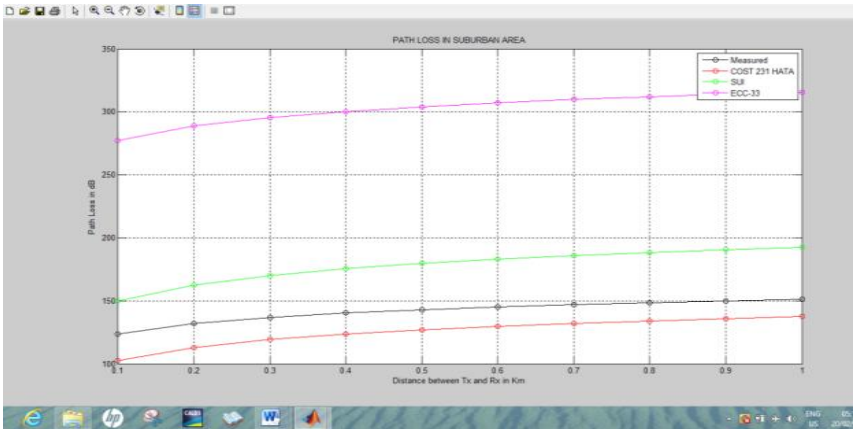

Figure 6: Comparison of path loss models with measurement from suburban area

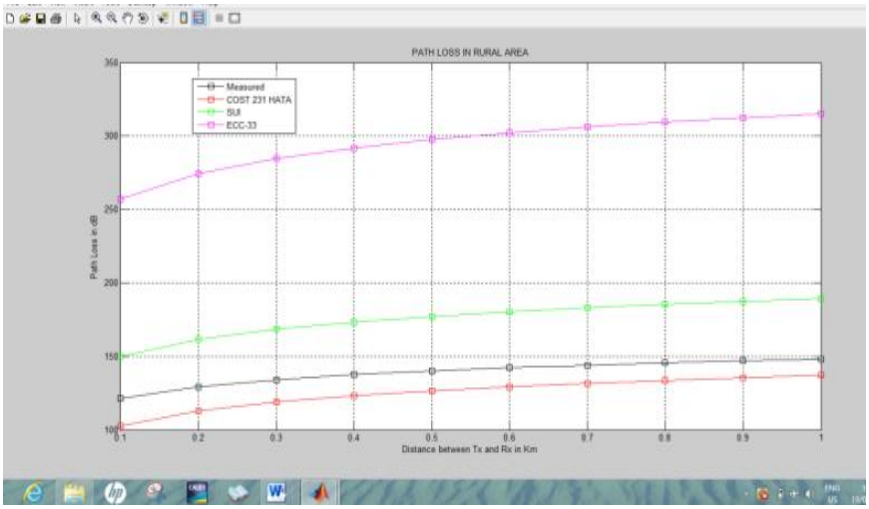

Figure 7: Comparison of path loss models with measurements from rural area

VI. CONCLUSIONS

A comparative analysis of three path loss prediction model for urban, suburban, and rural area in Rivers State is presented in this paper. The measured path loss for each location is extracted from the field data and compared with corresponding results obtained from the three models. COST 231 Hata model showed a better performance for path loss predictions in Rivers state. From the results obtained, it is recommended that for accurate prediction of radio signal characteristics for cellular transmission, COST 231 Hata model needs to be adjusted .

REFRENCES

[1] Harri H, Antti T,"WCDMA for UMTS Radio The measured path loss Access for Third Generation Mobile Communications

[2] Andrea Goldsmith Wireless Communications Stanford University, 2005, pp 27

[3] Rappaport, T.S " Wireless Communications, Second Edition, Pearson Publication, India, , pp 1392005,

[4] Rakesh N. , Srivasta S. K. "An Investigation on Propagation Path Loss in Urban Environments for Various Models at Transmitter Antenna Height of 5om and Receiver Antenna heights of 10m, 15m and 20m " International journal of research and reviews in Computer science, Vol. 3 ,no 4 , 2012, pp 1761-1767, .

[5] Bruno S.L Marcio R, Gervasio P, "Comparision Between Known Propagation Models Using Least Squares Tuning Algorithm on 5.8 GHz in Amazon Region Cities" Journal of Microwaves, Optoelectronics and Electromagnetic Applications, Vol.10, No,1, 2011,pp 106-113

[6] Nwaogazie I. L. "Probability Statistics for Science and Engineering Parctice 2006, pp 114-120.

[7] Nadir Z, Muhammed I. A "Pathloss Determination using Okumura –Hata Model And Cubic regression for Missing Data for Oman", Proceedings of the International Multi Conference of Engineers and Computer Scientists , *IAEN-ICCSA* 2010,Hong Kong 20Vol II1, pp 804-807.

American Journal of Engineering Research (AJER)
e-ISSN : 2320-0847 p-ISSN : 2320-0936
Volume-02, Issue-08, pp-32-43
www.ajer.org

Research Paper Open Access

Contribution of Night Time Yield to The Overall Water Production Capacity of A Simple Basin Solar Still Under Makurdi Climate

Edeoja, Alex Okibe[1], Ibrahim, J. Sunday[1]; Adaba, Sediyetu[1]
[1](*Mechanical Engineering Department, University of Agriculture, Makurdi, Nigeria)*

Abstract: - The yield of the simple solar still is relatively very low and several research efforts are going on to improve it. In this work, 2 solar stills of aperture 0.003 m^2 inclined at 10^0 were designed and constructed along with a rock bed thermal storage unit. One, still 1, was linked to the storage unit. Hourly ambient and still water temperatures, incident insolation and volumes of water distilled were measured daily from 10:00 to 16:00 hours daily for 6 days in May 2011. The water in still 1 was drained daily at 16:00 hour and water from the storage unit introduced into it. The temperatures of the water in the storage unit were measured at 10:00 and 16:00 hours daily. The volumes of the water distilled during the night by the stills were measured daily in the morning. The efficiencies of the stills were computed. Stills 1 and 2 distilled maximum daily daytime mean volumes of 78.2 and 57.3 cm^3 respectively on the 6^{th} day. The respective corresponding night time yields were 181 and 242 cm^3. The maximum mean daily distillation efficiencies were respectively 31.1 and 25.1%. The total night time yield was about 43% of the total. The cost of distilled water was computed to be about ₦52.50/litre/m^2. Hence, solar distillation remains a viable option for provision of potable in Makurdi metropolis and its environs.

Keywords: - *Cost of distilled water, Night time yield, Potable water, Solar radiation, Solar still, Thermal storage,*

I. INTRODUCTION

In developing countries, lack of safe and reliable drinking water constitutes a major problem. Makurdi Metropolis in Benue State, Nigeria faces serious water supply issues that are comparable to those found in many parts of the developing world. There are some parts of the town where pipe borne water is not in existence. Water vendors are common place within the town thereby diverting human resource that could positively impact the economy to carrying out the duties of an ineffective/nonexistent water supply system. Some of these vendors sell water directly obtained from the River Benue which flows by the town while the more reasonable or 'hardworking' ones push their water carts for long distances in order to obtain pipe borne water. For those that have access to the pipe borne water, the quality does not meet the standards acceptable for drinking even by physical observation. Many packaged water firms have sprung up and though a package sells for between ₦5.00 and ₦10.00 depending on the volume of business, time of the year, type of water or simply the location, the general consensus is that the quality is generally very low to the point that there is a call for an act of parliament to counter this obvious health hazard [1].

On both sides of the River Benue, there are unorganized communities that have limited infrastructural development, including water supply. Several hundreds of people that live along the river bank in *North Bank*, *Wurukum*, *Wadata* and along *Gboko Road* for which safe drinking water can only be acquired by purchasing and probably hauling portable water from elsewhere. In these locations municipal water supplies do not meet drinking water standards if and when available. The unorganized nature of the water supply network and the quality of the 'treated' water leaves so much to be desired.

Solar distillation could offer a real and effective solution for families in these locations to clean their water supplies on-site. Solar still has been proven to be the best solution to solve water problem in remote arid areas. Purifying water through distillation is a simple yet effective means of providing drinking water in a

reliable and cost-effective manner. Solar stills effectively eliminate all water borne pathogens, salts, and heavy metals, and produce ultrapure water that is proven to be superior to most commercial bottled water sources [2]. This device is however not popular because of its low productivity. Over the last few years, there have been efforts to develop simple solar distillation technologies that could be applied in these locations to meet drinking water needs [3-5].

Various efforts have been embarked upon to improve the production rate of this device. The methods that have been attempted to increase the productivity ranges from decrease the volumetric heat capacity of the basin, attachment of additional sub-systems and other major departures from the simple configuration. [6] designed, constructed and tested a prototype solar still having a vertical flat absorber of 0.817 m^2 outdoors. It was constructed using locally available materials as well as local technical assistance and had a total area of glass cover of 0.8769 m^2. The absorbing surface consisted of a set of a parallel black porous cloths wick plate located in an enclosure. The still was formed by a vertical absorbing surface, two transparent glass covers and a vertical back wall made of galvanized iron, darkened with black color internally and covered externally with 5 cm of glass wool as insulator.

Two solar stills (single basin and double decker) both having the same basin area (0.45m^2) were fabricated and tested by [7]. For the double-decker basin solar still, the upper glass cover and the first basin were tilted at 12^0 with respect to the horizontal, while for the single basin solar still, the glass cover was tilted at 36^0 with respect to the horizontal. Two types of measurements were performed; one with the still-sides insulated and the other without. The daily average still production for the double-basin still is around 40% higher than the production of the single-basin still. [8] carried out an experimental investigation to study the effect of coupling a flat plate solar collector on the productivity of solar stills. Other different parameters (i.e. water depth, direction of still, solar radiation) to enhance the productivity were also studied. Single slope solar still with mirrors fixed to its interior sides was coupled with a flat plate collector. It was found that coupling of a solar collector with a still increased the productivity by 36%. Also they reported that increase of water depth decreased the productivity, while the still productivity is found to be proportional to the solar radiation intensity.

A simple single basin solar still with optimum inclination of glass cover of 33.3^o for both summer and winter was designed by [9]. The average daily output of solar still based on data of 8 days in July 2004 was found to be 1.7 liters/day for basin area of 0.54 m^2 and the efficiency of the still was calculated as 30.65% with a maximum hourly output of 0.339 liters/hr at 1300 hrs. The drinking water produced had total dissolved solids (TDS), conductivity and pH of 84 ppm, 31 m S/cm and 5.74 after desalination with the values for TDS and pH agreeing with the WHO guidelines for drinking water quality. [10] fabricated and tested a stepped solar still and an effluent settling tank for desalinating the textile effluent. The effluent is purified in an effluent settling tank. For better performance, the stepped solar still consisted of 50 trays with two different depths. The first 25 trays with 10 mm height and the next 25 trays with 5 mm height were used. Fin, sponge, pebble and combination of the above are used for enhancing the productivity of the stepped solar still. A maximum increase in productivity of 98% occurred in stepped solar still when fin, sponge and pebbles are used in this basin.

[11] designed and fabricated a simple transportable hemispherical solar still and was evaluated its performance under outdoors of Dhahran climatic conditions. He reported that the daily distilled water output from the still ranged from 2.8 to 5.7 l/m^2 day with the daily average efficiency of the still reaching 33% and the corresponding conversion ratio near 50%. He also reported that the average efficiency of the still decreased by 8% when the saline water depth increased by 50%. An experimental investigation on the effect of internal and external reflectors inclined at angles 0° (vertical), 10°, 20° and 30° on the output of simple-basin solar stills in summer, autumn and winter was presented by [12]. The increase in the productivity of the still with reflector(s) compared to the still with no reflectors (increase ratio) is averaged at 19.9% and 34.5%, 34.4%, 34.8% and 24.7% for still with internal reflector only, still with internal and an inclined external reflector tilted at 0°, 10°, 20°, and 30° respectively. They also projected a comparable yearly productivity for external reflector angle ranging from vertical to 20°.

[13] presented a theoretical analysis of a tilted wick solar still with an external flat plate reflector. He found the optimum inclination angle of the still as well as the optimum inclination angle of the reflector for each month at 30°N latitude. He reported that the daily amount of distillate of the still can be increased by adjusting the inclination of both the still and reflector for any season, thus producing an average of about 21% more than a conventional tilted wick still throughout the year. A theoretical analysis of a basin type solar still with internal and external reflectors was presented by [14]. The external reflector is a flat plate that extends from the back wall of the still, and can presumably be inclined forwards or backwards according to the month. He found the optimum external reflector inclination for each month for a still with a glass cover inclination of 10–50. The increase in the average daily amount of distillate throughout the year of a still with inclined external reflector with optimum inclination in addition to an internal reflector, compared to a conventional basin type still was predicted to be 29%, 43% or 67% when the glass cover inclination is 10, 30 or 50 and the length of external

reflector is half the still's length.

[15] theoretically studied a basin solar still with internal and external reflectors. A theoretical analysis of a one step azimuth tracking tilted-wick solar still with a vertical flat plate reflector was presented by [16]. They found that the increase in the daily amount of distillate of a tilted-wick still would average about 41% for four days, and can be achieved by the simple modification of using a flat plate reflector, setting the still at proper tilt angle according to seasons and rotating the still just once a day. Based on a theoretical analysis of a tilted-wick solar still with an inclined flat plate external reflector on a winter solstice day at 30^0 N latitude and the daily amount of distillate [17] predicted for a still with an inclined reflector was about 15% or 27% greater than that with a vertical reflector when the reflector's length is a half of or the same as the still's length.

[18] considered the integration of energy utilization system and seawater desalination as an innovative technology enabling efficient simultaneous use of middle or low temperature thermal energy and supply freshwater. Three feasible approaches were considered and the findings indicate that combining seawater desalination with industrial processes is a feasible and promising way to solve the problems of the lack of freshwater and low efficient use of low temperature thermal energy in coastland areas. A new approach to improve the efficiency of a solar still by introducing a medium to provide large evaporation surface and utilize the latent heat of condensation was presented by [19]. They modified the conventional still by integrating an energy storage medium in the form of a jute cloth which is kept vertically in the middle of basin saline water and also attached with the rear wall of the still. It was found that the cumulative still yield in the regenerative still with jute cloth increases approximately by 20% and efficiency increases by 8% with low cost for this modification as the jute cloth is very cheap and easily available.

[20] produced a portable solar still and integrated a solar collector, a wall covered with black wool, and water sprinkling system to increase evaporation rate, and a thermoelectric cooling device to enhance water condensation due to the small size and low productivity in order to enhance and improve the performance. The performance of the still was tested under the climate condition of Semnan (35° 33′ N, 53° 23′ E), Iran. The experiments were carried out in nine winter days and the results were measured in the same manner for each day. The results show that ambient temperature and solar radiation have direct effect on still performance but water productivity decreases when the wind speed increases. By comparing the results for summer and winter, they concluded that the efficiency in summer is higher than in winter. Their results also show that the cost per litre of distilled water is comparable with that for other types of solar stills. The enhancement of solar still performance using a reciprocating spray feeding system was investigated by [21] while [22] carried out a study using a hybrid photovoltaic thermal double slope active solar still. [23] presented a study on a still with modification for enhanced condensation while [24] investigated a tilted wick still with an external flat plate reflector considering optimum still and reflector inclination.

The enhancement of the productivity of the solar desalination system, in a certain location, could be attained by a proper modification in the system design. However, the increase in the system productivity with high system cost may increase also the average annual cost of the distillate. [25] undertook a cost analysis of 17 design configurations of solar desalination units in order to evaluate the benefit of modification from the economical point of view using a simplified model. Their results show that, the best average and maximum daily productivity are obtained from solar stills of single-slope and pyramid-shaped. The higher average annual productivity for a solar still is about $1533 l/m^2$ using pyramid-shaped while the lower average annual productivity is about of $250 l/m^2$ using modified solar stills with sun tracking. The lowest cost of distilled water obtained from the pyramid-shaped solar still was estimated as 0.0135$/l while highest cost from the modified solar stills with sun tracking is estimated as 0.23$/l.

The Energy Systems Research Group of the Department of Mechanical Engineering at University of Agriculture, Makurdi has been working to further develop the technology and demonstrate its practicality as an innovative, effective, simple, and decentralized on-site water treatment system that can provide safe water in a cost effective and reliable manner. This effort began in earnest a few years ago and is still ongoing. This is because the abundant solar distillation feedstock (water) provided by the River Benue and the immense solar radiation that Makurdi is reputed for almost all year round can be harnessed to positively impact the availability of drinking water. Makurdi on latitude 7.7^0N and longitude 8.73^0E receives an average insolation of 35430 kJ/m^2/day from an average 6.13 hours of sunshine with the highest and lowest in August and December respectively [26].

Specific work has been done by [27] in investigating the effect of coupling a pre-heat tank and a reflector to a simple basin still at Makurdi. Also, [28] investigated the effect of a pebble thermal storage on the performance of a basin still. These and other unpublished works are aimed at making this simple technology to impact on provision of save drinking water in Makurdi Metropolis and its environs. The present study in which the contribution of night time distillation is investigated is also part of this effort. It is a deliberate attempt to incorporate the distillation process that definitely occurs during the night as a result of the temperature change

imposed on the water in the still during the day time. The usually cooler ambient temperatures at night should play a vital role in achieving a reasonable yield.

From the foregoing, it is obvious that the relative advantages of the simple basin solar still are being investigated in order to make it relevant in the potable water production mix especially in developing regions of the world. This becomes very appropriate because in most of these places, the political will to address the drinking water needs of the majority of the citizenry does not simply exist. This technology can however be developed to confer some level of control to the end user as far as the issue is concerned.

II. MATERIALS AND METHODS

The construction of the solar still was done using a procedure similar to those used by [28]. The design specifications are given in Table 1. Fig. 1 shows the orthographic representation of the solar still. The thermal storage unit has the following design specifications shown in the Table 2. Fig. 2 shows a sectional view of the storage medium.

Table 2: Design Specifications for the Solar Stills.

Parameters	Dimensions
Width of glass cover	607 mm
Length of glass cover	707 mm
Area of glass cover	429149 mm^2
Length of tank	600 mm
Width of tank	501 mm
Height of tank	200 mm
Volume of tank	60120000 mm^3
Height of distillate collector	11.5 mm
Length of distillate collector	4140 mm
Width of distillate collector	10 mm
Thickness of wood	1.875 mm & 1.25 mm (¾ & ½ in)
Insulation thickness for the sides	10 mm
Insulation for the base	5 mm
Diameter for PVC pipe	2.5 mm (1 in)
Angle of inclination	10^0
Diameter of water drainage	2.5 mm (1 in)

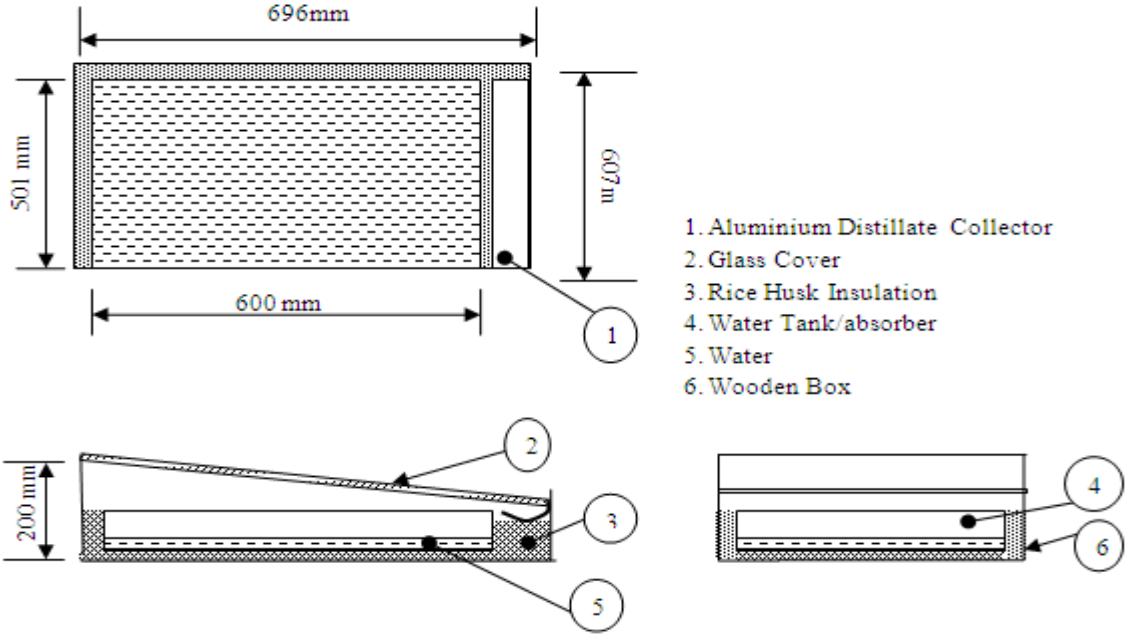

Fig.1: orthographic representation of the solar still

Table 3: Design Specifications for the Storage Medium

Parameters	Dimensions
Length of glass cover	703.5 mm
Width of glass cover	703.5 mm
Area of glass cover	494912.25 mm^2
Length of metal tank	355 mm
Width of metal tank	355 mm
Height of metal tank	150 mm
Volume of metal tank	18903750 mm^3
Width of wooden box	705 mm
Height of wooden box	39 mm
Volume of wooden box	27495 mm^2
Thickness of pebbles gap (base, sides and top)	10 cm

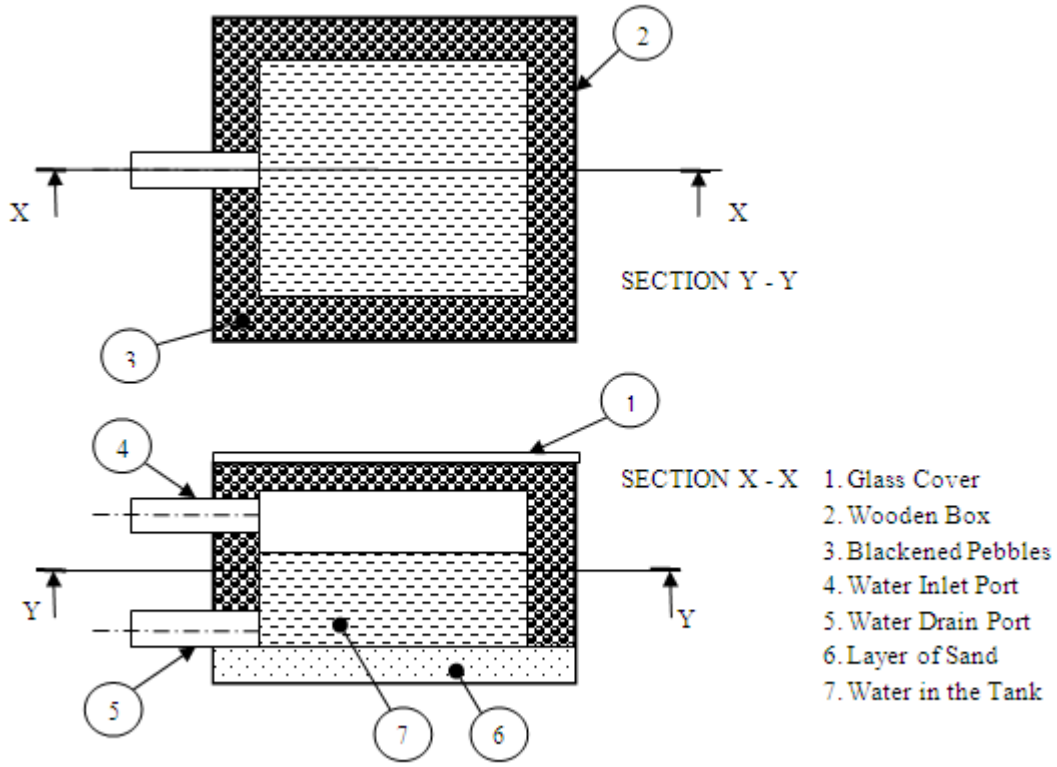

Fig.2: sections through the rock bed storage unit

The set up for the study was at the Engineering Complex at University of Agriculture, Makurdi. One of the solar still (still 1) and the solar storage medium were joined using a flexible hose linking the outlet tap from below the tank of the storage medium to the inlet pipe of the solar still while the other one (still 2) was mounted independently beside the first one. A flexible hose was used so that slight changes in elevation or orientation of the individual components (i.e. the still or the storage medium) could be made without affecting the position of the other component. The solar still was mounted above ground level. The pebbles storage medium was mounted on a higher level than the still so that water was able to flow freely as a result of the hydrostatic pressure head set up between the components by virtue of difference in the elevation when the tap is opened. A plastic container was place below the discharge pipe of the stills to collect the liquid distillate from them. Plate 1 shows the storage medium and the two solar stills.

Water was first of all poured into the solar storage medium through the inlet pipe after which water was added into the stills to an appropriate depth through the still inlet pipe and the pipe was closed. This was done in the morning at about 09.00 hours daily for the period of study. The water in the solar still was then left to distill using direct solar radiation from in the morning, while the water in the solar storage medium was left to absorb heat from the surrounded black coated pebbles across the metal tank walls.

The temperatures of the water fed into the storage medium and the stills as well as the temperature of

the water in the storage medium in the evening (after 16.00 hours) were recorded daily. The hourly ambient and still water temperatures as well as the available insolation were also recorded from 10.00 -16.00 hours daily during the period of study. The temperatures were measured using mercury in glass thermometers calibrated for accuracy with a thermocouple. The corresponding volumes of water distilled and collected were measured using a measuring cylinder and recorded. The available insolation was measured with a solarimeter (sun meter).

The water remaining in the still 1 was drained off after recording the final set of readings for each day. Water from the storage medium was the released into the still 1 through the flexible hose such that the distillation could occur during the night by making use of the stored thermal energy from the sun. In the morning the distillate volume was noted for both stills 1 and 2, and the water in both stills made the same before the commencement of another round of operation. The water used for the study was source around the University. The solar still efficiency, total output as well as other associated ratios were computed using (1) and (2):

Solar still production is given as

$$M_e = \frac{Q_e}{L} \quad (1)$$

The solar still efficiency is given as

$$\eta = \frac{Q_e}{Q_t} \quad (2)$$

$M_e =$ daily distilled water output (kg/m^2 day), $Q_e =$ quantity energy utilized in vaporizing water in the still (J/m^2 day), $L =$ latent heat of vaporization of water (J/kg), $\eta =$ Solar still efficiency and $Q_t =$ quantity of incident solar energy on the still (J/m^2/day) [29].

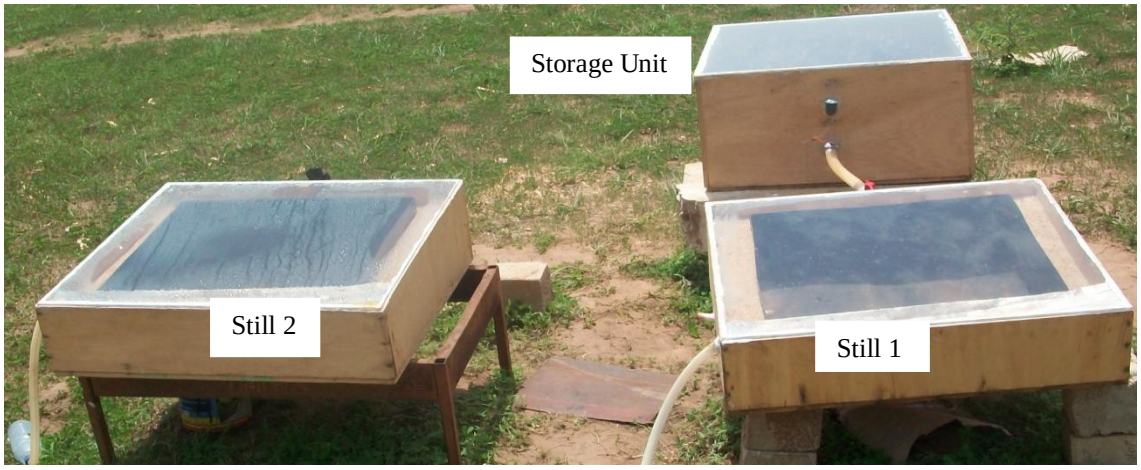

Plate 1: picture of the components of the set up for the study

III. RESULTS

Table 3 shows the temperatures associated with the operation of the storage medium used for this study and the measured volumes of water produced during the night time operation of the stills. Table 5 shows the mean daily measured and computed parameters for the two stills for day time operation. Table 6 shows the corresponding mean hourly values of the parameters.

Table 4: Storage Medium Temperatures and Volume of Water produced during the Night by the Stills

Day	T_1 (^{0}C)	T_2 (^{0}C)	□T (^{0}C)	V_1 (cm^3)	V_2 (cm^3)
1	30.0	38.0	8.0	68.0	150.0
2	32.0	40.0	8.0	190.0	302.0
3	30.0	38.0	8.0	160.0	175.0
4	31.0	45.0	14.0	251.0	175.0
5	31.0	38.0	7.0	157.0	300.0
6	30.0	45.0	15.0	260.0	350.0
Mean	**30.8**	**40.7**	**10.0**	**181.0**	**242.0**

Table 5: Daily Mean Values of Measured and Computed Still Parameters

Day	T_a (^{0}C)	T_{s1} (^{0}C)	T_{s2} (^{0}C)	V_{s1} (cm^3)	V_{s2} (cm^3)	η_{s1}	η_{s1}	I(W/m^2)
1	32.7	42.7	42.7	20.2	20.3	0.147	0.139	133.2
2	35.7	43.5	43.5	66.3	49.8	0.262	0.203	148.5
3	31.3	40.0	40.0	31.2	27.0	0.147	0.106	132.8
4	34.5	42.8	42.8	58.8	43.8	0.236	0.176	154.0
5	36.7	45.7	45.7	56.5	48.8	0.311	0.251	122.2
6	35.7	46.0	46.0	78.2	57.3	0.299	0.216	169.7

Table 6: Hourly Mean Values of Measured and Computed Still Parameters

Time	T_a (^{0}C)	T_{s1} (^{0}C)	T_{s2} (^{0}C)	V_{s1} (cm^3)	V_{s2} (cm^3)	η_{s1}	η_{s1}	I(W/m^2)
10-11	33.3	40.3	40.3	11.5	12.3	0.054	0.062	146.3
11-12	34.5	42.6	42.6	34.3	22.6	0.186	0.124	114.3
12-1	36.0	44.2	44.2	55.5	36.2	0.273	0.187	121.5
1-2	34.5	44.5	44.5	69.7	53.8	0.337	0.245	135.8
2-3	34.7	44.8	44.8	77.8	66.8	0.263	0.229	174.8
3-4	33.5	44.2	44.2	62.3	55.3	0.238	0.219	171.8

Figs. 3 to 5 show line graphs of the volume of water produced by the stills for night time operation, the daily mean volumes of water produced during the daytime and the corresponding hourly values. Figs. 6 and 7 show the relationship between the hourly mean efficiencies of the stills to the corresponding mean volumes of water produced. Figs. 8 and 9 show the corresponding relationships based on the hourly mean efficiencies and volumes. Figs. 10 and 11 show the relationships between the daily mean ambient temperature during the period of the study and the volume of water produced by the stills. Figs. 12 and 13 show the relationship of the mean available insolation to the volume of water produced.

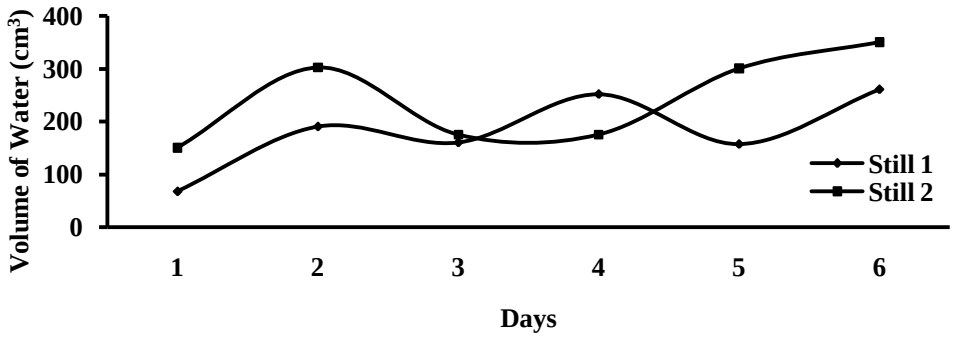

Fig. 3: volume of water produced by the water stills during the night

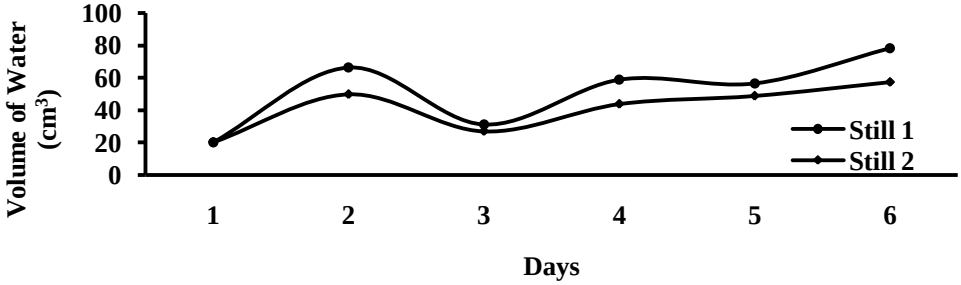

Fig. 4: daily mean volumes of water produced by the stills

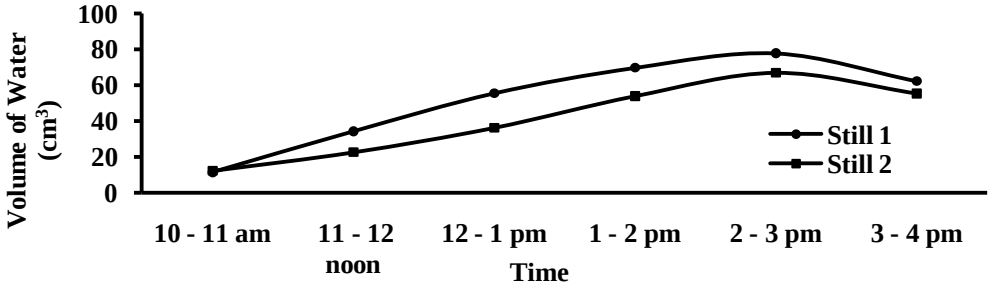

Fig. 5: hourly mean volumes of water produced by the stills

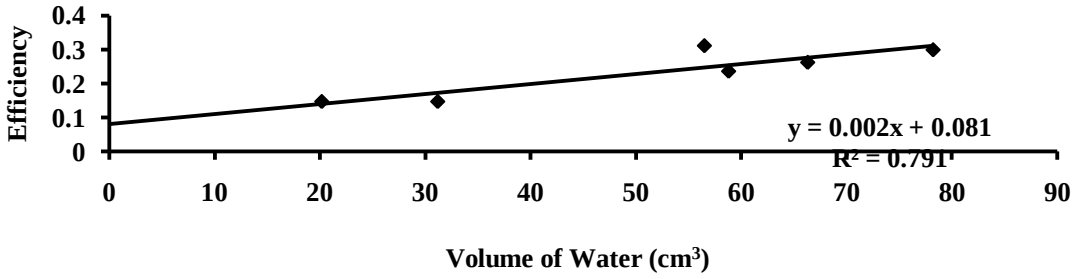

Fig. 6: daily mean efficiencies against volumes of water produced by still 1

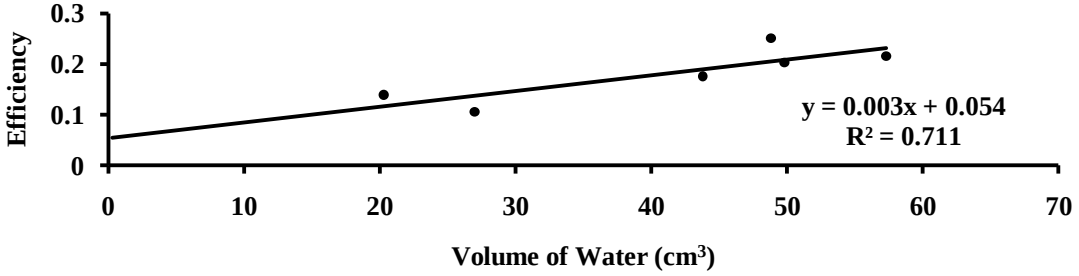

Fig. 7: daily mean efficiencies against volumes of water produced by still 2

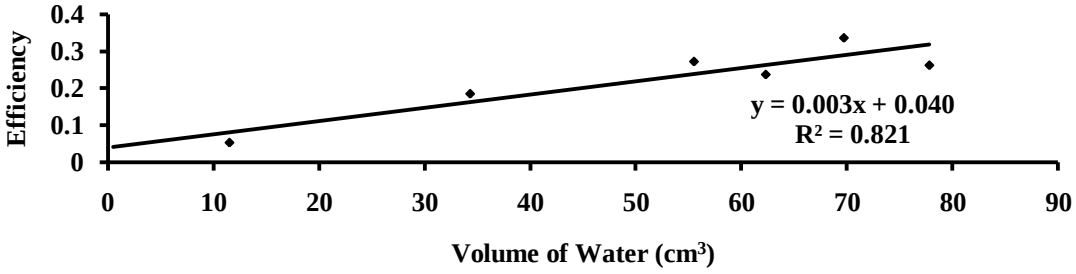

Fig. 8: hourly mean efficiencies against volumes of water produced by still 1

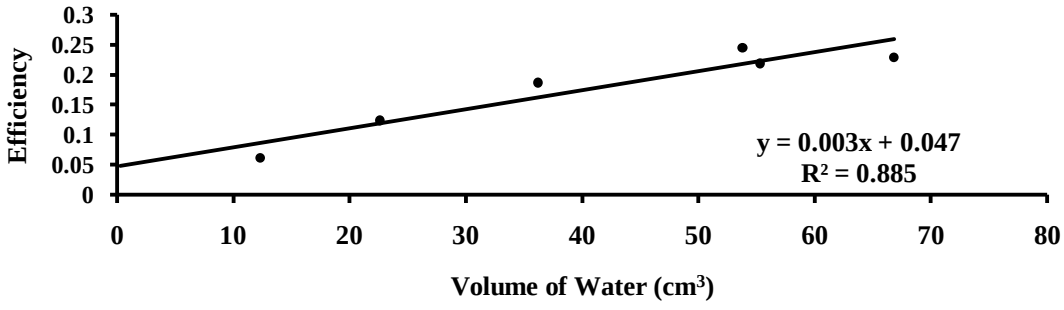

Fig. 9: hourly mean efficiencies against volumes of water produced by still

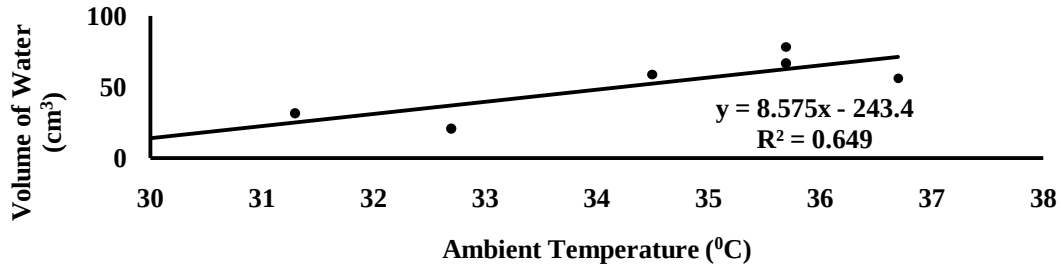

Fig. 10: variation of daily mean ambient temperatures with volume of water for still 1

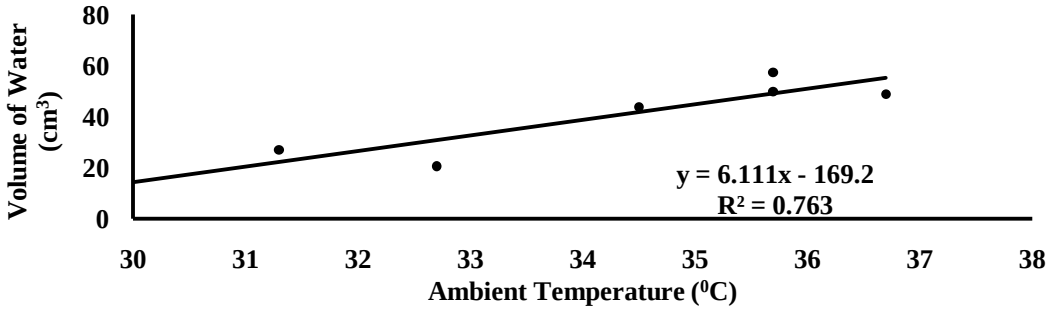

Fig. 11: variation of daily mean ambient temperatures with volume of water for still 2

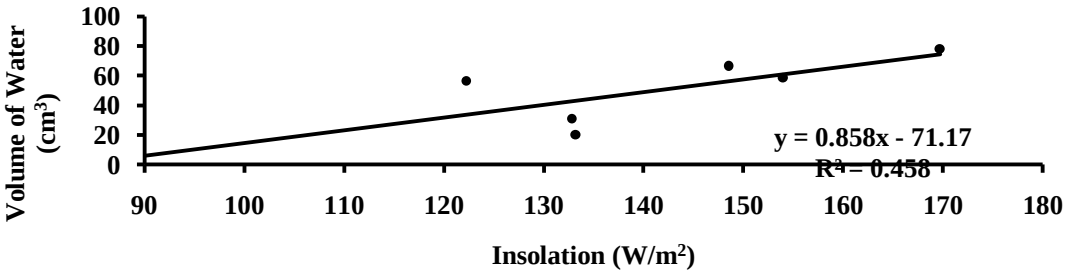

Fig. 12: daily means of available insolation against volume of water for still 1

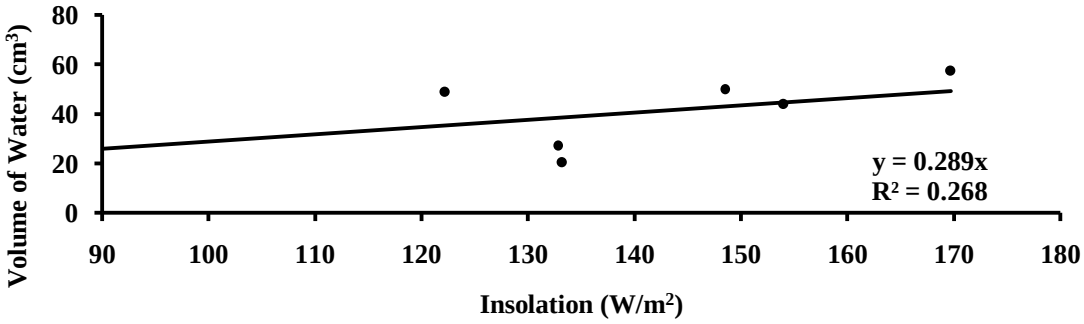

Fig. 13: Daily Means of Available Insolation against Volume of Water for Still 2

IV. DISCUSSION

Fig. 3 shows the volumes of water produced by the solar stills during the night for the period of the study. Still 1 was emptied in the evening daily and water from the thermal storage unit introduced into it while the water in still 2 was not changed. The figure shows that except on the fourth day still 2 had a better yield than still 2 which seems to contradict the claim of [28] that by using a separate thermal storage unit to supply water at a reasonably high temperature to a still in the evening it is possible to increase the cumulative yield of a simple basin still. Their assertion was based on the fact that the driving force for still operation depends largely on the difference in temperature between the still glass cover surface and the water. They maintained that the usually colder night temperatures will likely lower the cover surface temperature below what was obtained in the day

time thereby imposing a higher difference in temperature for the purpose of producing water. However, it appears on the other hand than their assertion could be valid as justified by the yield of still 1 on the fourth day. This is further strengthened by the fact that the mean final temperature of the water from the storage medium throughout the period was 40.7 ^{0}C as shown in Table 4. This was below the daily mean final temperatures for the normal day time operation of the two stills for all the days which ranged between 42 to 46 ^{0}C except on the third day (40 ^{0}C) as shown in Table 5. Also, it was below the mean hourly final temperature of 44.2 ^{0}C as shown in Table 6. The discrepancy could have resulted from an error in the design of the storage medium with respect to some unchecked heat losses or improper selection and/or proportion of the storage medium material which could be attended to in further work. This does not however invalidate the idea of using night time operation to supplement day time yield as a means of increasing the cumulative daily water yield of a simple basin solar still.

The mean temperature difference between the initial and final temperatures of the water in the storage medium was 10 ^{0}C as shown in Table 4. This translates to stored heat energy in the region of 42,000 kJ/kg of water. The quantity of energy stored could also have been affected drastically by the weather fluctuations during the period of the study with the change in temperature of the water reaching 14 ^{0}C and 15 ^{0}C only on the fourth and sixth day respectively. Only the initial and final temperatures of the water were recorded as the transfer of water from the medium into still 1 was done at the end of each day's work. The quantity of heat stored could have been more substantial if the period of the study was longer in terms of the number of hours per day. However, this advantage can be better harnessed during the period of the year with clearer sky conditions.

The mean volumes of water produced during the night operation as shown in Table 1 were 181 cm^3 and 242 cm^3 for stills 1 and 2 respectively. These translate to about 60,333.33 cm^3 and 80,666.67 cm^3 of water per square metre of still aperture. The total volume of water produced by the stills for night operation for the period of the study were 1086 cm^3 and 1452 cm^3 respectively for still 1 and still 2. These translate to 362,000 cm^3 and 484,000 cm^3 per square metre of still aperture. Hence, the potential estimate of the total water that can be produced for night operation by the two stills for the period of the study is 846,000 cm^3 which shows the existence of the capacity to supplement day time still operation in generating drinking water for residents in some locations like *North Bank*, *Wurukum* and *Wadata* in Makurdi Metropolis. An array of several simple basin stills carefully laid out can therefore go a long way in producing portable water very close to or at the point of use.

Figs. 4 and 5 show the daily and hourly means of volumes of water produced by the two stills for day time operation for the period of the study. For both categorizations of the data, still 1 produced a higher volume of water on all the days except on the first day. It produced the largest volume of water of 78.2 cm^3 on the sixth day against 57.3 cm^3 produced by still 2. This translates to 26,066.7 cm^3 and 19,100 cm^3 per square metre of still aperture. This difference is unexpected since the dimensions, orientations and angles of tilt of the stills were the same. It could have been as a result of some undetected fault in the assembly of still 2. However, the respective yields on the sixth day indicate that the available insolation affects the quantity of water produced by a solar still because the highest mean insolation for the study period of 169.7 W/m^2 was recorded that day. This value is much lower than the average value for Makurdi location [26]. This is indicated by the highest total daily volume of 469 cm^3 of water produced. Figs. 12 and 13 however, show that there was significant fluctuation in weather clearness during the period of the study. The mean insolation recorded on the fifth day was the lowest though the volume of water produced was not the least. Hence, other factors like relative humidity could have possibly played a role by affecting the ambient temperature but were not taken into account in this study. Further work may be carried out in which the effect of relative humidity in particular may be studied since humidity is exceptionally high in Makurdi for most part of a year.

Expectedly considering at the hourly mean values presented in Table 6 and plotted in figure 5, the stills performed better as from 12.00 noon with the tempo reaching a peak between 2.00 – 3.00 pm. The decline beyond this stage is not drastic and could have increased the total daily yield if the daily study period was extended to about 6.00 pm. For this study however, the yield for the remaining two hours of daylight is included in the volume obtained for night operation of the stills. The maximum hourly volumes produced for the two stills in this study as shown in Table 3 were 77.8 cm^3 and 66.8 cm^3 for stills 1 and 2 respectively. The corresponding minimum hourly mean values were expectedly low (11.5 and 12.3 cm^3 respectively). This was because the stills were just commencing operation after the night time yields have been harvested. It can be noted here that still 2 produced a little more water than still 1 during the first hour of operation. Coupled with the fact already mentioned about the superior night operation of still 2, it appears that it was able to perform better when the insolation was little or unavailable (in the night). This could mean that still 2 had better insulation and/or was better sealed. Both stills were however able to maintain an average daily and hourly difference in temperature between feed water and the water in the stills of 13.4 ^{0}C throughout the period of the study.

The total volumes of water produced by the still 1 for the study period was 1927 cm^3 while that for still

2 was 1483 cm^3. This represents a difference of 444 cm^3 or about 23% of the expected yield assuming that the yield of still 1 is taken as a reasonable guide and becomes substantial when the cumulative yield is considered. The difference between the respective day and night time yields for the stills was more significant for still1 (841 cm^3 as against 31 cm^3 for still 2). The total yields translate to 642,333.33 cm^3 for still 1 and 494,333.33 cm^3 per square metre of still aperture. The combined day time yield for the stills per metre square of still aperture was 1,136,666.66 cm^3. The combined yield for both day and night operations of the stills for the period was 1,982,666.66 cm^3 per square metre of still aperture or 330444.44 cm^3/m^2 of still aperture/day. The estimates for monthly and yearly yield can easily be made. Hence, the yield during the night represented 42.7% of this total. This shows that the capacity for the night time operation to supplement day time yield is quite significant and could play a vital role in producing on-site portable water for both rural and many so-called urban areas in Nigeria.

Figs. 6 to 13 are attempts to relate some of the operating parameters of the stills to the volume of water produced. In figs. 6 to 9, efficiency is shown to vary approximately linearly with the volume of water as expected. However, the R^2 values obtained showed that the daily mean efficiencies showed a better relationship for still 1 (R^2 = 0.791 as against 0.711 for still 2) while the hourly mean efficiencies showed a better relationship for still 2 (R^2 = 0.885 as against 0.821 for still 1). The higher R^2 value for the relationship in still 2 seems to further affirm the fact earlier mentioned that it appeared to have better insulation or less heat loss. In comparison, the hourly values showed a better relationship probably as a consequence of the fluctuation of the available insolation during the period of the study.

Figs. 10 and 11 show that the ambient temperature has a fairly linear relationship with the volume of water produced. Again the relationship for still 2 had the better R^2 value of 0.763 compared to 0.649 for still 1. This confirms that still 2 performed better in terms of the utilization of the daily ambient temperatures for the study period. The mean hourly ambient temperatures in Table 3 shows the usual pattern of variation of time on a normal day with lower values in the mornings, peak values in the afternoon and lower ones in the evening. However, these values do not show a linear relationship with the volume of water produced due to the fluctuation of weather experienced.

Figs. 12 and 13 show that the available insolation has a poor linear relationship with the volume of water produced. This ordinarily should not be the case. The general unpredictability of the weather largely blamed on human activities and the period when this study was carried out (just before the rainy season) could be responsible for this. There were intermittent sunny and cloudy conditions experienced throughout the period of the study which was part of the reason why the time for the daily commencement of the study was not earlier than 10.00 am. The hourly mean values of the available insolation showed a poorer relationship with the water volume for both stills. Still 1 however, had a better relationship than still 2.

Purity test was not conducted on the samples that were generated in this study. It was deliberate because the objective of this study was primarily to increase yield with reference to previous work carried out. Adequate facilities are available however, for testing for total dissolved solids (TDS), pH value, salinity and other contaminants in the Department of Food Science and Technology in University of Agriculture, Makurdi as well as at Water First, Makurdi. Moreover, a New Mexico State University pilot study showed that solar stills effectively eliminate all salts, heavy metals, bacteria, and microbes from contaminated water sources as long as they are carefully design and proper material selection is done. Testing even reported successful removal of some pesticides (due to UV rays, high temperatures, and atmospheric venting), although recommendations remain to use a carbon filter with stills for guaranteed removal of all volatile organic compounds [2].

The total project cost was about seventeen thousand naira, three hundred and fifty naira only (₦17, 350.00). This translates to 5.25 kobo/cm^3/m^2 of still aperture /day. This means about ₦52.50/litre/m^2 of still aperture/day which falls within the range of costs obtained by researchers in other locations depending on the time of the year [25]. The cost will expectedly be lower in the dry season and higher in the rainy season when acute cloudy weather is common place.

V. CONCLUSIONS AND RECOMMENDATIONS

The results of the present study indicate that the night time yield has a significant contribution to the overall productivity of the simple basin solar still. This has further strengthened the position of the Energy Research Group of the Department of Mechanical Engineering at University of Agriculture, Makurdi that the system can be adopted to play a role in the potable water supply program for the people living close to the River Benue. With more focused and deliberate funding the system can be developed to operate under Makurdi climate with very positive results, Consequently, it will be a step in the right direction if this area of research is drafted into the University of Agriculture, Makurdi Strategic Plan. Better documentation and dissemination of the information already gathered is the next step in order to create awareness among the end-users, NGOs and the Government with a view of promoting acceptability and getting commitment towards realizing the immense

potentials that this option provides. The Benue State Government appears to be determined to provide portable water for the citizenry as indicated by the commitment of several billions of Naira to a water project called the Greater Makurdi Water Works. A very small part of this revenue can be channeled into further development of solar still technology to make it impact on the populace.

REFERENCES

[1] J. Ahenjir, "Benue and the Menace of 'Pure' Water, The Voice Newspaper, Friday, June 10, 2011, 7, Published by Benue Printing & Publishing Corporation, Makurdi, Nigeria.

[2] A. Hanson, W. Zachritz, K. Stevens, L. Mimbela, R. Polka, & L. Cisneros, Distillate Water Quality of a Single Basin Solar Still: Laboratory and Field Studies, *Solar Energy*, *76(5)*, 2004.

[3] K. K. Murugavel & K. Srithar, Performance study on basin type double slope solar still with different wick materials and minimum mass of water, *Renewable Energy*, *36*, 2011, 612 – 620.

[4] K. K. Murugavel, K. K. S. K. Chockalingam & K. Srithar, Progresses in improving the effectiveness of the single basin passive solar still, *Desalination*, *220*, 2008, 677– 686.

[5] V. Velmurugan, M. Gopalakrishnan, R. Raghu & K. Srithar, Single Basin Solar Still with Fin for Enhancing Productivity, *Energy Conversion and Management*, *49*, 2008, 2602 – 2608.

[6] M. Boukar & A. Harmim, Development and testing of a vertical solar still, *Desalination*, (2003), 158 - 179.

[7] A.A. Al-Karaghouli & W.E. Alnaser, Performances of single and double basin solar-stills, *Applied Energy*, *78*, 2004, 347 – 354.

[8] O.O. Badran & H. A. Al-Tahaineh, The effect of coupling a flat-plate collector on the solar still productivity, *Desalination*, *183*, 2005, 137– 142.

[9] M. A. Samee, U. K. Mirza, T. Majeed & N. Ahmad, Design and performance of a simple single basin solar still, *Renewable and Sustainable Energy Reviews*, *11*, (2007), 543 – 549.

[10] V. Velmurugan, K. J. N. Kumar, T. N. Haq & K. Srithar, Performance analysis in stepped solar still for effluent desalination, *Energy*, *34*, 2009, 1179 – 1186.

[11] B. I. Ismail, Design and performance of a transportable hemispherical solar still, *Renewable Energy*, *34*, 2009, 145 – 150.

[12] A. J. N. Khalifa & H. A. Ibrahim, Effect of inclination of the external reflector on the performance of a basin type solar still at various seasons, *Energy for Sustainable Development*, *13*, 200), 244 – 249.

[13] H. Tanaka, Experimental study of a basin type solar still with internal and external reflectors in winter, *Desalination*, *249*, 2009a, 130 – 134.

[14] H. Tanaka, Monthly optimum inclination of glass cover and external reflector of a basin type solar still with internal and external reflector, *Solar Energy*, *84*, 2010, 1959–1966

[15] H. Tanaka, & Y. Nakatake, Theoretical Analysis of Basin type Solar Still with Internal and External Reflectors, *Desalination*, *197*, 2006, 205 – 216.

[16] H. Tanaka, & Y. Nakatake, One step azimuth tracking tilted-wick solar still with a vertical flat plate reflector, *Desalination*, *235*, 2009a, 1– 8.

[17] H. Tanaka, & Y. Nakatake, Increase in distillate productivity by inclining the flat plate external reflector of a tilted-wick solar still in winter, *Solar Energy*, *83*, 2009b,785–789.

[18] R., Deng, L. Xie, H, Lin, J. Liu, & W. Han, Integration of thermal energy and seawater desalination, *Energy*, 35, 2010, 4368 – 4374.

[19] M., Sakthivel, S. Shanmugasundaram, & T. Alwarsamy, An experimental study on a regenerative solar still with energy storage medium - Jute cloth, *Desalination*, *264*, 2010, 24 – 31

[20] J. A. Esfahani, N. Rahbar& M. Lavvaf, Utilization of thermoelectric cooling in a portable active solar still - An experimental study on winter days, *Desalination*, *269*, 2011, 198 – 205.

[21] A. M. El-Zahaby, A. E. Kabeel, A. I. Bakry, S.A. El-Agouz & O.M. Hawam, Enhancement of solar still performance using a reciprocating spray feeding system – An experimental approach, *Desalination*, 267, 2011, 209–216.

[22] G. Singh, S. Kumar & G. N. Tiwari, Design, fabrication and performance evaluation of a hybrid photovoltaic thermal (PVT) double slope active solar still, *Desalination*, 2011, Article in Press, Elsevier Science Ltd.

[23] K. V. Kumar & R. K. Bai, Performance study on solar still with enhanced condensation, *Desalination*, *230*, 2008, 51 – 61.

[24] H. Tanaka, Tilted wick solar still with external flat plate reflector: Optimum inclination of still and reflector, *Desalination*, *249*, 2009b, 411– 415.

[25] A. E. Kabeel, A. M., Hamed, & S. A. El-Agouz, Cost analysis of different solar Still configurations, *Energy*, *35*, 2010, 2901 – 2908.

[26] I. N. Itodo & A. U. Fulani, Development of a Passive Solar Crop Dryer with an Air Pre-heater Unit, *Proc. of the 5th International Conference and 26th AGM of the Nigerian Institution of Agricultural Engineers*, *26*, 2004, 406 - 411.

[27] J. S. Ibrahim, A. Kuhe, & A. O. Edeoja, Performance Test of the Effect of Coupling a Preheat Tank and Reflector to a Basin Still under Makurdi Humid Climate, Journal of Research in Engineering, *International Research and Development Journals*, 2008, Uyo, Nigeria.

[28] A. O. Edeoja, J. S. Ibrahim & M. Ekoja, Effect of a Thermal Storage Medium on the Performance of a Basin Solar Still in Makurdi, *International Journal of Engineering Science*, *1(2)*, 2009, Pan-African Book Company, Ghana.

[29] O. Kopsch, How to Convert Salt Water into Pure Drinking Water using Solar Power, 2003, Rosendahl Systems, Hannover, Germany.

American Journal of Engineering Research (AJER)
e-ISSN : 2320-0847 p-ISSN : 2320-0936
Volume-02, Issue-08, pp-44-50
www.ajer.org

Research Paper Open Access

Energy Analysis For Production Of Local Alcohol (*Burukutu*) In Benue State, Nigeria

Ibrahim J. Sunday[1], Alex O. Edeoja[1], Ierve I. Aondover[2]
[1]*Department of Mechanical Engineering, University of Agriculture, P.M.B. 2373, Makurdi, Nigeria.*
[2]*Works and Housing Department, Buruku Local Government Council, Buruku, Benue, Nigeria.*

Abstract: **-** Energy study in the production of local alcohol (Burukutu) was carried out in six (6) Local Government Councils, representative of the three senatorial districts of Benue State, Nigeria. Eighteen cases were randomly investigated within the locations. Types of energy utilization (manual, liquid fuel and wood fuel energy) in addition to unit operations were identified. Energy, time, and number of persons and mass/material data were collected and computed. The energy consumption pattern of the unit operations were evaluated for production of 642kg of finished product. The analysis revealed that seven unit operations were required for the production of Burukutu. Results showed no significant difference at 95% confidence level of the energy requirements for the 18 cases studied with respect to the identified unit process of production and the mean values of the total energy of consumption was found to be 3122.90MJ. The most intensive operation was boiling, which accounts for 97.76% of the total energy for the production of Burukutu. Optimization of the boiling process is suggested to make the system more energy efficient.

Keywords: **-** *Analysis, unit processes, burukutu, energy utilization, optimization energy efficiency, central region, local.*

I. INTRODUCTION

Energy is said to be the engine of growth and development in all economies of the world. In all parts of the world today, the demand for energy is increasing on a daily basis. In Nigeria, energy and in particular, oil, has continued to contribute over 70% of federated revenue [1]**.** It is also true that all activities for the production of goods and services in the Nation's major sector of the economy (Industries, transport, agriculture, health, politics, education and so on, have energy as an indispensable input.

Energy produced by crude oil has over the past five years contributed average of 13.5% of Nigeria's Gross Domestic Product (GDP), representing the highest contributor after crop production [1]. Consequently, energy in Nigeria stands unique as an input to the production of all goods and services as well as an instrument for politics, security and diplomacy. However, it is now universally accepted that fossil fuels which is the major source f energy in Nigeria are finite and it is only a matter of time before their reserves become exhausted. Extended use of these reserves, worldwide, in the current manner will continue for no more than some decades to come [2]. The increasing energy demand coupled with the finite energy resources, the rising cost of fossil fuel, deforestation and its attendant environmental impacts necessitate an understanding into the mechanisms, which degrade the quality of energy and energy systems. The processes that degrade the quality of the energy resource can only be identified through a detailed analysis of the whole system [3]. Quantifying the energy requirements will go a long way in determining the most efficient and effective way to use energy in *Burukutu* production.

Burukutu production relies on energy and mass (material input/output) to carry out the desired operations and obtain high processing efficiencies. Energy is primarily invested in various forms such as mechanical (human-labour), chemical (fossil fuel) and thermal (heat). The amount of energy used in *Burukutu* production is significantly high in order to meet the demand for the expanding population that consume the alcohol. The raw materials used in manufacturing the drink are produced in the tropical regions of Africa particularly in the Northern Guinea savanna areas of Nigeria [4, 5]. The beverage is very rich in calories,

vitamin B and essential amino-acids such as Lysin [6].

In Nigeria, *Burukutu* is consumed in various festivals and Nigerian ceremonies (marriage, birth, dowry and so on) and constitute a source of economic return for the women manufacturers. Currently the production of this beer is increasing because of the high cost of factory beer as one bottle of the least factory beer is N130.00 but a similar bottle of *Burukutu* is N40.00 yet it gives the same effect. According to [7], this *Burukutu* has come to provide a lot of women with Jobs, especially those living in rural and semi-urban areas. The annual growth rate in women employment in this enterprise is about 8 percent, while young girls and older women are keen on learning the trade. Many young girls learn it when helping their mothers in the local enterprise. Most women in the business confirmed that the business is lucrative.

Research works in the area of assessment of energy requirements generally and particularly in local cottage industries in Nigeria have been neglected; there is need to audit the energy consumption in these industries in order to salvage them from economic loses and environmental effects. A limited number of studies has been reported on energy analysis in process industries. [8] analyzed the 5 year energy consumption data for 25 tea factories in South India. The variation in energy consumption in kilowatt hour per kg of tea made in factories based on factors such as type of tea produced, production capacity of factories climate etc, were analyzed. They also studied the specific energy consumption for the different processes. The consumption of direct energy from major sources in tea industries in Assam India was studied by [9]. They submitted that a tea garden required an estimated 18, 408MJ/ha of human energy in the first year.

An energy study was conducted by [10] in an organic fertilizer plant in Ibadan, Nigeria, to determine the energy requirement for the production of both powdered and pelletized organic fertilizer. In their study they evaluated the energy consumption pattern of the unit operations for production of 9000kg of the finished products. Their analysis revealed that eight and nine defined unit operations were required for the production of powder and pellet, respectively. The electrical and manual energy required for the production of powdered fertilizer were 94.45 and 5.5% of the total energy, respectively, with corresponding 93.9 and 5.07% for the production of pelletized fertilizer. The respective average energy intensities were estimated to be 0.28 and 0.35 MJ/kg for powdered and pellets. The most energy intensities were estimated to be 0.28 and 0.35 MJ/kg for powder and pellets and the most energy intensive proportion of 33.4 and 27.0% of the total energy for production of powder and pellets. Optimization of the production system was suggested to make the system energy efficient. Analysis of energy usage in the production for three selected cassava – based foods in Nigeria was done by 11 . They used some energy accounting symbols. The computation of energy use was done using Microsoft Excel spreadsheet. In 12 , study on the energy consumption pattern in palm kernel oil processing operations, data on PKO production, quality of fossil fuels used, the electrical power used from state grid, and captive power generated were obtained for each of the seven readily defined unit operations. 13 studied the energy use pattern in medium- and small-scale rice parboiling outfits. Five set of par-boilers in the upper Benue River basin in Adamawa State, Nigeria were selected for the study: three small rural par-boilers and two medium-scale suburban par-boilers. The study reveals the need for optimized energy use for rice parboiling and it shows that in order for rural rice processing to be sustainable, energy sources must be carefully considered and the concept of recycling of fuel biomass should be integrated into the process. 14 Studied various types of energy pattern used in rice milling industries viz., thermal energy, mechanical energy, electrical energy and human energy. They noticed that though, wide variety of technologies have been evolved for efficient use of energy for various equipments of rice mills, so far, only a few have improved their energy efficiency levels. Most of the rice mills use old and locally available technologies and are also completely dependent on locally available technical personnel. They concluded that energy conservation in the rice industry would lead to reduction in the use of fuels and electricity.

There is therefore no known report of any work in the literature on the energy requirement in *Burukutu* production in Nigeria or elsewhere in the world. A similar procedure for the breakdown of the *Burukutu* production process into unit operations and determination of energy requirement in each was used. The objectives of this work can be summarized into:

(i) to determine by mass, material and energy balance, the process and unit operations of *Burukutu* production in Benue State;
(ii) to determine the energy requirements of each and the entire process; and
(iii) to identify the energy use pattern in the production system as a step towards optimization of the system.

II. MATERIALS AND METHODS

Processing data was obtained randomly from six commercially viable *Burukutu* producing Local Governments Councils in Benue State, Nigeria, namely Buruku, Gboko, Makurdi, Oju, Katsina–Ala and Vandeikya. The trend observed for Benue State is conveniently representative of other locations in the Middle Belt and some parts of the Northern Region of the country. Each local government was made up of three

randomly selected case areas (sites) of *Burukutu* processing industries. A total of eighteen sites were used for the study. The flow chart of the production system is shown in Fig. 1.

The primary energy resources utilized in the plant were identified to be manual (obtained from human labour), liquid fuel energy (obtained from fossil fuel), and wood fuel energy (obtained from wood fuel). Seven unit operations were defined for *Burukutu* production process: steeping, washing, grinding, filtering, mashing, boiling and re-filtering. The weight of sample input was measured from a weighing balance. An inventory of number of persons involved time required for production (h), quantity of fuel used (L), quantity of wood fuel used (kg) and material flow for the seven readily defined unit operations was made. The energy analysis was based on process analysis in which the direct energy consumption in every successive production step was estimated and the materials in put to each operation also indicated. These raw data were then converted to energy equivalents using (1), (2), and (3).

2.1 Estimation of Energy Input into each Unit Operation.

The energy components (manual, liquid fuel and wood fuel) for the production of for each of the unit operation were calculated for the production of 160.53kg of finished *Burukutu*. The following procedure was used:

2.1.1 Manual energy input

Manual energy estimation was based on the values recommended by 14 . They affirmed that at the maximum continuous energy consumption rate 0.30KW and conversion efficiency of 25% the physical power output of a normal human labour in the tropical climates is approximately 0.075KW sustained for an 8 – 10 hour workday; all other factors affecting manual energy expenditure were found insignificantly and therefore neglected.

To determine the manual energy for a given operation, the time spent by the worker on each operation was recorded. These include the intermittent resting periods. This was done mathematically as:

$$E_{m=} 0.075N.T_a \ \ (kW) \qquad (1)$$

where 0.075 = the average power of a normal human labour in kW, N = number of person involved in the operation; and T_a = useful time spent to accomplish a given task in hours.

2.1.2 Wood Fuel Energy Input

The wood fuel energy was estimated by measuring the amount of log that was consumed by the process, The wood fuel energy consumption Et is estimated from *W*, the amount of firewood used and *Ck*, the heating value of using the following relationship: $E \propto W$, 15

$$E = C_f W \qquad \text{(MJ)} \qquad (2)$$

where, C_f, is the constant of proportionality which represents the calorific value (heating value) of fuel used.

2.1.3 Fossil fuel energy input

The total quantity of energy consumed from fossil fuel (diesel and petrol) was estimated by multiplying the quantity of fuel consumed by its lower heating value, thus,

$$E_{FLD} = 47.8D, (MJ) \quad 16 \qquad (3)$$

where E_{FLD} = liquid fuel energy input for diesel (MJ), 47.8 = Unit energy value of diesel (MJL^{-1}), D = Amount of diesel fuel consumed per unit operation, (liter). For Petrol, $E_{LLP=} 42.3p\ (MJ)$, E_{LLP} = liquid fuel energy input for petrol (MJ), 42.3 = corresponding Unit value of petrol, and p = Amount of petrol consumed per unit operation (liters).

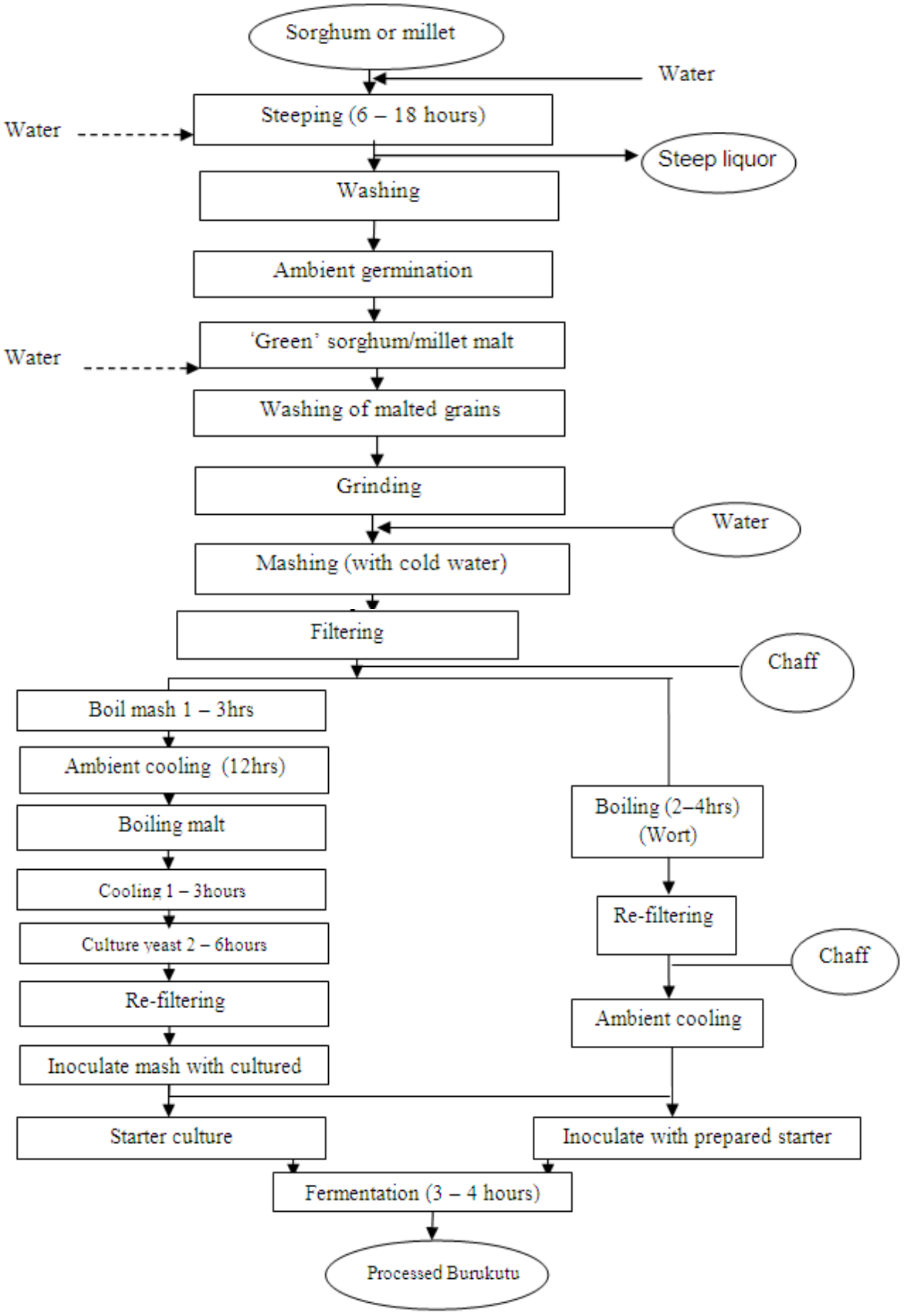

Figure 1: *buruktu* production process

2.2 Experimental Procedure

Before the commencement of grinding operation, known quantity of fuel was measured into the plastic tank. The tank was constructed from a white transparent plastic bucket. The capacity of the bucket was 4 liters. A 250ml measuring cylinder and water were used to calibrate the tank. After the completion of the batch, the quantity of fuel left in the tank was recorded. The difference in these readings represented the quantity of fuel used in (litres). The weight of fuel wood used was determined by similar difference. From this procedure, it was possible to assign, thermal energy, manual energy and liquid fuel energy, and a combination of two or all the forms of energies as the case may be, to each unit operation. The processing facilities of all the mills were very similar. All the mills selected were evaluated over the same period and seasons, and as a result the error of seasonal variation changes was eliminated. No prior experimental conditions were used as data collection in each locality was done as the mills were in operation. The following apparatus/materials were used for this study:

(i) Stop watch for measuring the production time;
(ii) 4 liters capacity constructed plastic tank used for measuring the quantity of fuel consumed during unit operation;
(iii) A measuring cylinder which was used to calibrate the constructed fuel tank; and
(iv) A weighing balance to measure the quantity of fuel

Using energy accounting symbols energy and mass flow diagrams were constructed Fig. 2 for typical *Burukutu* production mill.

III. RESULTS

3.1 Analysis of variance (ANOVA)

Analysis of variation (ANOVA) at 5% significant difference was conducted for the 18 cases which make up the locations of study for the energy requirement and the different unit operations for the production of the alcoholic local beverage as presented in Table 1.There was no significant difference in the energy requirements for all the 18 cases for at 95% confidence level implying that the system has been standardized. The mean values of the 18 cases were then considered for analysis.

Table 1: ANOVA for energy requirement for *burukutu* production

Source of Variation	*SS*	*Df*	*MS*	*F*	*P-value*	*F critical*
Rows	599483.5	17	35263.74	1.121219	0.344688	1.723833
Columns	1.43E+08	6	23753584	755.2512	3.96E-82	2.188761
Error	3208026	102	31451.24			
Total	1.46E+08	125				
Ho: F ≤ F Critical						α = 0.05
Ha: F > F Critical						

3.2 Energy Requirement for Production of *Burukutu*.

The average energy input at different stages of *Burukutu* production process is presented in Table 2 and Figure 2. From table 2 and figure 2, the energy consumption data obtained provides useful information on the sources of energy requirement of each processing unit. The data revealed that wood fuel was extensively used for operation. 97.06% of the average total average in all the six locations was obtained from wood fuel source, followed by 2.1% and 0.85% from liquid fuel and manual energy sources respectively. This clearly indicates that most of the tedious operation involved in *Burukutu* production were performed by heating and use of liquid fuel, with over 90% of the energy consumption attributed to the use wood fuel combustion over 2% of the energy consumption attributed to the use of internal combustion engine powered grinding mill.

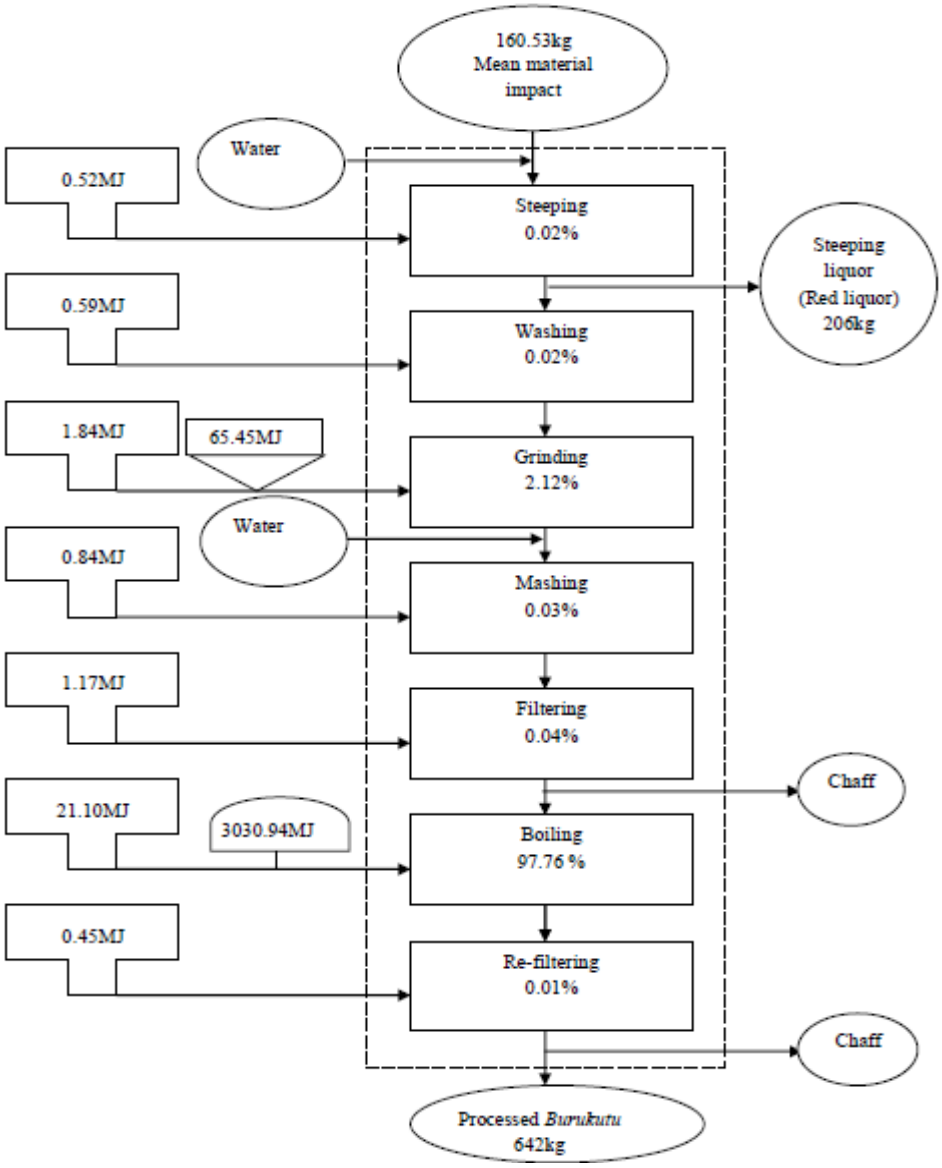

Figure 2: flow diagram for production of *buruktu* in the middle belt region of Nigeria

Table2: Mean Time and Energy Requirement for Production of *Burukutu* in the Middle Belt Region of Nigeria

S/No	Process	Time (hrs)	Manual Energy (MJ)	Wood Fuel Energy (MJ)	Liquid Fuel Energy (MJ)	Total Energy (MJ)	%Total Energy
1	Steeping	1.28	0.52	-	-	0.52	0.02
2	Washing	1.5	0.59	-	-	0.59	0.02
3	Grinding	1.55	1.84	-	65.45	67.3	2.12
4	Mashing	1.54	0.98	-	-	0.98	0.03
5	Filtering	1.77	1.17	-	-	1.17	0.04
6	Boiling	27.36	21.1	3030.93	-	3052.03	97.76
7	Re-filtering	0.72	0.45	-	-	0.45	0.01
	Total		26.51	3030.93	65.45	3122.9	100
	Mean Total%		0.85	97.06	2.1	100	

IV. CONCLUSIONS

The energy analysis for production of *Burukutu* in the middle belt region of Nigeria suggested that:

- Seven defined unit operations were required for the production of *Burukutu*.
- Wood fuel energy was the major energy input in the production of *Burukutu.*
- The most intensive operation was boiling, which accounts for 97.76% of the total energy for the production of *Burukutu*. Modification of the local stove to enhance more efficient utilization is hereby recommended and could be the subject of future work in this area.
- The use of waste biomass such as rice husks, combustible by-products from the production process as alternative fuel and modified stove may be key in ensuring sustainability of the boiling process.

REFERENCES

[1] M. S. Abubakar, Umar,B. and Ahmad, D. Energy use patterns in sugar production: A case study of savannah sugar company, Numan, Adamawa State, Nigeria. *J. of Applied science Research*. *6(4)*, 2010, 377-382.

[2] D.M. Considine, *Energy Technology Handbook*, McGraw Hill Book Company, 1977.

[3] M.A. Waheed, S.O. Jekayinfa, J.O. Ojediran, O.E. Imeokparia, Energertic analysis of fruit juice processing operation in Nigeria: *Energy, 33*, 2008, 35-45

[4] C. Ettasoe, *Sorghum and Pearl Millet*: in C. L. Leaky & J.B. Wills ed(s). Food Crops of lower Tropics. Oxford University Press, Great Britain, 1972, 191-192.

[5] J.J. Asiedu, *Processing tropical crops. A technological approach*, Macmillan Education Ltd, 1989, 189-222.

[6] F., Lyumugabe, G., Kamaliza, & B. Thonart, Microbiological and physico-chemical characteristics of Rwandese traditional beer *Ikage*. *African Journal of Biotechnology, 9(27)*, 2010, 4241 – 4246. Available online at http://www.academicjournals.org/AJB

[7] J.O. Alimba & J.U. Mgbada, Socio-economic consequences of technological change on the rural non-farm Igbo Women entrepreneurs of Southern Nigeria: Implications for farm and non-farm linkages. *African Technology Policy Studies Network Working Paper Series* No. 40. ATPS Communication Department, 2003, 52.

[8] C. Palaniappan & S.V. Subramanian, A study and analysis of energy consumption patterns in tea factories of South India for energy conservation solutions. *Journal of Agric. Mech. In Asia, Africa and Latin America*. *29(2)*, 1998, 12-16.

[9] D.C. Baruah & P.C. Bhattacharya, Energy utilization pattern in the manufacture of black tea. *Journal of Agric. Mech. In Asia, Africa and Latin America*, *27(4)*, 1996, 65-70.

[10] D.A. Fadare, O. A. Bamiro & A. O. Oni, Analysis for production of powdered and pelletinised organic fertilizer. *ARPN Journal of Engineering and Applied Sciences*, *4(4)*, 2009, 75 - 81

[11] S.O. Jekayinfa & J. O. Olajide, Analysis of energy usage in the production of three selected cassava-based foods in Nigeria. *Journal of Food Engineering, 82*, (2007, 217 - 226. Available online at: www.elsevier.com/locate/jfoodeng.

[12] I. A. Bamgboye & S. O. Jekayinfa, Energy consumption pattern in palm oil processing operation. Agricultural Engineering international: *CIGR EJournal*. Manuscript EE 05 013, *VIII*, 2006, 1-11

[13] M. Bakari, M. Ngadi, R. Kok, V Raghavan & A. Diagne, Energy analysis for small-and medium scale rural rice par-boiling in Sub-Saharan Africa. Second African rice congress, Bamako, Mali: innovations and partnership to realize Africa's rice potential, 2010, 6.6.1-6.6.5

[14] S. K. Goyal, S. V. Jogdand & A.V. Agrawal, Energy use pattern in rice industries- a critical appraisal. *J Food Sci Technol*., DOI 10.1007/s 13197-012-0747-3, 2012.

[15] E.U. Odigboh, Machines for crop production, In B.A. Stout (Ed), *Handbook of Agricultural engineering-plant production engineering*, American Society of Agricultural Engineers, 1997.

[16] R. K. Rajput *Thermal Engineering*. New Delhi. Laxmi Publications (P) Ltd, 2001, 434 - 464.

American Journal of Engineering Research (AJER)
e-ISSN: 2320-0847 p-ISSN : 2320-0936
Volume-02, Issue-08, pp-51-57
www.ajer.org

Research Paper Open Access

Experimental Validation of Hottel's Transmittance Model for Estimating Beam Radiation In Makurdi Location

[1]Edeoja, Alex Okibe and [1]Eloka-Eboka, C. Andrew
[1]*Mechanical Engineering Department, University of Agriculture, Makurdi, Nigeria*

Abstract: - Hottel's transmittance model for beam radiation was experimentally validated for Makurdi, Nigeria. Hourly, daily, weekly and monthly average beam radiation were determined from measured total/global radiation using a daystar sun-meter over a period July and November when the sun was at the northern hemisphere. These were correlated and compared with the average predicted by Hottel's model using analysis of variation (ANOVA) at 5% and 1% levels of significance, mean bias difference (MBD) and Root mean square difference (RMSD). The results indicated high significant differences at all levels tested with a variation of 2.9029 of the MBD and 3.1237 of RMSD and correlation coefficients of -0.8202 with measured normal radiation and -0.6397 with measured total radiation. This indicates a slim suitability of Hottel's model in Makurdi location. Climatic factors such as humidity, seasonal variation and weather may have caused the variation because they were not directly taken into consideration in the development of the model. The model could however be used by applying appropriate correction factors that can be obtained and employed which may make up for the limitation(s) for Makurdi and other locations. A model for Makurdi location like Hottel's is now of interest.

Keywords: - *Hottel's model, beam radiation, Analysis of variation, Mean bias difference, Root mean square difference, Climatic factors.*

I. INTRODUCTION

Solar energy is one of the most significant sources of energy on the globe. One of the most outstanding factors in predicting, studying and designing solar energy systems in each site is to have the exact information and statistics regarding the degree of solar radiation on that site, to the extent that it is necessary to estimate the amount of solar energy in each area before measurement and scheduling for its use [1]. The radiation emitted per unit area of the sun is approximately 6.33 x 10^7 W/hectare. If the energy coming from just 10 hectares of the surface of the sun could be harvested, it would be enough to supply sufficient energy to the world. This is however not possible since the amount of radiation leaving a unit area of the sun surface is not the same amount reaching equal unit area on the earth surface. The reason for this reduction is due to some predictable factors like the earth displacement from the sun, the earth's atmosphere and around the earth. As a result of these reductive factors, engineers and designers have found it important to know the estimation of radiation reaching the earth's surface based on the location for its usefulness in proper analysis of solar collection systems. The hourly and also instantaneous distribution of solar radiation is needed in various applications in the field of solar energy. The most reliable predictions of solar system performance are based on pyranometer data taken over a period of year at the place of interest. In many instances, however, available solar radiation data that have been collected are presented as a sum of integrated daily values [2–4]. In addition, the intensity of atmospheric radiant energy reaching the earth's surface could also be affected by the extent of cloud cover and dust particles as aerosol over a location. The radiation reaching the earth is reduced by 30% on a clear and by 90% on a hazy (cloudy) day. Therefore, it is appropriate to say that solar designed systems perform better on a clear day since there are more radiations. So, the need to ascertain the estimation of radiation (direct or beam, diffuse and total radiation) to a surface (vertical, horizontal and tilted) on a clear day in a particular location (s) using either analytical approach (models) or experimental measurements becomes very paramount and essential. These analytical methods whether simple or complex, were developed by different authors at different locations for

estimating solar radiations.

The successful design and effective utilization of solar energy systems and devices for application in various facets of human endeavors, such as power and water supply for industrial, agricultural and domestic uses, largely depend on the availability of information on solar radiation characteristic of the location in which the system and devices should be situated. [5]. Accurately computing solar irradiance on external facades is a prerequisite for reliably predicting thermal behavior and cooling loads of buildings, and other solar energy systems. Validation of radiation models and algorithms implemented in building energy simulation codes or other areas then becomes an essential endeavor for evaluating solar gain models [6-11]. .

Hourly radiation data is largely inexistent in Nigeria and in most places in the sub-Sahara regions of Africa, hence designers of solar energy systems usually resort to empirical models to evaluate hourly inputs of diffuse and beam irradiance for designs and optimization of different solar systems or more recently satellite information. There are several models which are available in literature used in predicting hourly solar irradiance. [12] presented an empirical model for determining the monthly average daily global solar radiation on a horizontal surface for Makurdi, Nigeria (Latitude $7^0$7'N and Longitude $8^0$6'E) was developed using the Angstrom-Page equation. The solar radiation (W/m^2), hours of bright sunshine and cloudiness were measured hourly from 0600 H to 1800 H daily for 18 months. The constants 'a' and 'b' of the Angstrom linear type equation were determined by plotting the clearness index (H/H_o) against the possible sunshine hours (ns/N) to obtain the line of best fit. The constant 'a' was obtained from the intercept of the line on the y-axis while the constant 'b' was obtained from the slope of the line. The developed model for determining the global horizontal solar radiation at the location was

$$H = H_o\left[0.17 + 0.68\left(\frac{n}{N}\right)\right] \quad (1)$$

with a coefficient of correlation of 0.78. The mean bias error and root mean square error that were used to test the performance of the constants were 0.17% and 1.22% respectively. The measured solar radiation was compared with the solar radiation predicted by the model and no significant difference was found between them using F-LSD at $P \geq 0.05$. [8] proposed a mono-variable model of monthly mean daily diffuse solar radiation on horizontal surfaces for some cities between 2°N and 5°N of Cameroon (Bertoua, Yokadouma, Yaoundé, Kribi, Kumba). The estimation was based on a correlation between clearance index and diffuse to global solar radiation ratio and was computed using monthly mean daily data set for global solar radiation on horizontal surfaces. The predictive efficiency of the proposed model was compared with the observed values and those believed to be universally applicable. The results suggest that the existing methods could be replaced by the developed model for a diffuse solar radiation data generation scheme. [13] investigated the effectiveness of an innovative procedure to calculate the global real sky irradiance of a mountain urban region, the city of Trento (Italy). The proposed methodology improves the predictive Bird's real-sky model by introducing in it both atmospheric parameters, specifically defined for the analyzed site, and a local cloud cover factor, based on experimental data, to calculate the global real sky irradiance. A multiple linear regression was applied to explain the relationship among Angstrom coefficients and geographical and meteorological data sets which were monthly mean clear sky or extraterrestrial radiation, the ratio of sunshine hours to day length, ambient and soil temperatures, relative humidity, sine of declination angle [14]. Variables in these equations were used to estimate the global solar radiation. Values calculated from models were compared with the meteorological values. Twenty four models having the best determination coefficient were compared with measured meteorological values by using statistical tests. In this study, first of all it was seen that the clear sky radiation can be used to estimate the global solar radiation in Bishkek. Finally, the using of the geographical and meteorological variables commonly has given the good results in estimating global solar radiation in Bishkek, Kyrgyzstan.

However, the complexity of some of them makes it difficult to put to appropriate use in Nigeria for radiation prediction. This is because the models require in many cases, meteorological inputs that may not be readily accessible due to the non-availability of measuring instrumentation. Angstrom turbidity coefficient, β, or Linke's turbidity factor, for example, cannot be easily measured in Nigeria. Other parameters not readily available include ground and sky albedos, ozone amount, predictable water vapor, illuminance, pyrheliometric instruments at narrow wavelengths and spectral irradiance. All these are contributory factors why complex models cannot be easily employed for estimation of solar radiation and therefore are not put to use. [9, 15-17]. There are some other very simple models which may not require any need of meteorological inputs to determine clear sky irradiance. However, as earlier established the utilization of simple or complex models require some level of validation in order to have an idea of the degree of relevance or applicability.

This present work considers an experimental validation of a simple model, Hottel's transmittance model for beam radiation on a clear day, for use in estimating solar irradiance in Makurdi generally and particularly for University of Agriculture, Makurdi as an experimental case point for data collection and

measurement.

1.2 Theoretical Background

Several radiation models have been postulated and are been utilized to estimate radiation values for various locations. For convenience, these models may be classified into those for inclined surfaces and the ones for horizontal surfaces. Many of these models are assumed to be applicable in locations with at least similar environmental conditions.

Hottel presented a simple model for the estimation of the transmittance of beam radiation in clear sky conditions [18]. The required inputs are the altitude of the location (in km above sea level), day number in the year and the zenith angle of the location. According to this model, the atmospheric transmittance for beam radiation τ_b is given by (2):

$$\tau_b = \frac{I_b}{I_o} \quad (2)$$

where, I_b is the hourly normal beam radiation, and I_o is the hourly beam radiation outside the Earth's atmosphere (extraterrestrial radiation) given by (3):

$$I_o = I_{SC}\left[1 + 0.033\left(\frac{360N}{365.25}\right)\right] \quad (3)$$

where I_{SC} is the solar constant approximately equal to 1367W/m^2 and $1 \leq N \leq 365$..

The clear sky beam normal radiation is given by (4):

$$I_{cnb} = I_o\tau_b \quad (4)$$

The clear sky horizontal beam radiation is given as in (5):

$$I_b = I_o\tau_b cos\theta_z \quad (5)$$

For a horizontal surface, the angle of incidence θ is obtained from (6):

$$cos\theta = cos\theta_z = sin\varphi sin\delta + cos\varphi cos\delta cos\omega \quad (6)$$

The declination angle δ which accounts for the seasonal changes of the sun's path through the sky throughout the months of the year is given in degrees by (7):

$$\delta = 23.45sin^{-1}\left[360\left(\frac{284+N}{365}\right)\right] \quad (7)$$

The hour angle ω can be determined from the expression given below in (8):.

$$\omega = 15(ST - 12) \quad (8)$$

ST is the solar time in hours and φ is the latitude of the location. Hottel defined the atmospheric transmittance as in (9):

$$\tau_b = a_o + a_1 e^{\left(-k/cos\,\theta_z\right)} \quad (9)$$

The constants a_o, a_1 and k can be determined using the correction factors shown below in (10) for all climates:

$$r_o = \frac{a_o}{\acute{a}_o}, \quad r_1 = \frac{a_1}{\acute{a}_1}, \quad and \quad r_k = \frac{k}{\acute{k}} \quad (10)$$

For tropical locations, r_o = 0.95, r_1 = 0.98 and r_k = 1.02. For altitudes less than 2.5km the constants $\acute{a}_o$, $\acute{a}_1$ and $\acute{k}$ are given by (11 – 13):

$$\acute{a}_o = 0.4237 - 0.0082(6 - A)^2 \quad (11)$$

$$\acute{a}_1 = 0.5055 + 0.0595(6.5 - A)^2 \quad (12)$$

$$\acute{k} = 0.2711 + 0.01858(2.5 - A)^2 \quad (13)$$

For an urban haze atmosphere, the constants are given by (14 – 16):

$$\acute{a}_o = 0.2538 - 0.0063(6 - A)^2 \quad (14)$$

$$\acute{a}_1 = 0.7678 + 0.01858(6.5 - A)^2 \quad (15)$$

$$\acute{k} = 0.249 + 0.081(2.5 - A)^2 \quad (16)$$

where A is the altitude of the location above sea level in kilometers. Thus, the transmittance of the standard atmosphere for beam radiation can be determined for any zenith angle and altitude below 2.5km.

II. MATERIALS AND METHODS

2.1 Generation of Data

Hourly, daily, weekly and monthly data were generated by experimental measurements at the Engineering Complex of the Federal University of Agriculture, Makurdi, Benue State of Nigeria. Measurements were carried out daily from 0800 – 1700 hours between July 2nd to November, 17th 2007 excluding Sundays and cloudy days. Hourly, daily, weekly and monthly data were also generated using Hottel's clear day model.

2.1.1 Experimental measurements of total/global radiation

Experimental measurements of the total radiation were obtained by the use of sun-meter during the 10 hours periods of experimentation (0800 -1700 hours) for insolation, bright cloud and cloudy parameters and converted using the prescribed equations. Hourly conversion from total radiation to direct normal radiation was calculated using equation (2).

2.1.2 Analytical method for beam radiation estimation using Hottel's model

Analytical data generation employed (9) with a_0, a_1 and k being determined using correction factor as described by (10 – 14). The declination angle, δ, which accounted for the seasonal changes of the sun's path through the sky throughout the months of the year, was used and it is given by (7). For the horizontal surface, the incidence angle, θ, was calculated by (6) and the hour angle, ω, was determined using (8); where ST is the solar time in hours and it is in reference to a particular location, in this case, Makurdi.

2.2 Analysis of Data

The data generated from the experimental and Hottel's model was statistically correlated, analyzed and compared using analysis of variance at different levels of significance; also with the mean bias difference (MBD) and the root square difference (RMSD) using the relationships (16 – 18):

$$MBD = \frac{\left(\sum\{I_p - I_m\}\right)}{\sum I_m} \tag{16}$$

$$RMSD = \frac{\sqrt{\left[\frac{\sum(I_p - I_m)^2}{N}\right]}}{\frac{(\sum I_m)}{N}} \tag{17}$$

$$\gamma = \frac{n\sum xy - \sum x \sum y}{\left\{\sqrt{[n\sum x^2 - (\sum x)^2]}.\sqrt{[n\sum y^2 - (\sum y)^2]}\right\}} \tag{18}$$

where N is the number of data, I_P and I_m are the predicted and measured hourly, weekly or monthly clear sky irradiance respectively; γ is the correlation coefficient for the relationship.

III. RESULTS

The mean weekly radiation predicted by Hottel's model, the total measured radiation and the beam radiation computed from the measured total radiation are shown in Table 1 representing the daily and monthly results for the period of the study. Tables 2 and 3 show the results of analysis of variation at 5 and 1% level of significance respectively.

Table 1: Average Weekly Hottel's Predicted Radiation and Measured Radiation for Makurdi Solar Location

Hottel's Direct Radiation (Weekly) (W/m²)	Makurdi Measured Weekly Normal Radiation (W/m²)	Makurdi Measured Weekly Total Radiation (W/m²)
544.45	78.88	307.32
547.45	168.32	397.84
551.7	105.84	341.14
556.81	122.33	323.25
562.03	35.39	246.01
566.81	23.56	244.68
570.51	57.43	342.63
572.41	23.89	232.35
572.01	20.97	259.53
569.17	Cloudy	Cloudy
563.64	104.19	322.8
555.6	112.83	341.17
545.19	183.92	382.48
533.42	161.42	362.35
521.57	341.6	432.03
507.89	462.4	475.59
495.08	194.47	372.19

Table 2: Analysis of Variance (ANOVA) of the Hottel's Model with Measured Values at 5% Significant Level

SUMMARY	*Count*	*Sum*	*Average*	*Variance*
Hottel's Direct Radiation	17	9335.74	549.1612	524.3668
Measured normal radiation	17	2197.44	129.2612	14661.56
Measured Total Radiation	17	5383.36	316.6682	11095.22

ANOVA

Source of Variation	*SS*	*df*	*MS*	*F*	*P-value*	*F crit*
Columns	1504446	2	752222.8	111.235	3.91E-15	3.294537
Error	216398.8	32	6762.464			
Total	1924944	50				

Ho: F ≤ F *crit* α = 0.05
Ha: F > F *crit*

Table 3: Analysis of Variance (ANOVA) of the Hottel's Model with Measured Values at 1% Significant Level

SUMMARY	*Count*	*Sum*	*Average*	*Variance*
Hottel's Direct Radiation	17	9335.74	549.1612	524.3668
Measured normal radiation	17	2197.44	129.2612	14661.56
Measured Total Radiation	17	5383.36	316.6682	11095.22

ANOVA

Source of Variation	*SS*	*df*	*MS*	*F*	*P-value*	*F crit*
Columns	1504446	2	752222.8	111.235	3.91E-15	5.336343
Error	216398.8	32	6762.464			
Total	1924944	50				

Ho: F ≤ F *crit* α= 0.01
Ha: F ≤ F *crit*

Table 4: Pearson Correlation Analysis of Hottel's Model with measured Data

		Hottel's Direct Radiation
Hottel's Direct Radiation	Pearson Correlation Coefficient	1
Measured normal radiation	Pearson Correlation Coefficient	-0.820170315
	R Standard Error	0.021821377
	t	-5.552172763
	Significance Level	5.54E-05
	Ho (5%)	rejected
Measured Total Radiation	Pearson Correlation Coefficient	-0.639715163
	R Standard Error	0.039384301
	t	-3.223480713
	Significance Level	0.005683868
	Ho (5%)	rejected

Source: Correlation Analysis using Biostat 2008 Professional

IV. DISCUSSION

The statistical tests carried out indicated that there was great variation between the radiation values predicted by Hottel's model and those computed from the measured values as indicated by the closeness of the MBD and RMSD values of 2.9029 and 3.1237 respectively. This variation could be due to climatic changes which are obviously not under control nor predictable. More significantly, the simplified Hottel's transmittance model, though generalized for tropical altitudes below 2.5km, may have considered some other factors that are not applicable to Makurdi location with an altitude of about 111m. Moreover, some natural occurrences which could not have been accounted for when the model was developed since 1976 are being reported daily all over the world. This includes reoccurring climate changes and actions of mitigations.

A closer look at Table 1 however, indicates some daily/weekly measured values which were higher than the values predicted by the model with glaring significant differences at 5% and 1% respectively. The significant difference at 1% is of 99% confidence level. The correlation coefficients are negative, quite distant from 'unity' of correlation. Though tangible conclusions cannot now be made based on these, they however indicate some magnitude of validity that remains to be verified. It should be noted however, that the general statistical trend in this case invalidates the model in Makurdi.

Obviously, a significant error margin may result from the use of models that are developed for and in a particular region when used in other regions. A possibility of reducing this error exists by obtaining some correction factors to apply to the results. The process of obtaining such factors is a subject for further study. The use of radiation models will definitely continue for quite a while due to the absence of basic equipment for direct measurement in many locations in the developing world where incidentally most of the solar radiation is obtainable and especially in Nigeria. There is therefore a need to develop a Makurdi-based model which may be in the mold of Hottel's simplified model taking into consideration the local factors required. As is the usual criteria for validity, this will take several years. It is however, a worthwhile considering the handicap of designers of solar systems requiring the use of beam radiation due to lack of basic equipment for measurement.

V. CONCLUSION AND RECOMMENDATION

Hottel's simplified transmittance model for topical altitudes below 2.5km may not be very suitable for use in Makurdi location with the knowledge that significant error margin exists. However, the accuracy will improve significantly if some correction factors are determined and applied to the predicted values of radiation.

A Makurdi-based model patterned after Hottel's model needs to however be developed that will incorporate the peculiar factors affecting beam radiation in the location. Further study is being conducted in order to obtain correction factors that could be applied to reduce the error margin and marginal variation associated with the use of Hottel's model in Makurdi.

REFERENCES

[1] F. Raeiszadeh & M. S. Behbahanizadeh, The Application of Empirical Models to Compute the Solar Radiation Energy in Shahrekord, *J. Basic. Appl. Sci. Res., 2(11),* 2012, 10832-10842.

[2] K. Bakirci, Correlations for Estimation of Solar Radiation on Horizontal Surfaces, *J. Energy Eng., 134(4),* 2008, 130–134.

[3] M. E. Vieira da Silva, A. Sandro de Araújo & M. R. Q. Medeiros, Adjustment of the Clear Sky Coefficients for the Transmission of Solar Radiation under the Ambient Conditions in Fortaleza, *World Climate & Energy Event, January 6-11,* 2002, RIO 02, 85 – 88.

[4] B. Y. H. Liu & R. C. Jordan, (1960). The Inter-relationship and Characteristic Distribution of direct, Diffuse and Total Solar Radiation, *Solar Energy,* 4(3), 1-19.

[5] J.L. Bosch, F.J. Batlles, L.F. Zarzalejo & G. López, Solar resources estimation combining digital terrain models and satellite images techniques, *Renewable Energy, 35,* 2010, 2853 – 2861.

[6] P.G. Loutzenhiser, H. Manz, C. Felsmann, P.A. Strachan, T. Frank, G.M. Maxwell, Empirical validation of models to compute solar irradiance on inclined surfaces for building energy simulation, *Solar Energy, 81,* 2007, 254–267.

[7] C. A. Gueymard, Direct solar transmittance and irradiance predictions with broadband models. Part I: detailed theoretical performance assessment, *Solar Energy, 74,* 2003, 355–379.

[8] T. Lealea & R. Tchinda, Estimation of Diffuse Solar Radiation in the South of Cameroon, *Journal of Energy Technologies and Policy, 3(6),* 2013, ISSN 2224-3232 (Paper) ISSN 2225-0573 (Online)

[9] M. J. Reno, C. W. Hansen, J. S. Stein, Global Horizontal Irradiance Clear Sky Models: Implementation and Analysis, Sandia Report, Sand2012-2389, Sandia National Laboratories, Albuquerque, New Mexico

[10] S. A.Al-Sanea, M. F. Zedan & S. A. Al-Ajlan, Adjustment factors for the ASHRAE clear-sky model based on solar-radiation measurements in Riyadh, *Applied Energy, 79(2),* 2004, 215–237.

[11] A. Louche, G. Simonnot, M. Iqbal & M. Mermier, (1982). Experimental Verification of some Clear Sky

Insolation Models, *Solar Energy*, 41, 273-279.
[12] J. K. Yohanna, I. N. Itodo & V. I. Umogbai, A model for determining the global solar radiation for Makurdi, Nigeria, *Renewable Energy*, *36*, 2011, 1989 – 1992.
[13] M. Grigiante, F. Mottes, D. Zardi, M. de Franceschi, Experimental solar radiation measurements and their effectiveness in setting up a real-sky irradiance model, *Renewable Energy*, *36*, 2011, 1 – 8.
[14] İ. T. Toğrul, Estimation of Solar Radiation from Angstroms Coefficients by using Geographical and Meteorological Data in Bishkek, Kyrgyzstan, *J. of Thermal Science and Technology*, *29(2)*, 2009, 99-108.
[15] M. M. Khan & M. J. Ahmad, Estimation of global solar radiation using clear sky radiation in Yemen, *Journal of Engineering Science and Technology Review*, *5(2)*, 2012, 12-19.
[16] A. Ianetz, V. Lyubansky, I. Setter, B. Kriheli, E. G. Evseev, & A. I. Kudish, Inter-comparison of different models for estimating clear sky solar global radiation for the Negev region of Israel, *Energy Conversion and Management*, *48(1)*, 2007, 259–268
[17] A. B. Aliyu & A. S. Sambo, (1991). Development of a Model for Total Component of Solar Radiation in Sokoto, *Nigerian Journal of Renewable Energy*, 2, pp. 10 -17.
[18] H. C. Hottel, A Simple Model for Estimating the Transmittance of Direct Solar Radiation Through Clear Atmospheres, *Solar Energy*, *18(2)*, 1976, 129 – 134.

American Journal of Engineering Research (AJER)
e-ISSN : 2320-0847 p-ISSN : 2320-0936
Volume-02, Issue-08, pp-58-64
www.ajer.org

Research Paper Open Access

Industrial electrochemical: a new teaching approach

Fernando B. Mainier, Luciane P. C. Monteiro, Antonio Carlos M. Rocha, Renata J. Mainier

Programa de Pós-Graduação em Engenharia Civil, Escola de Engenharia, Universidade Federal Fluminense, Niterói, RJ, Brazil.

Abstract: - The electrochemistry is a science with great range and applications in most industries. These applications include sensors, controllers, systems analysis, corrosion and anti-corrosion protection, surface technology, power generation, metal electrolytic production, materials and chemicals, recycling and wastewater treatment. The present work consists in an attempt to link and integrate two sciences, the industrial electrochemical and education, to develop a new technical and scientific approach that come admire the ideas generated and the experience gained in teaching and research of the electrochemical industrial processes. The aim of the creation of a discipline, the Industrial Electrochemical, vector learning based on historical formation of electrochemical principles, in breadth and in the application of various products of electrochemical industry and in laboratory experiments. In addition, the process of construction of knowledge in industrial electrochemistry converges in the formation of the critical technical conscience in electrochemistry, in the development of clean technologies and consequently on environmental preservation. Finally, it is concluded that the electrochemistry is the technique of the next millennium in both the production of metals, inorganic and organic products as in the treatment of industrial effluents.

Keywords: - *Industrial electrochemical, education, laboratory, environment.*

I. HISTORY

If it was possible to return to the past, in the late 18th century and early 19th century, to interview the precursors of electrochemistry, and, if possible, shoot their experiments and its laboratories, would probably be clarified and in situ evaluation of how the knowledge of this technique has spread.

Historical surveys and the biographies of the men of science of that era reveal that was a very fertile period, mainly in Europe, to the development of sciences and techniques. Names of scientists as Ampere, Biot, Fresnel, Oersted, Laplace, Lavosier, among others, attest and strengthen that were intense research, covering mathematics, optics (light), electricity, magnetism and the fundamentals of chemistry [1].

At the end of the 18th century, in 1786, Luigi Galvani conducted a series of experiments and observations on the seizures occurred in legs dissected frogs, suspended by a brass hook on an iron plate and subjected to a discharge of an electrostatic machine. At the time, concluded that the observed phenomenon was sourced from a new form of electricity, called "animal electricity" [2, 3].

In 1793, Alessandro Volta, Professor of Natural Philosophy at Pavia, Italy, disputes this theory and shows that this no longer happens when two metal hooks, brass and iron, was removed from the frog's leg. Although, still, I believed that muscles and nerves of the frog worked as a high sensitivity electroscope can detect a weak electric current.

In 1800, Volta proposals a electrochemical cell consists series of discs of zinc and silver separated by moist cardboard and arranged alternately to form a pile as shown in Figure 1

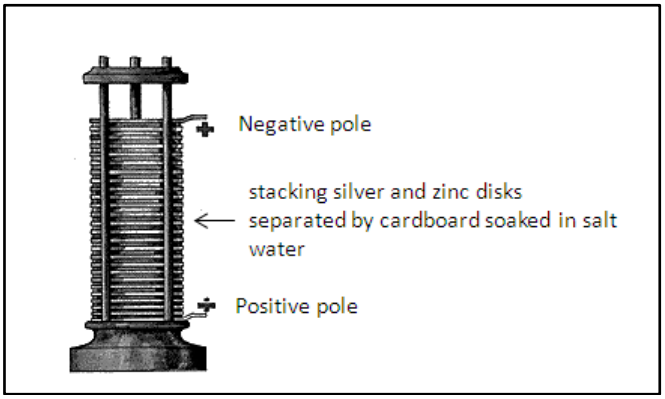

Figure 1-Cell batteries design developed by Alessandro Volta in 1800.

This historical fact has caused a great scientific twist at the time, marking the beginning of the knowledge of the "batteries", which, today, are already part of everyday life of man, is on the flashlight, portable radio, wristwatch or pacemaker, next to his heart.

A very interesting statement, dated December 1899, is the scientist Augusto Righi, who, speaking about the battery back, at the opening of the first National Congress of Italy's Electricity, said: this fact did not happen by chance, was the result of a long series of researches, insight, ingenious and intelligent experiments, inspired and based on successive logical deductions. Thanks to the pile (battery), the electricity had access, almost exclusively due to the object of this research, becoming a powerful energy source, fruitful and universal. Through this knowledge science offers a multiform energy, able to or intended to produce profound changes in human civilization, and may be compared to the power that the man obtained from fire in prehistoric eras [4].

All the evidence surveyed in the ancient literature come only confirm the importance of the discovery made by Alessandro Volta, because, without your direct participation, as experimenter, the company probably would not have enjoyed the scientific and technological development that has occurred and is still occurring in the modern world. If this does not happen, maybe the industrial development of Electrochemistry to take another direction or be waiting for 10 years! 20 years! or 100 years!

Quickly, this knowledge soon spread in the current science, because two months later, in May 1800, Nicholson and Carlisle were already the decomposition of water into oxygen and hydrogen, by means of electric current, using ideas based on the Volta. Even during the 19Th centuries, it is worth mentioning the important contributions that happened with the research and development of electrochemical techniques carried out by Humphry Davy [5, 6] and Michael Faraday [7, 8, 9].

The laboratory work performed by Humphry Davy, through the use of several batteries, allowed the discovery and elements such as sodium, potassium, magnesium, barium, strontium, calcium and chlorine. A critical appraisal of original publications of Davy shows, primarily through the diagrams and drawings of laboratory equipment, a certain amount of creativity, ingenuity and scientific criteria in the preparation of experiments, which in no way should the experiments of our century.

In 1813, Michael Faraday to 22 years went to work as an Assistant in the laboratory of the Royal Society and, from 1825, was Director of the Royal Society, replacing Hamphry Davy, President. His contribution to electrochemistry was instrumental, because quantitatively defined the relationship between the mass of an element and the electric charge, passed through an electrolyte, through two fundamental laws, known as Faraday's Laws. In the field of magnetism, made two important discoveries; one was to determine the existence of diamagnetism and the other, the identification of the influence of magnetism on the optical rotation of the polarized light, plans on the basis of certain types of glasses.

In 1832, Faraday published that, through laboratory experiments, had managed to convert the magnetism into electricity. The experiment was to pass a current through a coil of wire, that generating a magnetic field, which was very recollected an electric current in the second coil.

Shortly thereafter, in 1834, Faraday published quantitative studies concerning the relationship between the amount of electricity that passes in a conductive solution and the amount of substance transformed into each of the drivers used. Their experiences were to pass an electric current by the given time in an electrolytic tank. Observed in this experiment that there was production of certain amount of substance, proportional to the amount of electricity. From these observations, began developing concepts for the establishment of the fundamental laws governing the electrochemistry.

It is important to note that the laws developed by Faraday on the electrochemistry preceded the discovery of electrons (1897), and therefore, the atomistic theory of Bohr. However, he, as a scientist, "felt" that

there was a stream, still unknown at that time (the electrons), that turning the anode to the cathode, producing the reactions in electrolytic cell.

Another fact that deserves mention is the familiar lead-acid accumulators, used in motor vehicles invented by Planté, 1859. This energy accumulator consisted of two plates of lead, as electrodes, immersed in sulphuric acid solution to 28% by weight and density equal to 1.2. The great advantage of these cells is the reversibility, meaning they could be regenerated by passing an electric current [3, 10].

According to Rieger [11] only in 1868 was created to Georges Leclanché the first dry cell, similar to current batteries, called at the period, Leclanché cell. It was composed of a zinc electrode and electrode graphite, enveloped by manganese dioxide (MnO_2) and placed in a porous medium, along with a 20% solution of ammonium chloride (NH_4Cl). Zinc is the negative pole and the graphite is positive pole providing thus a potential difference of 1.3 to 1.5 volts [3, 11]. The cell Leclanché scheme is presented in Figure 2.

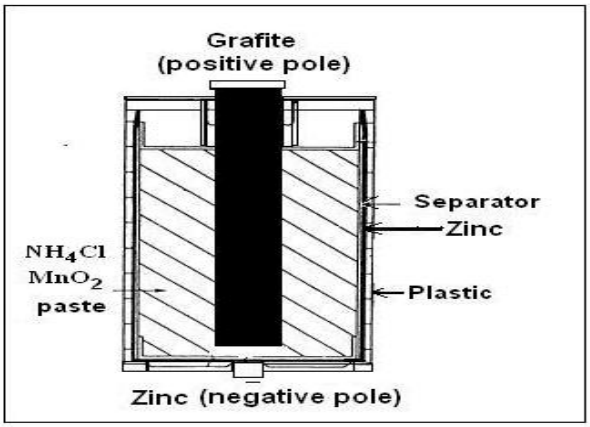

Figure 2 - The cell Leclanché scheme

The current theory about the electrode potential equating any previous knowledge of relations of electrochemistry was formulated by Nernst in 1889, to assume that every element is capable of forming an active electrode, partially dissolving when it is introduced in an electrolytic solution or pure water [12, 13, 14]. This means that in the solution, the free energy of the metal, metallic state is higher than the free energy of the metal in the ionic state. In this case, there is a tendency to pass thermodynamics of metal ions to the solution. This transfer of ions causes the metal plate to acquire negative charge due to the presence of electrons in it, and the solution get positive charge, due to new ions present in the solution [12, 13, 14].

This double layer on metal-solution interface, produces an electric field perpendicular to the interface, making the passage of more positive ions to the solution, causing the electrical current is reduced to zero, thus reaching the equilibrium State. This potential difference is called electrode potential. The value of this potential depends on the material that constitutes the electrode and electrolyte conditions (concentration, temperature, pressure).

Over the years, developed by electrochemistry Alessandro Volta, since 1800, has been solidified in more accurate theories and is currently classified as a segment of the physical chemistry and thus increasingly penetrates in other sciences that make interfaces with chemistry, finding applications in biochemistry, medicine and engineering, as show the technological segments presented below.

II. TECHNOLOGICAL SEGMENTS

The great progress of electrochemistry, directed to technology and called Industrial Electrochemistry, has provided a series of developments, reaching various segments and industrial applications, such as batteries, fuel cells, metal coatings, electrolytic refining of new metals, electrochemical synthesis of organic products, sensors, monitoring, controllers, analysers, anti-corrosion protection techniques, power generation, effluent treatment and recycling, etc [15, 16].

Electrochemistry, as science creates knowledge and applied technology develops and produces a product which, for the most part, brings benefits to society, but, on the other hand, these means of production and the final product thrown end up creating environmental impacts. But also, as a science, has the power to create knowledge in the area of cleaning up, through the development of efficient processes of contaminant removal in industrial effluents.

In this way, these applications can be classified into direct and indirect. The direct application assumes a process that uses, specifically, the electrochemical principles, whether spontaneous or non-spontaneous. The

indirect applications refer to processes that occur without a specific enforcement of the electrochemical potential, although there are grey areas difficult to be classified.

Currently, the Industrial Electrochemical no more restricted to aluminium, electrolytic copper or zinc, or the manufacture of chlorine and caustic soda and not to the production of hydrogen and oxygen by electrolysis of water; It has been designed in line with the clean technologies acting in the synthesis of new organic products, recycling and treatment of industrial effluents [15, 16, 17].

The processes and products generated through electrochemical technology represent, today, in the United States, a large share of the American market, with about 35 billion dollars.

III. ELECTROCHEMICAL INDUSTRIAL DISCIPLINE IN ENGINEERING COURSES: A CRITICAL VIEW

On the basis of the early 19th century to the present day, it turns out that a striking prints Electrochemistry in the various sectors of society, whether through the dissemination of batteries simple and rechargeable batteries sophisticated, is in obtaining metals, such as aluminium, or, in modern industrial dumps treatments aimed at the preservation of the environment. The technology demonstrates the great power of diffusion that this technology has left, through its brands and roots in various parts of the world and even in space conquest.

However, as knowledge diffusion, discipline is still tentatively presented or is jettisoned and virtually ignored in the teaching-learning process engineering education course.

To give you an insight into the importance and the relationship of electrochemistry in the context of knowledge, based on the daily life, seeking, without need of insights and interviews, the behaviour and the comments of a character of society, with social status set against electrochemistry, which, directly or indirectly, is part of your day-by-day on the way home-work-home.

Upon waking, hear the shrill sound of the alarm clock or radio music, noting that both are powered by batteries, but in his innocence is not able to assume that disposable battery, also called the "dry cell", was developed by Georges Leclanché, in 1880. In addition, does not have the dimension of that, currently, the production of disposable batteries in the world is about 13 billion per year.

At breakfast, the aluminized paper, involving the cream cracker or chocolate cake and the window with aluminium frames reflect, in this century, the presence of Electrochemistry in the great production of this metal. However, this only occurred due to the industrial electrochemical process, which transformed the cost of 1,500 dollars per kilogram aluminium in 1846 to a dollar in 2013.

To start the car, the common man never would remember of physicist Gaston Planté, man of science that developed in 1859, and lead-acid batteries in automobiles. The greatness of this invention can only be evaluated by determining the number of vehicles circulating on this planet in 100 years.

In the office, around the common man he sees the chrome coating of the chair, the cadmium coating of the door lock and the cell phone lithium battery, however, completely unaware that the computer in front of you has numerous electrochemical coated parts by metals and alloys, which provide state-of-the-art properties. The corrosive process that takes place in the city is also related to electrochemistry, electrochemical corrosion.

To get home, this citizen equal to others in society, while reflecting and questioning those times, is very clear your ignorance of the electrochemical action in number of inventions that has provided the welfare in your life. Leading him to think that without the diffusion of knowledge of electrochemistry in society, it is difficult to the understanding of these actions.

On the other hand, the birth of the critical conscience begins to take shape on the need to evaluate critically how the electrochemical technology, to be questioned about the advantages and disadvantages that this technique brings to man and the environment.

In raids made in University, technological centres, fundamentally it was noted that the scenario described for the common man is not very different from that found in the students and some teachers, especially in questions directed to technology and the environment.

There was widespread ignorance from the most important historical facts to manufacturing processes and products from these processes. Based on the assumptions of the reason of scientific and technological knowledge, it is unacceptable that is allowed to technologists and technology manager's lack of techniques and waste that such processes may cause environmental system. One of the examples of contamination can be quoted cadmium contamination both jackets as the nickel-cadmium [18].

In the same way that the Industrial Electrochemical can be used to decontaminate certain environmental contamination, she, like technology, has spawned and continues generating waste or products which, indirectly, cause environmental problems, as is the case of mercury cells for production of chlorine-soda, aluminium production, the production of electrolytic zinc and cadmium, among others. On the other hand, the power of industrial society moves precipitously and imposes its guidelines on commercial and industrial

transactions, forcing the development of processes that are often contrary to the well-being of society [18].

Today's technicians or engineers can no longer be adrift of the current technological revolution; it is increasingly important that this professional is formed in the critical view of industrial processes and have creativity, ability to work in group, multidisciplinary and a critical positioning of industrial processes that cause impacts on the environment.

It is difficult to make predictions, however, it is essential to the establishment of the responsibility of the future, mainly about the issue of contaminants and waste generation, although such liability is intrinsically linked to the permanent surveillance of environmental agencies, non-governmental organizations, to environmental and public health impact, making mandatory the knowledge of routes and the establishment of industrial standards and critical parameters.

IV. PROPOSED IMPLEMENTATION OF INDUSTRIAL ELECTROCHEMICAL DISCIPLINE COURSES IN CHEMICAL ENGINEERING AND INDUSTRIAL CHEMISTRY

Based on the requirements above is made, the following is a proposal for implementation of the teaching of Industrial courses Industrial Electrochemical discipline of Chemical Engineering and Industrial Chemistry consisting of the following parts:

IV.1 - OBJECTIVES

The discipline must achieve the following objectives:

- to demonstrate the importance of knowledge of electrochemistry since the 18th century;
- identify, interpret, and analyse the principles, laws and the mechanisms involved in the industrial electrochemical processes;
- critically evaluate the advantages and disadvantages of electrochemical processes and their products;
- analyse environmental problems, on the basis of electrochemical processes;
- expand the ability of the student to observe, reflect, analyse and develop the sense of searching and questioning, based on electrochemical experiments.

IV.2 – CONTENTS

The history of electrochemistry. Review the concepts of: oxidation-reduction reactions, electrode potential, electrochemical cells, electrolysis. Electrolytic and electrochemical corrosion. Cathodic protection. Electrochemical and electrolytic coatings. Anodizing. Electro analyses. Electrochemical synthesis: metals, inorganic and organic compounds. Electrolytic processes in industrial effluents.

IV.3 – PROGRAMME

Unit	Description
I	A vision of Electrochemistry in the timeline; technological areas of electrochemistry.
II	Review the concepts of: oxidation-reduction reactions; oxidation States; oxidation-reduction reactions balance; Ionic equations of reduction and oxidation; electrode potential; table of potential; spontaneous and non-spontaneous processes; electrochemical cells; battery types (different metal electrodes, concentration, temperature); Nernst equation; Leclanché cell; lead-sulphuric acid, nickel-cadmium and nickel-iron; fuel cells; solar cells; electrolysis; Faraday's laws.
III	Corrosion and anti-corrosion protection; electrochemical corrosion: mechanisms and types; Galvanic corrosion, dezincification, graphitic corrosion; electrolytic corrosion: mechanisms.
IV	Fundamentals of cathodic protection: criteria, galvanic anode, inert anode.
V	Electroplating; electrochemical coatings; electrodeposition of metals and alloys; metal deposition without the aid of electric current; anodizing; application of paint for electrophoresis; evaluation of zinc-based paint.
VI	Electrolytic processes of production of metals: alkali and alkaline earth metals, copper, zinc, cadmium, aluminium, silver and gold; electrolytic refining.
VII	Electrolytic processes of production of chemicals: sodium hydroxide, chlorine, hydrogen, oxygen, fluorine, hydrogen peroxide.
VIII	Electro analysis, pH meters, oxidation-reduction, selective electrodes conductivity for ions; polarography; biosensors.
IX	A vision of contaminants into the environment; clean technologies and electrolytic processes; electrolytic processes of industrial waste treatment: chromate, sulphide, cyanide; recovery of hydrogen and chlorine from residual hydrochloric acid; chlorine generators for treatment of seawater; Elimination of heavy metals (Cu, Ni, Cd, Pb).

IV.4 – PROPOSED EXPERIMENTS

Unit	Description
Fundamentals of electrochemical	Electrical conductivity of various liquids; electrochemical tensions qualitative determinations, galvanic cell; concentration cell; Leclanché cell; determination of the Faraday constant.
Electro synthesis of inorganic products	Obtaining sodium hydroxide, chlorine and hydrogen with mercury cell and diaphragm cell.
Electro synthesis of metals	Production of copper, from the acidic leaching of oxidized copper ore concentrates; electrolytic refining of copper from copper grosses (scrap); zinc production from zinc ore.
Battery	Sulphuric acid-lead battery.
Electrochemical monitoring	Determination of copper in brass; determination of resistivity of soils.
Treatment of metals and alloys	Anodizing; electroplating; metal deposition without the aid of electric current.
Corrosion and corrosion protection	Electrochemical corrosion; construction of cell $Cu/CuSO_4$ and potential measures; cathodic protection with galvanic anodes in seawater.
Treatment of industrial effluents	Removal of Cu^{2+}, Ni^{2+}, Pb^{2+}, chromate (CrO_4^{2-}) in industrial effluents.

As an example, then, a laboratory experiment is presented to demonstrate the concepts of carbon steel corrosion in seawater.

- **Description of Experiment: Corrosion of a steel plate without uncoated carbon steel compared to a steel sheet with two coats of epoxy paint risk penetrating.**

Two carbon steel plates (20 cm × 10 cm), one coated with two coats of epoxy paint with a total thickness of 250 µm, are fixed in the holder and immersed in a transparent acrylic container with a capacity of 50 L holding a solution containing 3.5% (by weight) sodium chloride, representing seawater, as shown in Figure 3. The plates should be immersed for 15 days to evaluate the performance of the corrosion process.

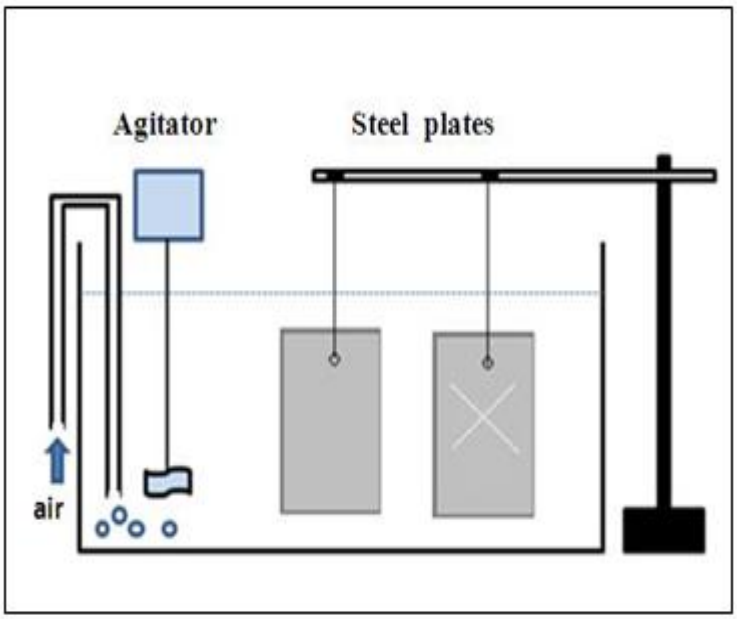

Figure 3 - Assay steel plates immersed in seawater

Figure 4 A illustrates the progress of the corrosion process in the laboratory experiment on steel plates with and without epoxy coating. The progress of the corrosion process is evidenced in steel plates photographed after three days of immersion in salt water, as shown in Figure 4 B. Note that the steel sheet is coated with epoxy which lines the corrosion area.

Figure 4– Development of the corrosion process (three days).

V. CONCLUSIONS

The experiments, the questions and the associated research made by students of the course of Chemical Engineering and Industrial Chemistry aim to:

- facilitate and broaden the understanding of electrochemistry and environment in the timeline;
- awaken in the student the need of development and clarification of physic-chemical mechanisms involved in each process;
- guide students towards research and questioning, giving them basic experience in the kind of physical and chemical measurements, leading to qualitative and quantitative results to relations with the environment;
- stimulate the relentless pursuit of technological innovation, through special projects, and if necessary to break through the direction of traditional experiments; form the critical technical and environmental consciousness.

REFERENCES

[1] J. L. Heilbron, Electricity in the 17th and 18th centuries, Berkeley, Los Angeles: University of California Press, 1979.
[2] R. M. Roberts, Descobertas acidentais em ciências, Campinas, SP: Papirus, 1995.
[3] I. McNeil, An encyclopaedia of the history of technology, Taylor & Francis e-Library, 2002.
[4] CCS – Centro di Cultura Scientifica "Alessandro Volta", Villa Olmo, Itália, 1997.
[5] J. Z. Fullmer, Young Humphry Davy: The Making of an Experimental Chemist, Volume 237, Philadelphia: American Philosophical Society, 2000.
[6] D. Knight, Humphry Davy: science and power, Cambridge: University of Cambridge, 1996.
[7] M. Faraday, Experimental researches in electricity, 1839, www.books,google.com.
[8] R. D. Tweney, Toward a Cognitive-Historical Understanding of Michael Faraday's Research: Editor's Introduction, Perspectives on Science, Spring 2006, Vol. 14, No. 1, p. 1-6, 2006.
[9] M. Shortland and R. Yeo, Telling Lives in Science Essays on Scientific Biography, Cambridge: University of Cambridge, 1996
[10] H. A. Kiehne, Battery Technology Handbook, New York: Marcel Decker, 2003
[11] P. H. Rieger, Electrochemistry, New York: Chapman & Hall, 1994.
[12] A. J. Bard and L. R. Faulkner, Electrochemical methods: fundamentals and applications, New York: John Wiley & Sons, 2001.
[13] J. O'M. Bockris and A. K. N. Reddy, New York: Kluwer Academic Publishers, 2002.
[14] R. G. Kelly, J. R. Scully, D. W. Shoesmith and R. G. Buchheit, Electrochemical Techniques in Corrosion Science and Engineering, New York: Marcel Dekker, Inc, 2003.
[15] K. Scott, Electrochemical Processes for Clean Technology, Cambridge: Royal Society of Chemistry, '1995.
[16] F. B. Mainier, R. J. Mainier and V. L. S. Cardoso, Clean technology and industrial safe: a right of society, International Journal of Multidisciplinary Science and Engineering, vol. 4, no. 5, June, 2013.
[17] F. B. Mainier, G. C. Sandres and R, J. Mainier, Integrated Management System for in-House Control of Accidental Hydrogen Sulfide Leaks in Oil Refineries, International Journal of Science and Advanced Technology, volume 2, issue 9, September, p. 76-84, 2012.
[18] F. B. Mainier, L. P. C. Monteiro, L. H. Fernandes and M. A. M. Oliveira, Restrictions on the Use Cadmium Coating in Industries, Journal of Science and Technology, vol. 3, No. 2, February, p. 176-180, 2013.

American Journal of Engineering Research (AJER)
e-ISSN : 2320-0847 p-ISSN : 2320-0936
Volume-02, Issue-08, pp-65-75
www.ajer.org

Research Paper Open Access

Sustainable Power Generation by Plasma Physics

Anyaegbunam F. N. C. (Ph.D.)
Department of Physics/Geology/Geophysics, Federal University Ndufu Alike Ikwo. Abakaliki Nigeria.

Abstract: - One of the greatest challenges of developing countries today is electric power generation. The demand for Electric power is far above generation and distribution capacities. For instance, only about 4000MW of electricity is available for nearly 170 million people in Nigeria today. On the other hand, the cities are littered with municipal solid wastes in open dumps which are dangerous to health and environment. Sustainable and successful waste management should be safe, effective, environmentally friendly and economically viable. Application of plasma Physics in waste to energy can be one of the novel ways of sustainable power generation. In plasma gasifying cupola, the organic waste materials are gasified to generate a syngas and steam which can be used to generate electricity by integrated gasification combine circle. The inorganic part of the waste is vitrified to a benign residue used for construction. This paper describes the physics and technology involved, reviews the power situation in Nigeria and the benefits of implementation of this technology in waste to electric power generation. This might be an environmentally Safe and sustainable economic solution for waste management and alternative clean power generation.

Keywords: - *Plasma physics, gasification, waste to energy, syngas, power generation.*

I. INTRODUCTION

Plasma physics and associated technologies could address power shortages in fast growing economies, especially in developing countries such as Nigeria. Nigeria, situated on the West Coast of Africa, occupies 92 million hectares of land or 923,773 square kilometers (about 76% is arable) and is home to an estimated population of 167 million people. With a GDP of US$196 billion in 2010, US$230 billion in 2011 and an average annual growth rate of 7%, [1] the Nigerian economy is at present one of the strongest economies in Sub Saharan Africa and this is expected to be sustained in the years to come yet possessing a huge potential to grow. Nigeria is a Federal Republic and gained independence on 1st October, 1960. It comprises of 36 States and the Federal Capital Territory, Abuja. There are 3 tiers of Government, namely Federal, State and Local Government. They are administered by the President, Governors and Local Government Chairmen respectively. The Federal Capital Territory is administered by a Minister appointed by the President. There are also 3 arms of Governance, namely Executive, Legislature and Judiciary. The Legislature is bi-cameral made up of the Senate and the House of Representatives. Growth has been broad based across all the major sectors of the economy, namely oil & gas, agriculture, commercial activities, construction, financial services, hotel & tourism and real estate.

1.1 Power Demand in Nigeria

As at 2004, Total installed generation capacity was 6,102MW, but only a maximum of 3,300MW has been produced at any given time in the history of the sector. Between 1999 and 2003, actual generation increased by about 200% from 1,080 to 3,300 mw. While installed capacity was raised to about 5,902MW from 2,257MW in the same period. According to the CBN Annual Report for the year ended 31 December 2005, the quantum of electricity generated declined in 2005. At 2,687.1 megawatt hour (MWH), aggregate electricity generation fell by 2.8%, in contrast to the increase of 15.2% in 2004. The installed electricity capacity of the PHCN stood at 5,800MW, while that of the Independent Power Plants (IPPs) was 300MW. Thus, PHCN accounted for 99.5% of total electricity generated, while the IPPs accounted for the remaining 0.5%. While it is difficult to properly estimate the current level of electricity demand, various authoritative sources have pegged demand for electricity at 6,000MW per annum. This implies that Nigeria is only generating about 45% of

current local demand. However, this figure could be more as demand in Nigeria can be categorized into two – those who are connected to the grid and those who do not have access to electricity. In addition, those connected to the grid can also be segmented into two – legal consumers (that is, accounted for by the PHCN) and the illegal customers (unlawful connection to the national grid). Industry sources stipulate that demand for electricity in Nigeria is growing at an estimated 7% yearly and according to PHCN, this peaks energy demand at 8000MW, 2000MW higher than the estimate of 6000MW. However, the Ministry of Power and Steel has estimated that the current estimated demand for electricity in urban areas alone is 10,000MW. Since, demand for power exceeds supply; PHCN usually embarks on load shedding in periods of extremely low supply. In the last quarter of 2006, due to significant number of problems experienced, total generation capacity which was in the region of 3000 to 3200 MW dropped significantly by 60% to less than 1500 MW. As a result, the country has been experiencing the worst black out and most erratic power supply since 1999.

1.2 Plasma Physics

Plasma is the fourth state of matter. About 99% of the matter in the universe is in the plasma state. Plasmas exist in astronomical bodies with temperatures in millions of degrees. Plasma is a gas in which an important fraction of the atoms is *ionized*, so that the electrons and ions are separately free. This occurs when the temperature is hot enough to overcome ionization threshold energy, about 13.6eV.

Balance between collisional ionization and recombination:

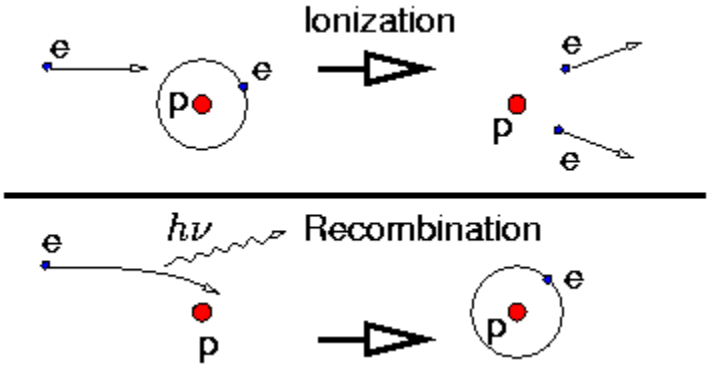

Figure 1. Ionization and Recombination

Recombination is much less probable.

Plasmas are said to be quasi neutral as Electrostatic force >> Kinetic Pressure Force.
This is one aspect of the fact that, because of being ionized, plasmas exhibit all sorts of collective behavior, different from neutral gases, mediated by the long distance electromagnetic forces E, B. In plasma, the Debye length,

$$\lambda_D \equiv \left(\frac{\epsilon_0 T_e}{e^2 n_\infty} \right)^{1/2}$$

<< Size of the plasma

Where the electron temperature is T_e as the particle density, n_∞ is very large in the plasma sheath.
Usually we include as part of the *definition* of a plasma that λ_D << the size of plasma. This ensures that collective effects, quasi-neutrality etc. are important. If N_D = Number of particles in the `Debye Sphere, then for plasmas, $N_D >> 1$ (Collective effects dominate over collisions)
Thus, Plasma is an *ionized* gas in which collective effects dominate over collisions.

$$[\ \lambda_D << \text{size of plasma} \ , \quad N_D >> 1\ ]$$

We have established two conditions under which an ionized gas can be plasma. A third condition has to do with oscillations [2]. If ω is the frequency of oscillation and τ is the mean period between oscillations, then $\omega\tau > 1$ for the gas to behave like plasma rather than a natural gas. Therefore, three conditions an ionized gas must satisfy to be called plasma are: λ_D << size of plasma, $N_D >> 1$, and $\omega\tau > 1$. The word plasma comes from Greek word: πλάσμα, -ατος , τό which implies fabricated or molded substance.

Apart from naturally occurring plasmas in the universe, artificial Plasma may be created in the laboratory by a variety of ways, including passing a gas, which serves as a dielectric, between objects with large electrical potential differences, or by exposing gases to high temperatures, as in the case of arc welding or graphite electrode torches. The potential difference and subsequent electric field causes ionization of the gas and electrons are pulled toward the anode while the nucleus pulled towards cathode. The current stresses the gas by electric polarization beyond its dielectric strength into a stage of electrical breakdown. The presence of this ionized gas allows the formation of an electric arc between the two electrodes, and the arc serves as a resistive heating element with the electric current creating heat which creates additional plasma that allows the arc to be sustained. A major advantage of the plasma arc as a resistive heating element is that it is formed in a gas and cannot melt or fail as can solid heating elements. Interaction between the arc and process gas introduced into the torch causes the temperature of the gas to be very high and the hot gas can exit the plasma torch at about 10,000°C. The ability to increase the temperature of the process gas to temperatures up to ten times higher than those attainable by conventional combustion makes plasma arc technology ideally suited for high temperature process applications such as gasification. The presence of a non-negligible number of charge carriers makes the plasma electrically conductive so that it responds strongly to electromagnetic fields[3].

1.3 Plasma Physics Applied to Gasification

Plasma technology was developed and employed in the metal industry during the late 1800s to provide extremely high heat. Plasma Arc heaters received renewed attention when the United States NASA Space program, during the early 1960s, evaluated and selected Plasma Arc Heating technology for simulating and recreating the extreme high heat of reentry into the earth's dense atmosphere encountered by spacecraft from orbit. Utilizing the same plasma physics, scientists who previously worked for NASA, have refined and improved the plasma arc technology in efficiency, cost, and wider user applications; the lead NASA scientist, Dr. S.L. Camacho used this technology to convert waste to energy [4]. The gaseous emission to the atmosphere were limited and very much under control. Waste materials are processed without any fly ashes that would require to be sent to a landfill. The environmental regulations are becoming more stringent and landfills are becoming outmoded. The harmful attributes of landfills to environment were predicted [5]. They suggested that Sustainable and successful waste management should be safe, effective, and environmentally friendly.

Plasma technology adaptation to large-scale solid waste disposal via gasification and recovery of energy from the generated gas is relatively new. As noted by [6], "Plasma gasification of municipal solid waste (MSW) is a fairly new application that combines well-established sub-systems into one new system. The sub-systems are waste processing and sorting, plasma treatment, gas cleaning, and energy production.

1.4 Plasma Gasification Technology

As mentioned above, artificial Plasma may be created by passing a gas between objects with large differences in electrical potential, as in the case of lightning, or by exposing gases to high temperatures, as in the case of arc welding or graphite electrode torches. Plasma arc torches utilize a combination of these techniques [7]. The extremely intense energy produced by the torch is powerful enough to disintegrate the MSW into its component elements. The subsequent reaction produces syngas and byproducts consisting of glass-like substances used as raw materials for construction, and also re-useable metals. Syngas is a mixture of hydrogen and carbon monoxide and it can be converted into fuels such as hydrogen, natural gas or ethanol. The Syngas so generated is fed into a heat recovery steam generator (HRSG) which generates steam. This steam is used to drive steam turbine which in turn produces electricity. The cooled gas is also used to drive a second turbine to generate additional electricity – The integrated gasification combine circle (IGCC) thus produce adequate electricity, part of which is used for the plant's load and the rest of the power generated is sold to the utility grid. Essentially the inorganic materials such as silica, soil, concrete, glass, gravel, including metals in the waste are vitrified and flow out the bottom of the reactor. There are no tars, furans or ashes enough to pollute the environment.

The principal advantages of gasification as opposed to direct combustion (incineration) for the recovery of energy from wastes such as Municipal Solid Waste (MSW) include:

- Production of a gaseous product that can be combusted more efficiently than a solid fuel, resulting in decreased requirement for excess air while reducing the potential for formation of products of incomplete combustion (PICs). This results in a reduction in the volume of emissions and lower total emissions when treated to the same concentration standards.
- Ability to clean the product gas prior to combustion, resulting in further reductions in emissions.
- Ability to utilize the Integrated Gasification Combined Cycle (IGCC) process for generation of electricity which results in much higher thermal efficiencies (40-45% energy recovery as electricity as opposed to 20-25 percent for mass burn facilities).

- The product gas can be transmitted by pipeline for use at locations at significant distances from the gasification facility.

Plasma gasification represents a clean and efficient option to convert various feed stocks into energy in an environmentally responsible manner [7]. Below are the environmental benefits of this process for power generation:

Gasification occurs in an oxygen starved environment, so feed stocks are gasified, not incinerated. Due to the high operating temperatures in the plasma gasification process:

- It produces no bottom ash or fly ash that requires treatment or landfill disposal.
- Metals not recovered from the waste stream prior to processing and most metallic compounds are reduced to their elemental state and recovered in a form that permits recycling.
- Non-combustible inorganic materials such as glass, concrete, and soil are melted and vitrified, producing an environmentally stable glass-like residue that can be sold for use as construction aggregate.
- The high heat output from the plasma torches in combination with the heat reservoir provided by the coke bed at the bottom of the vessel permits the plasma gasifier to accommodate wide variations in feedstock composition and characteristics.
- The absence of moving parts in the gasifier in combination with the high temperature and flexibility of the plasma heating system makes it possible to process materials such as carpet and tires that are difficult to process in conventional incinerators or other gasification processes.
- The gasifier operates under a slight negative pressure, minimizing the potential for escape of the product gas.
- Continuous discharge of the molten residue through the coke bed at the bottom of the vessel eliminates the need to maintain a molten pool of residue in the vessel and associated problems with freezing of taps required for discharge of the residue.
- Each plasma gasification application will have a differing environmental profile, but in general terms a plasma gasification facility will have very low emissions of NOx, SOx, dioxins and furans.

II. WASTES TO POWER GENERATION MATERIALS AND METHODS

Plasma physics applied to gasification represents a clean and efficient option to manage waste in an environmentally responsible manner. The plasma gasification technology is ideally suited to process wastes such as Municipal Solid Waste ("MSW"), common hazardous waste, industrial waste, chemical waste, sediment sludge and biomass. It can also vitrify fly ash from incinerators and any other types of ash. Converting waste into various energy outputs reduces reliance on the use of conventional fossil based fuels by using readily available waste.

In Nigeria like most developing countries, wastes are commonly dumped in open dumps uncontrolled landfills where a waste collection service is organized. Open dumping of waste is not a long-term environmental method of disposal. The dangers of open dumping are numerous; health hazard, pollution of ground water, spread of infectious diseases, highly toxic smoke from continuously smoldering fires, foul odors from decomposing refuse and emission of greenhouse methane gas. Several million tons of wastes have been deposited in open dumpsites across the country over the years. A new technology such as Plasma Physics applied to Gasification of MSW may prove to be an environmentally friendly and sustainable solution for wastes disposal and power generation.

2.1 Gasification Process

The gasification reaction for MSW is generally written as follows [5]:

$$CH_xO_y + wH_2O + mO_2 + 3.76mN_2 \rightarrow aH_2 + bCO + cCO_2 + dH_2O + eCH_4 + fN_2 + gC$$

Where waste material is described by its global analysis, CHxOy), w is the amount of water per mole of waste material, m is the amount of O_2 per mole of waste, a, b, c, d, e, f and g are the coefficients of the gaseous products and soot (all stoichiometric coefficients in moles). This overall equation has also been used for the calculation of chemical equilibrium occurring in the thermal plasma gasification with input electrical energy. The concentrations of each gas have been decided depending on the amount of injected O_2, H_2O, and input thermal plasma enthalpy.

The H_2 and CO generated during the gasification process can be a fuel source for power generation.

2.2 Plasma Gasification of Municipal Solid Waste (MSW)

Plasma gasification is an efficient and environmentally responsible form of thermal treatment [8] of wastes which occurs in oxygen starved environment so that waste is gasified, not incinerated. Westinghouse Plasma Corporation (WPC) has developed a plasma gasification system [9], [7],[10] which uses plasma heat in a vertical shaft cupola adopted from the foundry industry. The plasma gasification process is illustrated in Fig. 2 below. The heart of the process is the "Plasma Gasifier"; a vertical refractory lined vessel into which

the feed material is introduced near the top along with metallurgical coke and limestone. Plasma torches are located near the bottom of the vessel and direct the high temperature process gas into a bed of coke at the bottom of the vessel. Air or oxygen is introduced through tuyres located above the torches. The high temperature process gas introduced through the torch raises the temperature of the coke bed to a very high level to provide a heat reservoir and the process gas moves upward through the gasifying vessel to gasify the waste. The power of plasma gasification makes it environmentally clean technique. Plasma Gasification Plant projects [11] are being developed by many gas plasma companies, with real benefits obtained from this technology.

Additional heat is introduced from the reaction of the carbon in the waste with the oxygen introduced through the tuyres to produce carbon monoxide in the gasification process. The hot product gas, passing upward though the wastes, breaks down organic compounds and dries the wastes at the top of the "gasifier". As the waste moves downward through the "gasifying" vessel, inorganic materials such as metal, glass and soil are melted and produce a two phase liquid stream consisting of metals and a glass-like (vitrified) residue that flows to the bottom of the vessel. Discharge of the molten material into water results in the formation of metal nodules and a coarse sand-like material.

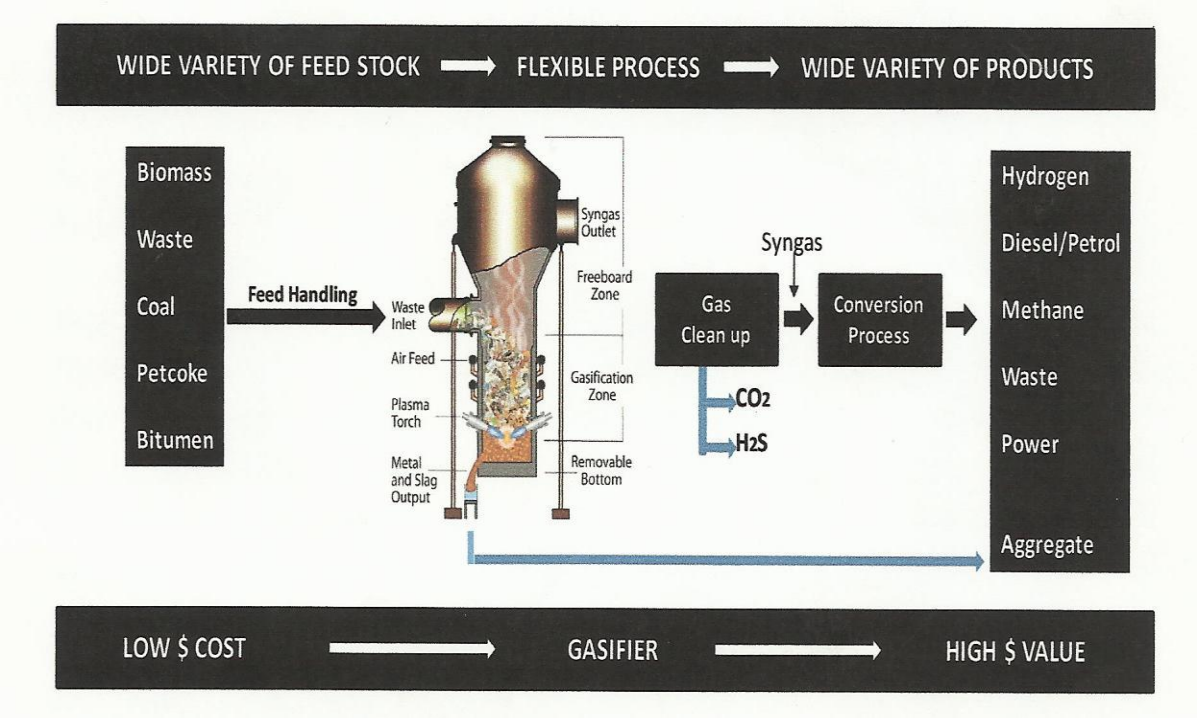

Fig. 2.0 Plasma gasification process

2.3 Power Generation: Integrated Gasification and Combined Cycle (IGCC)

For Power generation process, the product gas would be cooled prior to clean-up by passing through a heat recovery steam generator (HRSG) and the recovered heat used to generate steam. The cool gas would then be cleaned using readily available technologies, compressed, and used as fuel in a combustion turbine driving an electric generator. The hot turbine exhaust gas would pass through a second HRSG to produce additional steam prior to passing through a final emission control system designed to remove trace organics, metals and particulates prior to emission to the atmosphere. The steam from both HRSG units would be combined and used to produce additional electricity using a steam turbine generator. This is the process of integrated gasification combined cycle power generation.

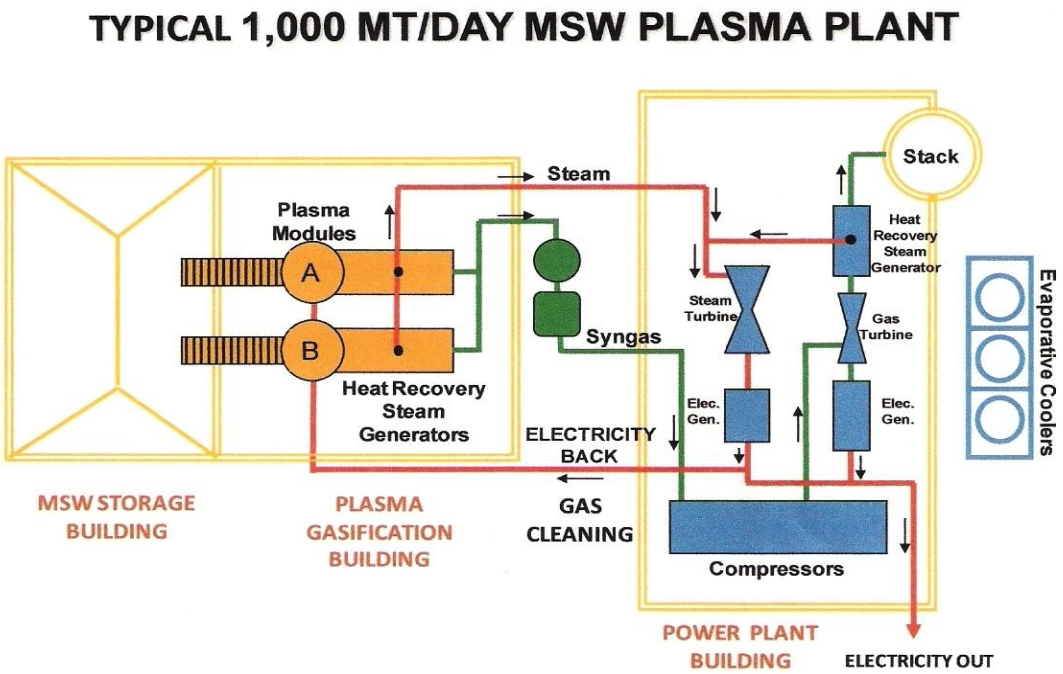

Fig.3 Typical 1000MT MSW plasma plant using ICCG for power generation

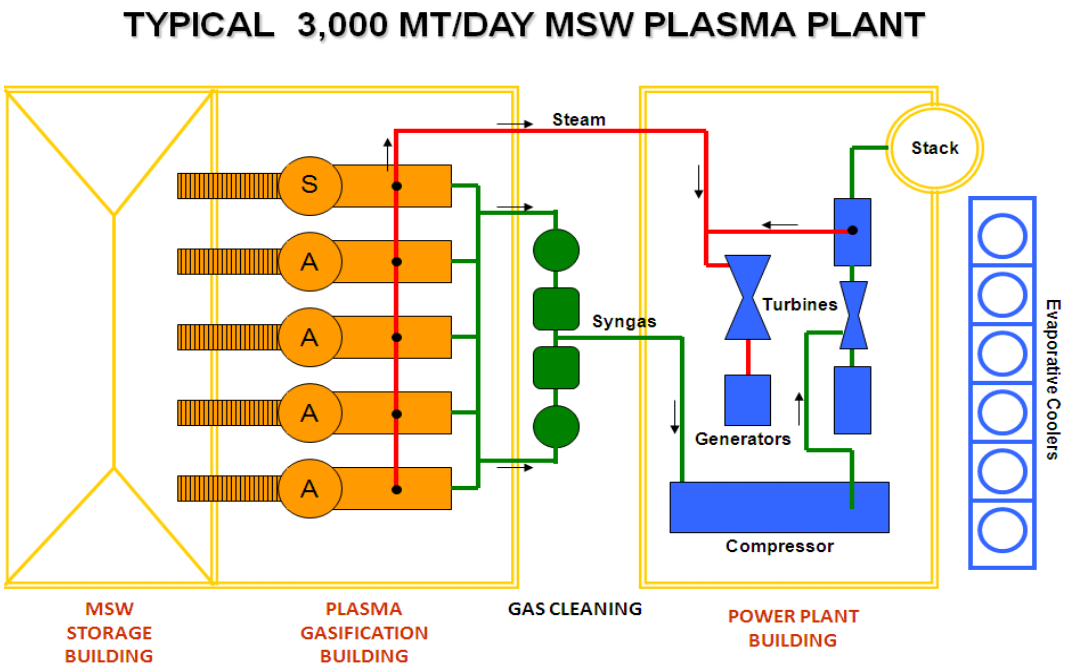

Figure 4: Plasma plant facility using IGCC for power generation

2.3.1 Scalability of the Plasma Power System

The diagrams (Fig.3 and Fig.4) illustrate typical plant layout configurations for plants having process capacities of 1000 MT per day and 3000 MT per day Municipal Solid Waste and demonstrate the relative ease by which plants can be expanded to meet increasing loadings through the use of standardized process modules with capacities of 500 and 750 MT/day. Note that in these examples, a standby module has been included in the design to assure that processing capacity can be maintained during periods of scheduled maintenance.

It should also be noted that a similar configuration in Fig.4 could be achieved by adding modules to the 1000 MT/day facility. The ability to increase capacity by adding modular components as waste loading increases is an important advantage to the plasma gasification process for power generation.

2.3.2 Efficiencies of Scale

As with many industrial processes, increasing the size of the project increases efficiency. In the case of plasma gasification for power generation, these increases result from a combination of factors including proportionately smaller increases in internal plant loads on a per unit basis and increased efficiency of electrical generation through the use of larger units capable of operating at higher temperature and pressures that result in higher thermal efficiencies. The expected effects of increasing plant capacity on thermal efficiency and power output per ton of material processed are summarized in Table 1 below.

We notice from the table that for a combine circle power generation with plant capacity of 500MT/day, power generation is 26.7MW and the overall efficiency is 32.1%. If the capacity is increased to 5000MT/day the overall efficiency increases to 38.9% and about 323MW of Electric power will be generated.

Table 1 Economies of Scale in Combined Cycle and Simple Cycle Plasma Gasification

		Conventional Steam Turbines					Combined Cycle (IGCC)				
Plant Capacity MT/day	Heat Input (MWht	Gross Mwe	Net Mwe	Plant Load	MWh / MT MSW	Overall Efficiency %	Gross Mwe	Net Mwe	Plant Load	MWh/ MT MSW	Overall Efficiency %
500	83.3	19.7	16.1	3.63	0.77	19.3	33.7	26.7	6.93	1.28	32.1
2500	416.4	122.0	103.7	18.26	1.00	24.9	186.9	152.1	34.76	1.46	36.5
5000	832.7	259.6	223.1	36.52	107	26.8	393.4	323.8	69.52	1.55	38.9

2.4 Environmental Sustainability of Plasma Gasification.

Plasma gasification represents a clean and efficient option to convert various feed stocks into energy in an environmentally responsible manner [7]. In the plasma gasification process, heat nearly as hot as the sun's surface is used to break down the molecular structure of any carbon-containing materials – such as municipal solid waste (MSW), tires, hazardous waste, biomass, river sediment, coal and petroleum coke – and convert them into synthesis gas (product gas) that can be used to generate Electric power, liquid fuels or other sustainable sources of energy.

Burning or incineration does not occur in a plasma gasification unit, and so compared with other thermal conversion processes, gasification is completely different from incineration (Table 2).

Table 2 Plasma Gasification and Incineration

Plasma Gasification	Incineration
Occurs in the absence or near absence of oxygen, prohibiting combustion.	Excess air is induced to ensure complete combustion.
Gases resulting from degradation of organics are collected and used for production of various forms of energy and/or industrial chemicals.	All potential energy converted to heat.
Products of degradation largely converted to inert (non-hazardous) glass-like slag of a volume 6% to 15% of the original solids volume.	Combustion results in ash (as much as 30% of original solids volume) that must often be treated as hazardous waste
Emissions substantially lower than those resulting from incineration.	Far greater emissions of GHG and other pollutants than with thermal gasification systems.

Virtually any material, including low-level radioactive waste under certain conditions, can be reduced using plasma gasification. Materials that can be safely and effectively treated include coal, sludge, incinerator ash, hazardous fly ash, automobile shredder residue, medical waste, pathological wastes, PCB oil pyrolysis products, ferrous chromium waste, ferro-manganese reduction compounds, titanium scrap melt, niobium recovery products, electric arc furnace dust, Portland cement manufacturing waste, paper, cardboard, plastics, fiberglass insulation and other products, asbestos, wood, glass, ceramics, rubber, tires, asphalt shingles, used roadway asphalt, oil sands, sewage sludge, harbor sludge, composite materials containing resins, linoleum, plastic piping, solvents, paints, and other carbon-containing materials including mixed solid waste [12].

The system will also handle such materials as steel beams and rebar; copper piping; steel, aluminum, and copper wire; and even concrete, stone, bricks, although it makes more sense from energy, environmental, and economic perspectives to remove such materials from the waste stream prior to processing [12], [13], [6]. Plasma gasification will also handle treated wood and even contaminated soils – both a problem currently for both landfill and incineration operations.

2.4.1 Waste Management and Power Generation Requirements

The rate of Carbon dioxide emission [14], [10] per MWH of electricity produced from different processes is very low for plasma gasification of MSW process.

Low Dioxin/Furan emissions:

– Less than 0.01 NG/NM³ of Dioxins/Furans
– Sulfur reports as Hydrogen Sulfide (H2S) easier to clean than Sox
– Tars are cracked prior to leaving the Gasifier.

"One technology which potentially can use various types of waste, produce electricity and hydrogen without emitting dioxin, furan and mercury, is plasma arc technology.

Municipalities can install a plasma arc facility which will eliminate land filling ..." - EPA

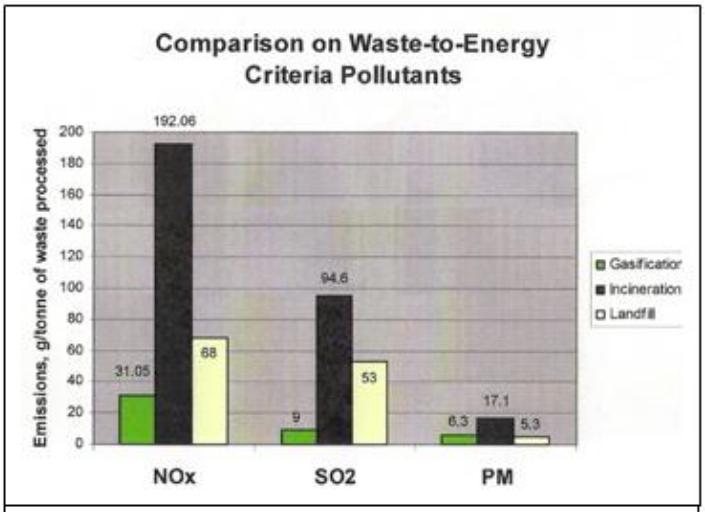

Figure 5. Comparison of emissions on waste to power generation from Gasification. Incineration and Landfill

Carbon Dioxide Emissions

Plasma gasification WTE facility avoids:
1. The release of methane that otherwise would be emitted when trash decomposes in landfills

2. The displacement of CO_2 that would have been emitted had the electricity been generated from fossil fuels such as coal.

This sophisticated waste destruction and electric power generating system operates on the principle of environment friendly waste destruction and sustainable generation of renewable energy.

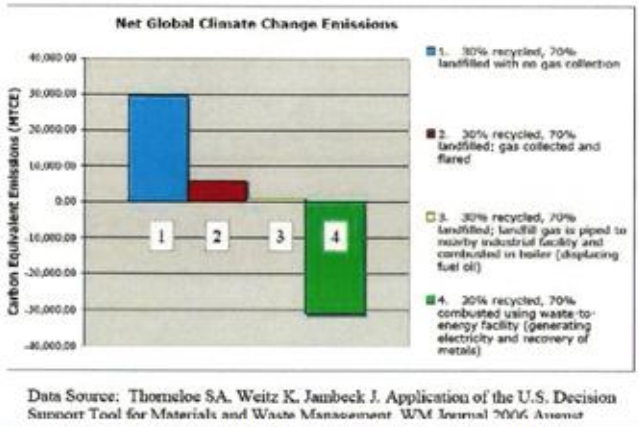

Data Source: Thomeloe SA. Weitz K. Jambeck J. Application of the U.S. Decision Support Tool for Materials and Waste Management. WM Journal 2006 August

Figure 6. Net climate change emissions are negative compared to other waste management options

Each plasma gasification application will have a differing environmental profile [7], but in general terms a plasma gasification facility will have very low emissions of NOx, SOx, dioxins and furans.

There is an emerging global ([15], [16] consensus to develop local level solutions and community participation for better MSW management. Emphasis has been given to citizens' awareness and involvement for better [17] waste management. A number of studies were carried out in the past to compare different methods of waste disposal and processing for different places. Study for the Netherlands [18] concluded that composting was the best option of waste management. Study for the United Kingdom concluded that refused derived fuel [19] was the best option. It can be inferred from the literature that no one method in isolation can solve the problem of waste management. The present paper aims to establish that plasma physics applied to gasification of MSW will not only lead to proper waste destruction but enhance alternative power generation.

The suitability of a particular technology for solving waste and power problems will depend on a number of factors which includes techno-economic viability, fuel availability, environmental factors, sustainability [20]

and geophysical background of the location. The Plasma Gasification [21], [10] technology seems to be a realistic solution for waste destruction and power generation. It is a disposal process that can get rid of almost any kind of waste by eliminating existing landfills, open dumps, and produce clean power for the national grid.

2.4.2 Land requirement

The land and transportation facilities are basic requirement for waste destruction/power generation. As per the provisions of Municipal Solid Waste (Management and Handling) Rules, 2000, the landfill site shall be large enough to last for 20-25 years [9]. It is the general experience that the land requirement for development of the MSW landfill site is around 0.2 ha/MT of MSW generation per day with minimum requirement of 2.0 ha land area. The projected minimum land requirement for Plasma Gasification Process (PGP),[7] , [10] is dependent on the processing capacity of the plant and ancillary processes that maybe included in the overall plant design. However, a standard IGCC configured plant having a capacity of 1000 M.T per day would require about 2.02 Hectares (5 Acres) of land. Increasing the capacity of the plant to 3000 M.T. per day would increase land requirement to about 4.04 Hectares (10 Acres).

2.4.3 Sustainability

The sustainability of any project depends up on the capital cost, running & maintenance cost, availability of raw materials (feedstock for the plant) and return on investment. Capital costs for a plasma gasification plant are similar to those for a municipal solid waste incineration power plant, but plasma gasification plants are more economical because the plant's inorganic byproduct can be sold to the market as bricks and concrete aggregate. Plasma gasification plants also produce up to 50% more electricity than other gasification technologies, [14] hence, reducing the payback period and increase return on investment. Nedcorp group plasma gasification system using Westinghouse Plasma Corporation plasma touches [7] uses 2 to 5% of energy input to produce 80% of energy output. Typical plasma gasification for waste to energy plant with a feedstock of 3,000 MT of MSW per day is estimated to cost over $400 million for installation and will generate about 120 MW of electricity [16]. Estimation for a 2,000 MT of MSW per day [22] is about $250 million. Most of the Plasma Gasification Plants require 120 Kwh of energy to process each ton of MSW and 816 kwh electricity is generated from the process. It is also projected [16] that each ton of MSW has the potential to produce 900 kWh. The same plant can produce 1,200 kWh for each ton of MSW if it is equipped with cogeneration auxiliaries i.e. steam turbine and gas turbine in an integrated gasification combine circle (IGCC). This implies that similar to any other new technology, the cost will decrease significantly after the commencement of mass production.

III. RESULTS AND DISCUSSION

The problems of Waste and Power shortages in the world can be resolved by a single process of plasma physics applied to gasification of municipal solid waste. The feasibility conducted[1] showed that power demand exceeds supply, and only a maximum of about 3,300MW of electricity is available at given time for a population of over 165 million in Nigeria. The solution of these twin problems seem to lie in the physics of Plasma Gasification. The Plasma Gasification Process of Municipal Solid Waste is a proven technology for waste to energy production [16]. The reaction processes in Plasma Gasification produce mainly syngas (Hydrogen and Carbon monoxide). The syngas is efficient in power generation using integrated gasification combined circle (ICCG) plasma process. Operation is environmentally responsible creating a product gas with very low quantities of NOx, SOx, dioxins and furans. Inorganic components get converted to glassy slag safe for use as a construction aggregate. The fuel gas emissions are also within prescribed limits [12], the process is environmentally safe in terms of rate of Carbon dioxide emission per MWH of electricity produced in comparison to different processes as depicted in Fig.6. The land requirement for management of Municipal Solid Waste through landfills would be around 600ha for 3000MT/day as per rule 2000. However, processing of 3000MT/day by plasma gasification process for power generation will require only 4ha of land. There is a significant reduction in the space required for MSW and power generation using plasma gasification process. The Plasma Gasification Processing plants will generate over 320MW of electricity when 5000MT/day is processed, Table 1 and this will be added to the national grid.

IV. CONCLUSION

Developing countries, should seek area-specific solutions to their problems [23] in the MSW management. Application of Plasma Gasification Process (PGP) in waste to energy, relieves the pressure on distressed landfills, and offers an environmentally benign method [21] of disposing MSW. Municipal solid waste is considered as a source of renewable energy, and plasma gasification technology is one of the leading-edge technologies available to harness this energy. In recent years, the US government officially declared the MSW as a renewable source of energy, and power generated through the use of MSW is

considered green power and qualified for all eligible incentives. Plasma physics applied to gasification is an economic and sustainable source of energy, and a reliable source of power generation in integrated gasification combined cycle (IGCC). There are many applications of Plasma Gasification Process and the profit potential of plasma conversion [22] is tremendous.

The plasma physics applied to gasification p of MSW has all the merits of adoption for power generation, even though there are many disagreements among scientists and policy makers on these matters, there is, however, consensus that alternative sources of energy and power that are sustainable, environmentally friendly and regionally available must be the best choice. Other challenges such as, skepticism about the technology, lack of historical data, a mislabeling of plasma gasification technology as another type of incineration have contributed to the lack of progress in development and utilization of this technology.

Plasma Physics applied to Gasification of MSW for power generation from abundant waste is viable and sustainable. The most important factor is the will of governments and people to change the existing system and develop something new and probably better. It is the author's considered opinion that scientists, engineers and governments should take the required initiatives to develop this technology for alternative power generation to address power shortages and reduce the use of fossils.

V. ACKNOWLEDGEMENT

I am grateful to the staff of Power Holding Company of Nigeria (PHCN) who assisted with relevant information. Also, I am thankful the Nedcorp Group for vital assistance.

REFERENCES

[1] Anyaegbunam F.N.C, JVL Capital (2012), Plasma Power Project Feasibility Report, prepared for Brain-Fintek Plasma Power Limited. BPP publications, July 2012.

[2] Langmuir I. (1928), Oscillations in ionized gases, Proceeding of National academy of science, U.S. 14(8), pp 628.

[3] Chen, Francis F. (1984), Plasma Physics and Controlled Fusion. Plenum Press. ISBN 0306413329

[4] Camacho S. L., 1996), Plasma Pyrolysis and Vitrification of Municipal Waste, U.S. Patent No. 5,544,597, Aug. 1996.

[5] Youngchul Byun, Moohyun Cho, Soon-Mo Hwang and Jaewoo Chung, (2012) Thermal Plasma Gasification of Municipal Solid Waste (MSW). (www.intechopen.com/thermal_plasma_gasification_of_municipal_solid_waste)

[6] Dodge, E. (2009) Plasma Gasification: Clean Renewable Fuel Through Vaporization of Waste. Emerson Process Management. WaterWorld. (http://www.waterworld.com/index/display/articledisplay/368649/articles/wastemanagement-world/volume-10/issue-4/features/plasma-gasification-cleanrenewable-fuelthrough-vaporization-of-waste.html)

[7] Nedcorp Group (2009) Environmentally Friendly Waste Destruction and Sustainable Renewable Energy. A feasibility document of Nedcorp group, July 2009.

[8] Evans Steve D, (2009), Plasma Gasification Plant Benefits for Municipal Waste Management, EzineArticles.com, available at http://www.articlesbase.com/literaturearticles/plasma-gasification-plant-benefits-for-municipal-waste-management-850915 . html, accessed during December 2011.

[9] Patel Munna Lal, Chauhan Janardan Singh (2012), Plasma Gasification: A Sustainable Solution for the Municipal Solid Waste Management in the State of Madhya Pradesh, India. INTERNATIONAL JOURNAL OF ENVIRONMENTAL SCIENCES Volume 3, No 1, 2012

[10] Anyaegbunam F.N.C., (2013), Plasma gasification in waste management and sustainable renewable energy in Nigeria. International Journal of Environmental Science and Technology, July 2013.

[11] Dighe, Shyam V. (2008), Westinghouse Plasma Corporation, Madison, Pennsylvania, USA, Plasma Gassification : a proven technology, Proceedings of NAWTEC16, 16th Annual North American Waste-to-Energy Conference, May 19-21, 2008, Philadelphia, Pennsylvania, USA.

[12] DOVETAIL PARTNERS, INC. (2010) Plasma Gasification: An examination of the Health, Safety, and Environmental Records of Established Facilities Prepared for the City of PALISADE, MINNESOTA June 7, 2010

[13] Thomas, R. (2007). Ability of Plasma Gasification to Handle Construction and Demolition Waste. (http://www.bape.gouv.qc.ca/sections/mandats/LET-danford-lake/documents/DM58-3.pdf) 16

[14] Circeo L. J, (2012), Plasma Arc Gasification of Municipal Solid Waste. Georgia Tech Research Institute, Environmental Science and Technology Program, Electro-Optical Systems laboratory.

[15] Rathi Sarika, (2007), Optimization model for integrated municipal solid waste management in Mumbai, India, Environment and Development Economics 12, pp 105-121.

[16] Pourali, M., (2010), Application of Plasma Gasification Technology in Waste to Energy—Challenges and Opportunities, The IEEE Xplore digital library (Institute of Electrical and Electronics Engineers), 1(3), pp 125-130,
[17] Beukering, (1999), Waste recovery in Bombay: a socio-economic and environmental assessment of different waste management options, Third World Planning Review 19(2),pp 163–187.
[18] Maimone, M., (1985), An application of multi-criteria evaluation in assessing MSW treatment and disposal systems, Waste Management and Research, 3, pp 217–231.
[19] Powell, J.C., (1996), The evaluation of waste management options, Waste Management and Research 14, pp 515–526, reprinted in Powell et al. 2001.
[20] Varma, R. Ajayakumar, (2009), Technoligical Options for Treatment of Municipal Solid Waste with special reference to Kerala, Workshop on Public Office Sanitation at State Municipal House on 25th Sept 2009, available at sanitation.kerala.gov.in/pdf/workshop/techno_2.pdf, accessed during December 2011.
[21] Lisa Zyga, (2012), Plasma Gasification Transforms Garbage into Clean Energy, Science Blogger, InventorSpot.com, via: Popular Science.
[22] Blees Tom, (2008), Prescription for the Planet, The Painless Remedy for our Energy & Environmental Crises, ISBN: 1-4196-5582-5, ISBN-13: 9781419655821 Library of Congress Control Number: 2008905155.
[23] Henry, (2006), Country report, Municipal solid waste management challenges in developing countries – Kenyan case study, Waste Management, 26, 92–100.

American Journal of Engineering Research (AJER)
e-ISSN : 2320-0847 p-ISSN : 2320-0936
Volume-02, Issue-08, pp-76-89
www.ajer.org

Research Paper Open Access

Optimum Position of Outrigger System for High-Rise Reinforced Concrete Buildings Under Wind And Earthquake Loadings

P.M.B. Raj Kiran Nanduri[1], B.Suresh[2], MD. Ihtesham Hussain[3]
[1](Department of civil engineering, Adama Science and technology university, Adama, Ethiopia)
[2](Department of civil engineering, Adama Science and technology university, Adama, Ethiopia)
[3](Department of civil engineering, Adama Science and technology university, Adama, Ethiopia)

Abstract: - Tall building development has been rapidly increasing worldwide introducing new challenges that need to be met through engineering judgment. In modern tall buildings, lateral loads induced by wind or earthquake are often resisted by a system of coupled shear walls. But when the building increases in height, the stiffness of the structure becomes more important and introduction of outrigger beams between the shear walls and external columns is often used to provide sufficient lateral stiffness to the structure.The outrigger and is commonly used as one of the structural system to effectively control the excessive drift due to lateral load, so that, during small or medium lateral load due to either wind or earthquake load, the risk of structural and non-structural damage can be minimized. For high-rise buildings, particularly in seismic active zone or wind load dominant, this system can be chosen as an appropriate structure. The objective of this thesis is to study the behavior of outrigger and, outrigger location optimization and the efficiency of each outrigger when three outriggers are used in the structure. In Nine 30−storey three dimensional models of outrigger and belt truss system are subjected to wind and earthquake load, analyzed and compared to find the lateral displacement reduction related to the outrigger and belt truss system location. For 30−storey model, 23% maximum displacement reduction can be achieved by providing first outrigger at the top and second outrigger in the structure height. The influence of second outrigger system is studied and important results are tabulated and drawn.

Keywords: *- Outrigger, Belt truss system, Wind, Earthquake, Lateral displacement.*

I. INTRODUCTION

1.1 Introduction to outriggers

Mankind had always fascinated for height and throughout our history, we have constantly sought to metaphorically reach for the stars. From the ancient pyramids to today's modern skyscraper, a civilization's power and wealth has been repeatedly expressed through spectacular and monumental structures. Today, the symbol of economic power and leadership is the skyscraper. There has been a demonstrated competitiveness that exists in mankind to proclaim to have the tallest building in the world.

This undying quest for height has laid out incredible opportunities for the building profession. From the early moment frames to today's ultra-efficient mega-braced structures, the structural engineering profession has come a long way. The recent development of structural analysis and design software coupled with advances in the finite element method has allowed the creation of many structural and architecturally innovative forms. However, increased reliance on computer analysis is not the solution to the challenges that lie ahead in the profession. The basic understanding of structural behavior while leveraging on computing tools are the elements that will change the way structures are designed and built.

The design of skyscrapers is usually governed by the lateral loads imposed on the structure. As buildings have gotten taller and narrower, the structural engineer has been increasingly challenged to meet the imposed drift requirements while minimizing the architectural impact of the structure. In response to this challenge, the profession has proposed a multitude of lateral schemes that are now expressed in tall buildings across the globe.

The design of tall and slender structures is controlled by three governing factors, strength (material capacity), stiffness (drift) and serviceability (motion perception and accelerations), produced by the action of lateral loading, such as wind. The overall geometry of a building often dictates which factor governs the overall design. As a building becomes taller and more slender, drift considerations become more significant. Proportioning member efficiency based on maximum lateral displacement supersedes design based on allowable stress criteria.

Through the design of a high-rise structure, numerous problems appear such as the number of columns or size and shape of concrete core or even basic dimensions of the structure itself. Having constraints for the building immediately defines and solves part of the unknown variables but it is the geometry of the structural system inside these basic parameters that identifies an efficient design.

Undoubtedly, the factor that governs the design for a tall and slender structure most of the times is not the fully stressed state but the drift of the building. There are numerous structural lateral systems used in high-rise building design such as: shear frames, shear trusses, frames with shear core, framed tubes, trussed tubes, super frames etc. However, the outriggers and belt trusses system is the one providing significant drift control for the building.

1.2 Structural concepts

The key idea in conceptualizing the structural system for a narrow tall building is to think of it as a beam cantilevering from the earth (fig 1.). The laterally directed force generated, either due to wind blowing against the building or due to the inertia forces induced by ground shaking, tends both to snap it (shear), and push it over (bending).

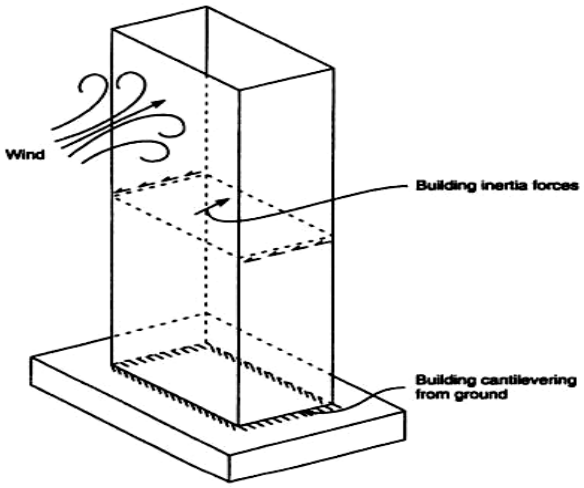

Fig. 2 Structural concept of tall building

Therefore, the building must have a system to resist shear as well as bending. In resisting shear forces, the building must not break by shearing off (fig.3.a), and must not strain beyond the limit of elastic recovery (fig.3.b).

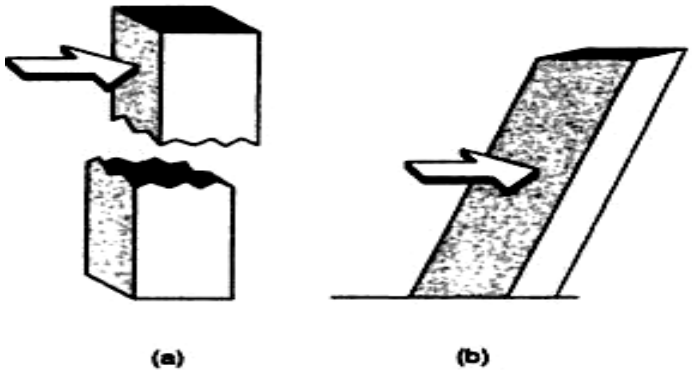

Fig.3 Building shear resistance; (a) building must not break (b) building must not deflect excessively in shear

Similarly, the system resisting the bending must satisfy three needs (fig.4). The building must not overturn from the combined forces of gravity and lateral loads due to wind or seismic effects; it must not break by premature failure of columns either by crushing or by excessive tensile forces: its bending deflection should not exceed the limit of elastic recovery.
In addition, a building in seismically active regions must be able to resist realistic earthquake forces without losing its vertical load carrying capacity.

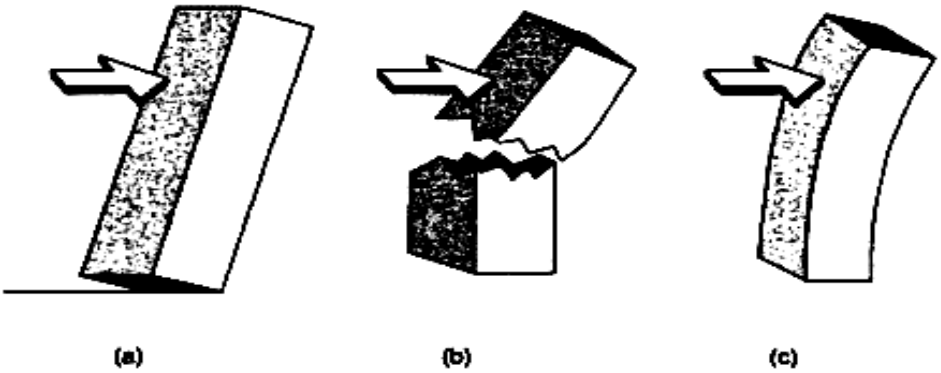

Fig. 4 Bending resistance of building (a) Building must not overturn (b) Columns must not fail in tension or compression
(c) Bending deflection must not be excessive

In the structure's resistance to bending and shear, a tug-of-war ensues that sets the building in motion, thus creating a third engineering problem; motion perception or vibration. If the building sways too much, human comfort is sacrificed, or more importantly, non-structural elements (glass fascia) may break resulting in expensive damage to the building contents and causing danger to the pedestrians.

1.3 Introduction to Outriggers

Although outriggers have been used for approximately four decades, their existence as a structural member has a much longer history. Outriggers have been used in the sailing ship industry for many years. They are used to resist wind. The slender mast provides the use of outriggers. As a comparison the core can be related to the mast, the outriggers are like the spreaders and the exterior columns are like the shrouds or stays.

Innovative structural schemes are continuously being sought in the field. Structural Design of High Rise Structures with the intention of limiting the Drift due to Lateral Loads to acceptable limits without paying a high premium in steel tonnage. The savings in steel tonnage and cost can be dramatic if certain techniques are employed to utilize the full capacities of the structural elements. Various wind bracing techniques have been developed in this regard; one such is an Outrigger System, in which the axial stiffness of the peripheral columns is invoked for increasing the resistance to overturning moments.

This efficient structural form consists of a central core, comprising either Braced Frames or Shear Walls, with horizontal cantilever trusses or girders known as outrigger Trusses, connecting the core to the outer columns. The core may be centrally located with outriggers extending on both sides (Fig.5.a) or it may be located on one side of the building with outriggers extending to the building columns on one side (Fig.5.b).

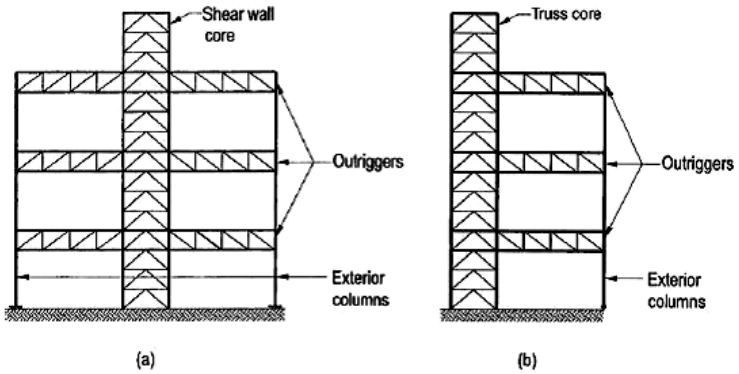

Fig.5 (a) Outrigger system with a central core (b) Outrigger system with offset core

When Horizontal loading acts on the building, the column restrained outriggers resist the rotation of the core, causing the lateral deflections and moments in the core to be smaller than if the free standing core alone resisted the loading. The result is to increase the effective depth of the structure when it flexes as a vertical cantilever, by inducing tension in the windward columns and Compression in the leeward columns.

In addition to those columns located at the ends of the outriggers, it is usual to also mobilize other peripheral columns to assist in restraining the outriggers. This is achieved by including a deep Spandrel Girder, or a Belt Truss, around the structure at the levels of the outriggers.

To make the Outriggers and Belt Truss adequately stiff in flexure and shear, they are made at least one, and often 2 – stories deep. It is also possible to use diagonals extending through several floors to act as outriggers. And finally, girders at each floor may be transformed into outriggers by moment connections to the core and, if desired, to the exterior columns as well.

Here, it should be noted that while the outrigger system is very effective in increasing the structure's flexural stiffness, it doesn't increase its resistance to shear, which has to be carried mainly by the core.

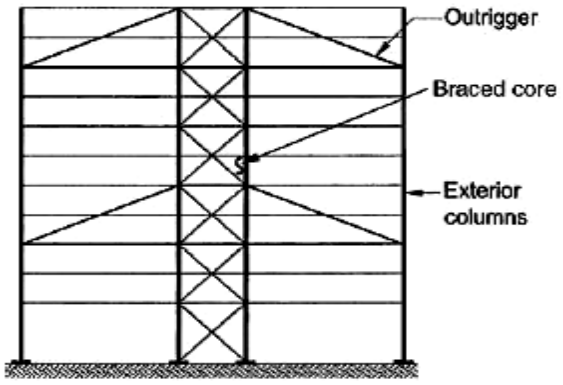

(c)

Fig.6 Diagonals acting as outriggers

In 1974, **Taranath** examined the optimum location of a belt truss which minimized the wind sway and discussed a simple method of analysis. **McNabb** et al (1975) extended their analysis to two outriggers and investigated governing factors in drift reduction. **McNabb** et al (1975) verified the **Taranath**'s optimum outrigger location result and showed that the optimum locations for two outriggers to be 0.312 and 0.685 of the total height from the top of the building. In 1985, **Moudarres** et al (1985) investigated the free vibration of high rise structures using dynamic analysis and this treatment took into account the effects of shear deformation and rotatory inertia of the core and included the inertia of the outrigger.

Chan and **Kuang** (1989a, 1989b) conducted studies on the effect of an intermediate stiffening beam at an arbitrary level along the height of the walls and indicated that the structural behavior of the structure could be significantly affected by the particular positioning of this stiffening beam.

For preliminary analysis of outrigger braced structures, simple approximate guidelines for the location of the outriggers were given in **Smith** et al (1991).

Moudarres [7] conducted the study of a pair of coupled shear walls stiffened at the top by a flexible outrigger, and investigated the outrigger's influence on the behavior of the walls. The treatment of coupled shear walls stiffened at the top by an outrigger is approached by considering the un-stiffened walls under the influences of external loads and internal forces, respectively. The vertical axial forces and the concentrated moments imposed at the top of the walls are internal forces due to the influence of the stiffening outrigger.

Alex Coull and W. H. Otto Lau [8] conducted a study of a multi outrigger-braced structure based on the continuum approach in which the set of outriggers is smeared over the height to give an equivalent uniform bracing system. After their detail analysis they concluded that, Continuum analysis can give reasonably accurate results for even a very small number of Outriggers. They also presented Design Curves for assessing the lateral drift and the core base moments for any structural configuration defined in terms of two controlling structural parameters. The curves allow a direct assessment of the effectiveness of any number of outriggers.

R. Shankar Nair [9] presented a paper on the detail study of various types of outriggers and their relative behavior and performance subjected to lateral loading along with their advantages and disadvantages. He also conducted an analysis for a typical steel structure employing various types of OUTRIGGERS.

The application and effectiveness of belt trusses as virtual outriggers is demonstrated through an example:

Table 1 Results of analysis of 75 – Storied Building

Type of outrigger	Lateral displacement at top due to wind (inches)
No outrigger	108.5
Convention outrigger	25.3
Belt truss as virtual outrigger	37.1
Belt truss as virtual outrigger : 10-fold increase in floor diaphragm stiffness	31.0
Belt truss as virtual outrigger : 10-fold increase in floor diaphragm stiffness, 10-fold increase in belt truss and stiffness	26

The conclusions of his study can be summarized as follows:

Techniques for using belt trusses and basements as "virtual" outriggers in tall buildings have been proposed. Belt trusses used as virtual outriggers offer many of the benefits of the outrigger concept, while avoiding most of the problems associated with conventional outriggers.

In many applications, the reduced effectiveness or efficiency of the virtual outrigger system (compared to conventional direct outriggers) will be more than compensated for by the following benefits offered by the proposed concept:

- There are no trusses in the space between the core and the building exterior.
- There are fewer constraints on the location of exterior columns. The need to locate large exterior columns where they can be directly engaged by outrigger trusses extending from the core is eliminated.
- All exterior columns (not just certain designated outrigger columns) participate in resisting overturning moment.
- The difficult connection of the outrigger trusses to the core is eliminated.
- Complications caused by differential shortening of the core and the outrigger columns are avoided.

In the lateral load analysis of a building with the proposed virtual outrigger system (or any other type of indirect or offset outrigger system), the in-plane stiffness of the floors that transfer horizontal forces from the core to the outriggers should be modeled accurately. These floors cannot reasonably be idealized as rigid diaphragms. **Su** et al (2005) investigated the complete load transfer mechanism between the outrigger brace and the core wall using strut-and-tie method.

Hoenderkamp et al (2008) presented a simple method of analysis for preliminary design of outrigger braced high-rise shear walls subjected to horizontal loading. Further, these studies showed that the position of the outrigger can substantially affect the behavior and lateral deflection of the structure.

Gerasimidis S, Efthymiou E & Baniotopoulos C. C. [10] conducted a basic design optimization technique of tall steel structures for lateral loads, mainly wind, into trying to find the optimum number of outriggers for a specific high-rise building. The structure is analyzed for an indicative wind loading. The geometry produced by stress based design, although below the stress limit, is very flexible and exhibits horizontal displacements and inter-story drifts much above the acceptable limits, due to the wind loading. Then the structure is analyzed with all the possible outrigger locations monitoring important factors, such as the drift of the building or the moments on the core. In the analysis, he included all the possible different analyses simulating the second outrigger in each one of the floors of the building.

N. Herath, N. Haritos, T. Ngo & P. Mendis [11] investigated the optimum number of the Outrigger Beams or Trusses subjected to Earth Quake forces, for an economical design on a 50 storied building. His study assessed the global behaviour of outrigger braced building under earthquake loads from which the following conclusions can be drawn based on the above results:

- The behaviour of a structure under earthquake load is different from earthquake to earthquake. This well known phenomenon is well presented in the lateral displacement results obtained for both of the options.
- The location of the outrigger beam has a critical influence on the lateral behaviour of the structure under earthquake load and the optimum outrigger locations of the building have to be carefully selected in the building design.

To control the time period and the fundamental frequencies and the vibrations induced due to lateral loads, the concept of Dampers was introduced. To gain insight into the conceptual design of such damped outrigger system in a tall structure, a simple beam-damper system model for a building with such dampers installed was developed and studied by **Y. Chen, D. M. McFarland, Z. Wang, B. F. Spencer. Jr. L. A.**

Bergman [12].

A closed-form analytical solution is developed for vibration of the beam by analyzing the regions above and below the damper separately using separation of variables. This solution was used to determine design curves for optimal damper position and size.

Research has pointed out that the damping ratio for a tall building will become smaller with an increase in its height; as a result, the system damping assumed in the design of buildings over 200 m may be overestimated in comparison with the damping found in as-built.

It was found that there exists an optimal damper size, which results in system modal damping approaching its maximum value, for an assigned damper location. Obviously, this maximum system modal damping varies with damper location and modal order.

There can be several layers of outriggers in a structure. There optimum placement depends on a multitude of structural factors such as location of the outriggers, the axial rigidity of the columns, the flexural rigidity of the core and the outriggers and the efficiency of each outrigger when several outriggers are used in the structure. These issues were discussed in depth by **Ali Lame [13]** and developed a program (using visual basic) to calculate the top deflection of the outrigger structure and the moment at the base. The algorithm used in the program can be used for infinite no. of outriggers.

1.4 Problems with Outriggers:

There are several problems associated with the use of outriggers, problems that limit the applicability of the concept in the real world:

1. The space occupied by the outrigger trusses (especially the diagonals) places constraints on the use of the floors at which the outriggers are located. Even in mechanical equipment floors, the presence of outrigger truss members can be a major problem.

2. Architectural and functional constraints may prevent placement of large outrigger columns where they could most conveniently be engaged by outrigger trusses extending out from the core.

3. The connections of the outrigger trusses to the core can be very complicated, especially when a concrete shear wall core is used.

4. In most instances, the core and the outrigger columns will not shorten equally under gravity load. The outrigger trusses, which need to be very stiff to be effective as outriggers, can be severely stressed as they try to restrain the differential shortening between the core and the outrigger columns. Elaborate and expensive means, such as delaying the completion of certain truss connections until after the building has been topped out, have been employed to alleviate the problems caused by differential shortening.

II. BEHAVIOR OF OUTRIGGERS

To understand the behaviour of an outrigger system, consider a building stiffened by a story high outrigger at top, as shown in Fig.7.c. Because the outrigger is at the top, the system is often referred to as a cap or hat truss system. The tie-down action of the cap truss generates a restoring couple at the building top, resulting in a point of contra-flexure in its deflection curve. This reversal in curvature reduces the bending moment in the core and hence, the building drifts.

The core may be considered as a single-redundant cantilever with the rotation restrained at the top by the stretching and shortening of windward and leeward columns. The result of the tensile and compressive forces is equivalent to a restoring couple opposing the rotation of the core. Therefore, the cap truss may be conceptualized as a restraining spring located at the top of the cantilever. Its rotational stiffness may be defined as the restoring couple due to a unit rotation of the core at the top.

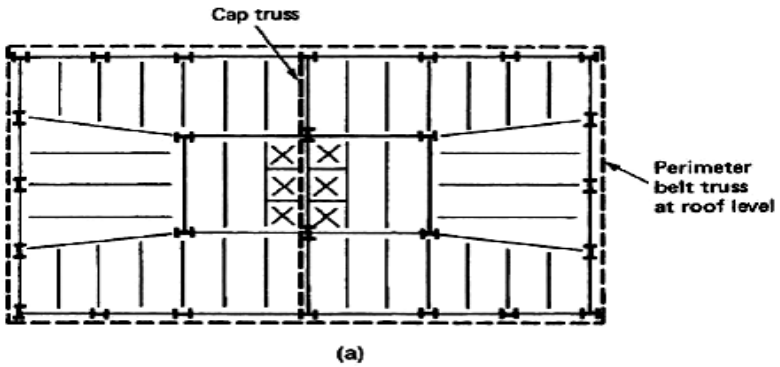

Fig. 7 (a) Building plan with cap truss

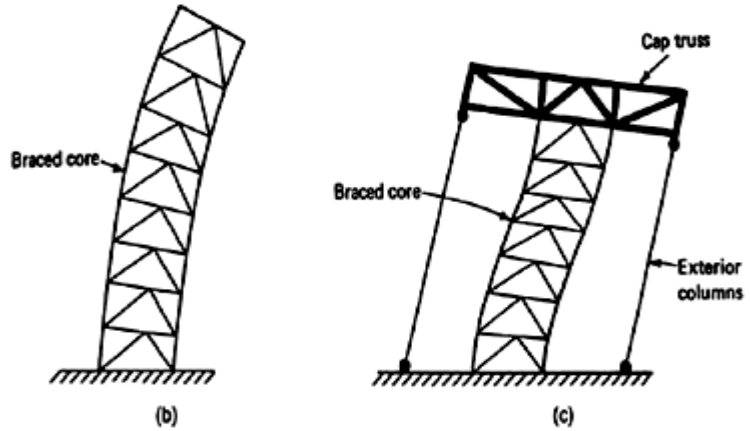

Fig. 7 (b) Cantilever bending of core; (c) tie-down action of cap truss.

Assuming the cap truss is infinitely rigid, the axial elongation and shortening of columns is equal to the rotation of the core multiplied by their respective distances from the center of the core. If the distance of the equivalent column is $d/2$ from the center of the core, the axial deformation of the columns is then equal to $\theta d/2$, where θ is the rotation of the core. Since the equivalent spring stiffness is calculated for unit rotation of the core (that is, $\theta = 1$), the axial deformation of the equivalent columns is equal to $1 \times d/2 = d/2$ units.

The corresponding axial load is given by ,

$$\boldsymbol{P = \frac{AEd}{2L}}$$

Where,

P = axial load in the columns

A = area of columns

E = modulus of elasticity

d = distance between the exterior columns

L = height of the building.

The restoring couple, that is, the rotational stiffness of the cap truss, is given by the axial load in the equivalent columns multiplied by their distance from the center of the core. Using the notation K for the rotational stiffness, and noting that there are two equivalent columns, each located at a distance $d/2$ from the core, we get

$$\boldsymbol{K = P.\frac{d}{2}.2}$$
$$\boldsymbol{=Pd}$$

The reduction in drift depends on the stiffness K and the magnitude of rotation θ at the top.

III. OBJECTIVES AND DETAILS OF THE PRESENT STUDY

The objective of the present work is to study the use of outrigger and belt truss placed at different location subjected to wind or earthquake load. The design of wind load was calculated based on IS 875 (Part 3) and the earthquake load obtained using IS 1893 (Part-1): 2002. The location of outrigger and belt truss for reducing lateral displacement, building drift and core moments can be obtained. The ETABS software program is selected to perform analysis.The present study is limited to reinforced concrete (RC) multi-storied symmetrical building. All the building models analyzed in the study have 30 storeys with constant storey height of 3 meters. Number of base and the bay-width along two horizontal directions are kept constant for all the models for convince.

In the present context of study an R.C.C. structure is taken into consideration and the analysis is done as per the Indian standards. This building does not represent a particular real structure that has been built or proposed. However, the dimensions, general layout and other characteristics have been selected to be representative of a building for which the use of outriggers would be a plausible solution. Till now all the studies have been performed on the steel structures and there was an absence of a research on slender concrete structure.

The model considered for this study is a 90m high rise reinforced concrete building frame. The building represents a 30 storied office building. The Plan area of the Structure is 38.50 x 38.50m with columns spaced at 5.5m from center to center. The height of each storey is 3.00m and all the floors are considered as Typical Floors. The location of the building is assumed to be at Hyderabad. An elevation and plan view of a typical structure is shown in fig. 8 and 9.

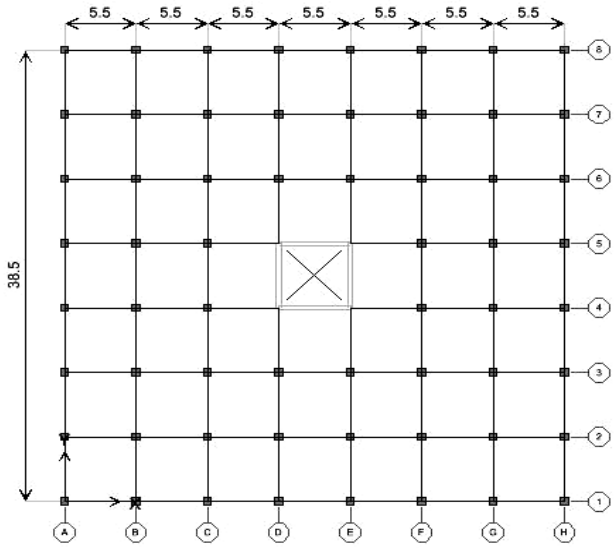

Fig.8 Building Plan dimensions and column centre spacing

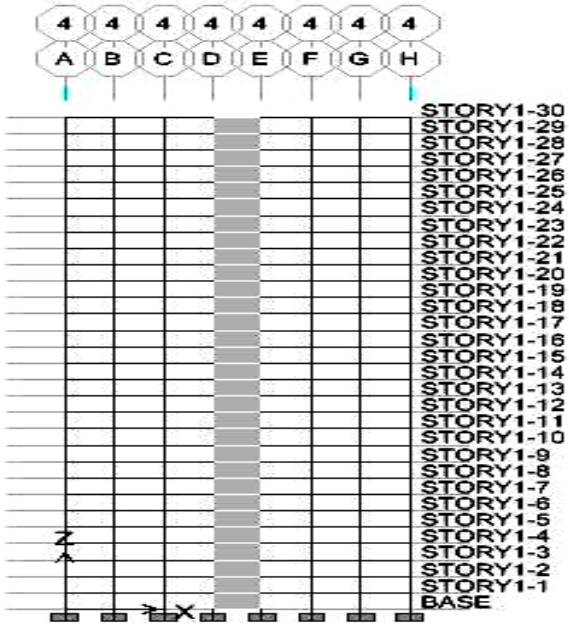

Fig.9 Building Elevation with central core portion.

In this present study a total of seven different arrangements of outriggers analyzed using ETABS software are:

1. Structural Model without Outrigger (SOM).
2. Structural Model with One Outrigger at the top floor (SOD – TOP).
3. Structural Model with One Outrigger at the top floor and another at 3/4th height of the building i.e. on 23rd storey (SOD – ¾).
4. Structural Model with One Outrigger at the top floor and another at mid height of the building i.e. on 15th storey. (SOD – ½)
5. Structural Model with One Outrigger at the top floor and another at 1/4th height of the building i.e. on 8th storey (SOD – ¼).
6. Structural Model with One Outrigger at the top floor with Belt Truss (SOD – BT – TOP).
7. Structural Model with One Outrigger at the top floor and another at 3/4th height of the building i.e. on 23rd storey with Belt Truss (SOD – BT – ¾).
8. Structural Model with One Outrigger at the top floor and another at mid height of the building i.e. on 15th storey with Belt Truss. (SOD – BT – ½).
9. Structural Model with One Outrigger at the top floor and another at 1/4th height of the building i.e. on 8th storey with Belt Truss (SOD – BT – 1/4).

All wall piers are identical with a uniform wall thickness of 350mm over the entire height. The Bracing beams (outriggers) and all other beams are 230mm wide and 600mm deep, Grade 40 (Mix – M40) concrete is considered (Compressive strength 40 N/mm^2) throughout the height of the building. And number of stories considered for all the cases are 30 stories, and roof height is considered as 90 M. And storey to storey height is 3.0 M. And the outer and inner columns sizes are considered as 600 x 600 mm and shear wall thickness is considered as 350 mm.

The method of analysis of the above mentioned system is based up on the assumptions that the outriggers are rigidly attached to the core; The core is rigidly attached to the foundation; The sectional properties of the core, beams and columns are uniform throughout the height; Tensional effects are not considered; Material behavior is in linear elastic range; The Outrigger Beams are flexurally rigid and induce only axial forces in the columns; The lateral resistance is provided only by the bending resistance of the core and the tie down action of the exterior columns connected to the outrigger; The rotation of the core due to the shear deformation is negligible.

Since the building is assumed to be a office building live load is considered as 3 kN/m². A floor load of 1.5 kN/m² is applied on all the slab panels on all the floors for the floor finishes and the other things. A member load as u.d.l. of 6 kN/m is considered on all beams for the wall load considering the wall to be made of Light Weight Bricks.

Wind load in this study is established in accordance with IS 875(part 3-Wind loads). The location selected is Hyderabad. The Basic wind speed as per the code is V_b=44m/s. The coefficients K_1 and K_2 are taken as 1.0. The terrain category is taken as 'Category 4' with structure class C. Taking internal pressure coefficient as ±0.2 the net pressure coefficient Cp (windward) works out as +0.8 and Cp (leeward) as -0.5 based on h/w and l/w ratio of table 4 of IS 875 (part3). Using the above data the **ETABS** automatically interpolates the coefficient K_3 and eventually calculates lateral wind load at each storey. Same load is applied along positive and negative X & Y axis one direction at a time to determine the worst loading condition.

Earthquake load in this study is established in accordance with IS 1893(part 1)-2002.The city of Hyderabad falls in "zone 2" (Z=0.10). The importance factor (I) of the building is taken as 1.0. The site is assumed to be hard/rocky site (Type I). The response reduction factor R is taken as 3.0 for all frames.

The fundamental time period (T_a) of all frames was calculated as per clause 7.6.1 of the aforementioned code.

$$\mathbf{T_a = 0.075 * h^{0.75}}$$

Based on the above data the **ETABS** calculates the design horizontal seismic coefficient (A_h) using the Sa/g value from the appropriate response spectrum. The A_h value calculated is utilized in calculating the design seismic base shear (V_B) as,

$$\mathbf{V_B = A_h * W.}$$

Where, W = seismic weight of the building.

The design seismic base shear so calculated is distributed along the height of the building as per the expression,

$$\mathbf{Q_i = V_B * (W_i * h_i^2) * (\square\ W_j * h_j^2)^{-1}}$$

Where, Q_i = Design lateral force at floor i.

W_i = seismic weight of the floor i

h_i = height of the floor I measured from base

j = 1 to n, n being no. of floors in the building at which masses are located.

The structure is analyzed as per the loading combinations provided in IS: 456-2000. The following load combinations are used to determine the maximum lateral deflection in the structure.

i) DL+LL
ii) DL+LL±$WL_{(x\ or\ y)}$
iii) DL+LL±$EL_{(x\ or\ y)}$
iv) DL±$WL_{(x\ or\ y)}$
v) DL±$EL_{(x\ or\ y)}$

The structure with above mentioned specifications and assumptions is analyzed using the program ETABS and bending moments, shear forces, lateral deflections are calculated for both Wind & Earthquake loading. Since the wind load cases are governing, the graph and tables are represents the same. The structure with above mentioned specifications and assumptions is analyzed using the program ETABS and bending moments, shear forces, lateral deflections are calculated for both Wind & Earthquake loading. Since the wind load cases are governing, the graph and tables are represents the same.

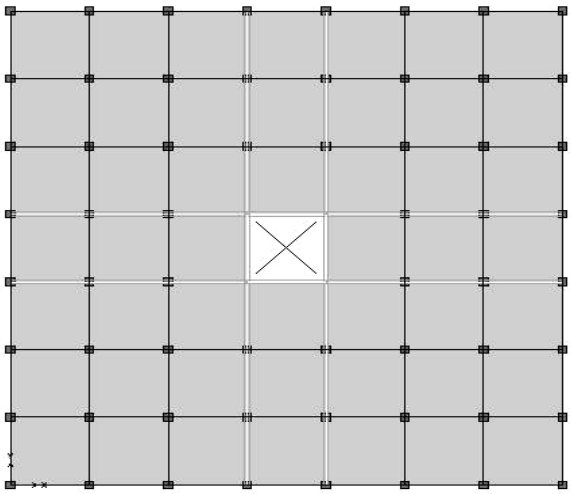

Fig.10 Plan view of the model with central core and extended outrigger on all the four sides.

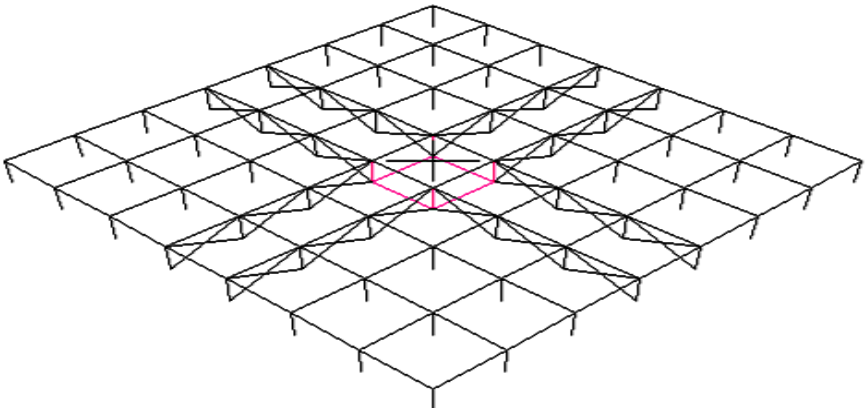

Fig.11 Perspective view of the model with central core and extended outrigger on all the four sides without belt truss.

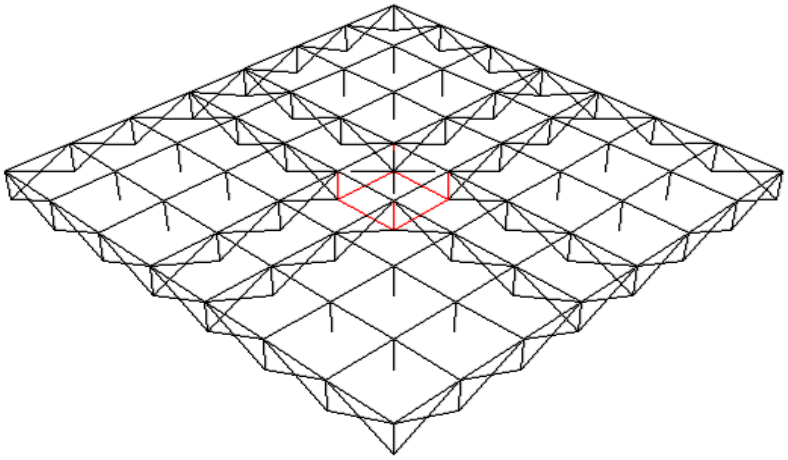

Fig.12 Perspective view of the model with central core and extended outrigger on all the four sides with belt truss.

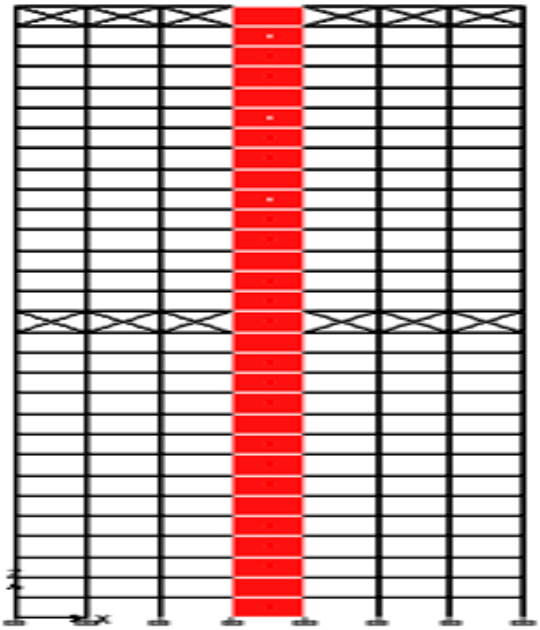

Fig.13 Elevation view of the model with central core and outrigger at 15th and 30th floor.

IV. RESULTS AND DISCUSSIONS

4.1 Drift

The most significant basic parameter monitored throughout the whole analysis process was drift at the top of the building. The following figure 14 shows the variation of drift and from the figure 14 it is observed as follows: It is observed that 4.8% of the drift is controlled by providing outrigger at top floor and 5.3% of the drift is controlled by providing outrigger with belt truss at top floor when compare to the building with core wall only. 18.55% and 23.06% of the drift is controlled by providing the system at middle height of the building. The optimum location of the second outrigger is the mid height of the building, according to drift control criteria.

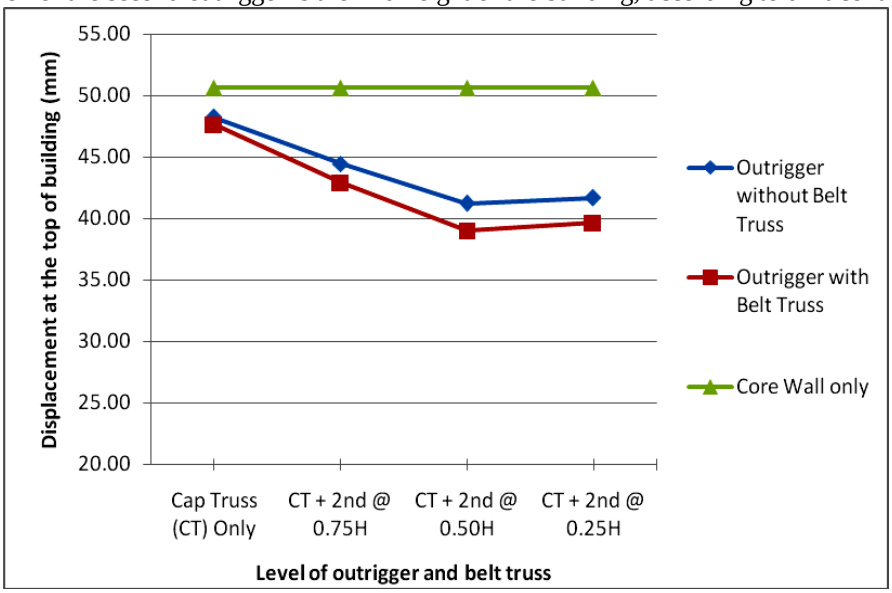

Fig.14 Lateral Displacement of the top storey as a function of level of outrigger and belt truss

5.2 Column axial forces

The structural scheme analyzed in the present study is activated once the outriggers are engaged and transfer the core bending moment to the outboard column as a couple of axial forces.
The behaviors of 3 columns are studied as given below:

(a) Interior Column – nearer to the core (C39)
(b) Interior Column – away from the core (C46)
(c) Exterior Column – periphery of the building (C53)

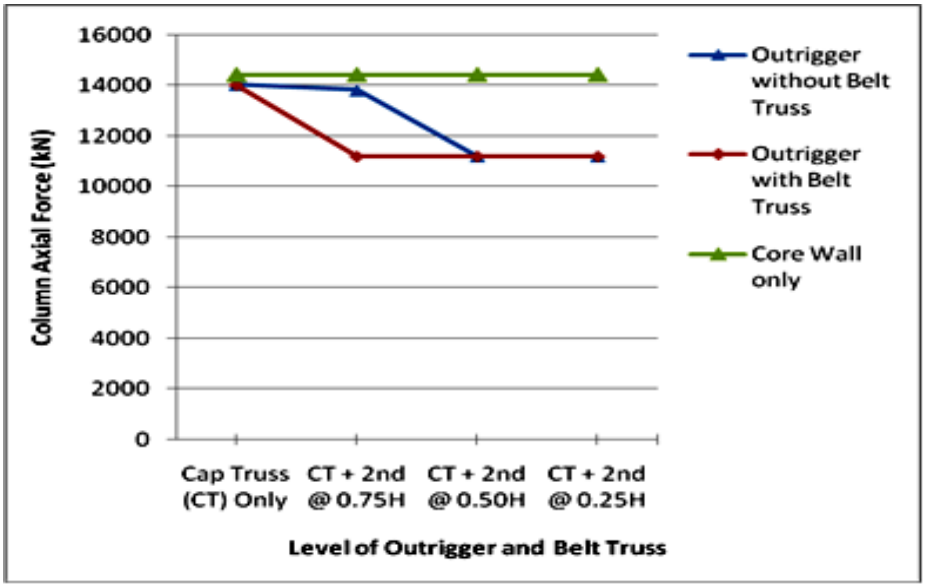

Fig. 15.a Compression forces in column(C39) for different levels of outrigger and belt truss.

From the above figure fig.15.a it is observed that the Inner columns are 2.76% and 2.85% less stressed than the building with core when compared to the cap truss with and without belt respectively.There is not much variation in the columns with respect to the position of second outrigger.

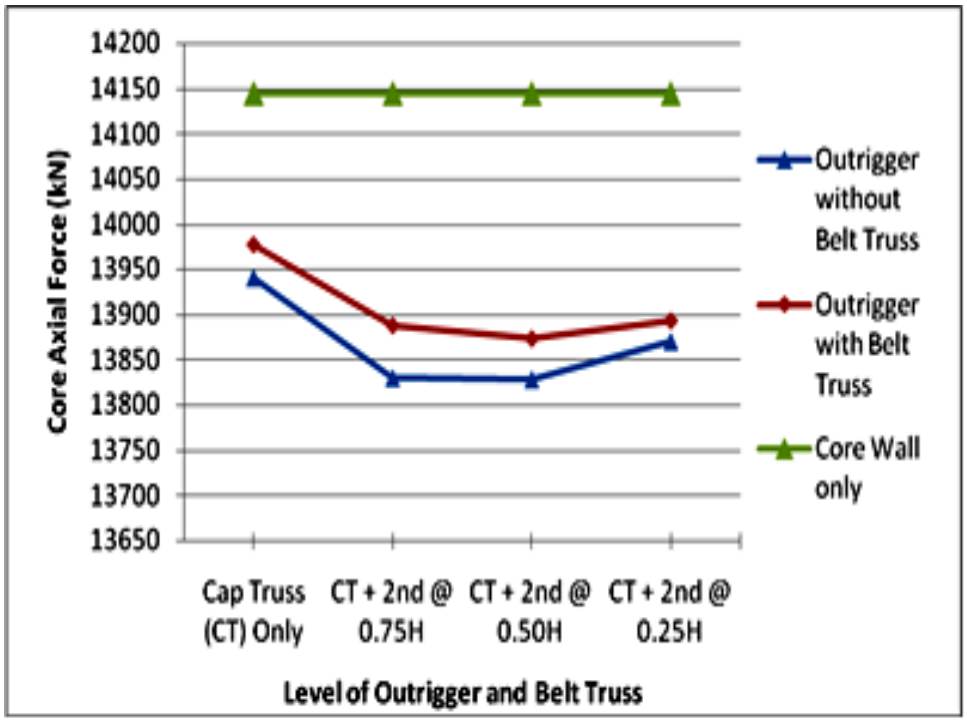

Fig. 15.b Compression forces in column(C46) for different levels of outrigger and belt truss.

From the above figure fig.15.b it is observed that the Inner columns are 1.44% and 2.24% less stressed than the building with core when compared to the cap truss with and without belt respectively. The optimum location of the outrigger system is proven to be at 0.5H, from the base.

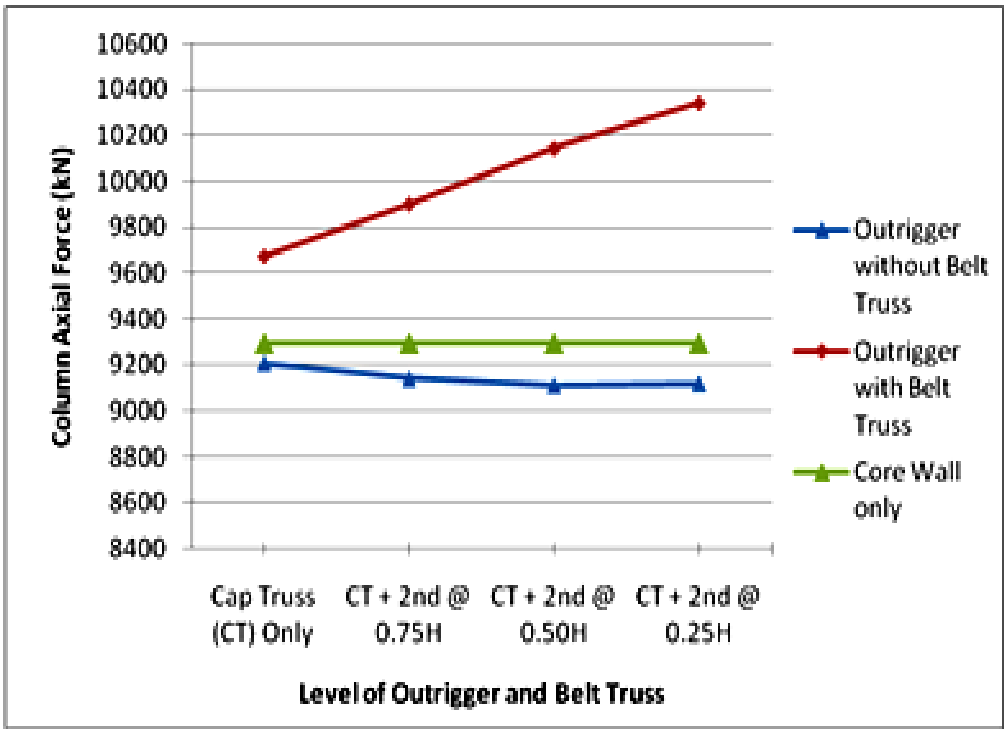

Fig.15.c Compression forces in column(C53) for different levels of outrigger and belt truss.

From the above figure fig.15.c it is observed that the columns are proven to be more stress in case of (cap truss) outrigger or belt truss system at bottom floor only.The columns seems to be lightly stress in case of second outrigger provided with the cap truss.

5.3 moments

Another very important factor that is monitored is the moments along the height of the concrete core. The moments that were monitored as shown in figure 5.3 and are

1. The moments below the first outrigger (cap truss).
2. The moments above the second outrigger.
3. The moment below the second outrigger.
4 . The core base moments.

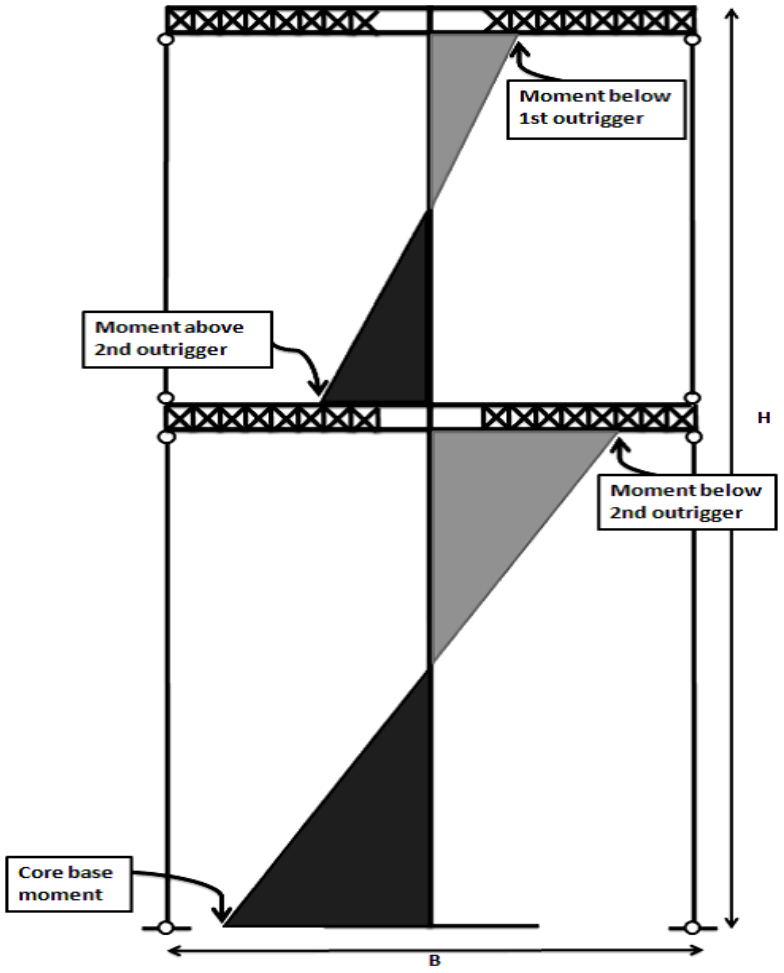

Fig. 16 The typical behaviour of a system with very stiff concrete core along with outrigger and belt truss.

V. CONCLUSIONS

The following conclusions are made from the present study

1. The use of outrigger and belt truss system in high-rise buildings increase the stiffness and makes the structural form efficient under lateral load.
2. The maximum drift at the top of structure when only core is employed is around 50.63 mm and this is reduced by suitably selecting the lateral system. The placing of outrigger at top storey as a cap truss is 48.20 mm and 47.63 mm with and without belt truss respectively. Hence there are not much reductions in drift with belt truss.
3. Using second outrigger with cap truss gives the reduction of 18.55% and 23.01% with and without belt truss. The optimum location of second outrigger is middle height of the building.
4. It can be conclude that the optimum location of the outrigger is between 0.5 times its height.

REFERENCES

[1] Indian Standard Code of Practice for Design Loads (other than earthquake) For Buildings And Structures, Part – 2 Live Loads, IS: 875 (Part 2) – 1987 (Second Revision), Bureau of Indian Standards, New Delhi, India.

[2] Indian Standard Code of Practice for Design Loads (other than earthquake) For Buildings And Structures, Part – 3 Wind Loads, IS: 875 (Part 3) – 1987 (Second Revision), Bureau of Indian Standards, New Delhi, India.

[3] Indian Standard Criteria for Earthquake Resistant Design of Structures, IS: 1893 (Part 1) 2002, Part 1 General Provisions and Buildings (Fifth Revision), Bureau of Indian Standards, New Delhi, India.

[4] Taranath, B. S , Steel concrete and composite design of tall buildings (Second Edition, Mc Graw – Hill Publications, 2001)

[5] Taranath, B. S, Wind and earthquake resistant buildings; structural analysis and design.(Second Edition, Mc Graw – Hill Publications, 1988)

[6] Smith, B. S. and Alex Coull, Tall building structures; Analysis and Design (John Wiley & Sons Inc, 1991)

[7] Moudarres, F.R , Outrigger Braced Coupled Shear Walls, Journal of Structural Engineering, ASCE, Vol. 110, No. 12, 1984.

[8] Alex Coull and Otto Lau.W.H , Multi Outrigger Braced Structures, Journal of Structural Engineering, ASCE, Vol. 115, No. 7, 1989.

[9] Shankar Nair, R , Belt Trusses and Basements as Virtual Outriggers for Tall Buildings, Engineering Journal , Fourth Quarter, Amercian journal of steel construction, 1998.

[10] Gerasimidis S., Efthymiou E. and Baniotopoulos C. C, Optimum outrigger locations for high rise steel buildings for wind loading, EACWE 5 Florence, Italy,19th – 23rd July 2009.

[11] Herath, N., Haritos, N., Ngo, T., and Mendis, P. (2009), Behavior of Outrigger Beams in High Rise Buildings under Earthquake Loads, Australian Earthquake Engineering Society Conference, 2009.

[12] Y. Chen, D. M. Mc Farland, Z. Wang, B. F. Spencer, J. R. L. A. Bergman "Analysis of tall buildings with damped outriggers, Journal of structural engineering, ASCE, 136(11), 1435-1443.

[13] Computer programming by Ali Lame.

American Journal of Engineering Research (AJER)
e-ISSN : 2320-0847 p-ISSN : 2320-0936
Volume-02, Issue-08, pp-90-107
www.ajer.org

Research Paper Open Access

Investigation of Brazed Plate Heat Exchangers With Variable Chevron Angles

S. Muthuraman
Professor, Higher College of Technology, Oman

Abstract: - Experiments to measure the condensation heat transfer coefficient and the pressure drop in brazed plate heat exchangers (BPHEs) were performed with the refrigerants R410A and R22. Brazed plate heat exchangers with different chevron angles of 45°, 35°, and 20° were used. Varying the mass flux, the condensation temperature, and the vapor quality of the refrigerant, we measured the condensation heat transfer coefficient and the pressure drops. Both the heat transfer coefficient and the pressure drop increased proportionally with the mass flux and the vapor quality and inversely with the condensation temperature and the chevron angle.

Keywords*: Compact heat exchanger, narrow channel, corrugation, CFD, Nusselt number, pressure drop, condensation, brazed plate heat exchanger, R410a, chevron angle, correlation.*

I. INTRODUCTION

Plate heat exchangers (PHEs) were introduced in the 1930s and were almost exclusively used as liquid/liquid heat exchangers in the food industries because of their ease of cleaning. Over the years, the development of the PHE has generally continued towards larger capacity, as well as higher working temperature and pressure. Recently, a gasket sealing was replaced by a brazed material, and each thermal plate was formed with a series of corrugations (herringbone or chevron). These greatly increased the pressure and the temperature capabilities.

The corrugated pattern on the thermal plate induces a highly turbulent fluid flow. The high turbulence in the PHE leads to an enhanced heat transfer, to a low fouling rate, and to a reduced heat transfer area. Therefore, PHEs can be used as alternatives to shell-and-tube heat exchangers. Due to ozone depletion, the refrigerant R22 is being replaced by R410A (a binary mixture of R32 and R125, mass fraction 50 %/50 %). R410A approximates an azeotropic behavior since it can be regarded as a pure substance because of the negligible temperature gliding. The heat transfer and the pressure drop characteristics in PHEs are related to the hydraulic diameter, the increased heat transfer area, the number of the flow channels, and the profile of the corrugation waviness, such as the inclination angle, the corrugation amplitude, and the corrugation wavelength. These geometric factors influence the separation, the boundary layer, and the vortex or swirl flow generation. However, earlier experimental and numerical works were restricted to a single-phase flow. Since the advent of a Brazed PHE (BPHE) in the 1990s, studies of the condensation and/or evaporation heat transfer have focused on their applications in refrigerating and air conditioning systems, but only a few studies have been done. Much work is needed to understand the features of the two-phase flow in the BPHEs with alternative refrigerants. Xiaoyang *et al.*, [1] experimented with the two-phase flow distribution in stacked PHEs at both vertical upward and downward flow orientations. They indicated that non-uniform distributions were found and that the flow distribution was strongly affected by the total inlet flow rate, the vapor quality, the flow channel orientation, and the geometry of the inlet port Holger [2].Theoretically predicted the performance of chevron-type PHEs under single-phase conditions and recommended the correlations for the friction factors and heat transfer coefficients as functions of the corrugation chevron angles. Lee *et al.*, [3] investigated the characteristics of the evaporation heat transfer and pressure drop in BPHEs with R404A and R407C. Kedzierski [4] reported the effect of inclination on the performance of a BPHE using R22 in both the condenser and the evaporator. Several single-phase correlations for heat transfer coefficients and friction factors have been proposed, but few correlations for the two-phase flow have been proposed. Yan *et al.*, [5] suggested a correlation of condensation with a chevron

angle of 30 for R134a. Yan *et al*., reported that the mass flux, the vapor quality, and the condensation pressure affected the heat transfer coefficients and the pressure drops. Hieh and Lin [6] developed the correlations for evaporation with a chevron angle of 30 for R410A.

The main objective of this work was to experimentally investigate the heat transfer coefficients and the pressure drops during condensation of R410A inside BPHEs. Three BPHEs with different chevron angles of 45, 35, and 20 were used. The results were then compared to those of R22. The geometric effects of the plate on the heat transfer and the pressure drop were investigated by varying the mass flux, the quality, and the condensation temperature. From the results, the geometric effects, especially the chevron angle, must be considered to develop the correlations for the Nusselt number and the friction factor. Correlations for the Nusselt number and the friction factor with the geometric parameters are suggested in this study.

Experiments to measure the condensation heat transfer coefficient and the pressure drop in brazed plate heat exchangers (BPHEs) were performed with the refrigerants R410A and R22. Brazed plate heat exchangers with different chevron angles of 45°, 35°, and 20° were used. Varying the mass flux, the condensation temperature, and the vapor quality of the refrigerant, we measured the condensation heat transfer coefficient and the pressure drops. Both the heat transfer coefficient and the pressure drop increased proportionally with the mass flux and the vapor quality and inversely with the condensation temperature and the chevron angle.

Correlations of the Nusselt number and the friction factor with the geometric parameters are suggested for the tested BPHEs. In an effort to study and optimize the design of a plate heat exchanger comprising of corrugated walls with herringbone design, a CFD code is employed. Due to the difficulties induced by the geometry and flow complexity, an approach through a simplified model was followed as a first step. This simple model, comprised of only one corrugated plate and a flat plate, was constructed and simulated. The Reynolds numbers examined are 400, 900, 1000, 1150, 1250 and 1400. The SST turbulence model was preferred over other flow models for the simulation.

The case where hot water (60^{o}C) is in contact with a constant-temperature wall (20^{o}C) was also simulated and the heat transfer rate was calculated. The results for the simplified model, presented in terms of velocity, shear stress and heat transfer coefficients, strongly encourage the simulation of one channel of the typical plate heat exchanger, i.e. the one that comprises of two corrugated plates with herringbone design having their crests nearly in contact. Preliminary results of this latter work, currently in progress, comply with visual observations.

In recent years, compact heat exchangers with corrugated plates are being rapidly adopted by food and chemical process industries, replacing conventional shell-and-tube exchangers. Compact heat exchangers consist of plates embossed with some form of corrugated surface pattern, usually the chevron (herringbone) geometry[1].The plates are assembled being abutting, with their corrugations forming narrow passages. This type of equipment offers high thermal effectiveness and close temperature approach, while allowing ease of inspection and cleaning [1],[2]. In order to be able to evaluate its performance, methods to predict the heat transfer coefficient and pressure drop must be developed. In this direction, CFD is considered an efficient tool for momentum and heat transfer rate estimation in this type of heat exchangers.

The type of flow in such narrow passages, which is associated with the choice of the most appropriate flow model for CFD simulation, is still an open issue in the literature. Due to the relatively high pressure drop, compared to shell-and-tube heat exchangers for equivalent flow rates, the Reynolds numbers used in this type of equipment must be lower so as the resulting pressure drops would be generally acceptable[1]. Moreover, when this equipment is used as a reflux condenser, the limit imposed by the onset of flooding reduces the maximum Reynolds number to a value less than 2000[3]. Ciofalo et al.[4], in a comprehensive review article concerning modeling heat transfer in narrow flow passages, state that, for the Reynolds number range of 1,500-3,000, transitional flow is expected, a kind of flow among the most difficult to simulate by conventional turbulence models.

On the other hand, Shah & Wanniarachchi[1] declare that, for the Reynolds number range 100-1500, there is evidence that the flow is already turbulent, a statement that is also supported by Vlasogiannis et al.[5], whose experiments in a plate heat exchanger verify that the flow is turbulent for Re>650. Lioumbas et al.[6], who studied experimentally the flow in narrow passages during counter-current gas-liquid flow, suggest that the flow exhibits the basic features of turbulent flow even for the relatively low gas Reynolds numbers tested (500<Re<1200).Focke & Knibbe[7] performed flow visualization experiments in narrow passages with corrugated walls. They concluded that the flow patterns in such geometries are complex, due to the existence of secondary swirling motions along the furrows of their test section and suggest that the local flow structure controls the heat transfer process in such narrow passages.

The most common two-equation turbulence model, based on the equations for the turbulence energy k and its dissipation ε, is the k-ε model[8]. To calculate the boundary layer, either "wall functions" are used, overriding the calculation of k and ε in the wall adjacent nodes[8], or integration is performed to the surface,

using a "low turbulent Reynolds (*low-Re*) *k-ε*" model[9]. Menter & Esch[9] state that, in standard *k-ε* the wall shear stress and heat flux are over predicted (especially for the lower range of the Reynolds number encountered in this kind of equipment) due to the over prediction of the turbulent length scale in the flow reattachment region, which is a characteristic phenomenon occurring on the corrugated surfaces in these geometries. Moreover, the standard *k-ε*, model requires a course grid near the wall, based on the value of y^+=11 [9],[10], which is difficult to accomplish in confined geometries. The low-Re *k-ε* model, which uses "dumping functions" near the wall[8],[9], is not considered capable of predicting the flow parameters in the complex geometry of a corrugated narrow channel[4], requires finer mesh near the wall, is computationally expensive compared to the standard *k-ε* model and it is unstable in convergence.

An alternative to *k-ε* model, is the *k-ω* model, developed by Wilcox[11]. This model, which uses the turbulence frequency *ω* instead of the turbulence diffusivity *ε*, appears to be more robust, even for complex applications, and does not require very fine grid near the wall[8]. However, it seems to be sensitive to the free stream values of turbulence frequency *ω* outside the boundary layer. A combination of the two models, *k-ε* and *k-ω*, is the *SST* (Shear-Stress Transport) model, which, by employing specific "blending functions", activates the Wilcox model near the wall and the *k-ε* model for the rest of the flow[9] and thus it benefits from the advantages of both models. Some efforts have been made wards the effective simulation of a plate heat exchanger. Due to the modular nature of a compact heat exchanger, a common practice is to think of it as composed of a large number of unit *cells* (Representative Element Units, *RES*) and obtain results by using a single cell as the computational domain and imposing periodicity conditions across its boundaries[4],[12]. However, the validity of this assumption is considered another open issue in the literature [4].

II. EXPERIMENTAL FACILITY

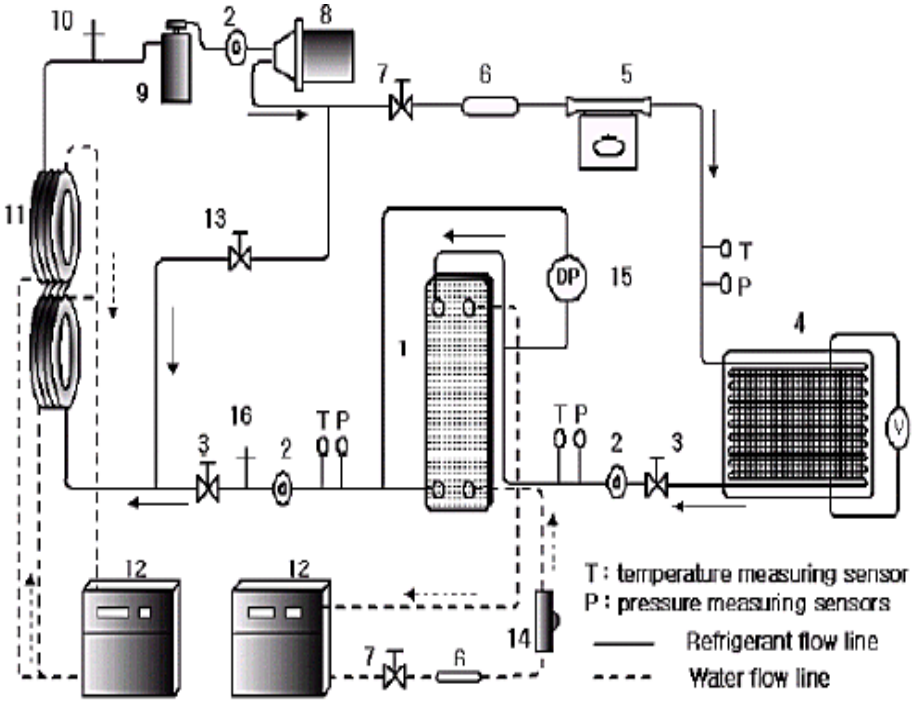

1. Plate heat exchanger	9. Liquid receiver
2. Sight glass	10. Charging port
3. On-off valve	11. Double-pipe heat exchanger
4. Pre-heater	12. Chiller
5. Mass flow meter	13. By-pass valve
6. Filter & dryer	14. Volumetric flow meter
7. Check valve	15. Differential pressure transducer
8. Magnetic gear pump	16. Discharge port

Fig. 1. Schematic diagram of the experimental system.

The experimental facility is capable of determining in plate heat transfer coefficients and measuring the pressure drops for the refrigerants. It consists of four main parts: a test section, a refrigerant loop, two water loops, and a data-acquisition system. A schematic of the test facility used in this study is shown in Figure-1, and detailed descriptions of the four main parts are mentioned below.

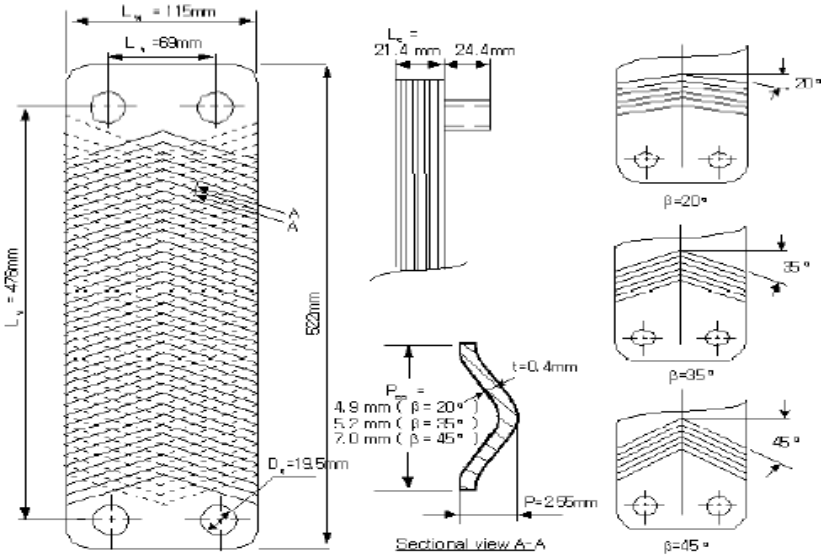

Fig. 2. Dimensions of the brazed plate heat exchangers.

1.1 Brazed plate heat exchangers

Three BPHEs with chevron angles of 45°, 35°, and 20° were used as the test sections. The angles of corrugation were measured from the horizontal axis. Each BPHE was composed of 4 thermal plates and 2 end plates, forming 5 flow channels. The dimensions of the BPHEs are shown in Figure-2. The refrigerant and cooling water were directed into the alternate passages between the plates through corner ports, creating counter flow conditions. The cooling water owed from the bottom to the top of every other channel on the basis of a central channel. On the other hand, the refrigerant owed from the top to the bottom in the rest of them.

1.2 Refrigerant loop

Refrigerant was supplied to the test section at specific conditions (i.e., temperature, flow rate, and quality) through the refrigerant loop. This loop contained a pre-heater, a double-pipe heat exchanger, a receiver, a magnetic gear pump, a differential pressure transducer, and a mass flow meter. Also included were thermocouples probes and pressure taps at the inlet/outlet of the test section. The refrigerant pump was driven by a DC motor which was controlled by a variable DC output motor controller.

The refrigerant flow rate was measured by using a mass flow meter installed between the magnetic gear pump and the pre-heater with an accuracy of _0.5 %. The pre-heater located before the test section was used to evaporate the refrigerant to a specified vapor quality at the inlet of the test section. The pressure drop of the refrigerant owing through the test section was measured with the differential pressure transducer, to an accuracy of _0.25 kPa. The refrigerant through the test section was subcooled at a double-pipe heat exchanger by the water cooled by the chiller and went into a liquid receiver. The subcooled refrigerant returned to the magnetic gear pump and circulated through the refrigerant loop repeatedly. Calibrated T-type thermocouples were used to measure the temperatures of the refrigerant at the inlet/outlet of the test section. The entire loop was insulated with fiberglass to prevent heat transfer to the environment.

1.3 Water loop

There are two closed water loops in this facility. One is for determining the condensation heat flux at the test section. The other is for making the subcooled refrigerant state at two double-pipe heat exchangers before it enters the magnetic gear pump. The water flow rates of the test section were measured by using a turbine flow meter, and T-type thermocouples were installed to evaluate the gain of the heat flux of the water of the test section.

1.4 Data acquisition

The data were recorded by a computer-controlled data-acquisition system with 40 channels scanned at the speed of 30 data per minute. The temperature and the pressure of both fluids were continuously recorded, and the thermodynamic properties of the refrigerant were obtained from a computer program. After steady-state conditions had been reached in the system, all measurements were taken for 10 minutes.

III. DATA REDUCTION AND UNCERTAINTY ANALYSIS

The hydraulic diameter of the channel, D_h, is defined as

D_h= 4XChannel flow area/Wetted perimeter=$4bL_w/2L_w\emptyset$ (1)

Where is φ=1.17. This value is given by the manufacturer.

The mean channel spacing, b, is defined as

b = p - t; t= Plate Thickness (2)

and the plate pitch p can be determined as, N_t=Total Number of plates

$$p= L_c/N_t-1 \quad (3)$$

The procedures to calculate the condensation heat transfer coefficient of the refrigerant side are described below. At first, the refrigerant quality at the inlet of the test section (x_{in}) should be selected to evaluate the condensation heat at a given quality. Its value is calculated from the amount of heat given by a pre-heater, which is the summation of the sensible heat and the latent heat:

$Q_{pre}= Q_{sens}+ Q_{lat}$

$$= m_rC_{p,r}(T_{r,sat}-T_{r,pre,in}) + m_ri_{fg}x_{in} \quad (4)$$

The refrigerant quality at the inlet of the test section can be written as

$$X_{in} = 1/i_{fg} [Q_{pre}/m_r –C_{p,r} (T_{r, sat} – T_{r,pre,in})] \quad (5)$$

The power gained by the pre-heater is calculated by measuring the voltage and the current with a power meter. The change in the refrigerant quality inside the test section was evaluated from the heat transferred in the test section and the refrigerant mass flow rate (6)

$$\Delta x=x_{in}-x_{out}=Q_w/m_rXi_{fg} \quad (6)$$

The condensing heat in the test section was calculated from an energy balance with water:

$$Q_w=m_wC_{p,w}(T_{w,out}-T_{w,in}) \quad (7)$$

The heat transfer coefficient of the refrigerant side (hr) was evaluated from the following equation:

$$1/h_r= (1/U)-(1/h_{w)}-R_{wall} \quad (8)$$

The overall heat transfer coefficient was determined using the log mean temperature difference

$$U=Q_w/A \text{ X LMTD}$$

$$LMTD=(T_{r,out}-T_{w,in})-(T_{r,in}-T_{w,out})/\ln\{(T_{r,out}-T_{w,in})-(T_{r,in}-T_{w,out})\} \quad (9)$$

The heat transfer coefficient of the water side (h_w) was obtained by using Eq. (10). Equation (10) was developed from the single-phase water to water pre-tests by K_{im} [7]. If the least-squares method and the multiple regression method are used, the heat transfer coefficient of the water side is correlated in terms of the Reynolds number, the Prandtl number, and the chevron angle:

$$h_w=0.295(k_w/D_{Eq})Re^{0.64}Pr^{0.32}(\pi/2-\beta)^{0.09} \quad (10)$$

The thermal resistance of the wall is negligible compared to the effect of convection. For the vertical downward flow, the total pressure drop in the test section is defined as

$$\Delta P_{total}=\Delta P_{fr}+\Delta P_a+\Delta P_s+\Delta P_p \quad (11)$$

And ΔP_{total} is measured by using a differential pressure transducer. The two-phase friction factor, f, is defined as

$$\Delta P_{fr}=fL_vN_{cp}G^2_{Eq}/D_h\rho_f \quad (12)$$

The port pressure loss in this experiment was less than 1 % of the total pressure loss. The static head loss can be written as and it has a negative value for vertical downward flow. The acceleration pressure drop for condensation is expressed as

$$\Delta P_p=1.4G^2_p/(2\rho_m) \quad (13)$$

An uncertainty analysis was done for all the measured data and the calculated quantities based on the methods described by Moffat [9]. The detailed results of the uncertainty analysis are shown in Table-1.

Table 1. Estimated uncertainty

Parameters	Uncertainty
Temperature	±0.2 ^{0}C
Pressure	±4.7 Pa
Pressure Drop	±250 Pa
Water Flow Rate	±2%
Refrigerant mass flux	±0.5%
Heat flux of test section	±5.7%
Vapor Quality	±0.03
Heat Transfer coefficients of water side	±10.1%
Heat transfer coefficients of refrigerant	±9.1%

Where

$$G_p=4m_{Eq}/\pi D^2_p \quad (14)$$

And

$$(1/\rho_m) = (x/\rho_g) + [(1-x)/\rho_f]. \quad (15)$$

The equivalent mass flow rate, m_{eq}, is defined as

$$m_{eq} = m\,[1-x+x(\rho_f/\rho_g)^{0.5} \quad (16)$$

The port pressure loss in this experiment was less than 1% of the total pressure loss. The static head loss can be written as

$$\Delta P_s = \rho_m g L_v \quad (17)$$

And it has a negative value for vertical downward flow, The acceleration pressure drop for condensation is expressed as

$$\Delta P_a = -\,[(G^2_{eq}x/\rho_{fg})in - (G^2_{eq}x/\rho_{fg})_{out}] \quad (18)$$

IV. RESULTS AND DISCUSSIONS

The condensation heat transfer coefficients and the pressure drops of R410A and R22 were measured in three BPHEs with chevron angles of 20°, 35°, and 45° by varying the mass flux (13 - 34 kg/m^{2}s), the vapor quality (0.9 - 0.15), and the condensing temperature (20°C and 30°C) under a given heat flux condition (4.7 -5.3 kW/m^2). R22 was tested under identical experimental conditions for comparison with R410A.

4.1 Flow regime

Before the behaviors of heat transfer are considered, it is necessary to predict what flow regime exists at a given set of operating conditions. The detailed flow regime map for the PHE has not been proposed yet because of the difficulty of flow visualization. Vlasogiannis *et al*., [10] suggested the criterion of a two-phase flow regime for a PHE in terms of superficial liquid (jf) and vapor velocities (jg) by using water and air under adiabatic conditions. They only simulated a mixture of water and air as a two-phase fluid. According to their work, the flow patterns in a PHE are significantly different from those inside the vertical round tubes. They

detected 3 types of flow patterns. The first was a gas continuous pattern with a liquid pocket at flow water flow rates (jf < 0.025 m/s) over wide range of air flow rates.

The second was the slug flow pattern, which was detected at sufficiently high air (jg > 2 m/s) and water flow rates (jf > 0.025 m/s). Thirdly, the liquid continuous pattern with a gas pocket or a gas bubble at the high water flow rates (jf >0.1 m/s) and low air flow rates (jg < 1 m/s).According to the flow regime map proposed by Vlasogiannis *et al*., the expected flow pattern in this experimental study is the gas continuous flow pattern with liquid pockets. However, their flow regime map has a significant limitation for use since many important features, such as the phase-change, the heating or cooling conditions, the densities or specific volumes of the working fluids, the geometries of the PHEs, etc., were not considered in detail. According to the flow regime map proposed by Crawford *et al*. [11], which was developed for vertical downward flow in a round tube, all experimental flow patterns are located in the intermittent flow regime, but this flow regime can not represent the correct flow regime in a BPHE due to the different geometries.

4.2 Condensation heat transfer

Figure-3 shows the effects of the refrigerant mass flux, the chevron angle, and the condensation temperature on the averaged heat transfer coefficient for R410A. The term "averaged heat transfer coefficient" means the average of the heat transfer coefficients calculated by varying the quality of the refrigerant from 0.15 to 0.9, and the coefficients were obtained from Eq. (19):

$$H_{averged} = \Sigma h_{local} x_{local} / x_{local} \qquad (19)$$

Where h_l is the local heat transfer coefficient at the local vapor quality. The experimental results indicate that the averaged heat transfer coefficients vary proportionally with the mass flux and inversely with the chevron angles and the condensation temperature. The small chevron angle forms narrow pitches to the flow direction, creating more abrupt changes in the velocity and the flow direction, thus increasing the effective contact length and time in a BHPE. The zigzag flow increases the heat transfer, and the turbulence created by the shape of the plate pattern is also important in addition to the turbulence created by the high flow rates. Increasing the mass flux at a given condensation temperature showed that the differences in the averaged heat transfer coefficients were significantly enlarged with decreasing chevron angle. This indicates that a PHE with the small chevron angle is more effective at a large mass flux (Gc > 25 kg/m^{2}s) than at a small mass flux.

The averaged heat transfer coefficient of R410A decreases with increasing condensation temperature. The vapor velocity is a more influential factor than the liquid film thickness for the heat transfer. Vapor bubbles in the flow enhance the disturbance in the bubble wake as a turbulence promoter, and the turbulence induced by the vapor bubbles increases with the vapor velocity. Also, since the specific volume of the vapor increases with decreasing condensation temperature, the vapor velocity increases for a fixed mass flux and quality. The vapor velocity at 20°C is faster than that at 30°C. The rates of the averaged heat transfer coefficients between condensation temperatures of 20°C and 30°C increased 5 % for a chevron angle of 45°, 9 % for 35°, and 16 % for 20°. These results show that different chevron angles lead partly to different flow pattern. Thus, we may conclude that the flow regime map should be modified by geometric considerations. The heat transfer coefficients in the high-quality region (fast velocity region) are larger than those in the low-quality region (slow velocity region). As mentioned above, this happens because the vapor velocity is the dominant effect on the heat transfer mechanism.

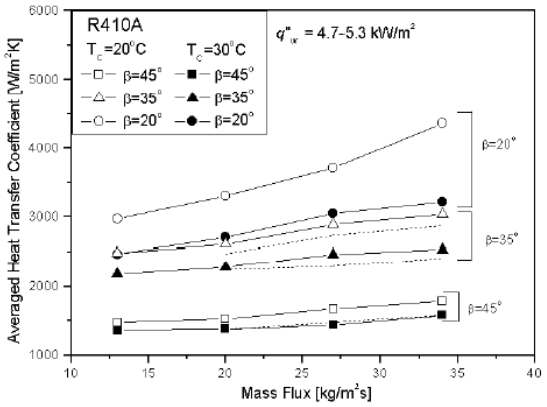

Fig. 3. Effect of mass flux on the averaged condensation heat transfer coefficient.

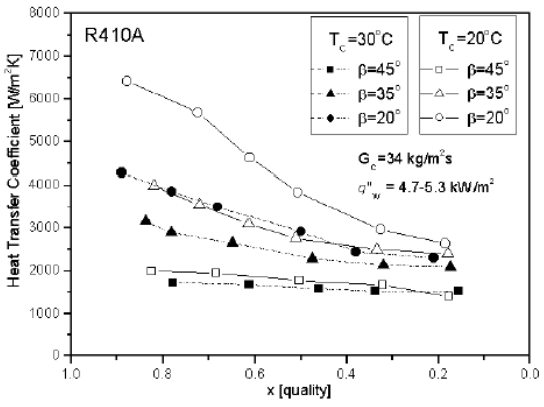

Fig. 4. Effect of quality on the condensation heat transfer coefficient.

Increasing the vapor quality at the same mass flux induces a faster bubble velocity, which increases the turbulence level and the convection heat transfer coefficient. The difference of heat transfer coefficients between the low-quality region and the high-quality region becomes larger with decreasing chevron angle. The PHE with a low chevron angle shows a better heat transfer performance in the high-quality region (i.e., the high vapor velocity region). Figure-4 also shows the variation of the heat transfer coefficients with the condensation temperatures. Like Figure-3, the heat transfer coefficients decreased with increasing condensation temperature. Also, the variations of the heat transfer coefficients with the condensation temperature are larger in the high-quality region. From the experimental results in Figures, 3 and 4, lowering the chevron angle and the condensation temperature gives the desired heat transfer effect.

4.3 Frictional pressure loss

The frictional pressure loss in a BPHE is obtained by subtracting the acceleration pressure loss, the static head loss, and the port pressure loss from the total pressure loss. Figure-5 shows the trend of the pressure drop along the mass flux, and Figure-6 shows the trend of the pressure drop along the quality at a mass flux of 34 kg/m^{2}s and a heat flux of 4.7-5.3 kW/m^2. The frictional pressure drops in the BPHEs increase with increasing mass flux and quality and decreasing condensation temperature and chevron angle. This trend is similar to that of the condensation heat transfer. As mentioned above, since the vapor velocity is much faster than the liquid velocity during the two-phase flow in the tube, the vapor velocity is the dominant influence on the pressure drop, as well as the heat transfer. A high vapor velocity also tends to increase the turbulence of the flow. From Figures 3, 4, 5 and 6, we may concluded that since the trends of the the condensation heat transfer and the pressure loss in BPHEs are similar, those effects must be carefully considered in the design of a BPHE.

4.4 Comparison of R410A with R22

The ratios of R410A to R22 for the condensation heat transfer coefficients and pressure drops at a condensation temperature of 30°C are shown in the Figure-7. The ratios for the heat transfer coefficients are relatively constant in the range of 1 -1.1, regardless of the mass flux, while the ratios for the pressure drops decrease with increasing mass flux, except for the data at a chevron angle of 20° in the present experimental range. For a chevron angle of 20°, the heat transfer ratios of R410A to R22 are about 1.1, and the pressure drop ratios about 0.8, which is a 10 % higher heat transfer and a 20 % lower pressure drop.The smaller specific volume of the vapor of R410A relative to that of R22 makes the vapor velocity slower and yields a small pressure drop under the same conditions of the mass flux. While the two fluids have almost equal values of their latent heats, the liquid-phase thermal conductivity of R410A is larger than that of R22. The higher thermal conductivity for R410A helps to produce better heat transfer even if a reduction in the specific volume occurs. Also, a BPHE with a small chevron angle is known to have more effective performance from the ratios when replacing R22 with R410A.

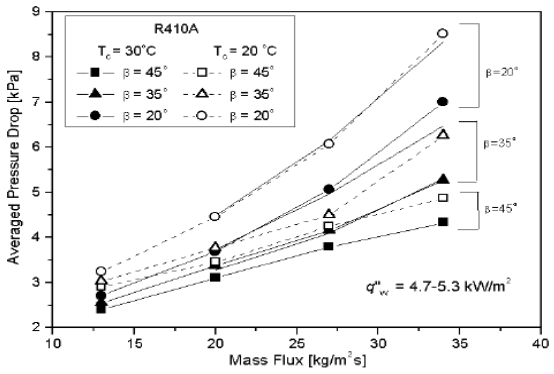

Fig. 5. Variation of the averaged condensation pressure drop with mass flux.

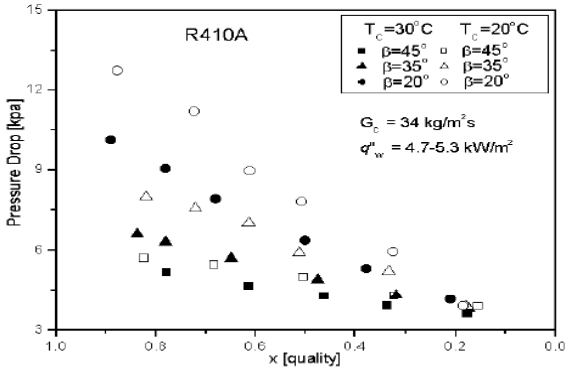

Fig. 6. Variation of the condensation pressure drop with quality.

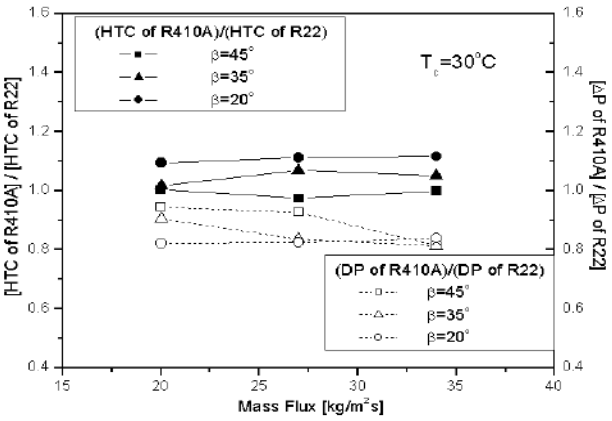

Fig. 7. Condensation heat transfer coefficient ratio and pressure drop ratio between R410A and R22.

4.5 Correlations of Nusselt number and friction factor for tested BPHEs

Based on the experimental data, the following correlations for Nu and f during condensation for the tested BPHEs are established: Where G_{e1}, G_{e2}, G_{e3}, and G_{e4} are non-dimensional geometric parameters that involve the corrugation pitch, the equivalent diameter, and the chevron angle. Re_{Eq} is the equivalent Reynolds number, and G_{Eq} the equivalent mass flux: where G_c is the channel mass flux. The suggested correlations for the Nusselt number and the friction factor can be applied in the range of Re_{Eq} from 300 to 4000. Figure-8(a) shows a comparison of the Nusselt number among the experimental data, the correlation proposed in this paper, and the correlation of Yan *et al.*, [5]. The correlation of Yan *et al.*, is

$$N_u = G_{e1} Re_{Eq}^{Ge1} Pr^{1/3} \quad (20)$$

$$Ge_1 = 11.22\,(p_{co}/D_h)^{-2.83}\,(\Pi/2-\beta)^{-4.5} \quad (21)$$

$$Ge_2 = 0.35\,(p_{co}/D_h)^{0.23}\,(\Pi/2-\beta)^{1.48} \quad (22)$$

$$f = Ge_3 Re_{Eq}^{Ge4} \quad (23)$$

$$Ge_3 = 3521.1\,(p_{co}/D_h)^{4.17}\,(\Pi/2-\beta)^{-7.75} \quad (24)$$

$$Ge_4 = -1.024\,(p_{co}/D_h)^{0.0925}\,(\Pi/2-\beta)^{-1.3} \quad (25)$$

$$Re_{Eq} = G_{Eq} D_h / \mu_f \quad (26)$$

$$G_{Eq} = G_c[1-x+x(\rho_f/\rho_g)^{1/2} \quad (27)$$

$$G_c = m / N_{ep} b L_w \quad (28)$$

and is obtained from one PHE with a chevron angle of 30° for R134a. Regardless of the BPHE types and refrigerants, most of the experimental data are within 20 % for the correlation proposed in this paper.

The correlation of Yan *et al.*(5), matched the data relatively well for β: 20 and 35 within30 %, but over-predicted the data quite a bit for 45. This discrepancy results from the correlation of Yan *et al.*, being developed for only a +30 PHE. Also,the correlation of Yan *et al.*

$$Nu = 4.118 Re_{eq}^{0.4} Pr^{1/3} \quad (29)$$

for the Nusselt number only adopted the equivalent Reynolds number and Prandtl number without any geometric parameters. Because a BPHE has a strong geometric effect, the correlation with geometric parameters must be developed for general applications. The root-mean-square (r.m.s.) of the deviations is defined as

$$\text{r.m.s.} = \sqrt{1/N_{data}\,\Sigma(Nu_{pred} - Nu_{exp}/Nu_{exp})^2 \times 100(\%)} \quad (28)$$

The r.m.s. deviation for the correlation of Yan *et al.*, [Eq. (29)] is 50.2 % and for Eq. (20), it is only 10.9 %. Figure-8(b) shows a comparison of the friction factor between the experimental data and the proposed

correlation. Similar to the correlation of the Nusselt number, the correlation of the friction factor includes the equivalent Reynolds number and the geometric parameters. Regardless of the BPHE types and refrigerants, most of the experimental data are within 15 % of the correlation proposed in this paper; the r.m.s. deviation for Eq. (23) is 10 %.

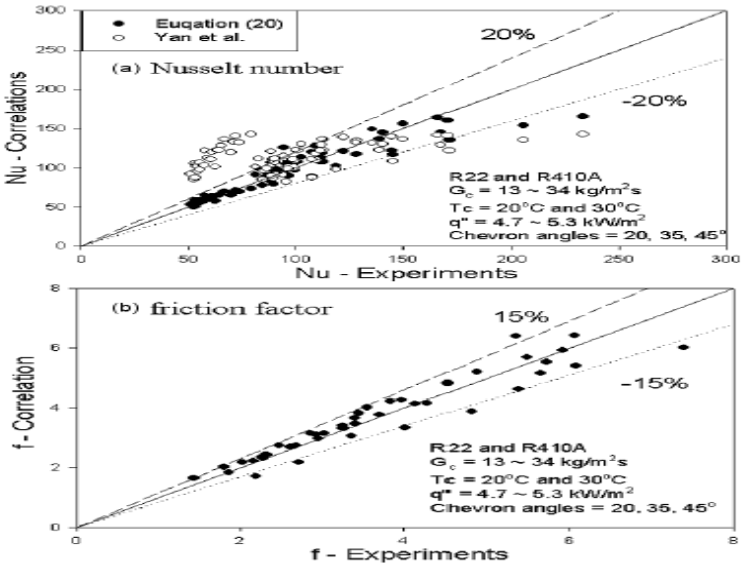

Fig. 8. Comparison of the correlations with the experimental data.

V. 5. STUDY OF A SIMPLIFIED GEOMETRY

In an effort to simulate the flow configuration, a ***simple*** channel was designed and constructed in order to conduct experiments and obtain formation on the flow pattern prevailing inside the furrows of the conduit. The flow configuration, apart from affecting the local momentum and heat transfer rates of a plate heat exchanger, suggests the appropriate flow model for the CFD simulation. A module of a plate heat exchanger is a single pass of the exchanger, consisting of only two plates. The simple channel examined is a single pass made of Plexiglas (***Figure 9***). It is formed by only ***one*** corrugated plate comprised of fourteen equal sized and uniformly spaced corrugations as well as a flat plate and it is used for pressure drop measurements and flow visualization. Details of the plate geometry are presented in ***Table 2***. This model was chosen in an attempt to simplify the complexity of the original plate heat exchanger and to reduce the computational demands. The geometry studied in the CFD simulations (similar to the test section) is shown in ***Figure 10***. The Reynolds numbers examined are 400, 900, 1000, 1150, 1250 and 1400, which are based on the distance between the plates at the entrance (d=10mm), the mean flow velocity and the properties of water at 60°C. In addition to isothermal flow, heat transfer simulations are carried out for the same Reynolds numbers, where hot water (60°C) is cooled in contact with a constant-temperature wall (20°C). The latter case is realized in condensers and evaporators. Additionally, it is assumed that heat is transferred only through the corrugated plate, while the rest of the walls are considered adiabatic.

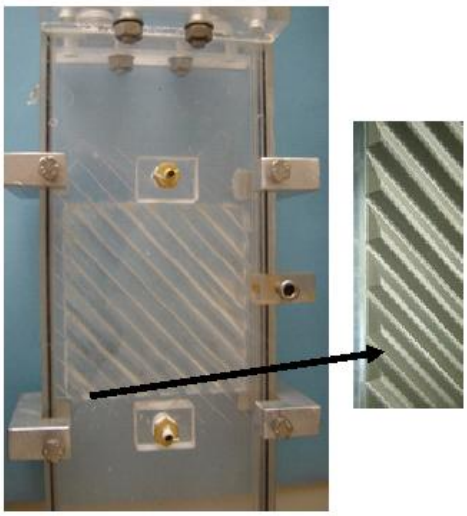

Figure 9 Simplified model and detail of the corrugated plate

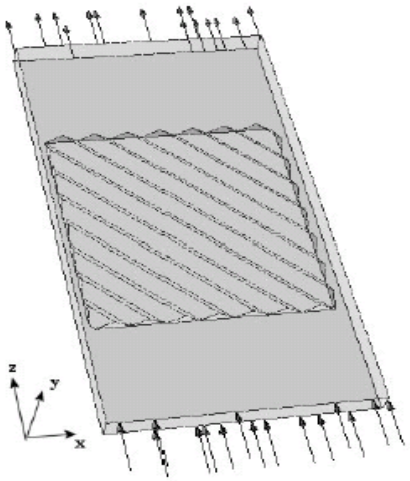

Figure 10 CFD model

A commercial CFD code, namely the *CFX ® 5.6* code developed by *AEA Technology*, was employed to explore its potential for computing detailed characteristics of this kind of flow. In general, the models used in CFD codes give reasonably good results for single-phase flow systems. The first step in obtaining a solution is the division of the physical domain into a solution mesh, in which the set of equations is discretised.

The grid size used is selected by performing a grid dependence study, since the accuracy of the solution greatly depends on the number and the size of the cells. The resulting mesh was also inspected for inappropriate generated cells (e.g. tetrahedral cells with sharp angles) and fixed, leading to a total number of 870,000 elements. The *SST* model was employed in the calculations for the reasons explained in the previous chapter. The mean velocity of the liquid phase was applied as boundary condition at the channel entrance (i.e. Dirichlet BC on the inlet velocity) and no slip conditions on the channel walls. A constant temperature boundary condition was applied only on the corrugated wall, whereas the rest of the walls are considered adiabatic. Calculations were performed on a *SGI O2* R10000 workstation with a 195MHz processor and 448Mb RAM. The *CFX ®5.6* code uses a finite volume method on a non-orthogonal body-fitted multi-block grid. In the present calculations, the *SIMPLEC* algorithm is used for pressure-velocity coupling and the *QUICK* scheme for discretisation of the momentum equations [31],[32].

Table 2 Simple Channel's plate geometric characteristics

Plate Length	0.200 m
Plate width	0.110 m
Maximum spacing between plates	0.010 m
Number of corrugations	14
Corrugation angle	45 ^{o}
Corrugation pitch	0.005 m
Corrugation width	0.014 m
Plate length before and after corrugations	0.050 m
Heat transfer area	2.7 x 10 $^{-2}$ m^2

The results of the present study suggest that fluid flow is mainly directed inside the furrows and follows them (***Figure 11a***). This type of flow behavior is also described by Focke & Knibbe[7], who made visual observations of the flow between two superposed corrugated plates ***(Figure 11b***). They confirm that the fluid, after entering a furrow, mostly follows it until it reaches the side wall, where it is reflected and enters the anti-symmetrical furrow of the plate above, a behavior similar to the one predicted by the CFD simulation. It seems that, in both cases, most of the flow passes through the furrows, where enhanced heat transfer characteristics are expected.

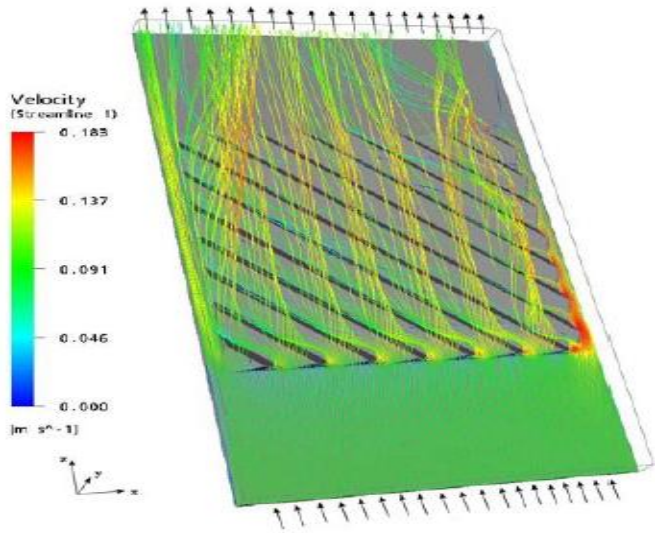

figure 11.a Typical flow pattern for the: a) simple channel, CFD results, Re=900

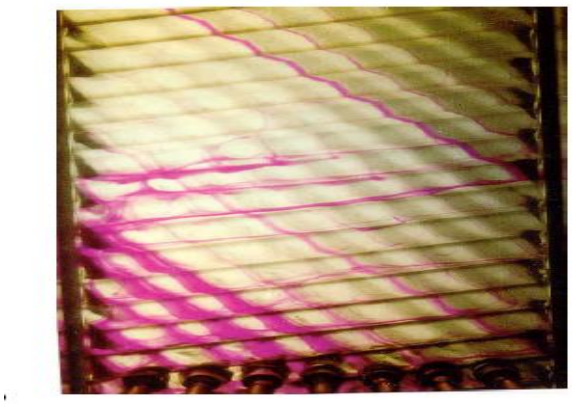

Figure 11.b) Flow visualization by Focke & Knibbe[7], Re=125

Figure 12 shows details of the flow inside a furrow for the simple model, where swirling flow is identified. This secondary flow is capable of bringing new fluid from the main stream close to the walls, augmenting heat transfer rates. Focke & Knibbe[18], who performed visualization experiments in similar geometries, also describe this kind of swirling flow. The values of the *z*-component of shear stress (***Figure13a***) increase with the Reynolds number –as expected–and the maximum value occurs at the crests of the corrugations. It may be argued that, during gas-liquid counter-current flow in such geometries, the shear stress distribution tends to prevent the liquid layer from falling over the crest of the corrugations and to keep it inside the furrows. The visual observations of Paras et al.[14] seem to confirm the above behavior. The heat flux through the wall of the corrugated plate was calculated by the CFD code. In addition, the local Nusselt number was calculated (by a user-Fortran subroutine) using the expression:

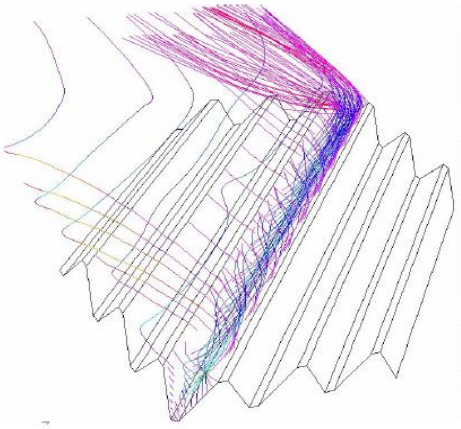

Figure 12 Swirling flow inside a furrow; Re=900

$$Nu_x = qd / (T_b - T_w)\, k \qquad (31)$$

Where *q'* is the local wall heat flux, *d* the distance between the plates at the entrance, *Tw* the wall temperature, *Tb* the local fluid temperature and *k* the thermal conductivity of the fluid. In addition to the local Nusselt number, mean Nusselt numbers were calculated as follows:

* A *mean Nu* calculated by numerical integration of the local *Nu* over the *corrugated* area ***only***, and
* An *overall* average *Nu* calculated using the total wall heat flux through the *whole* plate and the fluid temperatures at the channel entrance/exit.

The comparison of the values of the above Nusselt numbers shows that they do not differ more that 1%; therefore, the smooth part of the corrugated plate does not seem to influence the overall heat transfer. ***Figure 13b*** shows a typical local Nusselt number distribution over the corrugated wall for Re=900. All the Reynolds numbers studied exhibit similar distributions.

It is noticeable that local Nusselt numbers attain their maximum value at the top of the corrugations. This confirms the strong effect of the corrugations, not only on the flow distribution, but also on the heat transfer rate. To the best of author's knowledge, experimental values of heat transfer and pressure drop are very limited in the open literature for the corrugated plate geometry, since these data are proprietary. Therefore, the

data of Vlasogiannis et al.[16] were used to validate the simulation results. These data concern heat transfer coefficients measurements of both single (Re<1200) and two-phase flow in a plate heat exchanger with corrugated walls and a corrugation inclination angle of 60o. Heavner et al.[14] proposed a theoretical approach, supported by experimental data, to predict heat transfer coefficients of chevron-type plate heat exchangers. ***Figure14*** presents the experimental friction factors, obtained from the Plexiglas test section of ***Figure 9***, as well as the CFD predictions for the simple geometry studied, as a function of the Reynolds number. It appears that the experimental values follow a power law of the form:

$f = m\,Re^{-n}$ (32)

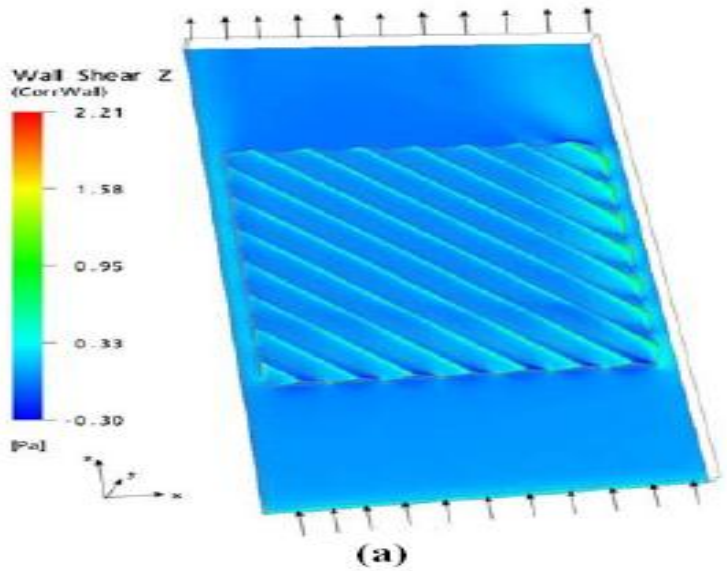

(a)

Figure 13. Typical results of the CFD simulation for Re=900; distributions of: (a) *z*-shear stress component

Where *m* and *n* constants with values 0.27 and 0.14 respectively. Heavner et al.[14] proposed a similar empirical correlation based on their experimental results on a single pass of a plate heat exchanger with 45o corrugation angle, but with two corrugated plates. In spite of the differences in geometry, it appears that the present results are in good agreement with the experimental data of Heavner et al.[14] (0.687 and 0.141 for the variables *m* and *n*, respectively).

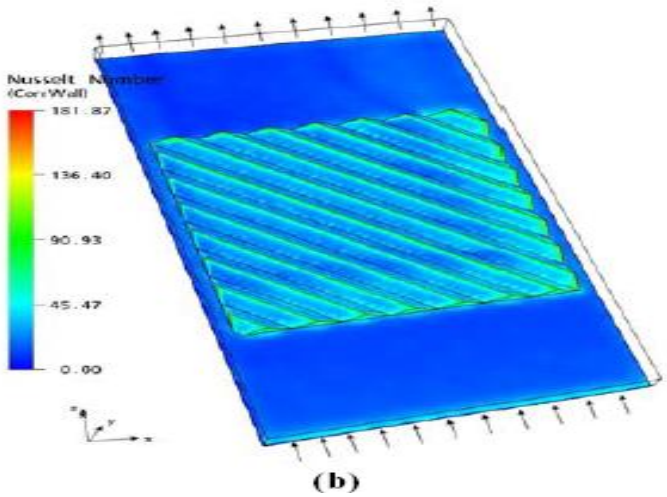

(b)

Figure 13. Typical results of the CFD simulation for Re=900; distributions of: (b) local Nusselt number

It must be noted that Focke et al.[15] , who also measured heat transfer coefficients in a corrugated plate heat exchanger having a partition of celluloid sheet between the two plates, reported that the overall heat transfer rate is the 65% of the corresponding value without the partition. ***Figure 15*** shows that the mean *j*-Colburn factor values calculated using the *overall* Nusselt number are practically equal to the 65% of the values measured by Vlasogiannis et al. This holds true for all Reynolds numbers except the smallest one (Re=400). In

the latter case the Nusselt number is greatly overpredicted by the CFD code. This is not unexpected, since the *two-equation turbulence* model is not capable to predict correctly the heat transfer characteristics for such low Reynolds number.The CFD results reveal that the corrugations enhance the heat transfer coefficient, whereas the pressure losses due to the augmentation of friction factor *f* are increased ***(Table 3)***, compared to a smooth-wall plate heat exchanger. Additionally, comparison of the normalized values of Nusselt number and the friction factor, with respect to the corresponding values for the smooth plate (*fsm*, *Nusm*), indicates that as the Reynolds number increases, heat transfer enhancement is slightly reduced, while the friction factor ratio, *f/f* , is increased. This is typical for plate heat exchangers with corrugations [16].

Table 3 Experimental values, calculated Nusselt numbers and normalised values of N_u and f

Re	Nu_{vlasog}	65% Nu_{vlasog}	Nu_{all}	Nu_{sm}	Nu_{ave}/ Nu_{sm}	F / f_{sm}
400	13.2	8.6	20.5	-	-	-
900	38.0	24.7	27.3	9.4	2.9	12.4
1000	41.2	26.8	28.6	10.2	2.8	12.8
1150	44.2	28.7	28.8	11.0	2.7	13.5
1250	46.8	30.4	30.9	11.7	2.7	13.9
1400	49.5	32.2	32.0	12.5	2.6	14.5

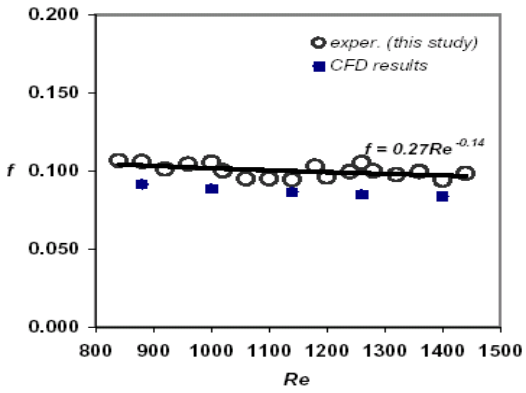

Figure 14. Comparison of friction factor predictions (CFD) with experimental data

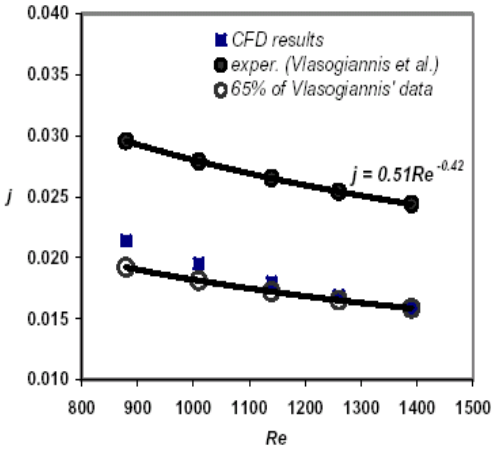

Figure 15. Comparison of *j*-Colburn factor predictions (CFD) with experimental data

VI. STUDY OF A HEAT EXCHANGER CHANNEL

The results for the simplified geometry confirm the validity of the CFD code and strongly encourage the simulation of a module (pass) consisting of two corrugated plates of a compact heat exchanger (***Figure16a***). In order to quantitatively evaluate the results of this simulation, the experimental setup of Vlasogiannis et al.[16]

was used as the design model (***Figure 16b***). Due to the increased computational demands, an AMD AthlonXP 1.7GHz workstation with 1GB RAM was used. The geometric characteristics of the new model are presented in ***Table 4.***

Table 4 Geometric characteristics of the model with two corrugated plates

Plate length	0.430 m
Plate width	0.100 m
Mean spacing between plates	0.024 m
Corrugation angles	60 ^{o}
Corrugation area length	0.352 m

Preliminary results of the present study, which is still in progress, are shown in ***Figure 17***. It is obvious that the herringbone design promotes a symmetric flow pattern (***Figure 16b***). Focusing on the left half of the channel (***Figure 17a***), a close-up of the flow streamlines (***Figure17b***) reveals a "*peacock-tail*" pattern as the liquid flows inside the furrows and over the corrugations. The same flow pattern, which is characteristic for this type of geometry, has also been observed by Paras et al.[14] in similar cross-corrugated geometries (***Figure17c***), where "dry areas" of ellipsoidal shape are formed around the points where the corrugations come into contact. The effect of fluid properties (e.g. surface tension, viscosity) on the shape and the extent of these areas, which are considered undesirable, will be examined in the course of this study.

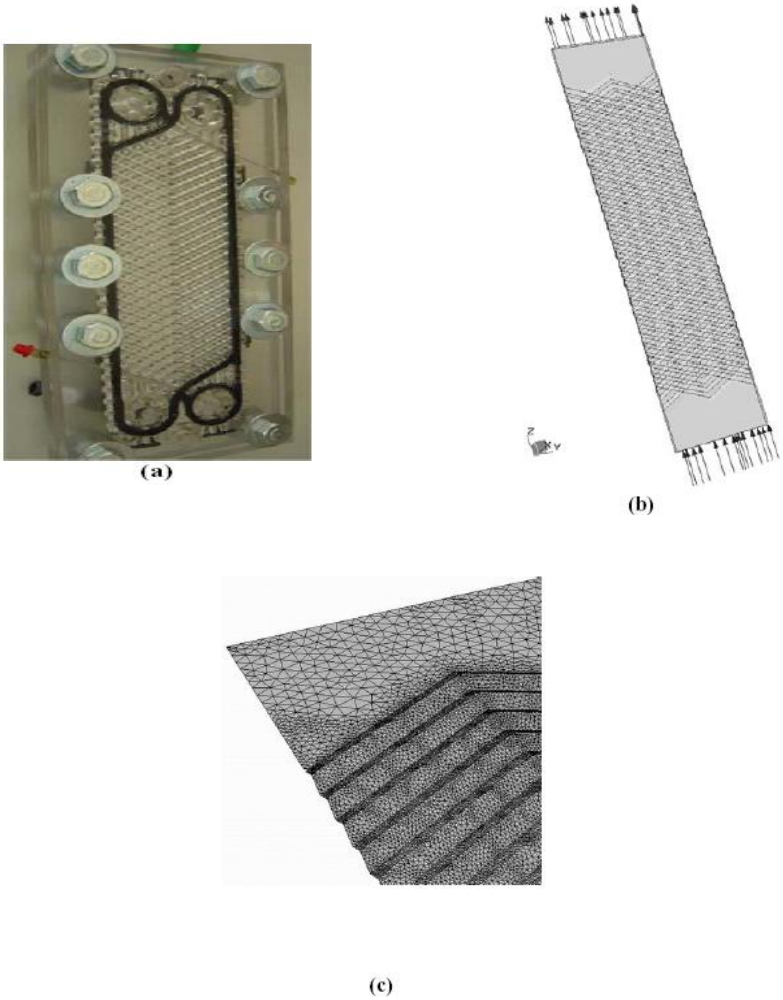

Figure 16. (a) Module of a corrugated plate exchanger; (b) The CFD model and (c) Detail of the grid distribution over the corrugated wall.

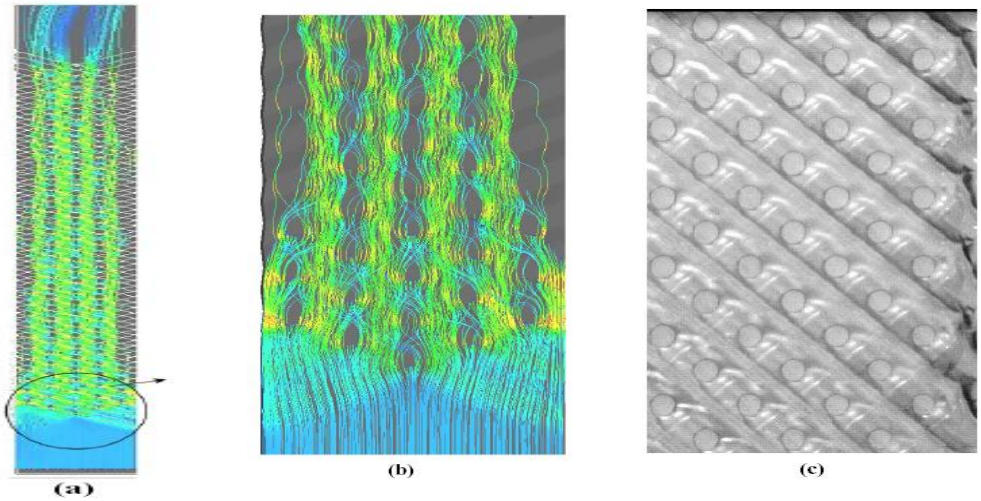

Figure 17. (a) Streamlines in the left half of the channel; (b) Close up of the flow pattern; (c) Photo of the flow in the cross-corrugated geometry [14]

VII. Conclusion

An experimental investigation has been conducted to measure the condensation heat transfer coefficient and the pressure drop of R410A and R22 in BPHEs with chevron angles of 20, 35, and 45 degrees. The experimental data were taken at two different condensation temperatures of 20°C and 30°C in the range of mass flux of 14-34 kg/m^{2}s with a heat flux of 4.7 -5.3 kW/m$^{2.}$

- Both the heat transfer coefficient and the pressure drop increased proportionally with the mass flux and the vapor quality and inversely with the condensation temperature and the chevron angle. Those effects must be carefully considered in the design of a BPHE due their opposing effects.
- A comparison of the data for R410A and R22 showed that the heat transfer coefficient for R410A was about 0 - 10 % larger and the pressure drop about 2- 21 % lower than those for R22. Therefore, R410A is a suitable alternative refrigerant for R22.

- Correlations for the Nusselt number and the friction factor with the geometric parameters were suggested for the tested BPHEs within 20 % (r.m.s. deviation: 10.9 %) for Nu and 15 % (r.m.s. deviation: 10 %) for f.

Although compact heat exchangers with corrugated plates offer many advantages compared to conventional heat exchangers, their main drawback is the absence of a general design method. The variation of their basic geometric details (i.e. aspect ratio, shape and angle of the corrugations) produces various design configurations, but this variety, although it increases the ability of compact heat exchangers to adapt to different applications, renders it very difficult to generate an adequate 'database' covering all possible configurations. Thus, CFD simulation is promising in this respect, as it allows computation for various geometries, and study of the effect of various design configurations on heat transfer and flow characteristics.

In an effort to investigate the complex flow and heat transfer inside this equipment, this work starts by simulating and studying a simplified channel and, after gaining adequate experience, it continues by the CFD simulation of a module of a compact heat exchanger consisting of two corrugated plates. The data acquired from former simulation is consistent with the single corrugated plate results and verifies the importance of corrugations on both flow distribution and heat transfer rate. To compensate for the limited experimental data concerning the flow and heat transfer characteristics, the results are validated by comparing the overall Nusselt numbers calculated for this simple channel to those of a commercial heat exchanger and are found to be in reasonably good agreement. In addition, the results of the simulation of a complete heat exchanger agree with the visual observations in similar geometries.

Since the simulation is computationally intensive, it is necessary to employ a cluster of parallel workstations, in order to use finer grid and more appropriate CFD flow models. The results of this study, apart from enhancing our physical understanding of the flow inside compact heat exchangers, can also contribute to the formulation of design equations that could be appended to commercial process simulators. Additional experimental work is needed to validate and support CFD results, and towards this direction there is work in progress on visualization and measurements of pressure drop, local velocity profiles and heat transfer coefficients in this type of equipment.

REFERENCES:

[1] X. Rong, M. Kawaji and J.G. Burgers, Two-phase header flow distribution in a stacked plate heat exchanger, *Proceedings ASME/JSME FED-Gas Liquid Flows* **225** (1995), pp. 115–122.

[2] H. Martin, 1996, A theoretical approach to predict the performance of chevron-type plate heat exchangers, Chemical Engineering and Processing: Process Intensification, Volume 35, Issue 4, Pages 301-310.

[3] G. J. Lee, J. Lee C. D. Jeon and O. K. Kwon. 1999. In: Plate Heat Exchanger with chevron angles ,Proceedings of the 1999 Summer Meeting of the SAREK, edited by C. S. Yim (SAREK, Nov.). p. 144.

[4] M. A. Kedzierski. 1997. Heat Exchanger Multiphase flow, Heat Transfer Engineering. Volume 5, issue 3 page 18: 25.

[5] Y. Y. Yan, H. C. Lio and T. F. Lin. 1999. Different Chevron angles in plate heat exchanger, of Heat and Mass Transfer. Volume 11, issue 4 pages 42: 93

[6] Y. Y. Hsieh and T. F. Lin. 2002.plate heat exchanger design theory, International journal of Heat and Mass Transfer. Volume 21, issue 9 pages 1033-45.

[7] Y. S. Kim. 1999. Plate heat exchanger design, M.S. Thesis. Yonsei University.

[8] S. Kakac and H. Liu. 1998. Heat Exchangers Selection, Rating and Thermal Design. CRC Press, Boca Raton. Volume 8, issue 9 pages 323-329

[9] R. J. Mo. 1982. Model of plate heat exchanger, ASME Journal of fluid engineering, Volume 11, issue 9 pages 173-179

[10] P. Vlasogiannis, G. Karajiannis. 2002. Compact heat exchangers, International journal Multiphase Flow.21, issue 9 pages 728: 757.

[11] T. J. Crawford, C. B. Weinberger and J. Weisman. 1985. heat exchangers International journal Multiphase Flow.21, issue 9 pages 291: 297.

[12] Shah, R.K., Wanniarachchi, A.S. (1991), Plate heat exchanger design theory, In: Buchlin, J.-M. (Ed.),Industrial Heat Exchangers, von Karman Institute Lecture Series 1991-04.

[13] Kays, W.M. & London, A.L. (1998), Compact heat exchangers, 3rd Ed. Krieger Publ. Co., Florida.

[14] Paras, S.V., Drosos, E.I.P., Karabelas, A.J, Chopard, F. (2001), "Counter-Current Gas/Liquid Flow Through Channels with Corrugated Walls–Visual Observations of Liquid Distribution and Flooding", World Conference on Experimental Heat Transfer, Fluid Mechanics & Thermodynamics, Thessaloniki, September 24-28.

[15] Ciofalo, M. Collins, M.W., Stasiek, J.A. (1998), Flow and heat transfer predictions in flow passages of air preheaters: assessment of alternative modeling approaches, In: Computer simulations in compact heat exchangers, Eds. B. Sunden, M.Faghri, Computational Mechanics Publ. U.K.

[16] Vlasogiannis, P., Karagiannis, G., Argyropoulos, P., Bontozoglou, V. (2002), "Air–water two-phase flow and heat transfer in a plate heat exchanger", Int. J. Multiphase Flow, 28, 5, pp. 757-772.

[17] Lioumbas, I.S., Mouza, A.A., Paras, S.V. (2002), "Local velocities inside the gas phase in counter current two-phase flow in a narrow vertical channel", Chemical Engineering Research & Design, 80, 6, pp. 667-673.

[18] Focke, W.W., Knibbe, P.G. (1986), "Flow visualization in parallel-plate ducts with corrugated walls", J.

[19] fluid Mech., 165, 73-77.

[20] Davidson, L. (2001), An Introduction to Turbulence Models, Department of Thermo and Fluid Dynamics, Chalmers University of Technology, Götemberg, Sweden.

[21] Menter, F., Esch, T. (2001), "Elements of Industrial Heat Transfer Predictions", 16th Brazilian Congress of Mechanical Engineering (COBEM), 26-30 Nov. 2001, Uberlandia, Brazil.

[22] AEA Technology (2003), CFX Release 5.6 User Guide, CFX International, Harwell, Didcot, UK.

[23] Wilcox,D(1988), "Reassessment of the scale-determining equation", AIAA Journal, 26,11.

[24] Mehrabian, M.A., Poulter, R. (2000), "Hydrodynamics and thermal characteristics of corrugated channels: computational approach", Applied Mathematical Modeling, 24**,** pp. 343-364.

APPENDIX

Nomenclature

A	heat transfer area of plate [m^2]
b	mean channel spacing [m]
C_p	constant pressure specific heat [J/kg K]
D	diameter [m]
f	friction factor
G	mass flux [kg/m^2s]

Ge	non-dimensional geometric parameter
g	gravitational acceleration [m/s^2]
h	heat transfer coefficient [W/m^{2}K]
i	enthalpy [J/kg]
j	superficial velocity [m/s]
L_c	distance between the end plates [m]
L_h	distance between the ports [m]
L_v	vertical length of the fluid path [m]
L_w	horizontal length of the plates [m]
LMTD	log mean temperature difference [°C]
m	mass flow rate [kg/s]
N_{cp}	number of channels for the refrigerant
N_{data}	total number of data
N_t	total number of plates
Nu	Nusselt number
Nu_{exp}	Nusselt number obtained from experiment
Nu_{pred}	Nusselt number obtained from correlation
p	plate pitch [m]
p_{co}	corrugation pitch [m]
Pr	Prandtl number [v]
Q	heat transfer rate [W]
q	heat flux [W/m^2]
Re	Reynolds number
T	temperature [°C]
t	plate thickness [m]
U	overall ht coefficient [W/m^2 K]
x	quality

Subscripts

a	acceleration
c	channel
Eq	equivalent
f	liquid
fg	difference the liquid phase and the vapor phase
fr	friction
g	vapor
in	inlet
lat	latent
m	mean
out	outlet
p	port
pre	pre-heater
r	refrigerant
s	static
sat	saturated
sens	sensible
w	water

American Journal of Engineering Research (AJER)
e-ISSN : 2320-0847 p-ISSN : 2320-0936
Volume-02, Issue-08, pp-108-114
www.ajer.org

Research Paper Open Access

Intelligent Power Economy System (Ipes)

Salman Afghani[1], Mehwish Iqbal[2], Tayyaba Sabir[3], Muhammad Ishfaq Javed[3]
[1,2,3,4] *(Electrical Engineering Department, Army Public College of Management and Sciences (APCOMS), Rawalpindi, Pakistan*

Abstract: - T This paper discusses an Intelligent Power Economy System which is an intelligent way of saving energy and it allows the user to allocate desired electrical power consumption and it also take care of the comfort level of the user. Intelligent Power Economy System (IPES) is very intelligent, compact, cost effective, and user-friendly device. IPES is truly intelligent because it has the ability to learn and can create a behavioural model of habitants of dwelling. It has a fully functional inference engine and knowledge base with 15 minute resolution and 14 days cycle is embedded into low end 8 bit microcontroller. IPES will provide a mean to move and work according to requirements and needs of the consumer. This system will take required input from the user and then regulates the power according to the mode selected i.e. Economy mode, Medium mode, Lavish mode. In this particular system user will be able to decide how much electricity he needs and it will be set by the user itself. Such system will be beneficial and conducive as we can set a required amount of power to be used at specific times.

Keywords: - *Compact, Intelligent, Cost Effective, User-Friendly, Controllers*

I. INTRODUCTION

Shortage of electricity is the major issue all over the world. This is the major motivation behind this research or project. Our Intelligent Power Economy System helps the individuals to control economy with no effects on comfort level. An individual using this system not only reduces the loss of energy but also make use of electrical power in economic way. Due to the instability in electrical power sector all over the world, we made efforts at grass root level to control this havoc and provide sufficient energy as is required. If this system saves 100 units a month from a house or industry etc then we can save many mega watts of electrical energy in a month and hence making shortfall of energy controllable and feasible.

Our proposed device is very intelligent and compact. IPES is intelligent in a way that it has the ability to learn and can capture behaviours and it can create a 14 days behavioural model and after 14 days it wil start repeating. This projects works on three modes and this system will take input from the user and then regulates the power according to the mode selected. Mode 1 will be Economy Mode and in this state less power will be consumed. Mode 2 will be Moderate Mode and this will give medium power. Mode 3 will be lavish mode and this will provide maximum or large amount of power when needed. Another feature of this device is that if it is not being used on regular basis then if mistakenly we forget to put the switch off, it will go off automatically after a preset interval of time. This enables us to keep record of consumption in our daily lives, participates in, or provides demand response solutions and services. By having information, customers could be assisted in to have knowledge of changes in energy usage from normal consumption patterns, either in response to changes in price or as incentives designed to encourage lower energy usage at times of peak demand periods or higher wholesale prices or during periods of low operational systems reliability. This system is not intended for hotels. This infrastructure includes software and hardware implementations to get the required work done. This system must be beneficial to use as it sets required amount of power to be used at specific times.

II. EXISTING SOLUTIONS

Shanty towns of South Africa have tough neighbourhoods; advance sensitive systems might not function in such towns. Specialized coins which are purchased from the market by the users to put their

electrical power on. The users insert their coins inside the machine kind of boxes that are placed outside their homes and as soon as the coin is placed inside the electricity is provided to their homes.

2. Smart Buildings In Rich Gulf States By LG:

These buildings are so intelligent that they are aware of the presence and needs of the habitants. Smart Building system allows operational monitoring and control of machinery, lighting, power equipment and provides facilities control from an alarm to responding according to the preset schedule in case of an event occurrence. It also provides analysis of energy consumption patterns and analyzes the collected information about various resources such as equipment, manpower, energy, supplies, etc which is needed for building management to improve the efficiency of maintenance and management tasks.

3. Project Oxygen: Pervasive, Human-Centric Computing – An Initial Experience:

[1]Project Oxygen is an intellectual efforts involving many research activities throughout the Laboratory for Computer Science (LCS) and the Artificial Intelligence Laboratory (AIL) at The Oxygen project's vision is to bring an abundance of computation and communication within easy reach of humans through natural perceptual interfaces of speech and vision so computation blends into peoples' lives enabling them to easily do tasks they want to do – collaborate, access knowledge, automate routine tasks and their environment. This project has a three-pronged approach by dividing the space into three broad categories: the H21, a hand-held device, the N21, an advanced network, and the E21, a sensor-rich environment (Figure 1).

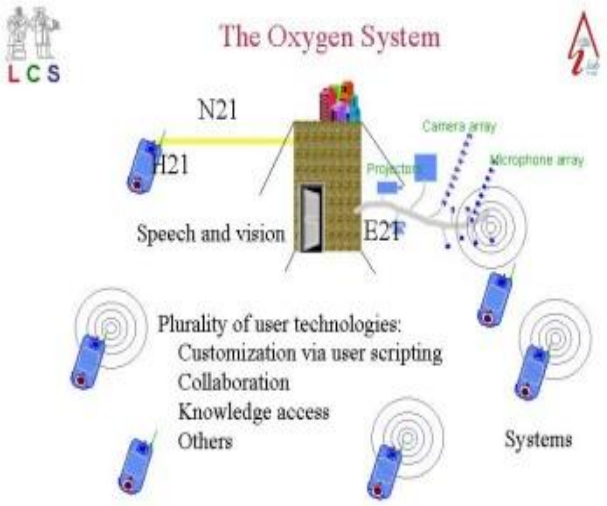

Figure 1: An overview of the Oxygen Infrastructure, showing the division into three parts: H21, a handheld digital device, N21, the network infrastructure, and E21, the environment infrastructure.

4. Honeywell Technology Solution Lab:

[2]HTSL Research group works with Honeywell product R&D groups and Honeywell Research Labs globally develops key technologies that enhance Honeywell products to benefit its customers. The computation and communication systems (CCS) lab concentrates on core research in the fields of computation systems with a primary focus on wireless system design. The Intelligence Vehicle Technologies group works on autonomous vehicle systems for various applications like Unmanned Air Vehicles, Mining, Agriculture, Smart transportation systems, Robot vehicles, Marine vessels, etc. The focus areas include navigation, perception sensing, guidance, x-by-wire controls, multi-sensor fusion, fault tolerance and reconfiguration, Smart communication and computing platforms with competencies ranging from multi-sensor fusion algorithms, Pattern Recognition, Machine Learning to Vision sensor processing techniques, etc. The Computer Vision and Image Analysis Group are dedicated to conducting basic and applied research in computer vision and image processing.

III. ARCHITECTURE OF THE SYSTEM

The basic knowledge used behind the whole architecture of Intelligent Power Economy System (IPES) is Learning and Automation. The basic technologies are Microcontroller Automation Design and Artificial Intelligence. Figure 2 and 3 shows the flow chart that gives a complete scenario of how the system will work, complete structure of learning and automation process.

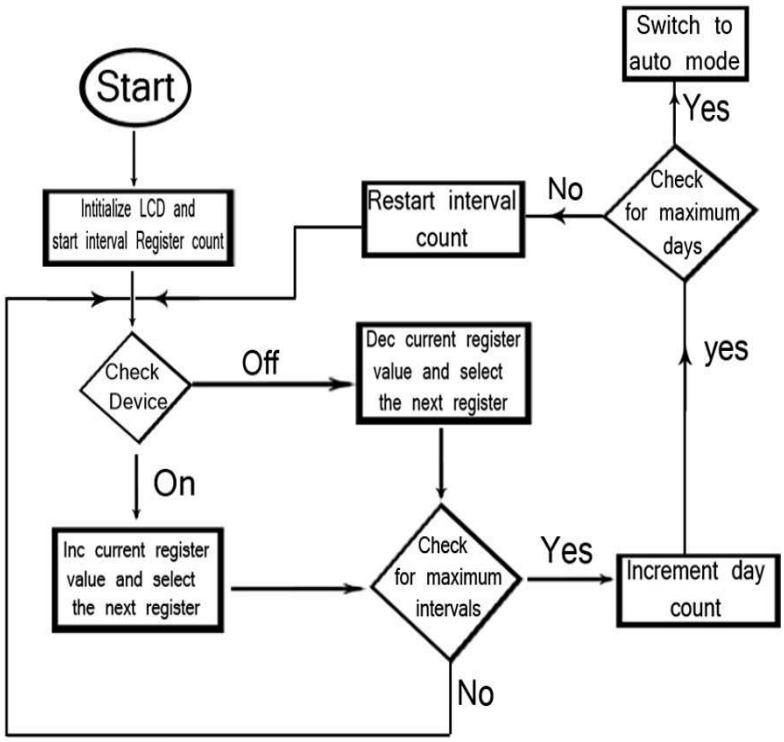

Figure 2: Learning Process

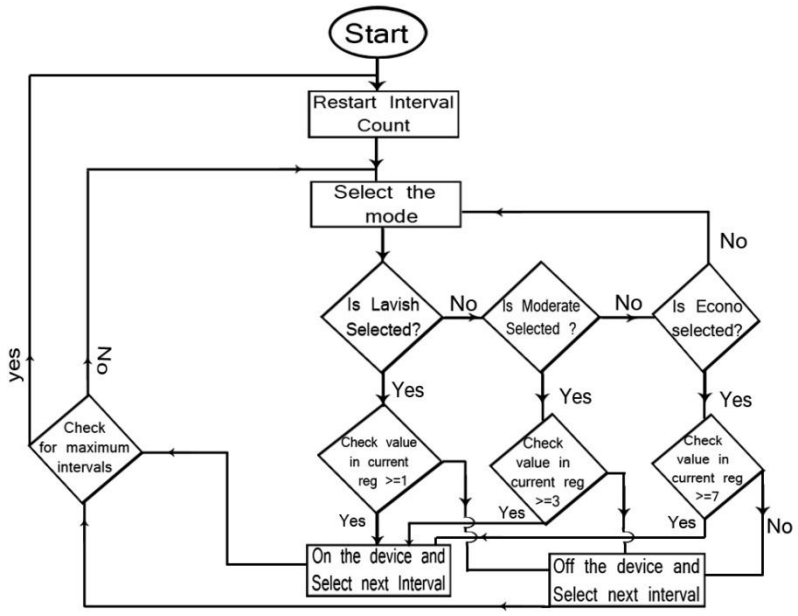

Figure 3: Automation Process

IV. SYSTEM DESIGN

Our proposed Intelligent Power Economy System (IPES) is an intelligent device. This device will get information from the user about his need of electricity at a particular time and place. After getting information it will provide electricity intelligently according to the priorities of the user. Its features are human interfaced, compact, user-friendly and cost effective.

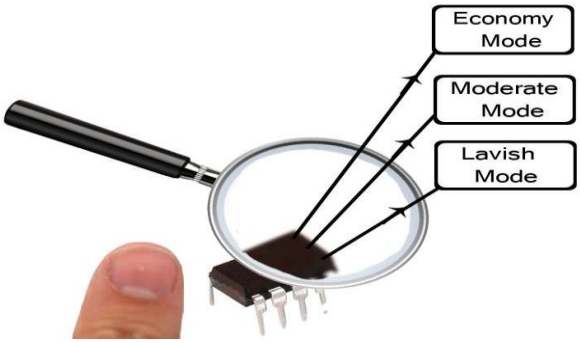

Figure 4: It shows the compactness of IPES device and describes the three modes.

1. Tri or Three State Switch:

This switch is very compact and its size is equivalent to the size of an IC on which all the three modes will be defined and it will be mounted in a room and it will work according to the Mode selected and LED will be attached to these modes which will indicate which mode is selected by the user. Mode 1 is the Economy mode and when it will be selected it will be indicated by red LED. Mode 2 is the Medium mode and is indicated by green LED. Mode 3 is the Lavish mode and is indicated by blue LED. After getting the mode selected from the switch the respective indication will be given by the LED and system will provide the electricity accordingly. This whole system will consist of an LED, Tri-state button and Processing Device. The system will be attached with appliances to regulate the power according to requirement.

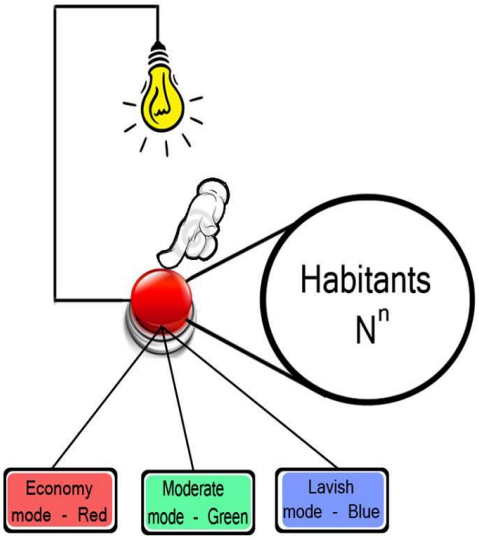

Figure 5: It shows that as soon the user will put this switch on the electricity will be switched on.

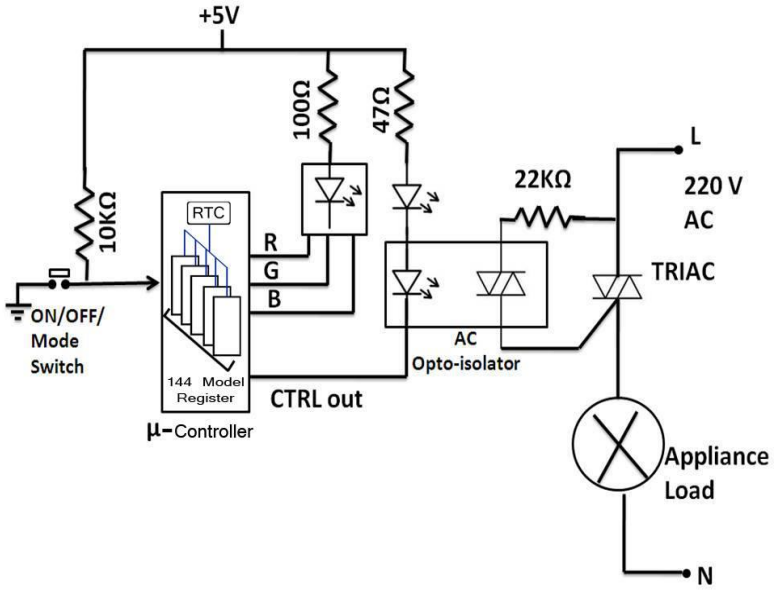

Figure 6: Hardware Implementation of IPES.

Figure 6 explains the complete hardware of IPES. The main components include microcontroller board, Opto-isolator for transfer of electrical signals using light. And a Triode for Alternating Current (TRIAC) that will conduct current, to which the appliances will be connected.

2. Inference Engine:

Inference engine is the branch of knowledge engineering and artificial intelligence; it is basically a computer program that derives answer from a knowledge base (Kb). There is no such thing as pure logic. Life at large is ambiguous and runs in chaos. Inference engine is a small device system that can capture the behaviour of people living in a house. There are two types of recognition techniques one class caters for physical appearance of human beings (bioinformatics) and second class deals with human behaviour (forensic science).

We have to record the different timings of usage of power from the user so it is important to have sequence of these intervals in which electricity will be used. When there will be a proper record of timings then it will be convenient for controller to run the corresponding code. Otherwise it will become troublesome for the system to operate efficiently.

The full mature model extracted by the inference engine is as follow:

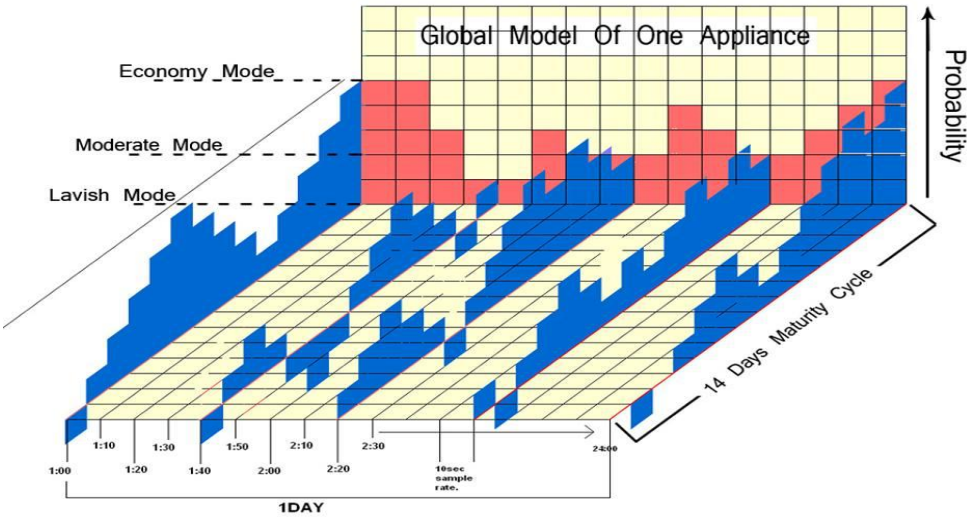

Figure 7: Model Extracted by the Inference Engine.

The inference engine derives the knowledge of usage of device in 14 days. The engine keeps the record of 1day and derives the next ones making the model mature enough to use the appliance accordingly.

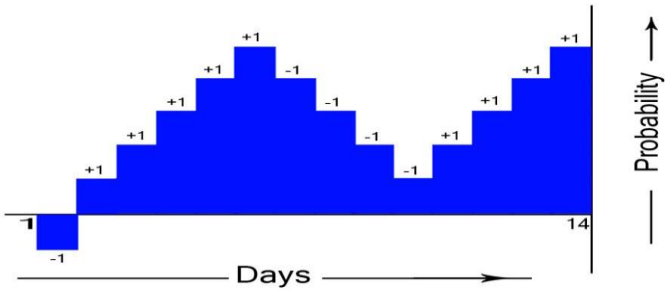

Figure 8: 14 Days maturity cycle graph

Inference engine derives the model by adding and subtracting the value of register if device is on and off respectively. Three modes of usage i.e. Economy, Medium, Lavish are set accordingly as the consumer uses the appliance.

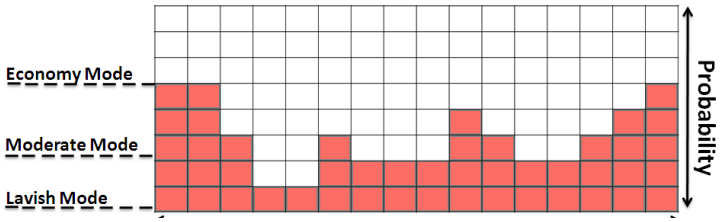

Figure 9: Global Model for One Appliance.

One day status of the appliance used by a consumer is given below. Intervals of 10mins are defined on which status of device is checked i.e. ON or OFF. So for one day we have 144 intervals of 10mins each. (+) sign indicates the ON status while, (-) sign indicates OFF status of device.

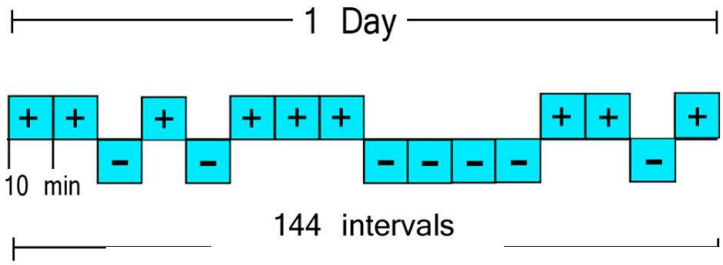

Figure 8: Daily Status (ON/OFF) of Appliance.

In the above diagram there are 144 Registers (Up/Down 8Bit Counters) are being used to accommodate running average of an appliance for each of the 144 segments of time in a day. Hence in 14 days each of the 144 registers holds the running average of an appliance for one of the 144 intervals in a day. And together the 144 registers form the "Global Model of an Appliance".

V. CONCLUSIONS

IPES is a very compact, cost effective, intelligent and user-friendly device. The user needs not to learn or think to use our proposed system (IPES). IPES will save energy intelligently and it will provide a mean to move and work according to the requirements and needs of the consumers. The system has three modes according to the electricity usage and modes are mode 1-economy mode, mode 2-medium mode, mode 3- lavish mode. The device itself has the capability to learn and capture behavior. The device will produce the behavioral model of 14 days and the cycle will repeat after then.

REFERENCES

[1] Rudolf, L. (2001) Project Oxygen: Pervasive, Human-Centric Computing – An Initial Experience,. Advance Information System Engineering, Switzerland.
[2] Honeywell energy efficient, innovative and productive company.
[3] Mark, D. (1998) Smart House And Home Automation Technologies,. Gross design machine group, Washington.
[4] Pipattanasomporn, M., Kuzlu, M and Rehman, S , An Algorithm for Intelligent Home Energy Management and Demand Response Analysis,. IEEE Transactions on Smart Grid.

AUTHORS

A Salman Afghani was born in 07/20/1958 in Pakistan and he is Professor, PhD, Advanced man machine systems, MPhil, Industrial automation, MS Mech Engg. He is working as HOD of R&D Department of Engineering Sciences at Army Public College of Management and Sciences (APCOMS), Rawalpindi Pakistan.

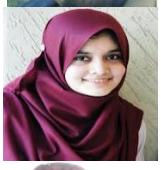

Mehwish Iqbal was born in 09/28/1990 in Pakistan. And she is Electrical Engineer with specialization in Telecommunication from Army Public College of Management and Sciences (APCOMS), Rawalpindi Pakistan.

Tayyaba Sabir was born in 10/27/1989 in Pakistan. And she is Electrical Engineer with specialization in Telecommunication from Army Public College of Management and Sciences (APCOMS), Rawalpindi Pakistan.

Muhammad Ishfaq Javed was born in 04/04/1989 in Pakistan. And he is Electrical Engineer with specialization in electronics from Army Public College of Management and Sciences (APCOMS), Rawalpindi Pakistan. He is working as Research Assistant in R&D Dept of Engineering and sciences APCOMS.

American Journal of Engineering Research (AJER)
e-ISSN : 2320-0847 p-ISSN : 2320-0936
Volume-02, Issue-08, pp-115-122
www.ajer.org

Research Paper Open Access

Studies on Relationship Between Water/Binder Ratio And Compressive Strength Of High Volume Fly Ash Concrete

Dr Sravana[1] Sarika.P[3] Dr.Srinivasa Rao[1] Dr.Seshadri Sekhar T [2] , Apparao.G[2] ,
[1] *Jawaharlal Nehru Technological University, College of Engineering, Hyderabad, Andhra Pradesh, India*
[2]*Professor , GITAM University*
3 Student, Dept of Civil Engineering, VNR&VJIET , Bachupally, Hyderabad.

Abstract: - Pozzolanic admixtures are generally being used along with the cement in concrete mixes so as to derive certain benefits like economy, durability, Chemical resistance in permeability etc. The use of high volumes of fly ash has become on of the current topics of research possibility promoted by the availability of a wide range of chemical and mineral admixtures. In the present experimental investigation fly ash has been used in large volumes as an additional ingredient in concrete mixes. The present experimental investigations was carried out to study the relationship between Water /Binder Ratio to Compressive strength of high volume fly ash concrete using fly ash as an additional material in the cement concrete. The studies have indicated that the high volumes fly ash used in concrete as an additional material would lead to enhanced properties in concrete and contribute towards development of high performance and high strength concrete which is the need of the hour.

Keywords: - *Water/Binder Ratio, High Volume Fly Ash Concrete, Compressive Strength.*

INTRODUCTION

The challenge for the civil engineering community in the near future will be to realize projects in harmony with the concept of sustainable development, and this involves the use of high-performance materials and products manufactured at reasonable cost with the lowest possible environmental impact. Concrete is the most widely used construction material worldwide. However, the production of Portland cement, an essential constituent of concrete, releases large amounts of CO_2 which is a major contributor to the greenhouse effect and the global warming of the planet and the developed countries are considering very severe regulations and limitations on CO_2 emissions. In this scenario, the use of supplementary cementing materials (SCMs), such fly ash, slag and silica fume, as a replacement for Portland cement in concrete presents one viable solution with multiple benefits for the sustainable development of the concrete industry. The most commonly available SCM worldwide is fly ash, a by-product from the combustion of pulverized coal in thermal power stations. Fly ash, if not utilized has to be disposed of in landfills, ponds or rejected in river systems, which may present serious environmental concerns since it is produced in large volumes. Far to be considered as a "Waste" product, research and development has shown that fly ash actually represents a highly valuable concrete material. In order to considerably increase the utilization of fly ash as replacement for cement, such concrete must meet engineering performance requirements that the comparable to those for conventional Portland cement concrete, and be cost effective. This is a particularly important issue for India, which currently produces over 100 million tons of Portland cement and 100 million tons of fly ash annually. Disposal of fly ash is a growing problem in India, only about fifteen percent of this amount is currently used; the remainder goes to landfill. The World Bank has reported that by 2015, disposal of fly ash will require 1,000 square kilometers, or 1 square meter of land per person. The Indian government has begun to take positive steps in the utilization of fly ash in construction, such as mandating the use of fly ash in road and building construction projects within a 100 km radius of a coal fired power plant.

NECESSITY AND AIM OF THE PRESENT STUDY

Mineral admixtures such as silica fume, fly ash, and ground granulated blast- furnace slag improve the engineering properties and performance of concrete when they are used as mineral additives or as a partial cement replacements. Economic (lower cement requirement) and environmental considerations have also played a great role in the rapid increase in usage of mineral admixtures. Compared with the rapid increase in usage of mineral admixtures , Compared with the Portland cement, cement with pozzolana helps to have concrete with less permeability and denser calcium silicate hydrate (C-S-H). Ground granulated blast furnace slag, silica fume, metakaolin, and rice-husk ash can be used in concrete as supplementary cementing materials (SCM) in addition to fly ash. Compared to fly ash, the availability of other materials is rather limited. One of the major institutional barriers against the use of fly ash and other supplementary cementing materials is the prescriptive type of specifications and standards.

LITERATURE REVIW:

ACI COMMITTEE REPORT NO. 226 [(1)] discussed the specifications for material testing, quality assurances for fly ash concrete and making use of good proportion of fly ash.**. ANDRE BISAILLON et.al** [(2)] presented the comparative data on high-volume fly ash concrete made with ASTM Type 1 cement, and control concrete for mass concrete applications made with ASTM Type 1 and a modified version of ASTM Type 11 cements. **ALAIN BILOIDEAU et.al**[(3)] discussed the challenge for the civil engineering community in the near future e to realize projects in harmony with the concept of sustainable development, and involving the use of high-performance materials produced at reasonable cost with the lowest possible environmental impact. **ALBERT N. NOUMOWE** [(4)] carried out investigations on the behavior of three concretes (high– strength concrete with and without polypropylene fibers and light weight aggregate concrete). The three groups of specimens were subjected to identical testing conditions. After a heating – and – cooling cycle at 200^0C, mechanical tests were carried out. Thermal gradient and concrete thermal stability during heating, compressive strength, modulus of elasticity, and splitting tensile strength were analyzed. **FRANCIS A.OLUOKUN** [(5)] investigated the applicability of Abram's law to concrete mixes containing fly ash. As initially expected, it was found that Abram's water cement ratio law is not directly applicable to mixes with fly ash. An alternative augmented water-cementitious material ratio law is proposed for designing concrete mixes containing fly ash. **DUNSTAN M.R.H** [(6)] in their investigations on fine aggregate proportions to aid pumping. This may require a higher cement to maintain an equal slump and water cement ratio and hence strength. Use of fly ash may reduce the amount of fine aggregate needed in these mixtures and allow better balance of fine and coarse aggregate. Today there are few mass concrete dams built in part of the world that contain fly ash in the concrete.

OBJECTIVES OF STUDY:

To develop relationship between water / binder ratio and compressive strength of High volume Fly Ash Concrete**.**

MATERIALS

Cement

Ordinary Portland cement of 53 grade which meets the physical requirements in accordance with IS: 12269-1987 and for chemical requirements in accordance with IS: 4032-1977 was used as Cement

Fly Ash

The Fly Ash obtained from Vijayawada thermal power station having the specific gravity of 2.12 and Blaine's fineness 577 m^2/kg and confirming with the IS requirements as per IS 3812-1981was used.

Fine Aggregate

The locally available river sand is used as fine aggregate in the present investigation. The sand is free from clay, silt and organic impurities. The sand is tested for various properties like specific gravity, bulk density etc., in accordance with IS 2386-1963

Coarse Aggregate

Machine crushed angular granite metal of 20mm nominal size from the local source is used as coarse aggregate. It is free from impurities such as dust, clay particles and organic matter etc. The course aggregate is also tested for its various properties. The specific gravity, bulk density and fineness modulus of coarse aggregate were found to be 2.62, 1580 kg/m^3 and 7.17 respectively.

Super plasticizer
Sulphonated naphthalene formaldehyde (SNF) superplasticizer Complying with IS: 9103 -1999, BS 5075, ASTM C- 494 was used.

Fibres
The fibres used in present investigation is mild steel wire of diameter 0.8 mm. Length of fibres is 40 mm and aspect ratio 50.

DISCUSSION OF RESULTS

Workability
The quantities of materials for one cubic meter of ordinary and high volume fly ash concrete along with compaction factor are shown in Table 1.0 and 2.0 . It can be seen from the table that a medium workability was maintained for almost all the mixes by addition of suitable quantities of super plasticizer.

Variation of Compressive Strength
From table 3.0 It can be seen that the strength various from 39.90 to 66.6 Mpa for ordinary concrete, with decrease in water/cement ratio . For the corresponding high volume fly ash concrete mixes the strength varies from 35.15 to 70.66 Mpa. From Table 3.0 the percentage variation of compressive strength of ordinary and high volume fly ash concrete at 28 days. The percentage increase in compressive strength in ordinary concrete is in between 10% to 15% for w/c 0.55 to 0.40. For lesser w/b ratios the high volume fly ash concrete have better strength compared to ordinary concrete.

Compressive strength and water/binder ratio
The variation of compressive strength with water/binder ratio is shown in Fig. 1-9, for both ordinary concrete and high volume fly ash concrete. It can be seen from Fig. 2, that the high volume fly ash concrete strength decreased as the water/binder ratio increased from 0.27 to 0.55. Fig. 3 shows the best fit curve for high volume fly ash concrete and ordinary concrete for different water/binder ratio. Fig. 4 shows the relationship between the compressive strength and water/cementitious material ratio (30% replacement fly ash) as suggested by R.K. Dhir, university of Dundee. Fig. 5 and 6 show the predicted compressive strength from the equation for various water/binder ratio for ordinary and high volume fly ash concrete. Fig. 7 represents the predicted compressive strength for both ordinary and high volume fly ash concrete. Fig. 8 shows the compressive strength at 28 days for ordinary and high volume fly ash concrete and also predicted compressive strength of ordinary and high volume fly ash concrete. Fig. 9 represents the relationship between the water/cement ratio and compressive strength from Bureau of Indian standards.

Equations for Compressive Strength of High Volume Fly ash Concrete
Mathematical equations were obtained expressing compressive strength in terms of water/binder ratio for ordinary concrete and high volume fly ash concrete. These are given below. Plot of these equations is shown in Fig. 7 for both ordinary concrete and high volume fly ash concrete.
The relationship between water/cement ratio and compressive strength is given by the equation

$$fc = \frac{111.37}{(5.86)^{(w/c)}}$$

For high volume fly ash concrete (50% fly ash used as additional material) the equation is

$$fc = \frac{155.02}{(15.08)^{(w/cm)}}$$

It can be seen that in both ordinary concrete and high volume fly ash concrete, equation for compressive strength is in the same form.

$$fc = \frac{a}{b^{(w/c)}}$$

This relation is similar to that given by Duff Abrams in 1918 relating compressive strength and water/cement ratio. The relation is also valid for high volume fly ash concrete with fly ash used as additional material.
Alternatively water/binder ratio of high volume fly ash concrete can be expressed as

$$w/b = \frac{12.60}{(fc)^{0.88}}$$

CONCLUSIONS

The fly ash used in these investigations exhibits good Pozzolanic properties and can be used in the production of high strength high volume fly ash concrete. High volumes of fly ash up to 50% can be used as additional material without sacrificing strength at lower w/b ratios. Further, addition of fly ash makes the concrete more impermeable due to micro filler action.

The relation between compressive strength and water binder ratio of high volume fly ash concrete is

$$fc = \frac{155.02}{(15.08)^{(w/cm)}}$$

Alternatively, the water/binder ratio can be expressed in terms of compressive strength of high volume fly ash concrete as

$$w/b = \frac{12.60}{(fc)^{0.88}}$$

REFERENCES

[1] ACI Committee Report NO. 226, BR8 "Use of Flyash"ACI Material Journal Sept/Oct 1987.

[2] Andre Bisaillon, Michael Rivest, and V.M.Malhotra " Performance of High – Volume Fly ash concrete in Large Experimental Monoliths" ACI Materials Journal, March/April, 1994

[3] Alain Biloideau and V.Mohan Malhotra "High-Volume Fly ash system: Concrete Solution for Sustainable Development" ACI Material Journal, January-February, 2000

[4] Albert N. Noumowe " Temperature Distribution and Mechanical Properties of High-Strength Silica Fume Concrete at Temperatu5res up to 200^{0}C" ACI Material Journal, July-August, 2003.

[5] Dunstan M.R.H. "Rolled concrete for dams – A laboratory study of High Fly ash concrete" Technical Note No. 105 Construction industry Research and information Association London. 1981. pp 94.

[6] Francis A. Oluokun "Fly Ash concrete Mix Design and the Water-Cement Ratio law" ACI Materials Journal / July – August 1994.

Table 1.0 Quantities of Materials for One Cubic Meter of Ordinary Concrete with Workability

w/c	Cement (Kg)	Fine Aggregate (Kg)	Coarse Aggregate (Kg)	Water (liters)	Super Plasticizer (ml)	Compaction Factor
0.55	320.0	684.0	1079.0	178	--	0.96
0.53	335.0	670.0	1080.0	178	--	0.95
0.50	350.0	657.0	1081.0	178	--	0.94
0.48	370.0	634.0	1088.0	178	1110.0	0.94
0.46	388.0	612.0	1096.0	178	1161.0	0.92
0.44	404.0	640.0	1053.0	178	1212.0	0.94
0.42	425.0	568.0	1110.0	178	1275.0	0.87
0.40	445.0	563.0	1099.0	178	1335.0	0.88
0.38	470.0	524.0	1118.0	178	2350.0	0.92
0.36	472.0	517.0	1129.0	178	2472.0	0.94
0.34	524.0	494.0	1104.0	178	2618.0	0.87
0.32	556.0	477.0	1093.0	178	2781.0	0.94
0.30	593.0	460.0	1077.0	178	2967.0	0.95
0.27	659.0	436.0	1047.0	178	3296.0	0.92

Table 2.0 Quantities of Materials of High Volume Fly Ash concrete along with Workability

w/b	w/c	Cementi-tious material (Kg)	Cement (Kg)	Fly ash (Kg)	Fine Aggregate (Kg)	Coarse Aggregate (Kg)	Water (liters)	Super Plasticizer (ml)	Compaction Factor
0.55	0.83	320.0	213.0	107.0	718.0	1134.0	178	--	0.96
0.53	0.79	335.0	223.0	112.0	706.0	1138.0	178	--	0.98
0.50	0.75	350.0	237.0	119.0	693.0	1140.0	178	--	0.95
0.48	0.72	370.0	246.0	124.0	672.0	1154.0	178	--	0.96
0.46	0.69	388.0	258.0	129.0	651.0	1165.0	178	--	0.95
0.44	0.66	404.0	270.0	134.0	630.0	1178.0	178	--	0.95
0.42	0.63	425.0	283.0	142.0	609.0	1190.0	178	--	0.91
0.40	0.60	445.0	296.0	149.0	588.0	1200.0	178	--	0.95
0.38	0.56	470.0	313.0	157.0	566.0	1209.0	178	--	0.90
0.36	0.54	472.0	330.0	165.0	553.0	1207.0	178	--	0.90
0.34	0.50	524.0	350.0	174.0	539.0	1205.0	178	--	0.90
0.32	0.48	556.0	370.0	186.0	525.0	1202.0	178	1112.0	0.90
0.30	0.45	593.0	396.0	198.0	511.0	1196.0	178	1188.0	0.95
0.27	0.40	659.0	440.0	220.0	491.0	1178.0	178	1320.0	0.95

Table 3.0 percentage variation of Ordinary And High Volume Fly ash Concrete

S.No.	w/c & w/b	Compressive Strength (MPa)		% Variation
		Ordinary concrete	High volume fly ash concrete	
1.	0.55	39.90	35.15	-11.90
2.	0.53	42.89	37.38	-12.85
3.	0.50	44.00	39.39	-10.47
4.	0.48	46.89	42.55	-9.26
5.	0.46	48.71	44.13	-9.40
6.	0.44	53.87	46.91	-12.92
7.	0.42	56.40	48.87	-13.35
8.	0.40	59.29	55.80	-5.88
9.	0.38	60.04	61.17	1.88
10.	0.36	61.65	62.66	1.64
11.	0.34	62.44	64.18	2.79
12.	0.32	63.42	66.40	4.69
13.	0.30	64.80	68.19	5.23
14.	0.27	66.60	70.66	6.10

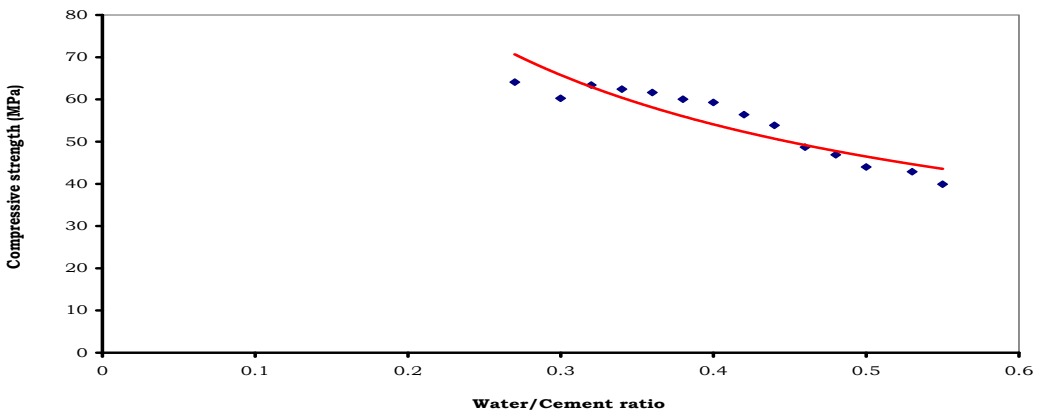

Fig 1.0 Compressive Strength Vs Water/ Cement Ratio for Ordinary Concrete

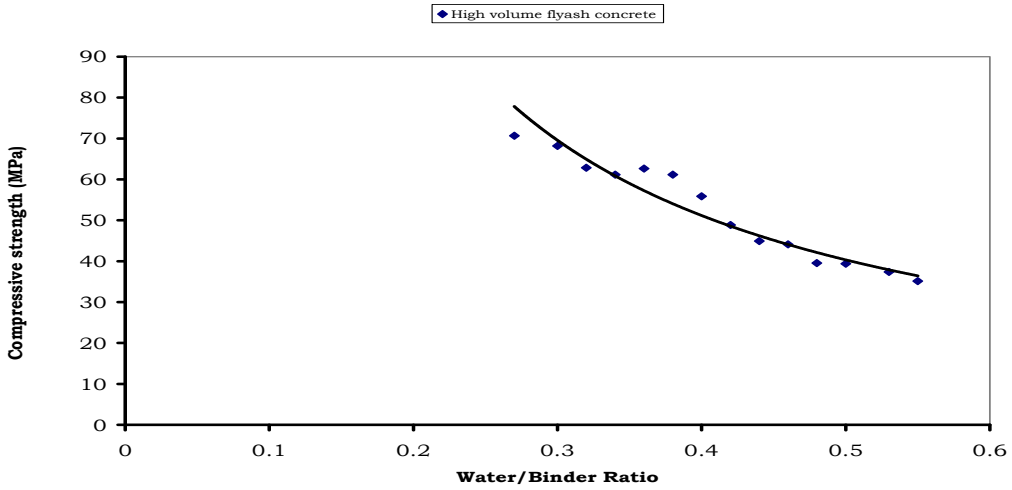

Fig 2.0 Compressive Strength Vs Water/Binder Ratio for High Volume Fly Ash Concrete

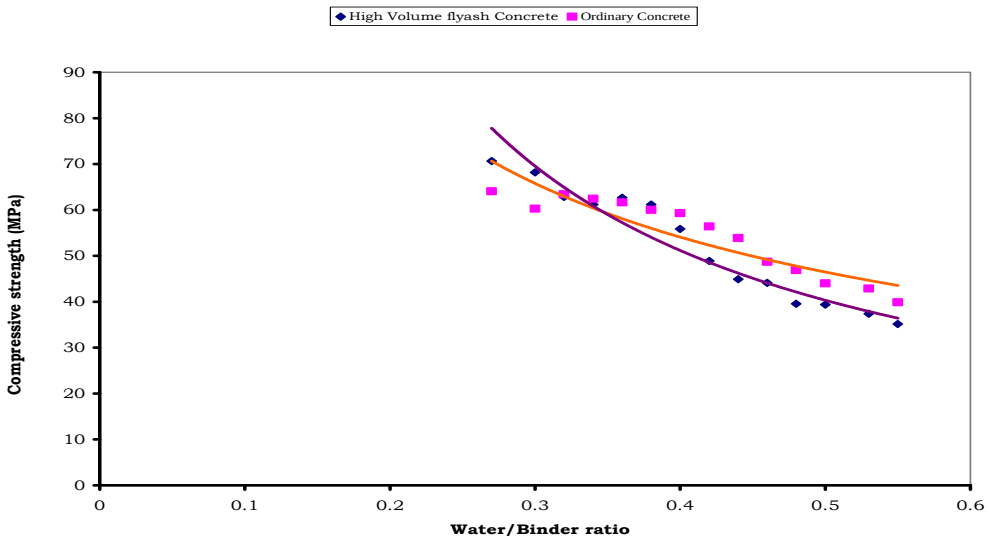

Fig 3.0 Compressive Strength Vs Water/Binder ratio

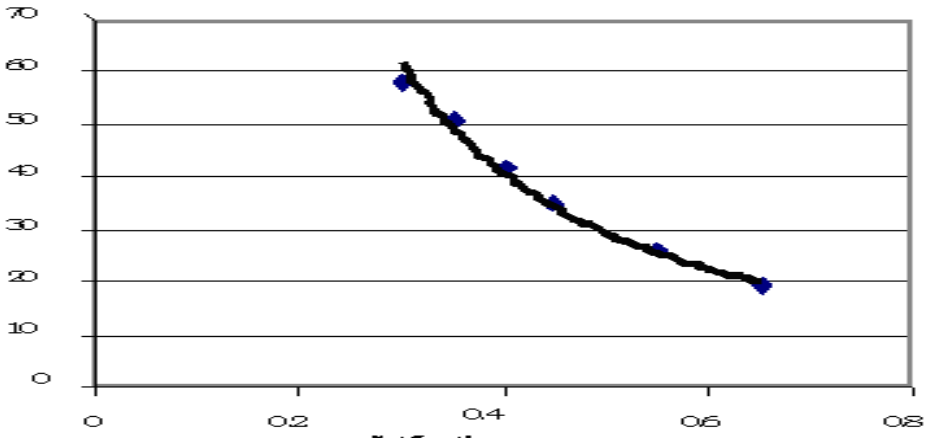

Fig 4.0 . Relation between water/ cement + flyash ratio 28 day cube strength (R.K.Dhir)

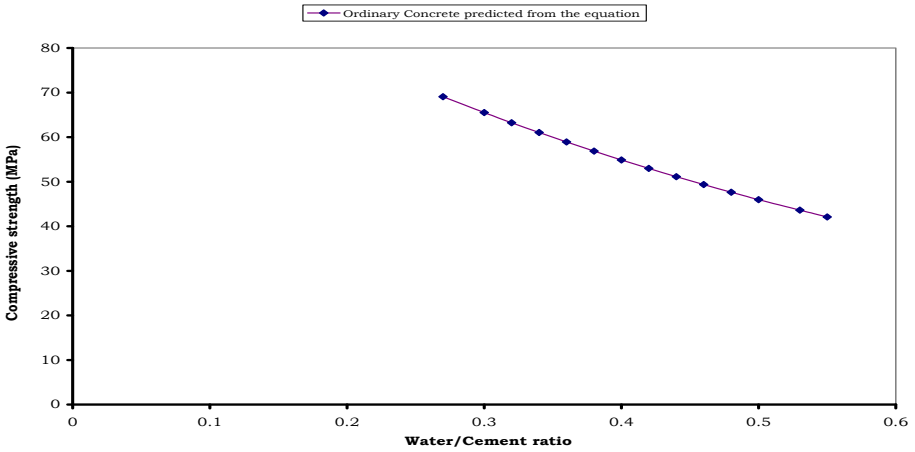

Fig 5.0 Compressive Strength Vs Water/ Cement Ratio For Ordinary Concrete

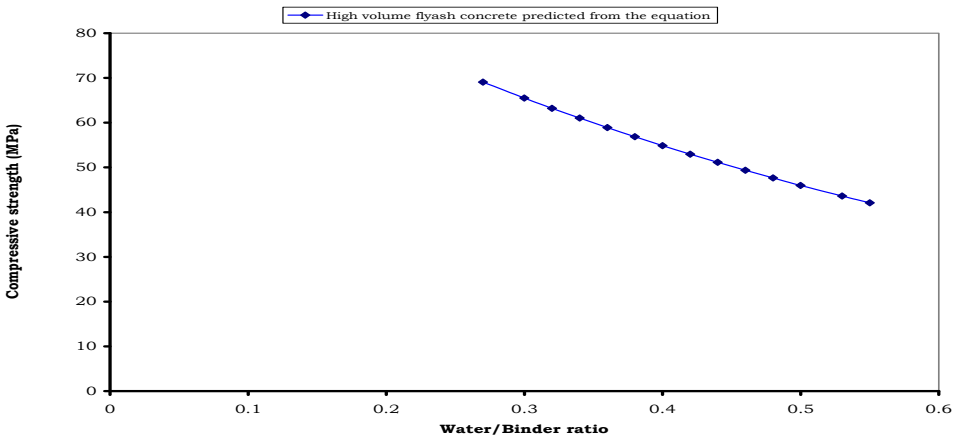

Fig 6.0 Compressive Strength Vs Water/ Binder Ratio for High Volume Fly Ash Concrete

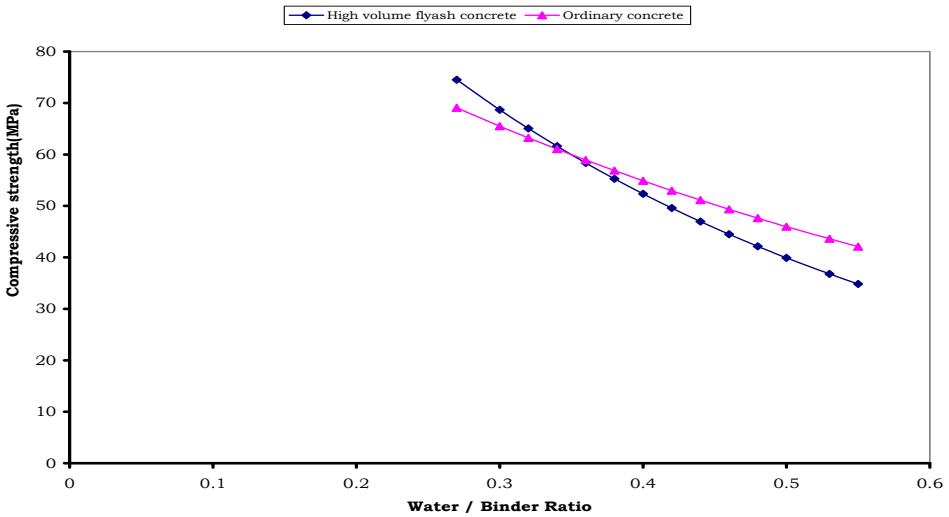

Fig 7.0 Compressive Strength Vs Water/ Binder ratio for Ordinary and High Volume Fly Ash Concrete

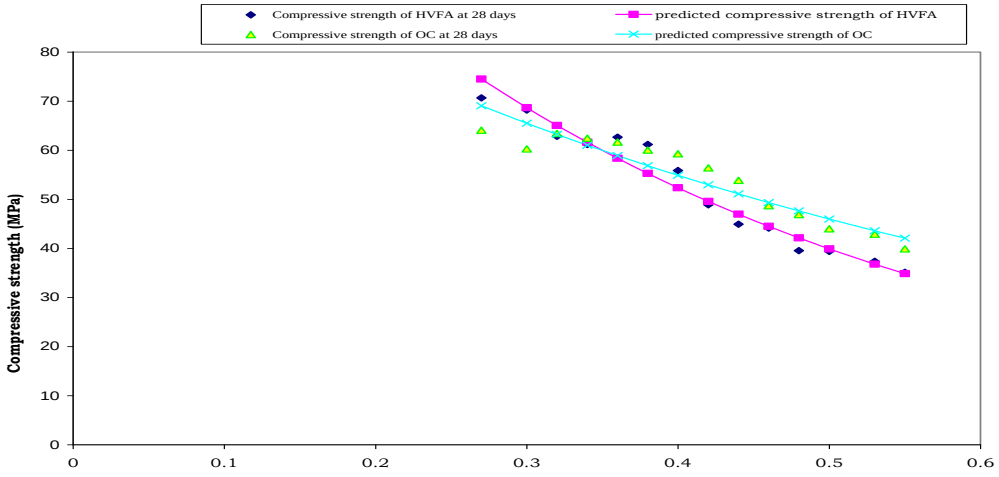

Fig 8.0 Compressive Strength Vs Water/ Binder ratio

Bibliography of Authors

Dr.P. Srinivasa Rao , Professor

Specialized in structural engineering. Research interests are Concrete Technology, Structural Design, High Performance Concrete, Prefabricating Structures, Special Concretes and use of Micro Silica, Fly Ash in Building Materials. He has been associated with a number of Design projects, for number of organizations and involved as a key person in Quality control and Mix Designs. Has 24 years of academic, research and industrial experience published over 100 research papers. He guided four Ph.D and 100 M.Tech projects. Guiding 15 Ph.D students delivered invited lecturers in other organizations and institutions. Member of ISTE, Member of ICI and Member of Institute of Engineers.

Dr. P.Sravana Professor

Specialized in transportation engineering. Research interests are Concrete Technology, High Performance Concrete, Special Concretes, use of Micro Silica, Fly Ash in Building Materials and Pavement Design. She has been associated with a number of Design projects, for number of organizations and involved as a key person in Quality control , Mix Designs and Bitumen Emulsion Tests . Has 15 years of academic, research and industrial experience published over 50 papers.

P.Sarika , Student

Pursuing B.Tech Civil Engineering from VNRVJIT , Bachupally, Nizampet , Hyderabad.

Dr. Seshadri Sekhar.T , Professor

Specialized in structural engineering. Research interests are Concrete Technology, High Performance Concrete, Special Concretes and use of Micro Silica, Fly Ash in Building Materials. Has 23 years of academic, research and industrial experience published over 100 research papers. He is associated with three Ph.Ds and presently guiding one Ph.D candidate and 25 M.Tech projects. Life Member of ISTE, Fellow Member of Institution of Engineers , Member institution of Civil Engineers India , Fellow of IETE and Member of IEEE.

Mr.Apparao Gandi, Assistant Professor

Specialized in Transportation Systems Engineering. Research interests are Pavement Materials, Highway Design, and Concrete Technology. He has 3 years of academic experience and published 6 research papers. He was guided 3 M.Tech projects and currently associated with numerous M.Tech and B.Tech Projects. He involved various consultancy works with private and state government projects. Associate member of ASCE, and Member of IRC.